

# Aeroacoustic analyses of the saxophone mouthpiece with applications to mouthpiece design

*Song Wang*



Music Technology Area, Department of Music Research  
Schulich School of Music  
McGill University  
Montreal, Canada

September 2023

---

A thesis submitted to McGill University in partial fulfillment of the requirements for the  
degree of PhD in Music Technology.

© 2023 Song Wang

## Abstract

The mouthpiece is one of the key components of a saxophone in determining its sound and playability. However, the design of mouthpieces still heavily relies on empirical approaches due to the lack of physical analyses connecting geometry variations with corresponding changes in sound quality and response. The objective of this research is to perform a series of analyses to better understand the mechanisms behind saxophone sound generation and the mouthpiece's impact on shaping the oscillation characteristics, consequently assisting in mouthpiece design.

The mouthpiece functions as both a linear passive acoustic filter that sculpts saxophone's acoustic features, and a nonlinear active sound generator that, in conjunction with the reed, transforms steady energy sources into unsteady oscillations. These two distinct roles of the mouthpiece are studied separately using acoustic and aeroacoustic analyses.

The acoustic analysis of the mouthpiece is conducted by analyzing its input impedance defined at the rectangle aperture at the tip of the mouthpiece. Two novel acoustic models for the mouthpiece are proposed, namely the transfer matrix model (TMM) and the transmission line model (TLM). TMM, derived from the finite element mouthpiece model using the two-load method, is validated by the input impedance measurement and proves to be an accurate and efficient model for acoustic characterization. TMM is also incorporated into real-time sound synthesis for oscillation characterization, which includes both sound and bifurcation analyses. TLM is a simpler model that represents the mouthpiece as piecewise cylindrical segments. A mouthpiece design interface is implemented based on TLM, which allows customizable one-dimensional mouthpiece geometries and provides instant synthesis of the input impedance and sound.

The aeroacoustic analysis of the mouthpiece is based on computational aeroacoustic modeling of the mouthpiece and the Ffowcs-Williams and Hawkings (FW-H) acoustic analogy. The two-dimensional computational model is built using the lattice-Boltzmann (LB) method. A characteristic-based time-domain impedance boundary condition (C-TDIBC) is proposed to improve simulation efficiency. C-TDIBC utilizes the input impedance to represent an acoustic resonator, which transforms the distributed acoustic field into a localized representation applied as a boundary condition to the end of the mouthpiece-reed system in the LB simulation. The FW-H acoustic analogy is applied on top of LB simulations, which helps characterize the sound generation mechanisms by decomposing the aeroacoustic source into

monopole, dipole, and quadrupole contributions.

Finally, the acoustic and aeroacoustic analysis routines are employed to investigate the influence of two design parameters, namely the chamber size and baffle height, on oscillations, which demonstrates the feasibility and capability of the proposed methodology for mouthpiece modeling.

## Résumé

Le bec est l'un des éléments les plus importants dans la production du son et la jouabilité du saxophone. Cependant, la conception des becs repose encore largement sur des approches empiriques en raison du manque d'analyses physiques reliant les variations de géométrie aux changements corrélatifs de la qualité du son et de la réponse acoustique. L'objectif de cette recherche est d'effectuer une série d'analyses afin de mieux comprendre les mécanismes à l'origine de la production du son du saxophone et l'impact du bec sur la formation des caractéristiques d'oscillation, ce qui contribuera à la conception du bec.

Le bec agit à la fois comme un filtre acoustique passif linéaire qui sculpte les caractéristiques acoustiques du saxophone, et comme un générateur de son actif non linéaire qui, en conjonction avec l'anche, transforme des sources d'énergie stables en oscillations instables. Ces deux rôles distincts du bec sont étudiés séparément à l'aide d'analyses acoustiques et aéroacoustiques.

L'étude acoustique du bec est réalisée en analysant son impédance d'entrée au niveau de l'ouverture rectangulaire située à l'extrémité du bec. Deux nouveaux modèles acoustiques pour le bec sont proposés: le modèle de matrice de transfert (TMM) et le modèle de ligne de transmission (TLM). Le TMM, qui est dérivé d'un modèle du bec à éléments finis basé sur la méthode des deux charges, est validé par la mesure de l'impédance d'entrée et s'avère être un modèle précis et efficace pour la caractérisation acoustique. Le TMM est également incorporé dans la synthèse sonore en temps réel pour la caractérisation de l'oscillation, qui comprend à la fois des analyses sonores et des analyses de bifurcation. Le TLM est un modèle plus simple qui représente le bec sous forme de segments cylindriques par morceaux. Basé sur le TLM, une interface conception de becs est proposé qui admet des géométries unidimensionnelles personnalisables et fournit une simulation instantanée de l'impédance d'entrée et du son produit.

L'analyse aéroacoustique du bec est basée sur une modélisation computationnelle aéroacoustique bidimensionnel construit à l'aide de la méthode Boltzmann sur réseau (LB pour lattice Boltzmann en anglais), et aussi sur l'analogie acoustique Ffowcs-Williams et Hawkings (FW-H). Une condition limite d'impédance caractéristique dans le domaine temporel (C-TDIBC) est proposée pour améliorer l'efficacité de la simulation. La C-TDIBC utilise l'impédance d'entrée pour représenter un résonateur acoustique en transformant le champ acoustique distribuée en une représentation localisée appliquée comme condition limite à

l'extrémité du système bec-anche dans la simulation LB. L'analogie acoustique FW-H est appliquée aux simulations LB, ce qui permet de caractériser les mécanismes de génération du son en décomposant la source aéroacoustique en contributions monopolaires, dipolaires et quadripolaires.

Enfin, les routines d'analyse acoustique et aéroacoustique sont utilisées pour étudier l'influence de deux paramètres de conception, à savoir la taille de la chambre et la hauteur du plafond, sur les oscillations, ce qui démontre la faisabilité et la capacité de la méthodologie proposée pour la modélisation du bec.

## Acknowledgments

First and foremost, I would like to sincerely thank my supervisor, Prof. Gary P. Scavone, for his remarkable support throughout my doctoral studies. I am fortunate to have had the opportunity to be part of CAML under his supervision, and his guidance, assistance, trust and encouragement have been invaluable for my thesis work.

I would extend my gratitude to Prof. Luc Mongeau for his generous support in granting me access to his lab facilities and for the precious suggestions and opportunities he has provided.

I am grateful to Dr. Esteban Maestre for kindly sharing the sound synthesis program that played a significant role in my research. I am thankful for his inspiring discussion and honored by his invitation to join Outer Echo.

I would like to thank Prof. Philippe Depalle for his exceptional teaching in digital signal processing and for agreeing to review my thesis. I am also thankful to Prof. Marcelo Wanderley for reminding me that a better synthesizer does not necessarily imply a better sound. I will keep in mind the importance of gesture control and mappings as I continue my journey towards better physical modeling of musical instruments.

My gratitude extends to Prof. Andrey da Silva for accepting to be a reader for my thesis and for the fruitful discussion we had following my comprehensive exam and during his visit back to CAML. I also wish to acknowledge Prof. Siva Nadarajah for his suggestions in the early stage of my research, Prof. Tim Lee for his informative seminar on fluid dynamics and his thoughtful career advice, Prof. Vasileios Chatziioannou for feedback on my research and sharing the code for the reed collision model, and Prof. Mico Hirschberg for the enlightening discussion on the application of the Ffowcs Williams and Hawkings acoustic analogy in a single-reed instrument.

I am thankful to Darryl Cameron for his constant assistance in solving various technical problems, which allowed me to stay focused on my thesis. I am grateful to Yves Méthot from CIRMMT for his help with 3D printing for my project. I would also like to thank Helene Drouin for her support in addressing various problems with registration and study permit.

I would like to thank my lovely colleagues in CAML, Lei Fu, Connor Kemp, Wen Xiao, Negin Abaeian, Douglas Beaton, Harish Venkatesan, Camilo Andrés Gómez Bonilla, Vincent Turcotte, Navin Kumar, Alberto Acquilino, Tianxing Zhong, Champ Darabundit, Margaret Hopkins, Miranda Jackson, Theodora Nestorova, Ninad Puranik, Matthew Skarha, Graham

Smith, for their collaboration, discussions, and enthusiasm. I will think of CAMLIans every time I see a chameleon, or, of course, a camel.

I would give special thanks to Connor Kemp for his assistance in building the artificial blower. The first time we played the saxophone with a tea-canister-made mouth box remains a memorable experience for me. I would like to thank Tianxing Zhong for his assistance in documenting my CAD mouthpiece model and writing a Python script for generating its cross-section area function. I would like to thank Shi Yong for generously sharing his LBM code and for sharing his personal experiences at McGill and Montréal prior to my arrival, which has greatly facilitated my smooth transition to the new environment. I am also deeply indebted to Prof. Zijin Li for the countless opportunities and support she has provided ever since I have known her.

I would also like to thank students and friends from Prof. Luc Mongeau's research group, particularly Zhengdong Lei, Zixin He, Sareh Taheri, and Guanyu Bao for their help with lab equipment and their patience in enduring the monotonous and loud noise during my acoustic experiment. I am also grateful to Mostafa Najafiyazdi, Miguel Chávez-Modena, Rayane Ait Oubahou, and Pooya Saberi for their valuable input during our conversations and meetings, which have enhanced my understanding of numerical simulations and the lattice Boltzmann method.

I would like to thank my friends in Music Technology, Yaolong Ju, Eduardo Meneses, Johnty Wang, Martha Thomae, Xin Wang, Lena Heng, Erica Huynh and many others, for their friendship throughout my journey.

I am thankful to the Schulich School of Music and CIRMMT for their financial support.

Finally, I would like to express my sincere gratitude to every member of my family. I am deeply grateful to my parents for their endless support and unconditional love, and to my parents-in-law for their companionship. I am thankful to my wife Wei for venturing on this journey alongside me, and to my son Aaron for joining midway, as their presence and support have brought immense joy and additional significance to my life and pursuits.

## Contribution of Authors

This document is formatted as a monograph dissertation and includes contents from the following publications:

### Chapter 5

- Wang, S., Maestre, E. and Scavone, G. Lattice Boltzmann modeling of a single-reed instrument using a time-domain impedance boundary condition. *Fourth Vienna Talk on Music Acoustics*, Vienna, Austria, 2022.

### Chapter 6 and Appendix C

- Wang, S., Maestre, E. and Scavone, G. Acoustical modeling of the saxophone mouthpiece as a transfer matrix. *The Journal of the Acoustical Society of America*, 149(3):1901-1912, 2021
- Wang, S., Scavone, G., and Maestre, E. Two methods for acoustic modeling of the saxophone mouthpiece. *The Journal of the Acoustical Society of America*, 148(3): 2611, 2020.

### Chapter 7

- Wang, S., Maestre, E., and Scavone, G. Characterization of Single-Reed Instrument Sound Generation Based on Ffowcs Williams-Hawkings Analogy. In *Proceedings of the Stockholm Music Acoustics Conference 2023*, Stockholm, Sweden, 2023.
- Wang, S., and Scavone, G. Computational aeroacoustic modeling of single-reed mouthpiece using Palabos. In *Proceeding of the International Symposium on Musical Acoustics 2019*, Detmold, Germany, 2019.

### Appendix B

- Wang, S., and Scavone, G. Computational aeroacoustics for low Mach number flow using the lattice Boltzmann method. *The Journal of the Acoustical Society of America*, 148(4): 2694, 2020.

The candidate was responsible for designing and conducting physical experiments, deriving and implementing the numerical models, and preparing manuscripts for the aforementioned publications. Dr. Gary Scavone provided comprehensive supervision throughout the

present research, including regular advisory meetings, manuscripts and presentation material reviews. He also offered necessary funding, equipment, software and measurement facilities. Dr. Esteban Maestre made valuable contributions by providing the programs for impedance fitting and saxophone sound synthesis, which were utilized in various parts of the thesis and resulted in collaborative publications.

---

# Contents

<b>1</b>	<b>Introduction</b>	<b>1</b>
1.1	Saxophone mouthpieces . . . . .	1
1.2	Literature review on mouthpieces . . . . .	4
1.3	Thesis objectives and scope . . . . .	4
1.4	Thesis outline . . . . .	6
<b>2</b>	<b>Literature Review</b>	<b>9</b>
2.1	Physics and modeling of single-reed instrument sound generation . . . . .	10
2.1.1	Early development of mathematical framework . . . . .	11
2.1.2	Reed vibration . . . . .	15
2.1.3	Airflow . . . . .	18
2.1.4	Resonator . . . . .	22
2.2	Oscillation characteristics of the dynamical system . . . . .	24
2.2.1	Reed . . . . .	25
2.2.2	Resonator . . . . .	26
2.2.3	Airflow . . . . .	28
2.2.4	Player . . . . .	28
2.3	Methodology Review . . . . .	30
2.3.1	Theoretical and analytical studies . . . . .	30
2.3.2	Experimental study . . . . .	31
2.3.3	Numerical study . . . . .	32
<b>3</b>	<b>Acoustics and aeroacoustics fundamentals</b>	<b>38</b>
3.1	Governing equations of fluid dynamics . . . . .	38
3.1.1	Continuity equation . . . . .	38

---

3.1.2	Momentum Equation . . . . .	39
3.1.3	Energy equation . . . . .	41
3.2	Acoustics fundamentals . . . . .	42
3.2.1	Speed of sound . . . . .	42
3.2.2	Acoustic wave equation . . . . .	43
3.2.3	Green's function . . . . .	43
3.2.4	Plane waves in cylindrical pipes . . . . .	45
3.2.5	Transfer matrix of cylindrical pipes . . . . .	47
3.3	Aeroacoustics analogy . . . . .	47
3.3.1	Lighthill's acoustic analogy . . . . .	47
3.3.2	Ffowcs Williams-Hawkings equation . . . . .	48
3.3.3	One dimensional FW-H acoustic analogy for internal flow aeroacoustic problems . . . . .	51
<b>4</b>	<b>Lattice Boltzmann method fundamentals</b>	<b>53</b>
4.1	From Boltzmann equation to lattice Boltzmann method . . . . .	53
4.1.1	The Boltzmann equation . . . . .	54
4.1.2	From Boltzmann equation to macroscopic equations . . . . .	57
4.1.3	Discretization in velocity space . . . . .	59
4.1.4	Discretization in time and space . . . . .	64
4.1.5	Lattice Boltzmann method . . . . .	65
4.1.6	Unit Conversion . . . . .	65
4.2	Recursive regularized lattice Boltzmann method . . . . .	67
4.2.1	Regularized BGK . . . . .	67
4.2.2	Recursive regularized BGK . . . . .	69
4.3	Boundary Conditions . . . . .	69
4.3.1	Dirichlet boundary condition . . . . .	70
4.3.2	Non-reflecting boundary conditions . . . . .	72
4.3.3	Immersed boundary method . . . . .	73
4.4	<i>Why LBM?</i> . . . . .	77
<b>5</b>	<b>Characteristic-based time-domain impedance boundary condition</b>	<b>79</b>
5.1	Characteristic boundary condition . . . . .	80

---

5.1.1	Characteristic decomposition of hyperbolic systems . . . . .	80
5.1.2	Navier-Stokes characteristic boundary conditions . . . . .	82
5.2	Plane wave masking . . . . .	87
5.2.1	PWM for non-reflecting boundary conditions . . . . .	88
5.2.2	PWM for reflecting boundary conditions . . . . .	89
5.3	Time-domain impedance boundary condition . . . . .	90
5.4	Implementation of C-TDIBC in LBM . . . . .	93
5.5	Validations of characteristic-based boundary conditions . . . . .	95
5.5.1	Non-reflecting boundary condition . . . . .	95
5.5.2	Characteristic-based time-domain impedance boundary condition . . . . .	99
<b>6</b>	<b>Acoustical Modeling of the Saxophone Mouthpiece</b>	<b>101</b>
6.1	Introduction . . . . .	101
6.2	Acoustic characterization of the mouthpiece . . . . .	103
6.2.1	Definition of the Mouthpiece Input Impedance . . . . .	103
6.2.2	Input Impedance Measurements . . . . .	105
6.3	Finite element modeling of the mouthpiece . . . . .	106
6.3.1	Validation of the finite element model . . . . .	107
6.4	Transfer matrix modeling of the mouthpiece . . . . .	107
6.4.1	Validation of the transfer matrix model . . . . .	110
6.4.2	Acoustic comparison between different mouthpiece models . . . . .	111
6.4.3	Sound and dynamics comparison between different mouthpiece models . . . . .	117
6.5	Transmission line modeling of the mouthpiece . . . . .	125
6.6	Discussion . . . . .	127
<b>7</b>	<b>Aeroacoustical Modeling of the Saxophone Mouthpiece</b>	<b>130</b>
7.1	Lattice Boltzmann aeroacoustic model of the mouthpiece . . . . .	131
7.1.1	Mouthpiece Model . . . . .	131
7.1.2	Reed Model . . . . .	132
7.2	Validation of C-TDIBC in aeroacoustic modeling of single-reed mouthpieces . . . . .	135
7.2.1	Validation procedure . . . . .	135
7.2.2	Simulation details . . . . .	136
7.2.3	Results and discussion . . . . .	137

---

7.2.4	Conclusion . . . . .	143
7.3	Sound generation characterization using Ffowcs-Williams and Hawkings acoustic analogy . . . . .	144
7.3.1	Definition of the integral domain . . . . .	144
7.3.2	Choices of Green’s function . . . . .	146
7.3.3	Simulation details . . . . .	151
7.3.4	Results and discussion . . . . .	152
7.3.5	Conclusion . . . . .	160
<b>8</b>	<b>Aeroacoustic study of the influence of saxophone mouthpiece design</b>	<b>164</b>
8.1	Analysis procedures . . . . .	165
8.1.1	Preprocessing . . . . .	165
8.1.2	Acoustic modeling . . . . .	167
8.1.3	Aeroacoustic modeling . . . . .	169
8.2	Influence of the chamber size . . . . .	170
8.3	Influence of the baffle height . . . . .	177
8.3.1	Acoustics modeling . . . . .	177
8.3.2	Aeroacoustic modeling . . . . .	183
8.4	Discussion . . . . .	186
<b>9</b>	<b>Conclusions and perspectives</b>	<b>188</b>
9.1	Contributions . . . . .	189
9.2	Suggestions for future work . . . . .	190
<b>A</b>	<b>Review on artificial blowers</b>	<b>193</b>
A.1	Control . . . . .	194
A.1.1	Blowing pressure . . . . .	194
A.1.2	Lip . . . . .	195
A.1.3	Tonguing . . . . .	196
A.2	Measurements . . . . .	196
A.2.1	Mouth and mouthpiece pressure . . . . .	196
A.2.2	Reed displacement and tip opening . . . . .	197
A.2.3	Air flow rate . . . . .	198
A.2.4	Lip force . . . . .	198

---

<b>B</b>	<b>LBM benchmark problems</b>	<b>199</b>
B.1	Acoustic Point Source . . . . .	199
B.2	Flow passing 2D cylinder . . . . .	200
B.3	Sound radiation of cylindrical ducts . . . . .	201
B.4	Sound radiation of horns . . . . .	203
B.5	Axisymmetric LBM . . . . .	206
<b>C</b>	<b>TLM-based mouthpiece design interface</b>	<b>208</b>
	<b>References</b>	<b>211</b>

---

# List of Figures

1.1	Mouthpiece's structure. . . . .	2
1.2	The illustration of the interaction between multiple physical fields. . . . .	3
1.3	Thesis outline. . . . .	8
2.1	Illustration of the single-reed instrument as a self-sustained oscillator. . . . .	11
2.2	Illustration of the single-reed instrument sound generation framework. . . . .	14
2.3	Illustration of the fluid field in a long reed channel mouthpiece ( $L/h \gg 1$ ) that involves all three different flow regimes. The fluid model labels indicate the range of $L$ to apply the corresponding fluid model. . . . .	21
2.4	A schematic of the regimes on the mouth pressure - lip force plane (left) and an example of the map (right). Reproduced from Almeida et al. (2013), with the permission of AIP Publishing. . . . .	29
3.1	Illustration of fluid domain with the function $f(\mathbf{x})$ that defines the surface. . . . .	49
3.2	The integral surface for FW-H analogy. . . . .	52
4.1	Illustration of different length scales. Inspired by Krüger et al. (2017, Fig. 1.3) and Horstmann (2018, Fig. 2.3). The picture for the macroscopic is a snapshot of the velocity field of a mouthpiece simulation. . . . .	54
4.2	The derivation framework of the lattice Boltzmann method. . . . .	55
4.3	The D2Q9 velocity set. . . . .	63

4.4	The illustration of the collision and streaming processes of the center node. The solid and dashed arrows represent pre- and post-collision populations, respectively, and the arrow length indicates the population strength. During the streaming process, the black arrows represent the outgoing populations from the center node, while the gray arrows represent incoming populations from adjacent nodes. For clarity, the pre-collision populations of neighboring nodes are not displayed in the leftmost figure. . . . .	66
4.5	The illustration of the general boundary problem. The empty and solid circles represent fluid and boundary nodes, respectively. The arrows represent the populations traveling at different directions, with the dashed ones indicating unknown populations after the streaming process. . . . .	70
4.6	The illustration of the (a) <i>link-wise</i> and (b) <i>wet-node</i> boundaries aligned with the $x$ -axis. The gray and white area represent the solid and fluid regions, respectively, while the empty and solid nodes represent the fluid and boundary nodes, correspondingly. The thick dashed lines represent the wall, which locates across the lattice links (dashed double lines) or aligns with the boundary nodes for the <i>link-wise</i> and <i>wet-node</i> boundaries, correspondingly. . . . .	71
4.7	Illustration of the <i>force spreading</i> and <i>velocity interpolation</i> . The open circles and filled squares represent the Eulerian fluid nodes and Lagrangian solid nodes, respectively. The gray squares represent the area covered by a kernel function. . . . .	74
4.8	Illustration of the IB force calculation. The open circles represent the fluid grids, whereas the filled squares represent the IB nodes. The gray and white regions represent the solid and fluid volumes, respectively. The dotted square denotes the kernel function range for a specific IB node (marked as the red square), and the light blue area encompasses the LB grids used to interpolate the IB force $\mathbf{F}_k$ . . . . .	77
5.1	Illustration of the computational domain with NSCBC applied on the right surface (green) perpendicular to the $x_1$ -axis. $\mathcal{L}_i$ represents wave amplitude variations and the arrows indicate the characteristic wave traveling direction.	86
5.2	The frequency response of the infinite impulse response low-pass filter. . . .	94
5.3	Isocontours of the $y$ -directional velocity at four different time steps. . . . .	96

5.4	Isocontours of pressure at four different time steps. . . . .	96
5.5	The schematic of the setup of wave propagation in a two-dimensional pipe. .	97
5.6	The comparison of measured reflection coefficients for various CBCs under quiescent flow. . . . .	98
5.7	The comparison of measured reflection coefficients for various CBCs under mean flow (Ma=0.1). . . . .	98
5.8	The comparison between the imposed impedance and the measured ones under quiescent flow and mean flow (Ma=0.1). . . . .	99
5.9	The comparison between the imposed reflection coefficients and the measured ones under quiescent flow and mean flow (Ma=0.1). . . . .	100
6.1	The illustration of the mouthpiece input and acoustic cavity, where ①, ② and ③ represent the mouthpiece inner cavity, the wedge-shaped complement, and a half of the mouthpiece, respectively. . . . .	104
6.2	The measured input impedances of the truncated cone, the closed mouthpiece, and the mouthpiece-cone system. . . . .	106
6.3	The measured input impedance of the closed mouthpiece and that simulated using the FE model. . . . .	108
6.4	The comparison of the modulus (top) and argument (bottom) of mouthpiece input impedances computed by the FE model and TMM. . . . .	109
6.5	An illustration of the junction between the mouthpiece and the resonator. . .	110
6.6	The measured input impedance of the mouthpiece-cone system and that cal- culated with TMM using Eq. 6.5. . . . .	111
6.7	The measured input impedance of the mouthpiece-cone system and that cal- culated using TMM, cylindrical mouthpiece model (Cyl.) and the lumped mouthpiece model (Lumped). . . . .	113
6.8	Comparisons of the input impedance and radiation transfer function with (solid lines) and without (dashed lines) the TM mouthpiece for the note B <sup>b</sup> 4 (written). The vertical solid and dashed lines correspond to the equal- tempered scale frequencies of the first and second harmonics of the note, respectively. The input impedance and radiation transfer function with the TM mouthpiece are calculated using Eqs. 6.5 and 6.8, respectively. . . . .	114

6.9	The deviation in cents between the first or second input impedance peak and the equal-tempered scale frequency of different notes. . . . .	115
6.10	Input impedance peak inharmonicities for the different mouthpiece representations. . . . .	116
6.11	Comparisons (from top to bottom) of the modulus of the physical input impedances, the modulus of the normalized input impedances, the argument of the normalized input impedances, the reflection functions, and the radiation transfer functions between the TM mouthpiece (solid lines), cylindrical mouthpiece (dashed lines) and the lumped mouthpiece (dotted lines) coupled with the measured impedance of the alto saxophone resonator for the note B <sup>b</sup> 4 (written). . . . .	117
6.12	The fitting of the modulus (top) and argument (middle) of the impedance and the radiation transfer function (bottom) of the lumped mouthpiece (left), cylindrical mouthpiece (center), and TM mouthpiece (right). In each plot, dashed lines (red) and solid lines (blue) are used to represent the original data and the model, respectively. . . . .	121
6.13	Comparisons of the bifurcation diagrams (top), playing frequencies (middle) and radiated sound spectral centroid (bottom) for increasing (left) and decreasing (right) mouth pressure profiles. The (inverse) oscillation thresholds and (inverse) extinction thresholds are shown in the bifurcation diagrams as vertical solid and dashed lines, correspondingly. . . . .	123
6.14	The comparison of the waveforms among three mouthpiece models when a) $\gamma = 0.8$ and b) $\gamma = 2$ . . . . .	124
6.15	The comparison of the bifurcation delays with different mouth pressure changing rate $k$ . . . . .	125
6.16	The illustration of the mouthpiece slices (vertical thin solid lines) following (a) the path (horizontal dashed lines) perpendicular to the tip window and (b) the path through the center line of the mouthpiece acoustic cavity. . . .	126
6.17	The area functions built based on two different paths. . . . .	126
6.18	The input impedance of a closed mouthpiece calculated by TLMs and FEM. . . . .	127
6.19	The input impedance of the saxophone for the note B <sup>b</sup> 4 (written) simulated with TLMs and TMM. . . . .	128

7.1	The schematic of the simulation setup. . . . .	132
7.2	The schematic view of the mouthpiece-reed-lip interaction. . . . .	133
7.3	The illustration of simulation setups in (a) step 1, (b) step 2, and (c) step 3. . . . .	136
7.4	A comparison of the approximated unflanged pipe radiation coefficients in the $s$ - and $z$ -domains with the analytical expression proposed by Levine and Schwinger (1948). . . . .	138
7.5	The comparison of tip opening in the time domain, with the two rows showing the first and last 0.05 s of signal. . . . .	139
7.6	The comparison of probed pressure in the time domain. . . . .	139
7.7	The comparison of probed velocity in the time domain. . . . .	140
7.8	The comparison of single-period time-domain signals. . . . .	140
7.9	The frequency-domain comparison between the measured tip openings in steps 2 and 3 (top), and the absolute amplitude deviations in dB of harmonics below 8 kHz (bottom). The +3 dB is shown as a reference in the bottom figure by the horizontal dashed line. . . . .	141
7.10	The frequency-domain comparison between the measured pressure in steps 2 and 3 (top), and the absolute amplitude deviations in dB of harmonics below 8 kHz (bottom). The +3 dB is shown as a reference in the bottom figure by the horizontal dashed line. . . . .	142
7.11	The illustration of (a) the definition of an integral domain based on research in confined flows, and (b) a simplified acoustic system comprising four interconnected pipes. . . . .	145
7.12	The integral domain for FW-H acoustic analogy in a saxophone mouthpiece. . . . .	146
7.13	The illustration of the nodes utilized for measuring inlet velocity and pressure. LB nodes on the inlet surface are shown in red circles, while the black squares represent the two additional intersection points of the inlet surface with the mouthpiece and the reed. . . . .	153
7.14	The time-domain comparison of the outgoing pressure between the LB simulation and FW-H with $G$ (fingering B <sup>b</sup> 4). . . . .	154
7.15	The comparison of the outgoing pressure spectra between the LB simulation and FW-H with $G$ (top), and the deviation in dB (bottom) (fingering B <sup>b</sup> 4). . . . .	154
7.16	The time-domain comparison of the outgoing pressure between the LB simulation and FW-H with $G_T$ (fingering B <sup>b</sup> 4). . . . .	155

7.17	The comparison of the outgoing pressure spectra between the LB simulation and FW-H with $G_T$ (top), and the deviation in dB (bottom) (fingering B <sup>b</sup> 4).	155
7.18	The comparison between different contributions to the outgoing pressure at the observer using FW-H with $G$ .	157
7.19	The comparison between different contributions to the outgoing pressure at the observer using FW-H with $G_T$ .	157
7.20	$p_{\text{rms}}$ ratio between different monopole and dipole sound sources at different playing frequencies.	158
7.21	$p_{\text{rms}}$ ratio between the $\rho v_1 v_1$ contribution and inlet monopole at different playing frequencies.	159
7.22	The time-domain comparison of dipole sound sources contributed by different solid walls (fingering B <sup>b</sup> 4).	160
7.23	(a) The $(p_{1j} n_j)_{\text{rms}}$ distribution along solid walls, and (b) the mouthpiece geometry.	161
7.24	(a) The $(p_{1j} n_j)_{\text{rms}}$ distribution along solid walls shown in left $y$ -axis, in compare to the absolute values of solid wall slopes $ dy/dx $ in right $y$ -axis (a) and the mouthpiece geometry (b).	162
8.1	Illustration of two different research categories.	165
8.2	The analysis procedures.	166
8.3	Comparison between inner cavities of mouthpieces with different chamber sizes. The chamber size increases from right to left.	170
8.4	Comparison of input impedances between closed mouthpieces with different chamber sizes.	171
8.5	Comparison of input impedances between saxophones consisting of mouthpieces with varying chamber sizes, and saxophone bodies with the fingering (a) B <sup>b</sup> 3, (b) B <sup>b</sup> 4, and (c) B <sup>b</sup> 5 (written).	172
8.6	Comparison of (a) frequency deviations of input impedance peaks from the equal-tempered scale frequency and (b) inharmonicities of different notes between mouthpieces with different chamber sizes.	173

8.7	Comparisons of the bifurcation diagrams, playing frequencies, radiated sound spectral centroid, and radiated sound energy for linearly increasing (left) and decreasing (right) mouth pressure profiles between mouthpieces with different chamber sizes attach to an alto saxophone (fingering B <sup>b</sup> 4). . . . .	175
8.8	Comparisons of the bifurcation diagrams, playing frequencies, radiated sound spectral centroid, and radiated sound energy for linearly increasing (left) and decreasing (right) mouth pressure profiles between mouthpieces with different chamber sizes attached to an alto saxophone (fingering B <sup>b</sup> 5). . . . .	176
8.9	Comparison of mouthpiece inner geometries with different baffle heights in the sagittal view. . . . .	177
8.10	Comparison of input impedances between closed mouthpieces with different baffle heights. . . . .	178
8.11	Comparison of input impedances between saxophones consisting of mouthpieces with varying baffle heights, and saxophone bodies with the fingering (a) B <sup>b</sup> 3, (b) B <sup>b</sup> 4, and (c) B <sup>b</sup> 5 (written). . . . .	179
8.12	Comparison of (a) frequency deviations of input impedance peaks from the equal-tempered scale frequency and (b) inharmonicities of different notes between mouthpieces with different baffle sizes. . . . .	180
8.13	Comparisons of the bifurcation diagrams, playing frequencies, radiated sound spectral centroid, and radiated sound energy for linearly increasing (left) and decreasing (right) mouth pressure profiles between mouthpieces with different baffle heights attach to an alto saxophone (fingering B <sup>b</sup> 4). . . . .	181
8.14	Comparisons of the bifurcation diagrams, playing frequencies, radiated sound spectral centroid, and radiated sound energy for linearly increasing (left) and decreasing (right) mouth pressure profiles between mouthpieces with different baffle heights attach to an alto saxophone (fingering B <sup>b</sup> 5). . . . .	182
8.15	Comparisons of spectra of FW-H estimation and different sound sources between mouthpieces with different baffle heights. . . . .	184
8.16	Comparisons of the spectral centroid of different sound sources between mouthpieces with different baffle heights. . . . .	184
8.17	Comparison of eight uniformly sampled snapshots of the velocity field within a single period between mouthpieces (a) “baffle 1” and (b) “baffle 4”. . . . .	185

---

B.1	Isocontours of $\rho'$ at time $t = 75\Delta t$ : (a) BGK; (b) MRT; (c) rrBGK. . . . .	200
B.2	Comparisons of $\rho'$ at $y = 50\Delta x$ and $t = 75\Delta t$ between three different collision models. (The $y$ -axis of the plot is zoomed-in to $[-0.001, 0.001]$ for a better comparison.) . . . . .	200
B.3	The snapshots of the vorticity (left) and acoustic (right) fields at $t$ (up) and $t + 2.74$ (bottom), where $t$ corresponds to the negative peak of lift coefficient. . . . .	201
B.4	(a) Comparison of acoustic pressure ( $r, 90^\circ$ ) at time $t + 1.83$ (—), $t + 2.28$ (—), $t + 2.74$ (—), with $t$ corresponding to the negative peak of the lift coefficient. (b) Decay of pressure peaks ( $\circ, \circ, \circ$ ) and the reference line of $r^{-1/2}$ (---). . . . .	202
B.5	Schematic view of the computational domain. . . . .	203
B.6	Comparison between LBM simulation results (---) and the analytical solution Gabard and Astley (2006) (—) at $\text{Ma}=0.036$ . . . . .	204
B.7	Comparison between LBM simulation results (---) and the analytical solution Gabard and Astley (2006) (—) at $\text{Ma}=0.15$ . . . . .	204
B.8	The comparison of $D(\theta, f)$ LBM simulation results of the horn ( $r = 2a$ ) for different flow speeds. . . . .	206
C.1	User interface of TLM-based mouthpiece design interface. . . . .	209
C.2	Comparison of AFs and closed mouthpiece input impedances. . . . .	210
C.3	Comparison of AFs and saxophone input impedances. . . . .	210

# List of Tables

4.1	The D2Q9 velocity set. . . . .	63
4.2	List of conversion factors. . . . .	67
7.1	Reed and lip parameters used in steps 2 and 3. . . . .	137
7.2	The playing parameters used in this section. . . . .	151
8.1	Oscillation thresholds for mouthpieces with different chamber sizes. . . . .	174
8.2	Oscillation thresholds for mouthpieces with different baffle heights. . . . .	180
B.1	The maximum $D(\theta, ka)$ in the $ka - \theta$ map. . . . .	205

# List of Abbreviations

**ABC** absorbing boundary condition.

**BGK** Bhatnagar-Gross-Krook.

**C-RBC** characteristic-based reflecting boundary condition.

**C-TDIBC** characteristic-based time-domain impedance boundary condition.

**CAA** computational aeroacoustic.

**CAD** computer-aided design.

**CBC** characteristic boundary condition.

**CFD** computational fluid dynamic.

**DVBE** discrete-velocity Boltzmann equation.

**FDM** finite difference method.

**FE** finite element.

**FEM** finite element method.

**FSAI** fluid-structure-acoustic interaction.

**FVM** finite volume method.

**FW-H** Ffowcs-Williams and Hawkings.

**IB** immersed boundary.

**IB-LBM** immersed-boundary lattice Boltzmann method.

**IBM** immersed boundary method.

**IIR** infinite impulse response.

**LB** lattice Boltzmann.

**LBE** lattice Boltzmann equation.

**LBM** lattice Boltzmann method.

**LGA** lattice gas automata.

**LODI** local one-dimensional inviscid.

**LODI-T** LODI model with transverse terms and transverse relaxation.

**LPF** low-pass filter.

**MRT** multirelaxation time.

**NRBC** non-reflecting boundary condition.

**NS** Navier-Stokes.

**NSCBC** Navier-Stokes characteristic boundary conditions.

**PWM** plane wave masking.

**rBGK** regularized BGK.

**rrBGK** recursive regularized BGK.

**TDIBC** time-domain impedance boundary condition.

**TLM** transmission line model.

**TM** transfer matrix.

**TMM** transfer matrix model.

**TMTC** two-microphone-three-calibration.

# Chapter 1

## Introduction

### 1.1 Saxophone mouthpieces

The saxophone, which consists of a conical bore and a single-reed mouthpiece, was invented by Adolphe Sax in the 1840s. The saxophone mouthpiece is similar to a clarinet mouthpiece but has a larger and round chamber in the original design (Hemke, 1975, Rose, 2020). The modern mouthpieces are adapted for jazz and other non-classical repertoires and typically have a smaller chamber, a wider tip opening, and more options of baffle shapes to produce a louder and brighter sound (Rose, 2020).

The mouthpiece structure is shown in Fig. 1.1 with the key features defined as:

- *table*: the flat surface to which the reed is clamped with the ligature.
- *facing curve*: the curved extension from the flat table to the tip of the mouthpiece, also known as the lay.
- *tip opening*: the distance between the tip of the reed and the mouthpiece.
- *window*: the opening of the mouthpiece that lies under the reed.
- *tip rail*: the narrow flat surface located between the tips of the window and the mouthpiece.
- *side rails*: the narrow flat surfaces that surround the window.
- *tip window*: a rectangle cross-section area viewed from the front of the mouthpiece and defined in between the tip rail and the reed, also known as the reed aperture.
- *side window*: the wedge-shaped area viewed from either side of the mouthpiece and defined in between the side rail and the reed.
- *reed channel*: the path in between the tip rail and the reed.

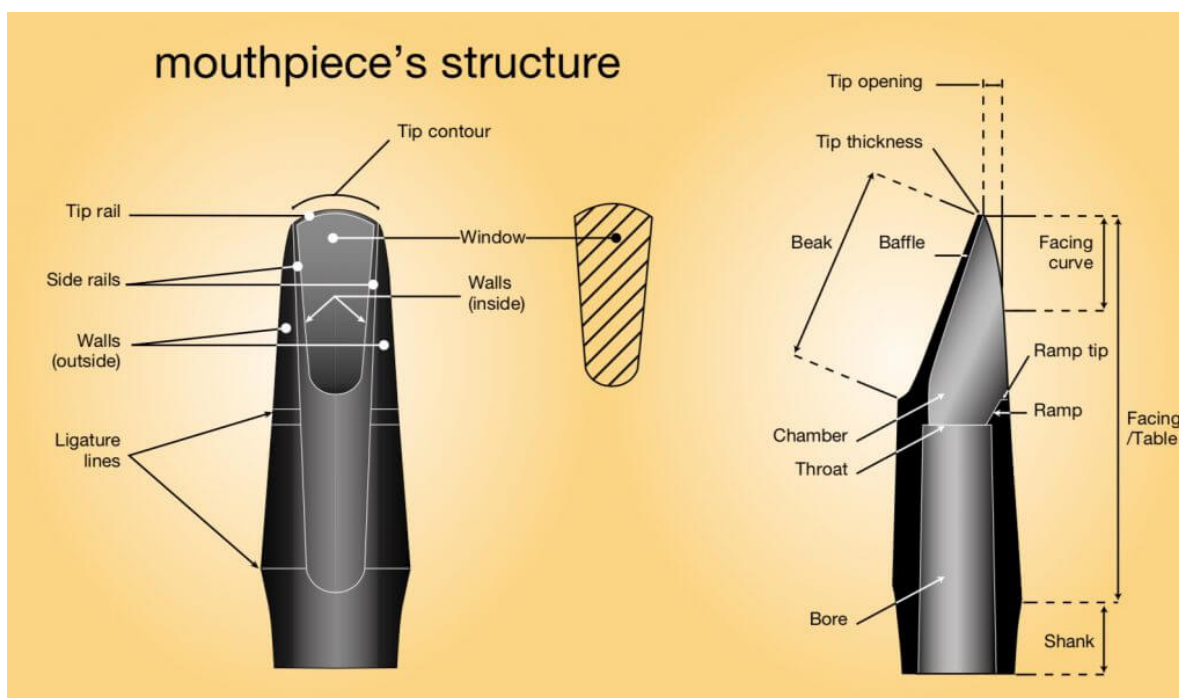


Fig. 1.1: Mouthpiece's structure<sup>1</sup>.

- *baffle*: a portion of the inner upper wall that extends a short distance from the tip rail.
- *bore*: the inner rear portion in which the neck of the saxophone fits, which normally has a circular cross-section area.
- *chamber*: the inner front space that is connected to the bore.
- *throat*: the interface between the bore and the chamber, represented by the cross-section area located on the chamber side if there is a discontinuity between the chamber and the bore.
- *ramp*: the inner portion that ramps from the rear of the window to the throat.
- *beak*: the upper outer roof where the player's upper teeth is placed against.

The mouthpiece is the most versatile component of a saxophone. Structurally, the mouthpiece helps complete the saxophone by providing an extension of the saxophone neck upon which the reed can be attached. Acoustically, the cavity inside the mouthpiece works as a linear acoustic filter, which helps sculpt the sound. From a fluid dynamic perspective, the mouthpiece rails and baffle confine the air flow that enters from the player's mouth into the mouthpiece, determining the aerodynamic force applied on the reed. Because of this versatility, the mouthpiece is one of the most important parts of a saxophone in determining

the sound and playability.

A multiphysics problem exists within the mouthpiece, which involves acoustics (sound wave), fluid (air flow), and solid (reed and mouthpiece) as illustrated in Fig. 1.2. The mouthpiece can thus be considered as “an energy transport hub” that permits energy from different physical fields to interact with each other. When a saxophonist plays a saxophone, the air blown from the player’s mouth serves as the energy source for the instrument. Such energy is partially transferred to the vibrational energy of the reed and drives the reed to vibrate. The reed vibration perturbs the air within the instrument and excites the acoustic resonator attached to the mouthpiece, transferring the vibrational energy to acoustic energy. The acoustic energy, on the other hand, provides feedback to the reed and helps maintain the reed vibration. Solving this multiphysics problem is key to understand the relationship between the mouthpiece geometry and the instrument’s sound and playability, and this research aims at a better understanding of the mouthpiece’s influences on the sound generation of the saxophone by studying the underlying multiphysics problems through acoustic and aeroacoustic analyses.

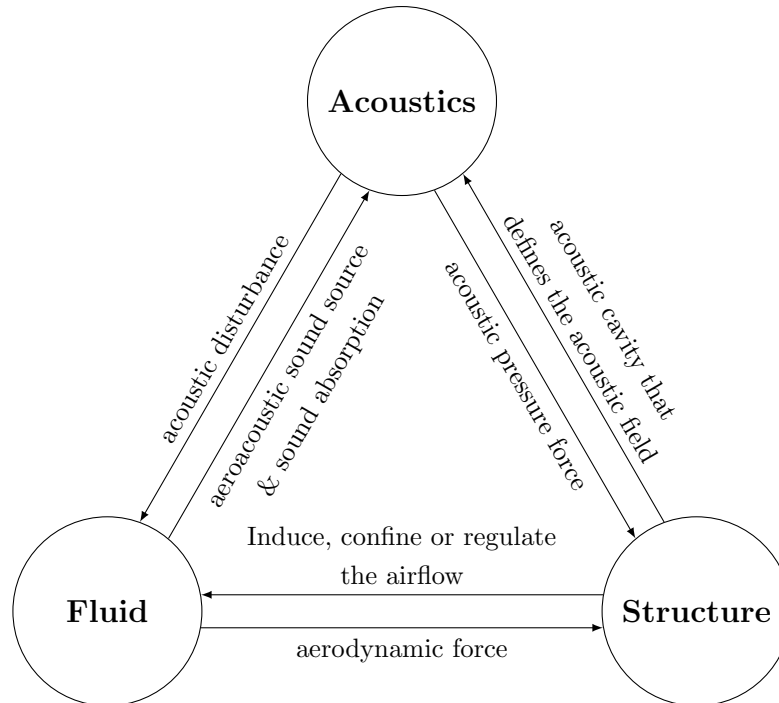


**Fig. 1.2:** The illustration of the interaction between multiple physical fields.

## 1.2 Literature review on mouthpieces

The literature on the saxophone mouthpiece can be broadly divided into two categories. The first type of research focuses on the sound analysis of different mouthpieces, either based on commercial mouthpieces (Pipes, 2018, Wyman, 1972) or customized 3D printed ones (Carral et al., 2015, Ozdemir et al., 2021). Such research connects the sound properties, such as spectra and subjective evaluations, to specific geometry features, which is helpful to guide the mouthpiece design. However, it often does not explicitly provide a thorough physical explanation on the connection between the sound properties and geometric features.

The second category of research aims at comprehending the sound generation mechanisms by investigating the multiphysics problem. Benade (1990) was one of the first to discuss the acoustic influence of a saxophone mouthpiece, showing that the mouthpiece primarily aids in the tuning of the saxophone’s fundamental frequency and the harmonics. It completes the truncated conical air column of the saxophone body by providing the volume equivalent to that of the missing part of the cone. Simplified acoustic mouthpiece models have been proposed for efficient sound synthesis (Kergomard et al., 2016, Scavone, 2002). However, they considered only the mouthpiece volume and ignored the geometry details. Andrieux et al. (2016) built the first 3D finite element model of the mouthpiece, making it possible to study the acoustic effects of various mouthpiece geometric parameters.

The study of fluid dynamics in single-reed instruments (e.g., a clarinet or a saxophone) began with the quasi-static empirical model proposed by Backus (1963). It was improved by Hirschberg et al. (1990), who also adapted fluid models to different flow regimes and reed channel profiles of the mouthpiece (van Zon et al., 1990). More recently, flow measurements (Gilbert, 1991, Lorenzoni and Ragni, 2012) and numerical simulations (da Silva et al., 2007, Shi, 2016, Yoshinaga et al., 2021) provided valuable insights into the fluid properties. However, the ways in which the mouthpiece influences the airflow and how the airflow alters the sound remain unresolved.

## 1.3 Thesis objectives and scope

The main objective of the present research is to investigate how a mouthpiece influences the sound and playability of a saxophone through acoustic and aeroacoustic analyses. A

---

<sup>1</sup><https://vandoren.fr/en/mouthpieces-technical-elements>. Last accessed: May 2023.

set of modeling tools has been developed for conducting these analyses, allowing a comparative study of mouthpieces with different geometries to understand the *geometry-physics-oscillation* relationship.

The acoustic modeling of the mouthpiece is focused on its linear acoustic properties, which is characterized by the input impedance. A variety of techniques are utilized to obtain mouthpiece input impedances, including physical input impedance measurements, the finite element model (FEM), and the newly proposed transfer matrix model (TMM) and transmission line model (TLM) of the mouthpiece. TMM, which is derived from FEM, provides an efficient way of modeling the mouthpiece while being accurate enough to retain complex geometry information, whereas TLM is a further simplified representation by dividing the mouthpiece into piecewise cylindrical segments. Along with acoustic mouthpiece characterization, TMM and TLM are applied to investigate oscillation characteristics by incorporating a sound synthesis model, which helps complete the *geometry-acoustics-oscillation* analysis routine. A mouthpiece design interface has been developed based on TLM, which allows customizable mouthpiece geometries within defined restraints, and an instant calculation of the input impedance and sound synthesis.

The aeroacoustic modeling of the mouthpiece involves fluid dynamics and its coupling with acoustics and solids. A two-dimensional computation aeroacoustic model was developed using the lattice Boltzmann (LB) method, where the fully-coupled fluid-structure-acoustic interactions are implemented. Traditionally, the simulation domain includes the entire instrument and surrounding radiation field. However, this research proposes a characterization-based time-domain impedance boundary condition (C-TDIBC) that models an acoustic system by representing its impedance or reflection coefficients as a boundary condition in a computational aeroacoustic model. C-TDIBC is essentially a combination of a time-domain impedance boundary condition (TDIBC) that models the impedance in the time domain, and a characteristic boundary condition (CBC) that solves the flow-acoustic coupling problem at the boundary. C-TDIBC is applied to the end of a mouthpiece-reed system to model the bore of the instrument with radiation properties, which significantly reduces the computational cost by truncating the domain of interest to a much smaller upstream section of the saxophone body. The Ffowcs Williams and Hawkings (FW-H) acoustic analogy is utilized to decompose the aeroacoustic source in the mouthpiece into monopole, dipole, and quadrupole contributions to further characterize sound generation mechanisms. The FW-H analysis provides the basis for the *geometry-aeroacoustic-oscillation* analysis routine, along

with oscillation properties obtained in the LB simulation, such as pressure and velocity of the flow, and displacement and velocity of the reed.

Finally, the influence of two mouthpiece design parameters are studied, namely, the chamber size and baffle height, to demonstrate the feasibility and capability of the proposed *geometry-physics-oscillation* analysis routines, targeting both quantitative and qualitative explanations of oscillation variations caused by the geometry differences.

This research focuses on the development of methods and tools for analyzing the influence of the mouthpiece in saxophone sound generation, with the aims at better explaining the underlying physics in the mouthpiece for more informed mouthpiece design and sound synthesis. Both TMM and TLM provide efficient ways of mouthpiece prototyping, and TLM additionally provides a way of interactive mouthpiece design. Both mouthpiece models can replace the traditional lumped mouthpiece model in the sound synthesis scheme, which helps better preserve the mouthpiece-related acoustic features in the synthesized sound. The computational aeroacoustic model helps uncover the structure-related flow patterns and flow-induced acoustic features in the mouthpiece, which offers rich information to be used in mouthpiece customization.

## 1.4 Thesis outline

The structure of the thesis is shown in Fig. 1.3. The thesis is mainly grouped in two parts, with Chs. 1 - 4 providing background knowledge and Chs. 6 - 8 covering the main contribution of the research.

The present chapter describes the motivation and the context of the research. The review provided in Sec. 1.2 briefly discusses research only on the mouthpiece, whereas Ch. 2 provides a broader literature review on the single-reed instrument. Chapter 3 introduces fundamental acoustic and aeroacoustic theories, focusing on the knowledge and techniques that will be used in the subsequent chapters.

Chapter 4 covers the fundamentals of the lattice Boltzmann method (LBM), including its derivation and development. The validation of LBM in aeroacoustic applications, as well as the research on the acoustic radiation of the horn in the mean flow, is presented in the Appendix B.

Chapter 5 focuses on the formulation of the characteristic boundary condition (CBC) and its coupling with the time-domain impedance boundary condition (TDIBC), referred

---

to as the characteristic-based time-domain impedance boundary condition (C-TDIBC) for modeling an acoustic resonator in the LBM context.

Chapters 6 and 7 present methods for acoustic and aeroacoustic modeling and analysis of the saxophone mouthpiece, respectively.

Chapter 8 applies methods presented in Chapters 6 and 7 to conduct a comparative analysis of mouthpieces with varied geometries, controlled by a few design parameters. In addition, Appendix C presents a mouthpiece design interface based on the transmission line mouthpiece model provided in Sec. 6.5.

Chapter 9 concludes the thesis and discusses the possible future work.

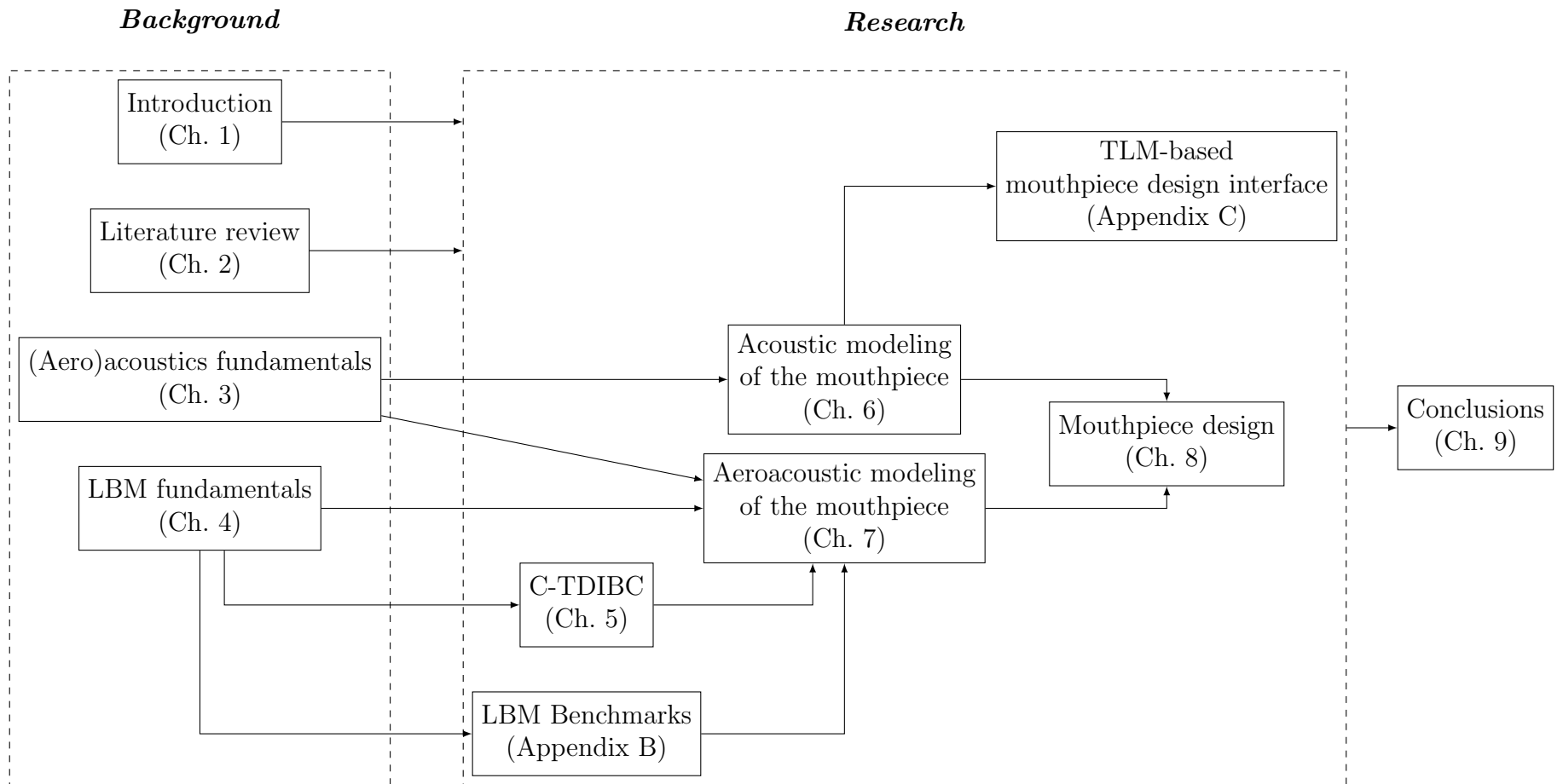


**Fig. 1.3:** Thesis outline.

## Chapter 2

# Literature Review

The present study aims to explore the connection between the saxophone mouthpiece geometry and the instrument sound generation. However, the mouthpiece alone cannot generate sound as it functions in conjunction with the reed and saxophone body as an integrated system. Additionally, the saxophone sound generation involves interactions with the player, who provides the energy source and controls the system. Viewed in this light, it is worth reviewing the research in general on the single-reed instrument rather than focusing solely on the mouthpiece.

The literature review in this chapter serves as support for the research on acoustic and aeroacoustic analyses of the mouthpiece. Therefore, it will emphasize research that directly inspires the present study or employs methodologies utilized in this research rather than attempting to exhaustively cover all relevant research topics.

This chapter is composed of three sections, each of which provides a separate focused literature review from a distinct perspective:

- ***Physics***: Section 2.1 introduces the overall physical description of the sound generation process, as well as the mathematical framework and basic assumptions commonly used in the majority of the single-reed instrument research. The section focuses on various aspects of physics, such as the reed vibration, airflow, sound wave propagation in the bore, and their interaction and coupling.
- ***Oscillation characteristics***: Section 2.2 focuses on research that takes the single-reed instrument as a nonlinear dynamical system to study the oscillation characteristics of the instrument and their dependence on system parameters. Such research aims at a

better understanding of how excitation parameters and instrument properties influence the sound and playability of the instrument.

- **Methodologies:** Section 2.3 provides a methodology review that categorizes the research based on the type of methodology, which covers analytical, experimental, and numerical studies.

## 2.1 Physics and modeling of single-reed instrument sound generation

The sound generation of a single-reed instrument involves a multiphysics problem, and the corresponding study relies on the relevant research and knowledge of the underlying physics such as vibration, acoustics and fluid dynamics. This section aims at providing physical descriptions and the mathematical framework of the single-reed instrument sound generation mechanism, which builds the base for the physical experiments and numerical simulations.

When a player plays the instrument, the air flows from the lungs toward the instrument and builds up pressure in the player's mouth. The mouth pressure provides the driving force exerted on the reed, and at the same time, it drives the air to flow through the reed aperture at the tip of the mouthpiece and into the instrument. The pressure on the reed forces it to move toward the mouthpiece, and the moving reed in turn modulates the airflow going through the reed channel. The moving reed also creates airflow, and the so-called reed-induced flow disturbs the air in the acoustic resonator together with the pressure-driven flow. The air disturbance travels back and forth in the pipe, and the reflected energy is fed into the mouthpiece-reed system to support the reed oscillation.

Self-sustained oscillations are produced by the single-reed instrument, which are periodic oscillations generated and sustained with a steady or slowly varying energy source. To study such oscillations, the single-reed instrument is typically simplified as a combination of an active generator and a passive resonator as illustrated in Fig. 2.1, with their interaction assumed to be localized at the input end of the resonator. The active generator takes a steady energy supply to produce oscillating signals that are transmitted to the passive resonator. The resonator, in turn, provides the generator with the essential feedback to maintain the oscillation.

The basic mathematical framework consists of two equations that model correspondingly the linear resonator and the nonlinear generator. The resonator comprises the mouthpiece,

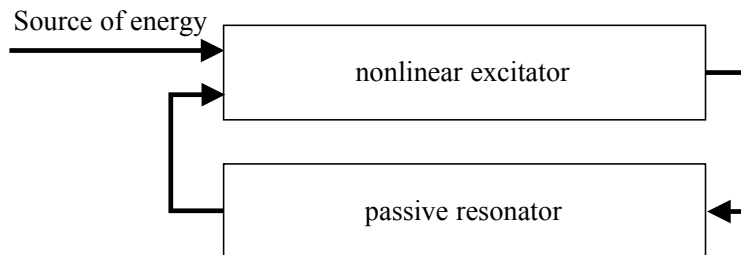


**Fig. 2.1:** Illustration of the single-reed instrument as a self-sustained oscillator.

the bore with toneholes, and the bell, and it can be represented by its frequency-domain input impedance

$$Z(f) = P(f)/U(f). \quad (2.1)$$

The generator is modeled by representing the airflow rate  $u(t)$  entering the resonator as a time-domain nonlinear function of the acoustic pressure  $p(t)$  at the entrance of the resonator.

$$u(t) = NL[p(t)], \quad (2.2)$$

The generator model can be further decomposed into a reed model and a fluid model, which will be discussed in the following sections.

The next section will review the initial efforts made to develop a mathematical framework. The research on reed vibration, airflow, and resonator physics will be addressed separately in the three sections that follow.

### 2.1.1 Early development of mathematical framework

Helmholtz (1885, Appendix VII) provided one of the earliest physical and mathematical discussions on the single-reed instrument sound generation<sup>1</sup>. He mathematically revealed the reinforced odd partial tones of the cylindrical pipe of a clarinet and discussed the interaction between the reed and the pipe.

Ghosh (1938) may have been the first to introduce a flow model into the reed-pipe system, in which the flow velocity through the reed aperture is assumed to be linearly proportional to the potential difference across the reed. Ghosh built the reed on a single-degree-of-freedom mass-spring system, and the flow-potential relationship is controlled by the reed-tip

<sup>1</sup>The second English edition is cited here while the first German edition was published in 1863.

displacement and the reed channel conductivity  $K$ , where  $K$  is also a function of the reed-tip displacement. A similar flow model was also used in the book by Morse et al. (1948, Ch. 23).

Backus (1963) further improved the model from different perspectives. He introduced the pipe dissipation into the system, and for the first time demonstrated the importance of the reed damping on the playing frequency. He may also be the first to use the steady-state Bernoulli equation to describe the air velocity through the reed channel,

$$\frac{1}{2}\rho v^2 = \Delta p, \quad (2.3)$$

where  $\Delta p = p_m - p$  is the pressure difference between the mouth pressure  $p_m$  and the pressure in the resonator  $p$ . The flow velocity  $v$  is proportional to the square root of the pressure difference, and the volume flow rate  $u$  is calculated by integrating the velocity over a rectangle reed aperture area  $A = hw$ , with  $h$  and  $w$  representing the height (tip opening) and width of the reed channel, respectively. The integration yields  $u = vA$  if a uniform flow is assumed through the tip window, equivalently written as,

$$u = hw\sqrt{2\Delta p/\rho}. \quad (2.4)$$

Later in the article, Backus proposed an analytical expression fitted to the experimental data, which correlates the flow rate to  $(\Delta p)^{2/3}$ , and the difference between  $u \propto \Delta p^{1/2}$  and  $u \propto \Delta p^{2/3}$  was attributed to the effect of the flexibility of the reed by him. However, the fitted expression has not been found to be valid in subsequent experiments (Gilbert, 1991, Maurin, 1992, van Zon et al., 1990), and the Bernoulli equation is more commonly applied as the basis of the flow model.

Backus (1963) analytically introduced and experimentally demonstrated the nonlinearity in the physical model and such a nonlinearity was further emphasized by Benade and Gans (1968). In Benade and Gans (1968)'s paper, the wind instrument is considered as a self-excited system composed of a valve driven by the reed dynamics, and the air column that takes the output of the valve as an input and provides feedback to the reed. They took the reed as a flow-controller, and stressed the importance of the nonlinearity in the excitation of the air column oscillation. Following this work, Worman (1971) further completed the single-reed instrument sound generation system in his thesis. The input impedance was used to

represent the pipe as defined in Eq. 2.1, and a single-degree-of-freedom mass-string-damping system was used to model the reed:

$$\frac{d^2y}{dt^2} + g_r \frac{dy}{dt} + \omega_r^2 y = -\frac{1}{m_r} \Delta p, \quad (2.5)$$

where  $\omega_r = 2\pi f_r$  with  $f_r$  the resonant frequency of the reed,  $g_r$  is the half-power bandwidth, and  $m_r$  is the effective mass per unit area.  $y$  is a measure of the reed tip displacement, with  $h = y + H$  representing the tip opening, where  $H$  is the tip opening at equilibrium.

Worman (1971) also introduced the reed-induced flow into the system by adding a parallel impedance to the resonator<sup>2</sup>. The flow rate through the reed channel  $u$  is decomposed into two parts as  $u = u_{\text{pipe}} + u_r$ , where  $u_{\text{pipe}}$  represents the part entering into the pipe, and  $u_r$  gives the portion that goes into the varying space created by the deflected reed, defined as

$$u_r = -S_r \frac{dy}{dt}, \quad (2.6)$$

where  $S_r$  is the effective reed area. However, Nederveen (1969) viewed the reed-induced flow differently by assuming a different relationship between  $u$ ,  $u_r$ , and  $u_{\text{pipe}}$  as

$$u_{\text{pipe}} = u + u_r. \quad (2.7)$$

This means that both the pressure-driven flow through the reed channel and the reed-induced flow contribute to the flow entering the pipe, and such an interpretation seems to be more adapted in the following research (Chaigne and Kergomard, 2016, Coyle et al., 2015, Dalmont et al., 1995).

The calculation of reed-induced flow requires the value of the effective reed area  $S_r$ . It is normally an empirical value, and Nederveen (1969) provided an estimated range of  $S_r \in (0.2w^2, 2w^2)$ , where  $w$  is the width of the reed.

Equations. 2.4, 2.5 and 2.7 build up the system of the nonlinear generator in Eq. 2.2, and together with the resonator represented by Eq. 2.1, they form the governing equations for the single-reed instrument sound generation. An illustration of the mathematical framework is shown in Fig. 2.2 to demonstrate concepts of different physical variables.

---

<sup>2</sup>It is worth noting that Worman attributed the introduction of the reed-induced flow to Wilhem Weber, as he stated that “We may parenthetically remark that it was Weber who first took explicit account of the effect of this  $Z_r$  on the natural frequencies of a pipe which is terminated by a reed.”

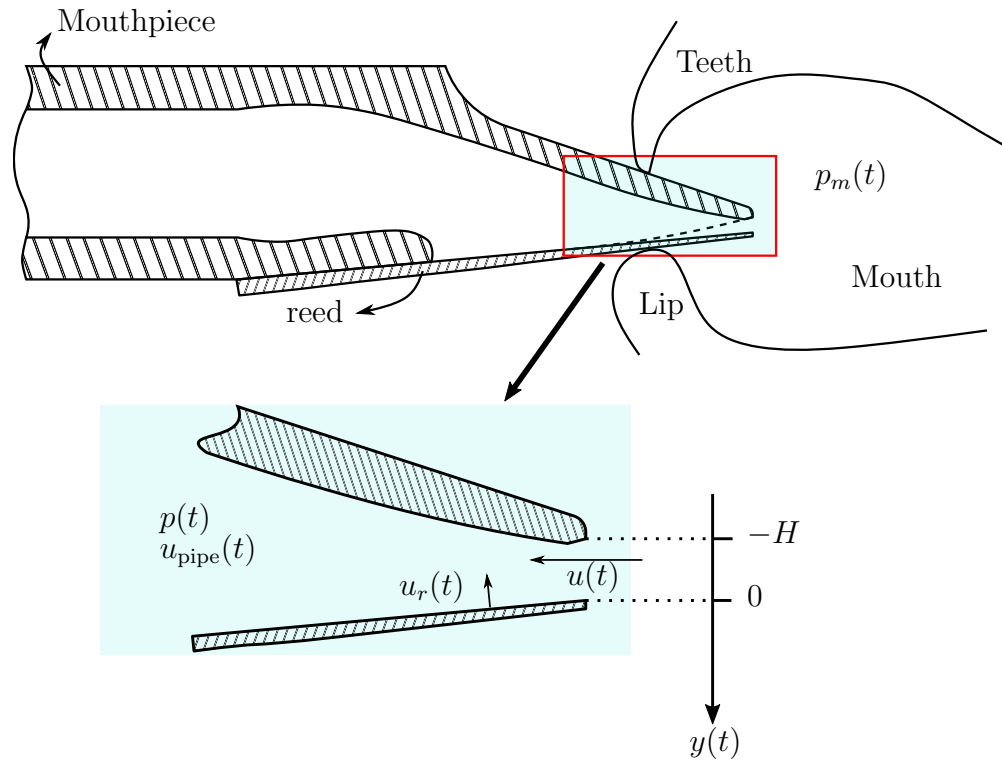


**Fig. 2.2:** Illustration of the single-reed instrument sound generation framework.

Such a mathematical framework has been widely applied, particularly to explore the oscillation characteristics of the system, which will be discussed in Sec. 2.2. It also forms the basis for research in developing sound synthesis and nonlinear dynamical systems (Sec. 2.3.3). Despite the power and versatility of the mathematical framework, there exist several limitations to the model, primarily due to various assumptions and simplifications made when developing the system, including:

- the resonator is assumed to be a linear system: this makes it possible to model the resonator by its input impedance, but it ignores all nonlinearities within the resonator, such as the influence of flow convection on the wave propagation and the nonlinear effects around the toneholes and the bell.
- the sound generator is assumed to have a localized nonlinearity, and this assumption has a few implications:
  - the distributed reed vibration is simplified as a single-degree-of-freedom oscillator.
  - the distributed airflow and its interaction with the reed is also simplified to a localized interaction at the tip of the reed.

- a localized interaction is assumed between the resonator and the generator: unlike the reed tip, which is assumed to be the localized point for the flow-reed interaction, defining the local site to couple the generator and resonator is more difficult. To facilitate the localized coupling, one can think of an imaginary area in the mouthpiece where the resonator's input impedance is defined. The pressure and flow rate are assumed to be uniform over this plane and equals to that at the reed tip in order to couple the resonator and the generator.
- the interaction between the reed and the mouthpiece is neglected in the reed model.
- the flow is assumed to be uniform through the tip window.
- the flow in the reed channel is assumed incompressible and quasi-stationary, so the Bernoulli equation can be applied.
- the flow is assumed to be two-dimensional, and the flow only enters the mouthpiece through the front tip window, i.e., the air that enters from the side slits is neglected.
- the hydrodynamic force on the reed due to the airflow is negligible.

One of the primary goals of the study on the single-reed instrument is to validate or disprove the above assumptions and simplifications. The following sections will review the study that further extends our understanding of the sound generation process, which investigates in-depth the physics of different components of the system and their interactions with one another.

### 2.1.2 Reed vibration

The physics of the reed vibration includes not only the reed itself, but also the elements that interact with the reed, such as the airflow, mouthpiece, and the player's lip and tongue. As a result, the modeling of the reed involves not just the reed mechanical system itself, but also the integration of other elements.

Muñoz Arancón (2017, Sec. 1.1.2) has provided a detailed review on the physical models of the reed, which are classified as the lumped model, beam model and plate model. The lumped model and the beam model are discussed here because they are applied correspondingly in the mouthpiece acoustic modeling in Ch. 6 and aeroacoustic modeling in Ch. 7.

### 2.1.2.1 Lumped model

The simplest lump model represents the reed as a massless spring,

$$k_r y = -\Delta p, \quad (2.8)$$

where  $k_r$  is the effective reed stiffness per unit area, and the pressure difference across the reed  $\Delta p = p_m - p$  works as a driving force.

Worman (1971) is one of the earliest researchers who introduced both the mass and damping into the system<sup>3</sup>. It is governed by Eq. 2.5, and is sometimes written in the form of

$$m_r \frac{d^2 y}{dt^2} + \mu_r \frac{dy}{dt} + k_r y = -\Delta p, \quad (2.9)$$

where  $\mu_r = g_r m_r$  is the effective damping per unit area, and  $\omega_r = \sqrt{k_r/m_r}$ .

While the interaction with the fluid is achieved by coupling the pressure difference  $\Delta p = p_m - p$  as the driving force, the interaction with the mouthpiece requires extra adaption of the model.

The collision model was inspired by research on the hammer-string interactions of a piano (Chaigne and Askenfelt, 1994, Hall, 1992), such that Chatziioannou and van Walstijn (2012) introduced the one-sided contact force between the reed and the lay based on the power law,

$$m_r \frac{d^2 y}{dt^2} + \mu_r \frac{dy}{dt} + k_r y - k_c ([y - y_c])^{\alpha_c} = -\Delta p, \quad (2.10)$$

and

$$[y - y_c] = \begin{cases} y - y_c, & \text{if } y < y_c, \\ 0, & \text{otherwise,} \end{cases} \quad (2.11)$$

where  $k_c$  is a stiffness coefficient,  $\alpha_c \geq 1$  is the power law exponent, and  $y_c$  is an empirical value that represents the displacement threshold below which the power law is active.

It is not easy to include the player's lip explicitly in a lumped model since the lip is in contact over a certain area with the reed. Therefore, the lip is commonly integrated by modifying the lumped model coefficients. Efforts have been made to estimate such coefficients from measurements (Chatziioannou and van Walstijn, 2012, Muñoz Arancón et al., 2016),

---

<sup>3</sup>Ghosh (1938) employed a mass-spring oscillator without the damping effect, while Nederveen (1969) introduced the damping term but neglected the mass.

and a larger lip force can result in a smaller tip opening  $H$ , larger damping  $\mu_r$  and hence a smaller resonance frequency  $\omega_r$ .

The incorporation of the tongue can be achieved similarly, and the tongue articulation was modeled empirically by modifying the reed coefficients, which specifically increase the mass  $m_r$  and damping  $\mu_r$ , and decreases the equilibrium tip opening  $H$  (Chatziioannou and Hofmann, 2013, 2015). The tongue was also modeled as a separate mass-spring-damping system by Ducasse (2003), with its equilibrium position controlled separately. Its interaction with the reed was achieved by forming the tongue oscillator and the reed oscillator as a single system. In addition, Almeida et al. (2017) proposed the water hammer model to simulate the initial transients of a clarinet, where the tonguing induces a sudden increase in airflow.

It is worth noting that the reed is sometimes represented by its equivalent capacitance (Coyle et al., 2015, Worman, 1971), where the transconductance of the reed is derived from Eq. 2.5 and is shown as

$$\frac{y}{\Delta p} = -\frac{1}{m_r(\omega_r^2 - \omega^2 + j\omega g_r)}. \quad (2.12)$$

The reed-induced impedance  $Z_r$  can then be calculated using Eqs. 2.6 and 2.12, and is expressed as follows if we neglect the impedance of the vocal tract:

$$Z_r = \frac{p}{u_r} = \frac{p}{S_r \frac{dy}{dt}} = -\frac{m_r}{j\omega S_r} (\omega_r^2 - \omega^2 + j\omega g_r). \quad (2.13)$$

It can be simplified at low frequencies

$$Z_r \approx -\frac{k_r}{j\omega S_r}, \quad (2.14)$$

which can be viewed as a parallel acoustic compliance  $C_r = S_r/k_r$  attached to the resonator, with an equivalent volume  $V_r^{\text{eq}} = \rho c^2 S_r/k_r$

### 2.1.2.2 Beam model

The beam model was first applied in single-reed instruments by Stewart and Strong (1980), where the reed transverse motion  $y(t)$  is governed by

$$\frac{\partial^2}{\partial x^2} \left( YI(x) \frac{\partial^2 y}{\partial x^2} \right) + \rho_r S(x) \frac{\partial^2 y}{\partial t^2} + R_r \frac{\partial y}{\partial t} = F(x, t), \quad (2.15)$$

where  $\rho_r$  represents the density,  $Y$  denotes Young's modulus,  $R_r$  represents the damping, and  $I(x) = S(x)\kappa^2(x)$  represents the moment of inertia about the longitudinal axis with  $\kappa(x)$  being the radius of gyration of the cross-section  $S(x) = wb(x)$ .  $w$  and  $b(x)$  denote the width and thickness of the reed, respectively. The force term  $F(x, t)$  includes the pressure difference across the reed and the Bernoulli force due to the flow passing through the reed channel.

Avanzini and van Walstijn (2004) further completed the model by introducing viscoelastic losses:

$$\frac{\partial^2}{\partial x^2} \left[ YI(x) \left( 1 + \eta \frac{\partial}{\partial t} \right) \frac{\partial^2 y}{\partial x^2} \right] + \rho_r S(x) \left[ \frac{\partial^2 y}{\partial t^2} + \gamma_B \frac{\partial y}{\partial t} \right] = F(x, t), \quad (2.16)$$

where  $\eta$  is magnitude of the internal viscoelastic losses, and  $\gamma_B$  is an alternative damping coefficient.

In addition, the force term involves not only the pressure difference but also the collision force between the reed and the lay, as well as the lip force distributed over a contact area. This model will be applied in the aeroacoustic modeling of the mouthpiece, and detailed in Sec. 7.1.2.

### 2.1.2.3 Other models

There exist other higher-dimension models such as the two-dimensional thin plate model using finite element method (Ducasse, 2001, Facchinetti et al., 2003) or finite difference method (Chatziioannou and van Walstijn, 2007), and the Mindlin thick plate model (Casadonte, 1995, Ch. V), and one can refer to corresponding articles for details.

### 2.1.3 Airflow

The unsteady Bernoulli equation can be derived from the Navier-Stokes equation (which will be introduced in Sec. 3.1) by assuming a frictionless flow along a streamline. If the streamline follows the  $x$  direction, then we have,

$$\rho \int_a^b \frac{\partial v}{\partial t} dx + p_b - p_a + \frac{1}{2} \rho (v_b^2 - v_a^2) = 0, \quad (2.17)$$

where  $a$  and  $b$  represent two points along the streamline.

The steady Bernoulli equation can be obtained by dropping the unsteady term  $\partial v / \partial t$

from the above equation:

$$p_a + \frac{1}{2}\rho v_a^2 = p_b + \frac{1}{2}\rho v_b^2 = \text{const.} \quad (2.18)$$

Applying the Bernoulli equation to the flow within the reed channel and assuming a zero velocity in the mouth leads to the expression of the jet velocity in terms of the pressure difference shown in Eq. 2.3, and the corresponding flow rate in Eq. 2.4 by assuming a uniform flow passing through a rectangular tip window.

Hirschberg et al. (1990) made an analogy of the reed channel to the Borda tube. The flow is assumed to separate at the tips of the mouthpiece and the reed and forms a free jet in the channel. The jet height  $h_j$  is shorter than that of the tip opening, so that leads to a smaller integration area of the Bernoulli flow. The vena contract coefficient  $\alpha = h_j/h$  is introduced and Eq. 2.4 is modified as

$$u = \alpha h w \sqrt{2(p_m - p)/\rho}. \quad (2.19)$$

More theoretical fluid models were proposed under the quasi-steady state assumption in the 1990s (Hirschberg et al., 1990, van Zon et al., 1990, van Zon, 1989). The fluid is classified based on the dimensionless reed channel length  $L/h$  with  $L$  representing the physical reed channel length, and the Reynolds number defined as

$$\text{Re} = \frac{u}{\nu w}, \quad (2.20)$$

where  $\nu$  is the kinematic viscosity of the air. A list of all available fluid models at the time<sup>4</sup> was provided in van Zon (1989, Ch. 2.7)'s thesis, which is shown below,

1. *the empirical model* proposed by Backus (1963), which states that  $u \propto p^{2/3}h^{4/3}$
2. *the Bernoulli flow model* based on Eq. 2.4
3. *the free jet model*: the introduction vena contracta coefficient  $h_j/h = \alpha$  leads to Eq. 2.19 by assuming the flow separation at the entrance of the reed channel. It is also assumed that  $L/h < 1$ , so that the jet goes over the entire reed channel without reattaching to the wall after the initial separation. Hirschberg et al. (1990) defines the range of the vena contracta coefficient  $0.5 < \alpha \leq 0.611$  based on the potential flow theory.
4. *the boundary layer flow model*: the flow reattaches to the wall at  $x = l_r$  after the initial

---

<sup>4</sup>To the best of the author's knowledge, no new fluid models have been proposed since then.

separation at the entrance of the reed when  $L/h > 1$ , and it is assumed that  $l_r \sim h$  and a uniform flow at the reattachment point (van Zon et al., 1990). It starts to develop toward the Poiseuille flow after the reattachment, and the flow exits the reed channel before it is fully developed. Such a transition is modeled as a boundary layer flow with a linear boundary layer velocity profile assumed, and the vena contracta coefficient is given as:

$$\alpha_{\text{bl}} = 1 - \hat{\delta}(L),$$

where the  $\hat{\delta}(L) = \delta(L)/h$  is the dimensionless boundary layer thickness at the end of the reed channel.

5. *the Poiseuille flow model*: the reed channel is longer than the previous case  $L/h \gg 1$  so that the flow has already been fully developed at  $x = l_p$  before the reed channel exit, and flow rate is calculated using the following expressions:

$$u = \frac{\nu w}{Ch}(l_p - l_r),$$

where  $l_p - l_r$  is the length of the boundary layer flow between the reattachment point and the Poiseuille flow

$$\frac{l_p - l_r}{L - l_r} = \frac{12C(1 - \hat{\delta}_c)^2}{24C - 1} \left[ 1 - \sqrt{1 - \frac{h^4(24C - 1)\Delta p}{72\rho\nu^2(L - l_r)^2(1 - \hat{\delta}_c)^2}} \right],$$

with  $\hat{\delta}_c = \delta_c/h \approx 0.2688$  the dimensionless critical boundary layer thickness for a channel of height  $h$ , and  $C = \left[ 4\hat{\delta}_c + 9 \ln(1 - \hat{\delta}_c) + 5\frac{\hat{\delta}_c}{1 - \hat{\delta}_c} \right] \approx 0.01594$  (da Silva et al., 2007). Figure 2.3 illustrates the flow field in a long reed channel mouthpiece ( $L/h \gg 1$ ), which involves three different flow regimes that occur consecutively from the entrance to the exit of the reed channel.

6. *the turbulent flow model*: the free jet transits to a turbulent flow in the reed channel,

$$\alpha_{\text{turb}} = \frac{\alpha^2}{2\alpha^2 - 2\alpha + 1},$$

where  $\alpha$  is the vena contracta coefficient of the free jet model.

Efforts have been made in past decades to validate the proposed fluid models and one widely studied subject is the value of the vena contracta coefficient. The vena contracta

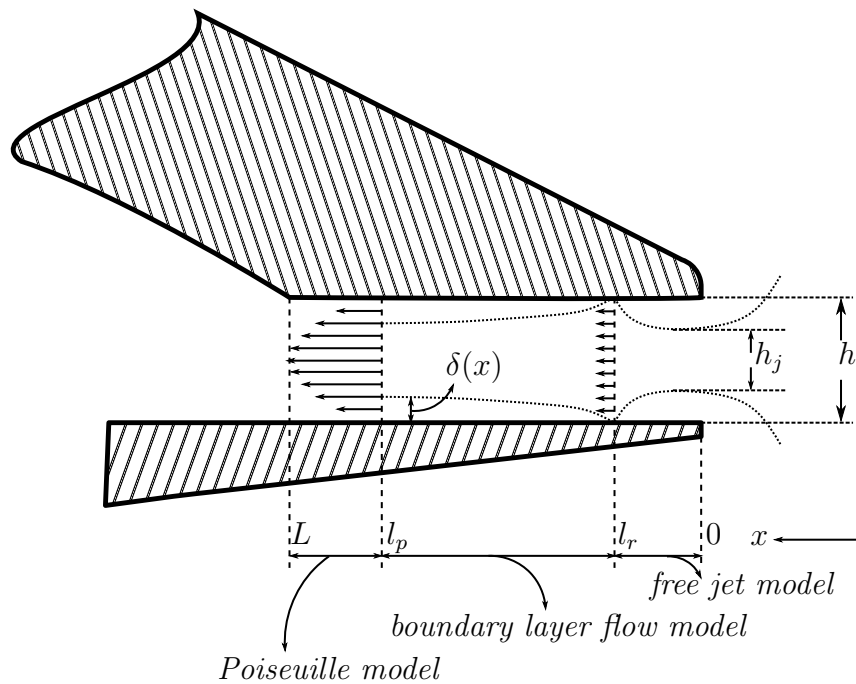


**Fig. 2.3:** Illustration of the fluid field in a long reed channel mouthpiece ( $L/h \gg 1$ ) that involves all three different flow regimes. The fluid model labels indicate the range of  $L$  to apply the corresponding fluid model.

coefficient of a stationary regime flow was measured in a two-dimensional mouthpiece by van Zon et al. (1990), and calculated using a 2D lattice Boltzmann simulation by da Silva and Scavone (2007), and both results confirm the validity of the *free jet model* for a 2D flow. However, a quasi-static measurement in a real 3D mouthpiece by Dalmont et al. (2003) showed a larger  $\alpha \in (0.85, 1.30)$ , which was attributed to the flow through the lateral side slits by the authors. Such a result was later confirmed by a 3D computational aeroacoustic simulation by Yoshinaga et al. (2021). Another interesting finding in the literature is that both Dalmont et al. (2003) and da Silva and Scavone (2007) showed a constant  $\alpha$  for a relatively large tip opening, but it decreases quickly when the reed tends to close. Such a result is not surprising because the viscous effect will play a more important role for a narrower channel, in which case a flow model similar to the *Poiseuille model* or *boundary layer flow model* should be applied instead of the *free jet model*.

It is worth reiterating that all the fluid models that have been proposed so far are based on the quasi-stationary assumption, which assumes the time-varying flow as a series of steady flow rates at each time frame, with unsteady effects neglected. Such an assumption normally

works well in fluid dynamics for a small Strouhal number flow, so that the unsteady term in Eq. 2.17 can be dropped. The quasi-stationary assumption was verified in the application to pulsating jets through an orifice (Zhang et al., 2002) but its validity in single-reed instrument application is still questionable.

Gilbert (1991) measured the contraction coefficients of the single-reed instrument with the help of a hot-wire anemometry. This work used a real mouthpiece coupled to a resonator with the first resonant frequency of 140 Hz. The agreement between the coefficients measured under the static regime and the dynamic regime confirms the validity of the quasi-stationary assumption in the single-reed instrument. Maurin (1992) showed the same result for the 140 Hz resonator, however, he observed a large hysteresis for the measurement using a 640 Hz cylindrical pipe, which violates the quasi-stationary assumption. Earlier measurements by van Zon et al. (1990) for the dynamic flow without a resonator also displayed the hysteresis, as well as a large discrepancy between the measured data and the theoretical fluid model. This indicates that, even for a small Strouhal number (it measured  $St = 0.01$ ), there is still hysteresis which cannot be described by the quasi-stationary model. The hysteresis was also found by other researchers, particularly when playing the instrument at higher frequencies (1000 Hz by da Silva et al. (2013), 584 Hz by Shi (2016), and 1800 Hz by da Silva and Scavone (2007)).

The hysteresis effect shows its dependency on the mouthpiece geometry (Maurin, 1992), the playing frequency and excitation parameters (da Silva et al., 2013). Further research is required to reveal the underlying physics and to propose a proper unsteady fluid model for the single-reed sound generation.

### 2.1.4 Resonator

The acoustic resonator is composed of various components, including the pipe (which may involve bends), toneholes, and the bell. Each component has generated interest among acousticians, not only in musical acoustics but also in other research fields.

The **pipe** is a crucial component in determining the oscillation characteristics of an instrument. The length of the pipe, to a large extent, determines the playing frequency while the shape of the pipe determines the timbre. Most research has focused on acoustic waves below the cutoff frequency, where non-planar waves are considered evanescent and attenuate quickly, resulting in the propagation of only planar waves through the pipe. The

cutoff frequency is given by  $\omega_c = 1.84c/a$ , where  $a$  is the radius of the pipe. For a more extensive discussion of the acoustics of pipes, please check the books by Fletcher and Rossing (1998, Ch. 8) and Chaigne and Kergomard (2016, Ch. 7).

**Toneholes** are placed along the bore of the single-reed instrument to allow it to play various notes. In general, toneholes are known to function as low-pass filters that pass high-frequency components to the lower bore while reflecting low-frequency components back to the upper bore. Such reflections cause a standing wave in the upper bore to support the reed vibration. Benade (1960) and Keefe (1982a,b) conducted early studies on the physics of the tonehole, which was considered as an acoustic side branch positioned on the main pipe. The acoustics of the side branch was theoretically explored using the modal decomposition and variational method (Dubos et al., 1999, Keefe, 1982b), and a lumped model was proposed by representing the tonehole as a combination of series and shunt impedances in an equivalent circuit. The tonehole geometry affects the series and shunt impedances, which are commonly expressed as a function of tonehole height  $t$  and the radius ratio  $\delta = b/a$ , where  $b$  and  $a$  represent the tonehole radius and main pipe radius, respectively. The series impedances are generally negative acoustic inertances, which provide for negative length corrections accounting for the decreased kinetic energy density due to the flow penetration into the tonehole cavity, as well as influences of the evanescent mode of the side branch (Dubos et al., 1999). The shunt impedance incorporates multiple effects, including the impedance of the side branch itself, length corrections of the side branch, and the radiation impedance for an open tonehole (Dalmont et al., 2002).

Benade (1960) also pioneered the study of the tonehole lattice effect on the cutoff frequency of the instrument. Such effects have been later examined in detail for both cylindrical (Moers and Kergomard, 2011, Petersen et al., 2020b) and conical resonators (Petersen et al., 2020a).

**Sound radiation** is another important topic in the context of musical instruments, and it is often characterized using a radiation impedance. The radiation impedances for unflanged and flanged circular pipes were derived by Levine and Schwinger (1948) and Nomura et al. (1960), respectively. Corresponding approximation formulations, such as those proposed by Norris and Sheng (1989), Dalmont et al. (2001), and Silva et al. (2009), have been developed to aid in efficient radiation impedance calculations. In addition to circular pipes with simple flanges, Dalmont et al. (2001) explored radiation impedances with various flanges and provided approximated formulae for the end correction, and H elie and Rodet (2003)

proposed analytical expressions for radiation of a pulsating portion of a sphere, which can be applied to a horn or a conical pipe.

The **player's vocal tract** is considered as another resonator located upstream of the reed. It can be represented by its input impedance looking at the reed into the mouth, which is in series with the impedance of the resonator (Benade, 1986). Experienced players often tune their vocal tracts to play in the altissimo register for both clarinet (Fritz and Wolfe, 2005) and saxophone (Chen et al., 2008). The player adjusts the impedance of the vocal tract to reinforce the overall impedance around the playing frequency to make it easier for the reed to oscillate at the instrument's resonance frequency. In addition, the vocal tract can be used for performing special effects such as pitch bends, multiphonics and glissandi (Chen et al., 2011, Fritz and Wolfe, 2005, Scavone et al., 2008).

## 2.2 Oscillation characteristics of the dynamical system

The single-reed instrument can be considered as a nonlinear dynamical system that is characterized by a time-dependent function. The function is governed by a number of system parameters defined by the instrument characteristics and the player's embouchure. The oscillation characteristics of the system, such as the playing frequency and the oscillation threshold, naturally infer the sound quality and the playability of the instrument. Therefore, it is essential to investigate the oscillation characteristics of the system and their dependence on the system parameters in order to establish a link between an instrument's physical properties or the playing embouchure and the performance of the instrument.

This section provides a literature review on the research that studies the dependency of the oscillation characteristics on different factors. The oscillation characteristics mainly involve sound properties such as the playing frequency, spectrum and sound level, as well as the bifurcation characteristics, which indicates the stability and thresholds of different regimes. There exists multiple regimes in such a single-reed system, such as<sup>5</sup>

- the *static regime*, where there is no oscillation or sound produced,
- the *periodic oscillation regime*, where the system undergoes a periodic oscillation, and
- the *quasi-periodic oscillation regime*, where the system generates a quasi-periodic oscillation and produces a multiphonic sound.

---

<sup>5</sup>There exists also other regimes such as chaotic regime (Maganza et al., 1986), which is, however, not listed here due to its lack of study and less musical interests.

The bifurcation analysis helps explore the playability of the instrument by investigating different thresholds (e.g, the oscillation thresholds and the extinction thresholds), the playing frequency at these thresholds, as well as their dependence on different control variables. The control variables are contributed by both the instrument and the player as listed below, and their influences on the oscillation characteristics will be discussed in the following sections:

- *reed*: the reed stiffness, reed damping, reed-induced flow.
- *resonator*: the bore shape (cylindrical or conical), losses, inharmonicity, cutoff.
- *airflow*: the vena contracta coefficient.
- *player*: the mouth pressure, lip force, lip position, and the effect of the vocal tract.

### 2.2.1 Reed

Backus (1963) derived the analytical expressions for the blowing pressure threshold and the negative frequency shift of the small-amplitude oscillation, which are shown to be linearly and inversely proportional to the reed stiffness. Wilson and Beavers (1974) made use of a similar method to explore the effect of the reed damping. It is found that the reed damping plays the main role in helping the reed to oscillate at the resonant frequencies of the pipe. Wilson and Beavers (1974) plotted dimensionless playing frequency  $\theta$  and the dimensionless mouth pressure oscillation threshold  $\gamma$  as a function of the dimensionless wavenumber  $k_r L$ , where  $k_r = 2\pi f_r/c$  is the resonant wavenumber of the reed, and  $L$  represents the length of the cylinder. While the playing frequency decreases monotonically with the  $k_r L$ , the mouth pressure threshold's dependence on  $k_r L$  shows a more complex behavior. However, at a larger reed damping, the mouth pressure threshold is shown to decrease nearly monotonically with the reed resonant frequency.

Nederveen (1969) investigated the effect of the reed-induced flow and the reed damping on the playing frequency. The playing frequency shifts are expressed as length corrections of the cylindrical pipe, which is found to increase with the tip opening at the equilibrium state.

The length correction due to the reed-induced flow can be expressed as (Dalmont et al., 1995)

$$\Delta l_r = \frac{\rho c^2 S_r}{k_r S}, \quad (2.21)$$

where  $S_r$  is the equivalent reed area,  $S$  is the cross-section of the cylinder, and  $k_r$  is the stiffness of the reed. Though the equilibrium tip opening  $H$  is not included in Eq. 2.21, it

can be inferred that  $S_r$  will decrease and  $k_r$  will increase when the reed moves closer to the lay (smaller  $H$ ) due to a tighter embouchure and thus,  $\Delta l_r$  should decrease with a smaller  $H$ .

Silva et al. (2008) conducted a similar analysis as Wilson and Beavers (1974) and proposed an analytical expression for the length correction due to the damping effect:

$$\Delta l_q \approx \zeta \frac{q_r}{\sqrt{3}k_r}, \quad (2.22)$$

where  $\zeta = wZ_c\sqrt{2H/\rho k_r}$  is a dimensionless number proportional to the maximum flow rate, and  $q_r$  is the damping coefficient of the reed. It showed that  $\Delta l_q$  increases with the reed damping and tip opening, and it will decrease with the reed resonant frequency. Such behavior was also confirmed for higher registers by Karkar et al. (2012) who solved the problem with a numerical continuation approach.

Karkar et al. (2012) also explored the dependency of the oscillation threshold. They showed that while the mouth pressure oscillation threshold rises with the reed damping, the reed resonant frequency has a more complex impact. The mouth pressure threshold, however, is shown to decrease monotonically with the reed resonant frequency at higher reed damping, which is consistent with the results shown by Wilson and Beavers (1974) and Silva et al. (2008).

It is worth mentioning that both  $\Delta l_r$  and  $\Delta l_q$  increase with the tip opening, which suggests that stronger mouth pressure and lip force can reduce the length correction and increase the playing frequency. Such embouchure effects will be discussed in Sec. 2.2.4.

### 2.2.2 Resonator

The resonator is known as a key component of the wind instrument in determining its sound properties. For example, the pipe length determines the fundamental frequency of the instrument, and different bore shapes can result in distinct harmonic amplitudes of the resulting sound. This section will focus on how the resonator geometry affects the playability of the instrument.

Grand et al. (1997) conducted an analytical study of the nature of the bifurcation for small oscillations of a single-reed instrument. The bifurcation analysis was performance based on the Taylor expansion of the nonlinear flow-pressure relationship  $u = u_0 + Ap +$

$Bp^2 + Cp^3$ , and the linear flow admittance  $A$  is chosen as the control parameter. The solution is expressed in terms of the expansion coefficients  $A$ ,  $B$ ,  $C$ , and the resonator admittance  $A_n$  at the  $n$ -th resonant frequency. It revealed that the impedance peak amplitude  $A_n$  is significant in defining the bifurcation nature, and changing the peak amplitudes can cause a subcritical (inverse) bifurcation, which indicates a sudden emergence of the oscillation at the bifurcation point. Dalmont et al. (2000) applied a similar technique to study the conical reed instrument, and the conical resonator was modeled as a sequence of lossless stepped cylinders. It demonstrated the supercritical bifurcation in the cylindrical instrument and the subcritical bifurcation in the conical instrument. Multiple regimes were seen at the fundamental frequency of the conical instruments, including both the Helmholtz motion and the inverted Helmholtz motion, as later demonstrated by Dalmont (2007).

In addition to the amplitude, the frequencies of impedance peaks, particularly the inharmonicity between the first two resonant frequencies, also affect the oscillation characteristics. The inharmonicity can be influenced by a variety of factors such as the geometry of truncated cone (e.g., the length and the conicity) (Ayers et al., 1985) and the viscothermal losses in the bore (Kergomard et al., 2000). A greater inharmonicity not only produces a larger deviation of the playing frequency from the impedance peak (Coyle et al., 2015, Kergomard et al., 2000, 2017), but it also makes it more difficult to play the instrument, as demonstrated both experimentally (Dalmont et al., 1995) and numerically using the continuation method (Gilbert et al., 2019, 2020). In addition, the inharmonicity is found to be a necessity of the quasi-periodic regimes (Doc and Vergez, 2015, Doc et al., 2014).

Losses in the system are another important factor affecting the oscillations. In addition to the above-mentioned influence of the viscothermal losses by inducing the inharmonicity, it also influences the ease of playing of the instrument. Atig et al. (2004) simulated the clarinet oscillation with Raman's model, which assumes frequency-independent losses, and found that a larger loss leads to a lower extinction threshold of the mouth pressure. Dalmont et al. (2005)'s analytical analysis with Raman's model showed a similar result. In addition, it showed an increasing oscillation threshold with losses. The effect of the nonlinear losses, particularly the losses influenced by termination geometry, is experimentally and numerically studied by Atig et al. (2004), which showed that larger nonlinear losses result in a smaller playing range and dynamic level.

### 2.2.3 Airflow

There is little research studying the influence of the airflow on the oscillation characteristics. Experimentally, this is due to the difficulty of measuring the flow field quantities in the mouthpiece, and numerically and analytically, this is because that the current flow model is built based on the 2D flow theory and there is lack of a well-established realistic 3D flow model. The vena contracta effect is the only factor that has been examined. It was studied analytically (Silva et al., 2008) and numerically (Chatziioannou and van Walstijn, 2008) by introducing the contraction coefficient  $\alpha$  into the fluid model. Chatziioannou and van Walstijn (2008) showed that a smaller  $\alpha$  shifts upwards the harmonic frequencies, and comparing a varying  $\alpha$  and a constant  $\alpha$ , the difference is significant in the transients but small for steady-state signals.

### 2.2.4 Player

When it comes to the mouth pressure, the majority of the research has focused on the pressure thresholds at which the oscillation starts, extinguishes, or changes the regime, and studies on how such thresholds change with other parameters. However, the mouth pressure can be regarded as a control variable itself, which alters the other oscillation characteristics such as the playing frequency and the sound level.

Both increasing mouth pressure and lip force were observed to reduce the playing frequency in experiments (Almeida et al., 2013, Bak and Dømler, 1987, Mayer, 2003) as mentioned in Sec. 2.2.1. This result is supported by Dalmont and Frappe (2007)'s experiment. It showed that the maximum flow rate, which theoretically equals  $\frac{2}{3\sqrt{3}}\zeta$ , decreases with increasing lip force. The experiment (Almeida et al., 2013, Mayer, 2003) revealed more complicated behaviors under certain conditions. With a lower lip force, for example, a rising mouth pressure first decreases and then increases the playing frequency.

Almeida et al. (2013)'s experiments also revealed that as the lip force drops, it requires a higher mouth pressure to excite the instrument. Such an observation can also be explained with existing knowledge, because increasing the lip force increases the equivalent damping of the reed (Gazengel et al., 2007), which raises the mouth pressure threshold as discussed previously.

To better illustrate the player's influence on the sound generation, a map resembling the Schelleng diagram for string instruments can be created from the measured data (Almeida

et al., 2013, Mayer, 2003). A schematic illustration and an example are shown in Fig. 2.4. The map typically displays different oscillation characteristics in a space spanned by the mouth pressure and the lip force. It helps not only reveal the dependence of oscillation properties on the playing parameters, but also helps identify different regimes and corresponding thresholds of different playing parameters.

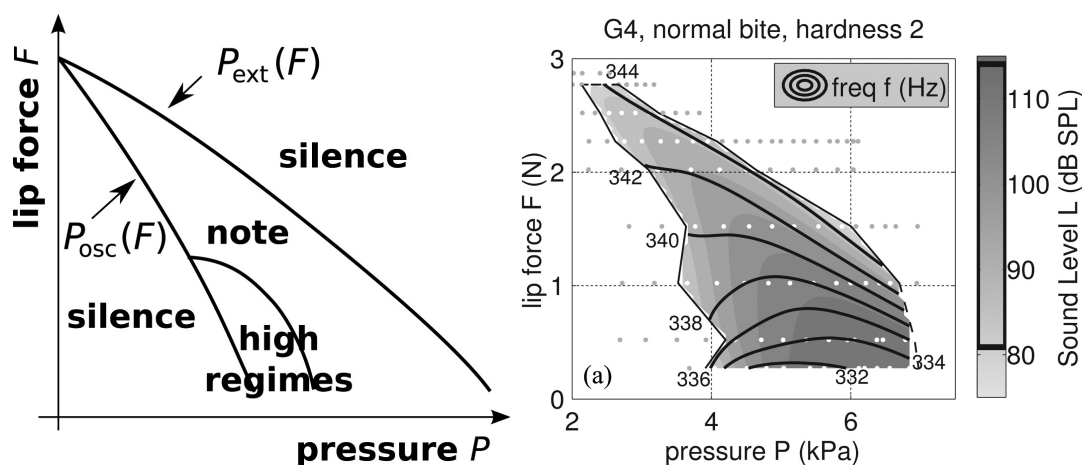


**Fig. 2.4:** A schematic of the regimes on the mouth pressure - lip force plane (left) and an example of the map (right). Reproduced from Almeida et al. (2013), with the permission of AIP Publishing.

As discussed in Sec. 2.1.4, a player adjusts his/her vocal tract to help perform in the altissimo register or for special effects. Furthermore, the vocal tract is known to influence the timbre of the instrument. Li et al. (2015) found that harmonics of radiated sound can be reinforced by adjusting the vocal tract to make its input impedance magnitude comparable with that of the bore. Various studies have observed a similar effect (Benade, 1986, Scavone et al., 2008).

Tonguing is another important aspect of single-reed instrument performance that is known to influence various transients. However, a review on the tonguing effects will not be covered here (readers are referred to Almeida et al. (2017), Li et al. (2016a,b) and Pàmies-Vilà et al. (2018) for more detailed discussion).

## 2.3 Methodology Review

From the point of view of methodologies, the research on the single-reed instrument is classified into three categories as theoretical/analytical, experimental<sup>6</sup>, and numerical studies.

### 2.3.1 Theoretical and analytical studies

The theoretical study aims at proposing a proper physical description and mathematical model to explain the observed physical phenomenon throughout the single-reed instrument sound generating process. It serves as the foundation for analytical and numerical research and is continuously refined with the support of physical and numerical experiments. Early development of the mathematical framework relied largely on the theoretical study as discussed in Sec. 2.1.1.

The analytical research presented here is specifically concerned with studies that analytically calculate the oscillation and analyze the oscillation characteristics based on the mathematical model. Backus (1963) assumed a small amplitude vibration, and linearized the system by expressing the variables as a sum of an equilibrium value and a small sinusoidal perturbation. A characteristic equation of the linearized system is constructed in the frequency domain, which connects the resonator admittance and the embouchure parameters such as the mouth pressure. The analytical solutions to the characteristic equation are used to investigate the basic characteristics of the oscillation such as the mouth pressure and frequencies at the oscillation thresholds, and oscillation's dependence on other system parameters (Silva et al., 2008, Wilson and Beavers, 1974).

Another type of frequency-domain analytical study relies on the Fourier expansion of the pressure and the Taylor expansion of the nonlinear Eq. 2.2 (Benade and Gans, 1968, Grand et al., 1997, Kergomard, 1995). The system solution provides expressions of the Fourier expansion coefficients, i.e., the amplitudes of harmonics of the pressure signal, and the expression is written in terms of the Taylor expansion coefficients and the resonator admittance at the respective resonant frequencies, either of which can be used as a control variable to study its influence on the oscillation characteristics.

In addition to the frequency-domain impedance or admittance, the time-domain reflection function was applied for analytical studies of oscillation thresholds and stability (Kergomard,

---

<sup>6</sup>It means physical experiments here.

1995, Ch. 6.3), as well as to investigate the effect of resonator losses using Raman's model (Dalmont et al., 2005, Taillard and Kergomard, 2015).

### 2.3.2 Experimental study

Experimental studies are classified into two categories based on the condition of the instrument during the measurement, including measurements with and without players.

#### 2.3.2.1 Measurements without players

The measurement of an instrument at rest normally aims at investigating the linear properties of the instrument. Such measurement ignores the influence of the performer on the instrument and focuses on the properties of the instrument itself.

The most typical example is the input impedance measurement of the resonator. The measured input impedance is used not only to characterize the resonator acoustics, but also for oscillation characterization and sound synthesis. Readers might refer to the papers by Dalmont (2001a,b) and Dickens et al. (2007, Sec. II) to learn about the various available techniques. There are two most commonly applied techniques for measuring wind instruments. The first one is based on the two-microphone-three-calibration (TMTC) technique (Gibiat and Laloë, 1990). The primary component is the measurement head, which is typically a cylindrical pipe with one side closed by a loudspeaker and the other side connected to the object to be measured. Two microphones are installed at different points along the pipe to measure the acoustic signal, which is then utilized to calculate the input impedance in conjunction with the coefficients obtained during the calibration process. There exist variants of TMTC, which may include more microphones or a different set of calibrations to improve measuring accuracy and range (Dickens et al., 2007, van Walstijn et al., 2005). Another widely used equipment was developed jointly by CTTM (Centre de Transfert de Technologie du Man) and LAUM (Laboratoire d'Acoustique de l'Université du Maine) (Dalmont and Le Roux, 2008, Macaluso and Dalmont, 2011). The setup includes a small cavity, which is separated by a piezoelectric buzzer into a fully-sealed back cavity and a front cavity connected to the acoustic component to be measured. Two microphones are flush mounted to the two cavities, and the measured signal is used to compute the input impedance with two analytical variables determined by the cavity shape and the microphone sensitivity.

### 2.3.2.2 Measurements with players

Measurements of musical instruments under the playing condition provide the dynamic characteristics of the system. They are mostly used to investigate the oscillation characteristics of the instrument, as well as their dependence on the player's embouchure or the instrument's properties, as detailed in Sec. 2.2. Such measurements also help capture the nonlinear phenomena of the system that are not available without playing the instrument, such as the turbulent flow in the mouthpiece (Lorenzoni and Ragni, 2012) and the nonlinear losses at the pipe termination (Atig et al., 2004).

Though a human player can play the instrument during the measurement, mechanical (artificial) players are more commonly used for measurements that require a great repeatability or accurate control of the embouchure. Appendix A presents a more in-depth review on the artificial player, including methods of controlling the embouchure, measurable signals and the selection of equipment.

### 2.3.3 Numerical study

The numerical study can be roughly categorized into the following three groups based on the research objectives and applications:

- high-fidelity physical models,
- nonlinear dynamic systems, and
- sound synthesis.

#### 2.3.3.1 High-fidelity physical models

The high-fidelity computational model is normally applied to study the physics of the instrument, and it involves a governing equation system to model the physical problem. The governing equation system is typically composed of partial differential equations and boundary conditions, which describe the corresponding physical fields. Examples include the wave equation in time-domain acoustic problems, the Helmholtz equation in frequency-domain problems, and the Navier-Stokes equation for fluid dynamic problems. The physical field first requires domain discretization, after which numerical methods are applied to solve the problem. The finite element method (FEM) is often used to solve the frequency-domain acoustic problem, such as the frequency-domain acoustic characterization of various resonator components including the mouthpiece (Andrieux et al., 2014) and the tonehole (Lefebvre and

Scavone, 2012), to name a few. In addition, it can also be applied for the modal analysis of the reed (Facchinetti et al., 2003). It is also possible to apply FEM in a time-domain simulation, however, the finite difference method (FDM) is most commonly applied in time-domain simulations of the single-reed instrument (Giordano and Thacker, 2020, Yokoyama et al., 2020, Yoshinaga et al., 2021). Such simulations also involve an FDM solver of the reed vibration as proposed by Avanzini and van Walstijn (2004). Different from FEM and FDM, which is applicable to a variety of physical domains, the lattice Boltzmann method (LBM) is used exclusively in the fluid dynamic simulation <sup>7</sup> (da Silva, 2008, Shi, 2016). Furthermore, LBM describes physics at the mesoscopic level and solves the Boltzmann equation, rather than the macroscopic level Navier-Stokes equation as solved by FEM and FDM. Ch. 4 will go into greater detail on LBM and its application to aeroacoustic problems.

### 2.3.3.2 Nonlinear dynamic system

Another type of numerical method is used to calculate and analyze the oscillation of the nonlinear dynamical system. The differential equation and the difference equation (also known as the iterated map) are two types of dynamical systems that are defined in continuous time and discrete time, respectively (Strogatz, 2015, 1.2).

McIntyre et al. (1983, Appendix A) for the first time considered the sound generation model of the clarinet as a nonlinear iterated map, allowing them to graphically obtain the oscillation at different regimes and explore the bifurcation in the clarinet-like system (Maganza et al., 1986, Taillard et al., 2010).

Karkar et al. (2010, 2012) for the first time rewrote the system of a clarinet as an ordinary differential equation system:

$$\dot{\mathbf{x}}(t) = \mathbf{f}(\mathbf{x}(t), \lambda), \quad (2.23)$$

where  $\mathbf{x} \in \mathbb{R}^n$  is the state vector (unknowns) of the system,  $\dot{\mathbf{x}}$  is its time derivative and  $\lambda \in \mathbb{R}$  is the chosen control parameter such as the mouth pressure. This type of system can be numerically solved using the numerical continuation method (also known as the path-following method), which requires first calculating the static or periodic solutions of the system and then continuing the solutions with the varying control parameter. While the continuation of the static solution relies on the algebraic equation  $\mathbf{f}(\mathbf{x}(t), \lambda) = 0$ , the continuation of periodic solutions is based on the mathematical framework proposed by

---

<sup>7</sup>It is possible, though less common, to use LBM for pure acoustic problems.

Cochelin and Vergez (2009), which combines the harmonic balance method (HBM) and the asymptotic numerical method (ANM). More recently, the same method was used to investigate the oscillation characteristics of the saxophone (Colinot et al., 2019, 2020, 2021).

### 2.3.3.3 Sound Synthesis

The last type of research discussed in this section is the physical modeling-based sound synthesis of the single-reed instrument. The sound synthesis does not only serve for music purposes, but more importantly, to explore the dynamics and oscillation characteristics of the instrument (Colinot et al., 2019, Kergomard et al., 2016, Petersen et al., 2020b). It can also be applied in inverse modeling for estimating and analyzing reed (Chatziioannou and van Walstijn, 2012) and articulatory (Chatziioannou and Hofmann, 2015) parameters.

Most of the synthesis schemes were based on the mathematical framework as discussed in Sec. 2.1.1, and Schumacher (1981) was the first to apply such a framework in the clarinet sound synthesis. In such a framework, the reed, flow and the acoustic resonator are modeled with three equations, and it is assumed a localized interaction between them at the entrance of the resonator or the tip of the reed. Here follows a brief review on the various ways of modeling and discretizing the reed, flow, and the resonator.

**The reed** is usually modeled as a single-degree-of-freedom harmonic oscillator as shown in Eq. 2.5 that may be discretized and solved with methods such as central finite difference (Guillemain et al., 2005), the bilinear transform (Scavone and Smith, 2006), and the impulse invariant method (van Walstijn and Avanzini, 2007). Even though less common, the 1D distributed reed model has also been used in the synthesis (Sommerfeldt and Strong, 1988, Stewart and Strong, 1980).

The only **flow model** applied in sound synthesis is the Bernoulli equation-based model, including the models with (*the free jet model*) and without (*the Bernoulli model*) the contraction coefficients. Chatziioannou and van Walstijn (2008) might be the only exception, who used the *Poiseuille model* to investigate the effect of a variable vena contracta coefficient. The results showed a minor effect on the steady-state signal but a large influence on the transients of the sound.

The **resonator** can be modeled with a frequency-domain input impedance or reflectance. However, such frequency-domain representations need to be converted to the time domain for sound synthesis. The impulse response or the reflection function, the time-domain equiv-

alents of the input impedance and the reflectance, respectively, can be used to model the air column. Using the time-domain response for the sound synthesis involves convolutions, which are more numerically expensive for longer responses. As a result, the reflection function is preferred over the impulse response due to its much shorter length. The reflection function was firstly applied to single-reed instrument simulation by Schumacher (1981), and was afterwards used by other authors (Gazengel et al., 1995, McIntyre et al., 1983).

Another way of converting the frequency-domain input impedance to the time-domain simulation is achieved with the help of the modal expansion (Coyle et al., 2015, Silva et al., 2014):

$$Z(\omega) = j\omega \sum_n \frac{F_n}{\omega_n^2 - \omega^2 + j\omega\omega_n/Q_n} = \sum_n \frac{C_n}{j\omega - s_n}, \quad (2.24)$$

where the input impedance is decomposed into contributions by a series of Helmholtz resonators controlled by  $\omega_n$ ,  $Q_n$  and  $F_n$ , representing the resonance frequency, quality factor and the modal “amplitude” of the  $n$ -th mode.  $s_n$  and  $C_n$  contribute to an alternative form of the modal expansion, which represents the poles and the residues, respectively. A corresponding time-domain model is typically constructed with a series of parallel one-zero, two-pole IIR filters (Maestre et al., 2016, 2017, Taillard et al., 2018), with the modal coefficients derived from the measured input impedance. Taillard et al. (2018) derived the coefficients by applying Prony’s method to fit the impulse response. Maestre et al. (2017) extracted the coefficients through linear constrained pole optimization (Maestre et al., 2016). It is worth mentioning that the modal expansion must be truncated to a finite order  $N$  before being applied to the sound synthesis. However, such a truncation causes the reflectance modulus to approach unity as the frequency approaches the Nyquist frequency. Such a problem can be fixed by employing a low-pass filter as used by Guillemain and Silva (2010), or by including an additional set of poles distributed from the maximum frequency of interest to the Nyquist frequency (Maestre et al., 2017, Taillard et al., 2018). Compared to the time-domain response, the modal representation helps avoid convolutions, which makes the simulation more efficient.

With either the reflection function or the modal representation, the resonator model can be expressed as a difference equation in the form of

$$p[n] = B_0 u[n] + q[n], \quad (2.25)$$

where  $n$  represents the current time step,  $B_0$  is a constant and  $q[n]$  depends on the pressure and velocity history, i.e.,  $p[n - k]$  and  $u[n - k]$  with  $k \geq 1$ .

Other than using a measured or simulated frequency-domain input impedance, the resonator can be simulated in the time-domain using the digital waveguide method (Scavone, 1997, Smith, 1986) or the finite difference method (Billbao, 2009a,b). Such methods require explicit modelings of all components of the resonator such as the bore, tonehole and the bell. The coupling between the resonator and the other synthesis components such as the reed-flow model and radiation domain are modeled through lumped elements or boundary conditions.

There are two special components that also act as resonators, which are the mouthpiece and the player’s vocal tract. The mouthpiece in a clarinet is mostly modeled by elongating the cylindrical pipe with a certain extra length that has an equivalent volume of the mouthpiece. For a saxophone, either a parallel acoustic compliance (Kergomard et al., 2016) or a cylinder (Scavone, 2002) can be used to represent the mouthpiece, which also requires the corresponding volume to equal that of the mouthpiece. There has also been other attempts such as using a cylinder and a truncated cone to represent the mouthpiece (Chatziioannou and Hofmann, 2015, Chatziioannou and van Walstijn, 2012), or a series of “cylinder segments” with vary cross-section areas (Stewart and Strong, 1980).

The modeling of the vocal tract is generally similar to that of the bore, and can be represented as a pipe with varying cross-section areas (Sommerfeldt and Strong, 1988). In addition, by assuming that a single resonance of the vocal tract is tuned to control the reed vibration, the vocal tract can be simplified as an upstream windway with a single resonance, and such a simplified representation can be modeled by a simple equivalent circuit as proposed by Scavone (2003).

The **player**’s control over the instrument is mainly achieved through the control of the mouth pressure. The incorporation of the lip and tongue is typically obtained by equivalently modifying reed parameters as discussed in Sec. 2.1.2. A separate oscillator is used to represent the tongue in Ducasse (2003)’s model, which provides an explicit and physics-informed way to control the tonguing. However, such a model is less commonly applied in other research, either to keep the model simple or because the lack of interests in studying the tonguing effect.

The **coupling** of different components in the discrete-time domain, such as the incorporation of Eq. 2.25 for the resonator, Eq. 2.4 for the airflow, and Eq. 2.5 for the reed, requires

to solve an implicit nonlinear system of equations. Such a system can be explicitly solved if the modeling of the reed displacement does not involve a delay-free loop (Guillemain et al., 2005, Scavone and Smith, 2006). Otherwise, an implicit method is required, such as the Newton-Raphson method, to solve the nonlinear system (Gazengel et al., 1995).

The last puzzle of sound synthesis is the **external sound** or radiated sound, which is typically calculated using synthesized acoustic variables in the mouthpiece with a model that transfers the mouthpiece variables to external sound pressure.

Guillemain et al. (2005) proposed the following approximation for the radiated pressure from a cylindrical clarinet

$$p_{\text{ext}} = \frac{\partial}{\partial t}(p(t) + u(t)), \quad (2.26)$$

where  $p(t)$  and  $u(t)$  represent the pressure and flow rate in the mouthpiece, respectively. It neglects the losses and delay of the traveling wave so that will result in a brighter sound.

Taillard (2018, Ch. 7) designed a numerical filter to represent a global radiation transfer function between the external pressure and the mouthpiece pressure, which was derived from experimental data for all the fingerings of a clarinet.

Maestre et al. (2018) modeled the radiation transfer function as a recursive parallel filter in conjunction with that of the input impedance. It allowed a fingering-dependent transfer function, and provided an accurate and efficient way of calculating the radiated pressure.

## Chapter 3

# Acoustics and aeroacoustics fundamentals

This chapter introduces the fundamental theories of acoustics and aeroacoustics including the governing equations and basic concepts required for modeling and analysis in the following chapters.

### 3.1 Governing equations of fluid dynamics

#### 3.1.1 Continuity equation

The continuity equation is based on mass conservation as described in the following equation, which states that the rate of change of mass within a volume  $V$  equals mass influx across the surface  $S$

$$\frac{\partial}{\partial t} \int_V \rho \, dV = - \oint_S \rho (\mathbf{v} \cdot \mathbf{n}) \, dS. \quad (3.1)$$

There is a negative sign on the right-hand side (RHS) because the normal vector to the boundary is pointing outward, so that the influx points in the opposite direction.

The surface integral on the RHS is transformed to a volume integral by applying the divergence theorem

$$\int_V (\nabla \cdot \mathbf{F}) \, dV = \oint_S (\mathbf{F} \cdot \mathbf{n}) \, dS, \quad (3.2)$$

so that  $\oint_S \rho (\mathbf{v} \cdot \mathbf{n}) \, dS = \int_V \nabla \cdot (\rho \mathbf{v}) \, dV$ .

The equation of continuity is obtained by differentiating both sides of the equation to eliminate a volume integral, written as

$$\frac{\partial \rho}{\partial t} + \nabla \cdot (\rho \mathbf{v}) = 0, \quad (3.3)$$

or in the index notation

$$\frac{\partial \rho}{\partial t} + \frac{\partial \rho v_i}{\partial x_i} = 0. \quad (3.4)$$

### 3.1.2 Momentum Equation

The momentum equation is based on Newton's second law, which states that the rate of change of momentum is driven by the force acting on the system  $\mathbf{F}$ , which is denoted as

$$\frac{d(\rho \mathbf{v})}{dt} = \mathbf{F}. \quad (3.5)$$

The rate of change of momentum is rewritten into the control volume formulation

$$\frac{d(\rho \mathbf{v})}{dt} = \frac{\partial}{\partial t} \int_V \rho \mathbf{v} dV + \oint_S \mathbf{v} \rho (\mathbf{v} \cdot \mathbf{n}) dS, \quad (3.6)$$

where the first term on the RHS represents the rate of change of momentum within the control volume, and the second term is the contribution by the momentum flux through the surface.

The force acting on the system is comprised of the surface force  $-\oint_S \mathbf{p} \cdot \mathbf{n} dS$  contributed by the compressive stress tensor  $\mathbf{p}$ , and the body force  $\int_V \mathbf{f}_{body} dV$ , though the body force is typically ignored for acoustic problems. The momentum equation is derived using the divergence theorem and differentiation, following a process similar to that used to derive the continuity equation,

$$\frac{\partial(\rho \mathbf{v})}{\partial t} + \nabla \cdot \rho \mathbf{v} \mathbf{v} = -\nabla \cdot \mathbf{p}, \quad (3.7)$$

with the corresponding form in index notation

$$\frac{\partial \rho v_i}{\partial t} + \frac{\partial \rho v_i v_j}{\partial x_j} = -\frac{\partial p_{ij}}{\partial x_j}. \quad (3.8)$$

The term  $p_{ij}$  denotes the compressive stress tensor in the  $i$  direction acting on the surface normal to the  $j$  direction. It is composed of an isotropic stress tensor  $p\delta_{ij}$  and viscous stress tensor  $-\tau_{ij}$ , i.e.,  $p_{ij} = p\delta_{ij} - \tau_{ij}$ <sup>1</sup>.

The viscous stress tensor is defined as follows

$$\tau_{ij} = \mu \left( \frac{\partial v_i}{\partial x_j} + \frac{\partial v_j}{\partial x_i} - \frac{2}{3} \delta_{ij} \frac{\partial v_k}{\partial x_k} \right) + \mu_B \delta_{ij} \frac{\partial v_k}{\partial x_k}, \quad (3.9)$$

where  $\mu$  is the dynamic viscosity coefficient,  $\mu_B = 2\mu/3 + \lambda$  is the bulk viscosity coefficient with  $\lambda$  the second viscosity coefficient. It is sometimes written in terms of the rate of strain tensor  $\varepsilon_{ij} = \frac{1}{2} \left( \frac{\partial v_i}{\partial x_j} + \frac{\partial v_j}{\partial x_i} \right)$ , and  $\frac{\partial v_k}{\partial x_k}$  is also known as the rate of expansion of the flow.

The bulk viscosity  $\mu_B$  can be assumed to be zero based on the Stokes' hypothesis<sup>2</sup>, and the viscous stress tensor can be simplified as

$$\tau_{ij} = \mu \left( \frac{\partial v_i}{\partial x_j} + \frac{\partial v_j}{\partial x_i} - \frac{2}{3} \delta_{ij} \frac{\partial v_k}{\partial x_k} \right).$$

The left-hand side (LHS) of Eq. 3.8 can be further simplified

$$\frac{\partial \rho v_i}{\partial t} + \frac{\partial \rho v_i v_j}{\partial x_j} = \rho \frac{\partial v_i}{\partial t} + \underbrace{v_i \frac{\partial \rho}{\partial t} + v_i \frac{\partial \rho v_j}{\partial x_j}}_{\text{LHS of Continuity Equation times } v_i} + \rho v_j \frac{\partial v_i}{\partial x_j} = \rho \frac{\partial v_i}{\partial t} + \rho v_j \frac{\partial v_i}{\partial x_j},$$

which helps rewrite the momentum equation into the convective (non-conservation) form

$$\rho \frac{dv_i}{dt} = -\frac{\partial p_{ij}}{\partial x_j}, \quad (3.10)$$

where  $\frac{dv_i}{dt} = \frac{\partial v_i}{\partial t} + v_j \frac{\partial v_i}{\partial x_j}$ .

<sup>1</sup>This notation is more generally used in aeroacoustics, while in fluid dynamics, it is more commonly written as  $\sigma_{ij} = -p\delta_{ij} + \tau_{ij}$  (the sign is flipped) in the fluid dynamics context (Glegg and Devenport, 2017, Sec. 2.3).

<sup>2</sup>The relationship between the dynamic viscosity  $\mu$  and second viscosity  $\lambda$  is assumed to be  $\lambda + \frac{2}{3}\mu = 0$  by Stokes (1845).

### 3.1.3 Energy equation

The energy equation is derived based on the first law of thermodynamics, which states that the rate of change of energy equals the rate of heat transfer into the system minus the rate of work done by the system,

$$\frac{dE_e}{dt} = \frac{dQ_e}{dt} - \frac{dW_e}{dt}, \quad (3.11)$$

and

- the energy comprises the internal energy  $e$  and the kinetic energy  $\frac{1}{2}v^2$ , so that  $\frac{dE_e}{dt} = \frac{d}{dt} \int_V \rho \left( e + \frac{1}{2}v^2 \right) dV$ ,
- the heat transfer rate through the surface gives  $\frac{dQ_e}{dt} = - \int_S \mathbf{q}_e \cdot \mathbf{n} dS$ , where  $\mathbf{q}_e$  is the heat flux density. It becomes  $\frac{dQ_e}{dt} = \int_S \kappa_e \nabla T_e \cdot \mathbf{n} dS$  by applying Fourier's law  $\mathbf{q}_e = -\kappa_e \nabla T_e$ , where  $\kappa_e$  is the heat conductivity and  $T_e$  is the temperature, and
- the rate of work done by the system is mainly attributed to the surface stress tensor  $\mathbf{p}$ , which gives  $\frac{dW_e}{dt} = \int_S \mathbf{p} \cdot \mathbf{v} \cdot \mathbf{n} dS$ .

The energy equation is written as

$$\frac{\partial}{\partial t} \left[ \rho \left( e + \frac{1}{2}v^2 \right) \right] + \frac{\partial}{\partial x_i} \left[ \rho v_i \left( e + \frac{1}{2}v^2 \right) \right] = \kappa_e \frac{\partial^2 T_e}{\partial x_i^2} - \frac{\partial p_{ij} v_i}{\partial x_j}. \quad (3.12)$$

It can be simplified by subtracting  $\{\text{Eq. 3.10} \times v_i\}$ , which leads to

$$\rho \frac{de}{dt} = -p \frac{\partial v_i}{\partial x_i} + \tau_{ij} \frac{\partial v_i}{\partial x_j} + \kappa_e \frac{\partial^2 T_e}{\partial x_i^2}. \quad (3.13)$$

For adiabatic flow where  $\mathbf{q} = 0$ , it is further simplified as

$$\rho \frac{de}{dt} = -p \frac{\partial v_i}{\partial x_i} + \tau_{ij} \frac{\partial v_i}{\partial x_j}. \quad (3.14)$$

The governing equation system comprises the continuity equation Eq. 3.4, the momentum equation Eq. 3.8, and the energy equation Eq. 3.14, which has five equations<sup>3</sup> in a three-dimensional (3D) system but involve six unknowns  $\rho$ ,  $p$ ,  $\mathbf{v}$  and  $e$ , where  $\mathbf{v}$  is a vector with

<sup>3</sup>Equation 3.8 composes three equations, which correspond to the three directions in a 3D system, respectively.

three components  $v_1, v_2, v_3$ . An additional equation is necessary to close the system and this is generally accomplished with an equation of state, which is essentially a thermodynamic equation that relates state variables such as pressure, density, entropy, and temperature.

For a calorically perfect gas with constant specific heats, the internal energy can be expressed in terms of the pressure

$$e = \frac{p}{\rho(\gamma - 1)}, \quad (3.15)$$

where  $\gamma = c_p/c_v$  is the ratio of specific heat with  $c_p$  and  $c_v$  the specific heat capacities for constant pressure and volume, respectively.

Equation. 3.14 can then be reformed as follows:

$$\frac{\partial p}{\partial t} + v_i \frac{\partial p}{\partial x_i} + \gamma p \frac{\partial v_i}{\partial x_i} = (\gamma - 1) \tau_{ij} \frac{\partial v_i}{\partial x_j}. \quad (3.16)$$

## 3.2 Acoustics fundamentals

### 3.2.1 Speed of sound

An isentropic flow is normally assumed for acoustic problems (Pierce, 2019, Ch. 1), where the specific entropy  $s = c_v \ln(Cp/\rho^\gamma)$  constant ( $C$  is a constant of integration), which indicates that

$$\frac{p}{\rho^\gamma} \equiv \text{const.} \quad (3.17)$$

The speed of sound is found to be

$$c = \sqrt{\left(\frac{\partial p}{\partial \rho}\right)_s} = \sqrt{\frac{\gamma p}{\rho}}, \quad (3.18)$$

which is related to the adiabatic bulk modulus  $B_s = \rho(\partial p/\partial \rho)_s$ . For isentropic flow, the pressure is a function of only the density  $p = p(\rho)$ . Considering the acoustic disturbance as a small fluctuation on top of an ambient value, i.e.,  $p = p_0 + p'$ , and  $\rho = \rho_0 + \rho'$ , the Taylor expansion of  $p$  around  $p_0$  in  $\rho'$  gives

$$p' = \left(\frac{\partial p}{\partial \rho}\right)_s \rho' + \mathcal{O}((\rho')^2), \quad (3.19)$$

which indicates the acoustic pressure-density relationship

$$p' \approx c^2 \rho'. \quad (3.20)$$

### 3.2.2 Acoustic wave equation

The wave equation is derived through the linearization of the continuity and inviscid momentum equations ( $\mu = 0$ , so that  $p_{ij} = p\delta_{ij}$ ). The acoustic variables are considered to be small-amplitude fluctuations (superscript ') on top of the ambient value (subscript 0)

$$p = p_0 + p', \quad (3.21a)$$

$$\rho = \rho_0 + \rho', \quad (3.21b)$$

$$\mathbf{v} = \mathbf{v}_0 + \mathbf{v}', \quad (3.21c)$$

where  $\mathbf{v}_0 = \mathbf{0}$  for the quiescent flow.

The linearized continuity and momentum equations can be constructed by plugging the above expressions into Eqs. 3.4 and 3.8, and keeping only the first order terms,

$$\frac{\partial \rho'}{\partial t} + \rho_0 \frac{\partial v'_i}{\partial x_i} = 0, \quad (3.22)$$

$$\rho_0 \frac{\partial v'_i}{\partial t} + \frac{\partial p'}{\partial x_i} = 0. \quad (3.23)$$

The linear acoustic wave equation is obtained by subtracting the divergence of the linearized momentum equation from the time-derivative of the linearized continuity equation  $\left[ \frac{\partial}{\partial t}(\text{Eq. 3.22}) - \frac{\partial}{\partial x_i}(\text{Eq. 3.23}) \right]$ , and making use of the pressure-density relationship in Eq. 3.20,

$$\frac{1}{c^2} \frac{\partial^2 p'}{\partial t^2} - \frac{\partial^2 p'}{\partial x_i^2} = 0. \quad (3.24)$$

### 3.2.3 Green's function

The Green's function  $G(\mathbf{x}, t | \mathbf{y}, \tau)$  is defined as the solution to the inhomogeneous wave equation

$$\left( \frac{1}{c_0^2} \frac{\partial^2}{\partial t^2} - \nabla^2 \right) G(\mathbf{x}, t | \mathbf{y}, \tau) = \delta(\mathbf{x} - \mathbf{y}) \delta(t - \tau), \quad (3.25)$$

where  $\delta(\mathbf{x} - \mathbf{y})\delta(t - \tau)$  can be considered as the impulse source emitted at the location  $\mathbf{x} = \mathbf{y}$  and time  $t = \tau$ , and the Green's function corresponds to the resulting pressure distribution, which is essentially the impulse response of the system.

The Green's function can be used to solve the wave equation with an arbitrary sound source  $Q_s(\mathbf{x}, t)$

$$\left(\frac{1}{c_0^2} \frac{\partial^2}{\partial t^2} - \nabla^2\right) p(\mathbf{x}, t) = Q_s(\mathbf{x}, t). \quad (3.26)$$

The general solution is achieved by writing down the equation  $p \cdot$  (Eq. 3.25)  $- G \cdot$  (Eq. 3.26), which gives

$$\frac{1}{c^2} \left( p \frac{\partial^2 G}{\partial t^2} - G \frac{\partial^2 p}{\partial t^2} \right) - \left( p \frac{\partial^2 G}{\partial x_i^2} - G \frac{\partial^2 p}{\partial x_i^2} \right) = p \delta(\mathbf{x} - \mathbf{y}) \delta(t - \tau) - Q_s G, \quad (3.27)$$

and then integrating both sides over the time  $\tau$  and the volume  $V_{\mathbf{y}}$ , which results in the following expression

$$p(\mathbf{x}, t) = \int_{-\infty}^t \int_V \left[ \frac{1}{c^2} \left( p \frac{\partial^2 G}{\partial \tau^2} - G \frac{\partial^2 p}{\partial \tau^2} \right) - \left( p \frac{\partial^2 G}{\partial y_i^2} - G \frac{\partial^2 p}{\partial y_i^2} \right) + Q_s G \right] dV(\mathbf{y}) d\tau. \quad (3.28)$$

The first term on RHS is equal to 0 under a zero initial pressure and the causality condition, and the volume integral of the second term is simplified to the surface integral by applying Green's second identity, so that

$$\int_V \left( p \frac{\partial^2 G}{\partial y_i^2} - G \frac{\partial^2 p}{\partial y_i^2} \right) dV(\mathbf{y}) = \int_S \left( p \frac{\partial G}{\partial y_i} - G \frac{\partial p}{\partial y_i} \right) n_i dS(\mathbf{y}).$$

The solution can then be written as

$$p(\mathbf{x}, t) = \int_{-\infty}^t \int_V Q_s(\mathbf{y}, \tau) G(\mathbf{x}, t | \mathbf{y}, \tau) dV(\mathbf{y}) d\tau + \int_{-\infty}^t \int_S \left( p \frac{\partial G}{\partial y_i} - G \frac{\partial p}{\partial y_i} \right) n_i dS(\mathbf{y}) d\tau. \quad (3.29)$$

The first term in Eq. 3.29 represents the contribution of the source term  $Q$ , and the second term is attributed to the presence of the boundary in the fluid field. The second term is further subdivided into two contributions, with  $p \partial G / \partial y_i$  representing the contribution by the force exerted on the fluid by the boundary, and  $G \partial p / \partial y_i$  representing the contribution

due to the surface vibration<sup>4</sup>.

For unbounded fluids, the surface integrals vanish and the solution is simplified as

$$p(\mathbf{x}, t) = \int_{-\infty}^t \int_V Q_s(\mathbf{y}, \tau) G(\mathbf{x}, t | \mathbf{y}, \tau) dV(\mathbf{y}) d\tau. \quad (3.30)$$

In a three-dimensional case, the free-space Green's function is given as

$$G(\mathbf{x}, t | \mathbf{y}, \tau) = \frac{\delta\left(t - \tau - \frac{|\mathbf{x} - \mathbf{y}|}{c}\right)}{4\pi |\mathbf{x} - \mathbf{y}|}. \quad (3.31)$$

Substituting the Green's function into Eq. 3.30 gives

$$p(\mathbf{x}, t) = \frac{1}{4\pi} \int_V \frac{Q_s(\mathbf{y}, t^*)}{|\mathbf{x} - \mathbf{y}|} dV(\mathbf{y}), \quad (3.32)$$

where  $t^* = t - |\mathbf{x} - \mathbf{y}|/c$  is the retarded time.

### 3.2.4 Plane waves in cylindrical pipes

The plane wave propagation in a cylindrical pipe is governed by the one-dimensional wave equation

$$\frac{1}{c^2} \frac{\partial^2 p}{\partial t^2} - \frac{\partial^2 p}{\partial x^2} = 0, \quad (3.33)$$

whose sinusoidal solution is presented in the form of

$$p(x, t) = p^+ e^{j(\omega t - kx)} + p^- e^{j(\omega t + kx)}, \quad (3.34)$$

where  $p^+ e^{j(\omega t - kx)}$  and  $p^- e^{j(\omega t + kx)}$  represent the left and right traveling waves, correspondingly, with  $p^\pm$  the wave amplitude,  $\omega$  the radian frequency and  $k = \omega/c$  the wave number.

The momentum equation in the pipe reduces to

$$\frac{\partial p}{\partial x} = -\rho \frac{\partial v}{\partial t} = -\frac{\rho}{S} \frac{\partial u}{\partial t}, \quad (3.35)$$

where  $u(x, t) = v(x, t)S$  is the volume flow rate with  $S$  the cross-section area of the cylindrical

---

<sup>4</sup>This is because the inviscid momentum equation gives  $\frac{\partial p}{\partial y_i} n_i = -\rho_0 \frac{\partial v_i}{\partial \tau} n_i$ , so that the contribution is clearly related to the surface acceleration.

pipe.

The volume flow rate can be derived from the above momentum equation, which yields

$$u(x, t) = u^+ e^{j(\omega t - kx)} - u^- e^{j(\omega t + kx)}, \quad (3.36)$$

with the flow rate amplitudes

$$u^\pm = p^\pm / Z_c, \quad (3.37)$$

where  $Z_c = \rho c / S$  is the characteristic impedance of the pipe.

The Fourier transform of  $p$  and  $u$  gives the frequency-domain pressure  $P$  and volume flow rate  $U$ , and the pressure  $P$  is the solution to Helmholtz equation (the frequency-domain equivalent of the wave equation)

$$\nabla P + k^2 P = 0. \quad (3.38)$$

The acoustic impedance in the pipe is defined as the ratio of the frequency-domain pressure to the volume flow rate

$$Z(x, \omega) = \frac{P(x, \omega)}{U(x, \omega)}, \quad (3.39)$$

and the input impedance is the acoustic impedance defined at the input end of the pipe ( $x = 0$ ), which is denoted as,

$$Z_{\text{in}}(\omega) = Z(0, \omega) = \frac{P(0, \omega)}{U(0, \omega)}. \quad (3.40)$$

The reflectance is defined as

$$R(x, \omega) = \frac{P^-(x, \omega)}{P^+(x, \omega)} = \frac{U^-(x, \omega)}{U^+(x, \omega)}, \quad (3.41)$$

and its relationship with the impedance is given as

$$R = \frac{Z - Z_c}{Z + Z_c}, \quad (3.42)$$

$$Z = \frac{Z_c + R}{Z_c - R}. \quad (3.43)$$

### 3.2.5 Transfer matrix of cylindrical pipes

Considering a cylindrical pipe as an acoustical two-port system, a two-by-two transfer matrix  $\mathbf{T}$  can be used to describe the relationship between the pipe's input  $(P_1, U_1)$  and output  $(P_2, U_2)$ ,

$$\begin{bmatrix} P_1 \\ U_1 \end{bmatrix} = T \begin{bmatrix} P_2 \\ U_2 \end{bmatrix}, \quad (3.44)$$

where

$$\mathbf{T} = \begin{bmatrix} T_{11} & T_{12} \\ T_{21} & T_{22} \end{bmatrix}.$$

For a cylinder of length  $L$ , the transfer matrix is written as

$$\mathbf{T} = \begin{bmatrix} \cos(kL) & jZ_c \sin(kL) \\ jZ_c^{-1} \sin(kL) & \cos(kL) \end{bmatrix}. \quad (3.45)$$

The losses can be included by introducing the complex wavenumber  $k_c = \omega/v_p - j\alpha$ , where  $v_p$  is the phase velocity and  $\alpha$  is the loss coefficient, and the corresponding transfer matrix is defined as

$$\mathbf{T} = \begin{bmatrix} \cosh(\Gamma L) & Z_c \sinh(\Gamma L) \\ Z_c^{-1} \sinh(\Gamma L) & \cosh(\Gamma L) \end{bmatrix}, \quad (3.46)$$

where the parameter  $\Gamma = jk_c$  depends on the acoustic constants of the air (Chaigne and Kergomard, 2016, Ch. 5).

## 3.3 Aeroacoustics analogy

This section provides the aeroacoustics fundamentals with a focus on the aeroacoustic analogy, which will be applied in the aeroacoustic study of the saxophone mouthpiece in Chapter 7.

### 3.3.1 Lighthill's acoustic analogy

The Lighthill's acoustic analogy was proposed by Lighthill (1952, 1954), who reformulated the fluid dynamic governing equation in a wave equation-like format, which is known as the Lighthill equation. The Lighthill equation is derived in the same way as the wave equation,

but is based on the original continuity and momentum equations instead of the linearized ones. It subtracts the divergence of the momentum equation Eq. 3.8 from the time derivative of the continuity equation Eq. 3.4, then subtracts both sides with  $c_\infty^2 \partial^2 \rho / \partial x_i^2$ , yielding

$$\frac{\partial^2 \rho}{\partial t^2} - c_\infty^2 \frac{\partial^2 \rho}{\partial x_i^2} = \frac{\partial^2}{\partial x_i \partial x_j} [\rho v_i v_j + p_{ij} - \rho \delta_{ij}],$$

where  $c_\infty$  denotes the speed of sound at quiescent fluid surrounding the listener.

The density and pressure are written as the sum of the reference value at quiescent fluid and the fluctuation on top of it, i.e.,  $\rho = \rho_\infty + \rho'$  and  $p = p_\infty + p'$ . This implies that  $\partial^2 \rho / \partial t^2 = \partial^2 \rho' / \partial t^2$ , and  $\partial^2 p / \partial x_i^2 = \partial^2 p' / \partial x_i^2$ , resulting in Lighthill equation

$$\frac{\partial^2 \rho'}{\partial t^2} - c_\infty^2 \frac{\partial^2 \rho'}{\partial x_i^2} = \frac{\partial^2 T_{ij}}{\partial x_i \partial x_j}, \quad (3.47)$$

where  $T_{ij} = \rho v_i v_j + [p' - \rho' c_\infty^2] \delta_{ij} - \tau_{ij}$  is the Lighthill stress tensor.

The Lighthill equation can also be written in the same form as Eq. 3.26

$$\frac{1}{c_\infty^2} \frac{\partial^2 \rho' c_\infty^2}{\partial t^2} - \frac{\partial^2 \rho' c_\infty^2}{\partial x_i^2} = \frac{\partial^2 T_{ij}}{\partial x_i \partial x_j}, \quad (3.48)$$

and the corresponding solution is achieved by plugging the Lighthill stress tensor in Eq. 3.32 as the source ( $Q_s(\mathbf{x}, t) = \partial^2 T_{ij} / \partial x_i \partial x_j$ )

$$\rho'(\mathbf{x}, \mathbf{t}) c_\infty^2 = \frac{1}{4\pi} \frac{\partial^2}{\partial x_i \partial x_j} \int_V \frac{T_{ij}(\mathbf{y}, t^*)}{|\mathbf{x} - \mathbf{y}|} dV(\mathbf{y}). \quad (3.49)$$

### 3.3.2 Ffowcs Williams-Hawkings equation

Lighthill (1952) originally considered an unbounded field and Curle (1955) extended Lighthill's formulation to deal with solid bodies in a fluid field, and Ffowcs Williams and Hawkings (1969) generalized it further for moving boundary problems. While Curle (1955) used Eq. 3.29 to introduce the contribution of solid boundaries to the sound source, Ffowcs Williams and Hawkings (1969) generalized the Lighthill equation by introducing the control surface of the fluid domain, as illustrated in Fig. 3.1, with the closed control surface  $S$  defined by the function

$$f(\mathbf{x}) = 0, \quad (3.50)$$

where  $f(\mathbf{x}) > 0$  for the outside volume  $V$  and  $f(\mathbf{x}) < 0$  within  $S$ , and the outward pointing unit normal vector on  $S$  is given by

$$\mathbf{n} = \frac{\nabla f}{|\nabla f|}. \quad (3.51)$$

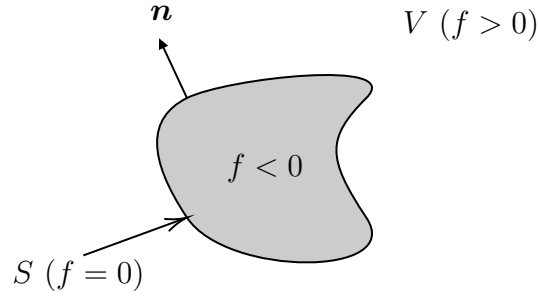


**Fig. 3.1:** Illustration of fluid domain with the function  $f(\mathbf{x})$  that defines the surface.

The continuity and momentum equations are expressed in terms of a new set of variables  $pH$ ,  $\rho H$ , and  $\mathbf{v}H$  defined across an unbounded region to generalize the Lighthill equation, where  $H(f)$  is the Heaviside unit function defined as

$$H(f) = \begin{cases} 1, & \text{for } f > 0 \\ 0, & \text{for } f < 0. \end{cases} \quad (3.52)$$

with its gradient and time derivative given as

$$\frac{\partial H(f)}{\partial x_j} = \delta(f) \frac{\partial f}{\partial x_j} = n_j \delta(f) |\nabla(f)|, \quad (3.53)$$

$$\frac{\partial H(f)}{\partial t} = -\bar{v}_j \frac{\partial H(f)}{\partial x_j}, \quad (3.54)$$

where  $\bar{v}_j$  is the velocity of the surface  $S$ .

The new continuity and momentum equations are given as <sup>5</sup>

$$\frac{\partial \rho' H}{\partial t} + \frac{\partial \rho v_i H}{\partial x_i} = (\rho v_j - \rho' \bar{v}_j) n_j \delta(f) |\nabla f|, \quad (3.55)$$

<sup>5</sup>The derivation in detail can be found in either (Glegg and Devenport, 2017, Ch. 5) or (Howe, 1998, Sec. 2.2).

$$\frac{\partial \rho v_i H}{\partial t} + \frac{\partial \rho v_i v_j H + p_{ij} H}{\partial x_j} = (\rho v_i (v_j - \bar{v}_j) + p_{ij}) n_j \delta(f) |\nabla f|, \quad (3.56)$$

and the Ffowcs Williams-Hawkings (FW-H) equation is derived using the same method as the Lighthill equation,

$$\left( \frac{1}{c_\infty^2} \frac{\partial^2}{\partial t^2} - \frac{\partial^2}{\partial x_i^2} \right) [\rho' c_\infty^2 H] = \frac{\partial^2 (HT_{ij})}{\partial x_i \partial x_j} + \frac{\partial F_i}{\partial x_i} + \frac{\partial Q}{\partial t}, \quad (3.57)$$

where

$$\begin{aligned} T_{ij} &= \rho v_i v_j + [p' - \rho' c_\infty^2] \delta_{ij} - \tau_{ij}, \\ F_i &= -(\rho v_i (v_j - \bar{v}_j) + p_{ij}) n_j \delta(f) |\nabla f|, \\ Q &= (\rho v_j - \rho' \bar{v}_j) n_j \delta(f) |\nabla f| \end{aligned}$$

correspond respectively to the contributions to

- the *quadrupole* sound source  $\partial^2 (HT_{ij}) / \partial x_i \partial x_j$  by the distributed Lighthill stress tensor  $T_{ij}$  in the volume,
- the *dipole* sound source  $\partial F_i / \partial x_i$  by
  - the compressive stress  $p_{ij}$  applied to the fluid by the surface and
  - the momentum flux  $\rho v_i (v_j - \bar{v}_j)$  through the surface, and
- the *monopole* sound source  $\partial Q / \partial t$  by the mass flux  $\rho v_j - \rho' \bar{v}_j$  across the surface.

Since the dependent variables are defined in the unbounded fluid, we can use Eq. 3.30 for expressing the solution by substituting  $Q_s(\mathbf{y}, \tau)$  with the RHS of Eq. 3.57,

$$\rho'(\mathbf{x}, t) c_\infty^2 H = \int_{-\infty}^t \int_V \left( \frac{\partial^2 (HT_{ij})}{\partial y_i \partial y_j} + \frac{\partial F_i}{\partial y_i} + \frac{\partial Q}{\partial \tau} \right) G(\mathbf{x}, t | \mathbf{y}, \tau) dV(\mathbf{y}) d\tau, \quad (3.58)$$

and is written in the following form after a series of simplifications

$$\begin{aligned} \rho'(\mathbf{x}, t) c_\infty^2 H &= \int_{-\infty}^t \int_V \frac{\partial^2 G}{\partial y_i \partial y_j} T_{ij} dV(\mathbf{y}) d\tau \\ &+ \int_{-\infty}^t \int_S \frac{\partial G}{\partial y_i} [\rho v_i (v_j - \bar{v}_j) + p_{ij}] n_j dS(\mathbf{y}) d\tau \\ &- \int_{-\infty}^t \int_S \frac{\partial G}{\partial \tau} [(\rho v_j - \rho' \bar{v}_j) n_j] dS(\mathbf{y}) d\tau. \end{aligned} \quad (3.59)$$

For an impenetrable surface where  $v_j n_j = \bar{v}_j n_j$ , the solution can be further simplified as

$$\begin{aligned} \rho'(\mathbf{x}, t) c_\infty^2 &= \int_{-\infty}^t \int_V \frac{\partial^2 G}{\partial y_i \partial y_j} T_{ij} dV(\mathbf{y}) d\tau \\ &+ \int_{-\infty}^t \int_S \frac{\partial G}{\partial y_i} p_{ij} n_j dS(\mathbf{y}) d\tau \\ &- \int_{-\infty}^t \int_S \frac{\partial G}{\partial \tau} \rho_\infty \bar{v}_j n_j dS(\mathbf{y}) d\tau. \end{aligned} \quad (3.60)$$

### 3.3.3 One dimensional FW-H acoustic analogy for internal flow aeroacoustic problems

Equation. 3.59 provides a general solution to the FW-H equation. It is expressed in terms of Green's function  $G$ , and the choice of the Green's function is problem-dependent. While the 3D free-field Green's function is typically applied to study external flow problems such as the noise of the jet (Mendez et al., 2013), the one-dimensional (1D) Green's function for an infinite long pipe has been widely applied to study aeroacoustic problems of internal flows, such as the flow passing through a diaphragm (Hofmans, 1998) or vocal folds (Zhao et al., 2001, 2002). The 1D Green's function for an infinite long pipe can be considered as an equivalent of the 3D free-field Green's function in 1D, which assumes an acoustic compact domain and a plane wave traveling in a pipe, and it is written as

$$G(x_1, t | y_1, \tau) = \frac{c}{2S} H(t - \tau - |x_1 - y_1|/c), \quad (3.61)$$

where  $S$  is the cross-section area. Its time-derivative and gradient give

$$\frac{\partial G}{\partial \tau} = -\frac{c}{2S} \delta(t - \tau - |x_1 - y_1|/c), \quad (3.62)$$

and

$$\frac{\partial G}{\partial y_1} = \frac{1}{2S} \text{sign}(x_1 - y_1) \delta(t - \tau - |x_1 - y_1|/c). \quad (3.63)$$

Taking an internal flow in a straight pipe with a diaphragm as an example, the FW-H integral domain can be defined to estimate the acoustic pressure at the observer, as illustrated in Fig. 3.2. The integral surface involves both solid walls such as the pipe walls, and permeable surfaces such as the inlet boundary  $S_{\text{in}}$  and outlet boundary  $S_{\text{out}}$ . Substituting

the 1D Green's function (Eq. 3.61) and its derivatives (Eqs. 3.62-3.63) into Eq. 3.59 yields the pressure at the observer:

$$\rho'(x_1, t)c_\infty^2 = \frac{1}{2c_\infty S} \frac{\partial}{\partial t} \int_V [T_{11}]|_{t^*} dV(\mathbf{y}) \quad (\text{I})$$

$$+ \frac{1}{2S} \int_{S_w} [p_{1j} n_j \text{sign}(x_1 - y_1)]|_{t^*} dS(\mathbf{y}) \quad (\text{II})$$

$$+ \frac{c_\infty}{2S} \int_{S_w} [\rho_\infty \bar{v}_j n_j]|_{t^*} dS(\mathbf{y}) \quad (\text{III})$$

$$+ \frac{1}{2S} \int_{S_{\text{in}}+S_{\text{out}}} [(\rho v_1 v_j + p_{1j}) n_j \text{sign}(x_1 - y_1) + \rho c_\infty v_j n_j]|_{t^*} dS(\mathbf{y}) \quad (\text{IV})$$

(3.64)

where  $t^* = t - |x - y|/c$  is the retarded time. The four different terms represent, correspondingly,

- (I) the quadrupole source contributed by Lighthill stress tensor  $T_{11}$  in the volume  $V$ ,
- (II) the dipole source due to the unsteady force exerted by the solid wall on the fluid in the  $x_1$  direction,
- (III) the monopole source due to the displacement flow induced by the wall movement, i.e., when  $\bar{v}_j \neq 0$ ,
- (IV) the sound source contributed by the inlet or outlet, which can be further decomposed as sources due to
  - the incoming acoustic wave  $p + \rho c v_j n_j$ , where  $p \delta_{1j} = p_{1j} + \tau_{1j}$ ,
  - the shear stress  $\tau_{1j}$ , and
  - the Reynolds stress  $\rho v_1 v_j n_j$ .

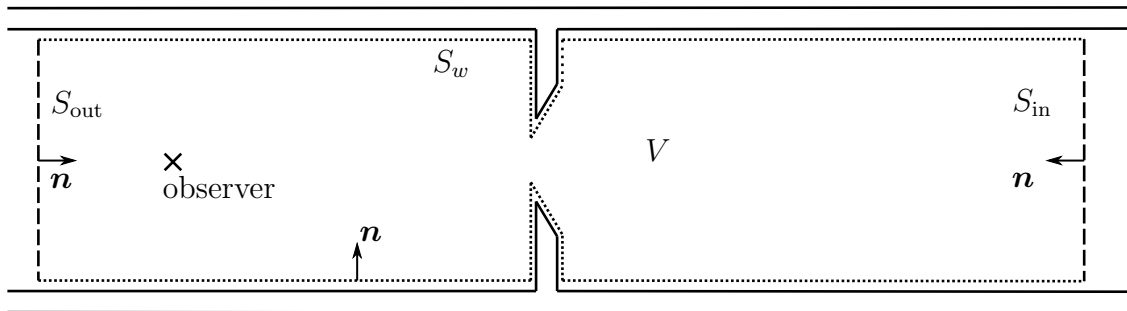


**Fig. 3.2:** The integral surface for FW-H analogy.

## Chapter 4

# Lattice Boltzmann method fundamentals

### 4.1 From Boltzmann equation to lattice Boltzmann method

The description of the fluid can be categorized into three classes based on different length and time scales as illustrated in Fig. 4.1. The *microscopic* description is defined at the molecular level, which tracks the movements and interactions of individual molecules on the length scale of the fluid molecule size  $l_m$ . The *macroscopic* description is established in the context of continuum mechanics, and the governing equations of fluid motion, as introduced in Sec. 3.1, are based on tangible quantities such as density, flow velocity, pressure, and temperature. The *mesoscopic* scale is defined on the length scale of the mean free path  $l_{\text{mfp}}$ , i.e., the average traveling distance between two successive collisions of molecules, and it lies in between the *microscopic* and *macroscopic* scales. It is developed in the context of statistical mechanics and is based on the kinetic theory of gases, which describes the fluid with regard to the distribution of a collection of fluid particles instead of individual particle motions.

The lattice Boltzmann method (LBM) is a mesoscopic model that originated from the lattice gas automata (LGA) (Frisch et al., 1986, Hardy et al., 1973), which simulates the gas or fluid dynamics on the *microscopic* scale. LGA is defined on a regular lattice of linked nodes, with each node storing a set of boolean variables that indicate the presence of a particle traveling in the direction of the node's links. The system evolves through a local collision

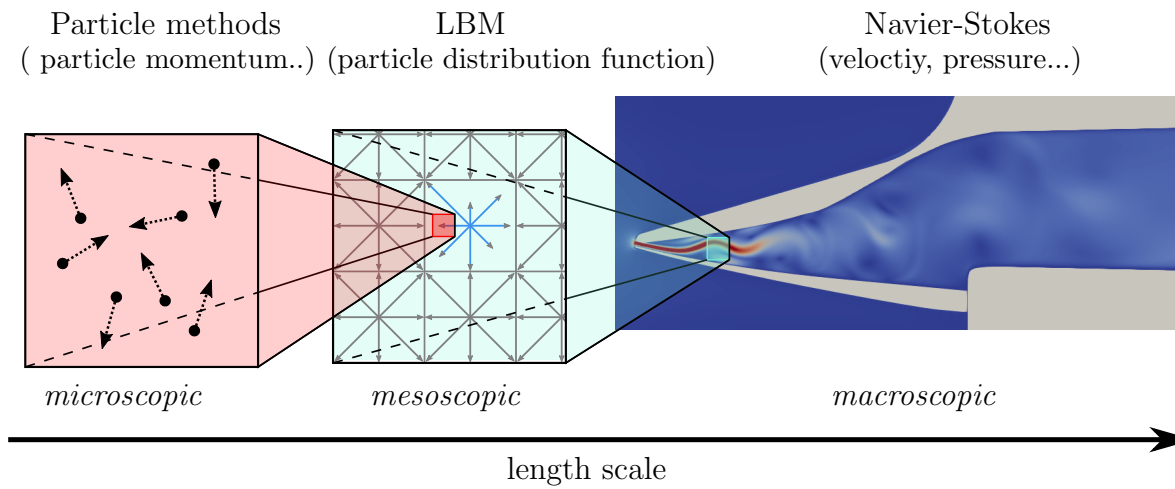


**Fig. 4.1:** Illustration of different length scales. Inspired by Krüger et al. (2017, Fig. 1.3) and Horstmann (2018, Fig. 2.3). The picture for the macroscopic is a snapshot of the velocity field of a mouthpiece simulation.

process and a post-collision streaming process. The collision process redirects particles on the node when they meet (collide), and the particles move on to a neighboring node following its traveling direction during the streaming process. LBM was first proposed by McNamara and Zanetti (1988), who translated LGA into a related Boltzmann model in which boolean state variables are replaced with distribution functions to represent the particle population. He and Luo (1997) demonstrated that LBM can develop from the continuum Boltzmann equation independently of LGA. This derivation will be discussed in the present chapter, following the map shown in Fig. 4.2.

The objective of this section is to present the fundamentals of LBM, including its derivation, as well as the advanced collision operators and boundary conditions that will be used for computational aeroacoustic modeling of the mouthpiece (Ch. 7). Readers seeking a more comprehensive understanding of LBM might refer to the book by Krüger et al. (2017) as well as theses by authors such as Coreixas (2018) and Vigen (2014).

#### 4.1.1 The Boltzmann equation

The *particle distribution function*  $f(\mathbf{x}, \boldsymbol{\xi}, t)$ , also known as the particle density function or probability density function, is used in the mesoscopic description of fluids based on kinetic

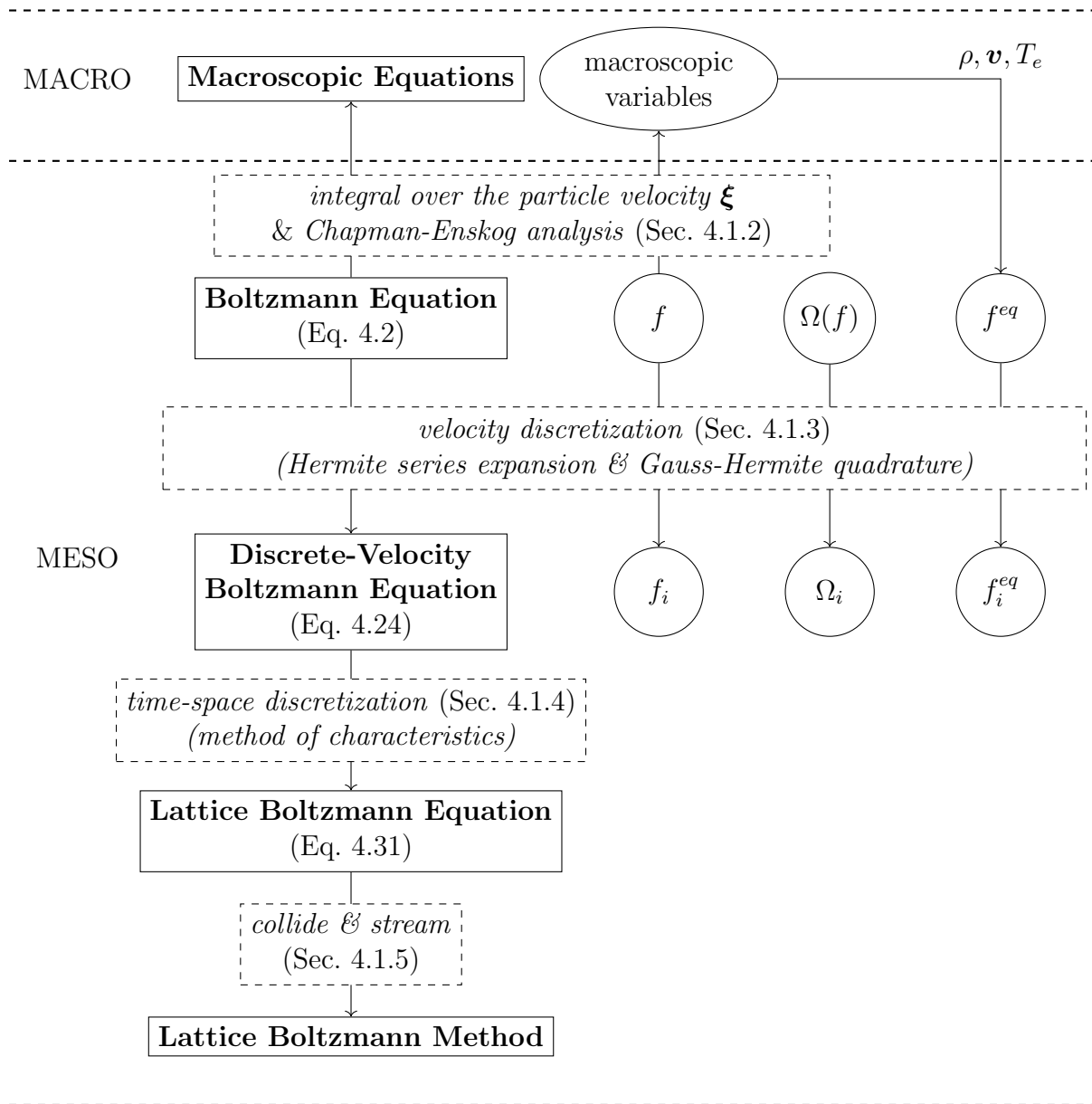


**Fig. 4.2:** The derivation framework of the lattice Boltzmann method.

theory. It is a function of physical space  $\mathbf{x}$ , velocity space  $\boldsymbol{\xi}$ , and time  $t$ .<sup>1</sup> The  $f$  can also be considered as a generalization of the macroscopic density  $\rho(\mathbf{x}, t)$ , which introduces additional dependence on  $\boldsymbol{\xi}$ .

The **Boltzmann equation** describes the evolution of  $f$  over time by relating the time rate of change of  $f$ , i.e.,  $df/dt$ , to the local redistribution of  $f$  due to the collision, represented by the collision operator  $\Omega(f)$ :

$$\frac{df}{dt} = \Omega(f). \quad (4.1)$$

By applying the chain rule to the total derivative  $df/dt$ , the Boltzmann equation is written as

$$\frac{\partial f}{\partial t} + \xi_\beta \frac{\partial f}{\partial x} + \frac{F_\beta}{\rho} \frac{\partial f}{\partial \xi_\beta} = \Omega(f), \quad (4.2)$$

where  $\xi_\beta = \frac{dx_\beta}{dt}$  and  $\frac{F_\beta}{\rho} = \frac{d\xi_\beta}{dt}$  specify the particle velocity and the body force, respectively.

The Bhatnagar-Gross-Krook (BGK) collision model, named after the three authors Bhatnagar, Gross, and Krook (Bhatnagar et al., 1954), defines one of the most basic collision operators

$$\Omega(f) = -\frac{1}{\tau}(f - f^{eq}). \quad (4.3)$$

It indicates that the distribution function is relaxed toward the local equilibrium distribution  $f^{eq}$  within the relaxation time  $\tau$  after collisions, and the equilibrium distribution is based on the **Maxwell-Boltzmann distribution** defined as

$$f^{eq}(\mathbf{x}, |\mathbf{c}|, t) = \frac{\rho}{(2\pi RT_e)^{D/2}} e^{-|\mathbf{c}|^2/(2RT_e)}, \quad (4.4)$$

where  $\mathbf{c} = \boldsymbol{\xi} - \mathbf{v}$  is the peculiar velocity, also known as the intrinsic velocity, representing the deviation of the particle velocity from the local mean velocity.  $R$  is the molar gas constant,  $T_e$  is the thermodynamic temperature, and  $D$  is the system dimension.

The dimensionless equilibrium distribution is written as

$$f^{eq}(\rho, |\mathbf{c}|, \theta) = \frac{\rho}{(2\pi\theta)^{D/2}} e^{-|\mathbf{c}|^2/(2\theta)}, \quad (4.5)$$

where  $\theta$  is the dimensionless temperature and  $\theta = 1$  for an isothermal system.

LBM is a numerical approach for solving the Boltzmann equation that relies on dis-

---

<sup>1</sup>The combination of  $\mathbf{x}$  and  $\boldsymbol{\xi}$  is known as the phase space  $(\mathbf{x}, \boldsymbol{\xi})$ .

cretizing the Boltzmann equation in physical space  $\mathbf{x}$ , time  $t$ , and particle velocity  $\boldsymbol{\xi}$ . The Boltzmann equation is first discretized in velocity space to establish the discrete-velocity Boltzmann equation (DVBE), which is then discretized in time and space to obtain the lattice Boltzmann equation (LBE). For simplicity, the following derivation is based on the isothermal force-free flow ( $\theta = 1$  and  $F_\beta = 0$ ).

#### 4.1.2 From Boltzmann equation to macroscopic equations

The macroscopic quantities, i.e., the density  $\rho$ , momentum density  $\rho\mathbf{v}$ , total energy density  $\rho E$ , and internal energy density  $\rho e$  can be recovered from the distribution function  $f$  by integrating its moments over the velocity  $\boldsymbol{\xi}$ .

$$\rho(\mathbf{x}, t) = \int f(x, \boldsymbol{\xi}, t) d\boldsymbol{\xi}, \quad (4.6a)$$

$$\rho(\mathbf{x}, t)\mathbf{v}(\mathbf{x}, t) = \int f(x, \boldsymbol{\xi}, t)\boldsymbol{\xi} d\boldsymbol{\xi}, \quad (4.6b)$$

$$\rho(\mathbf{x}, t)E(\mathbf{x}, t) = \frac{1}{2} \int f(x, \boldsymbol{\xi}, t)|\boldsymbol{\xi}|^2 d\boldsymbol{\xi}, \quad (4.6c)$$

$$\rho(\mathbf{x}, t)e(\mathbf{x}, t) = \int f(x, \boldsymbol{\xi}, t)|\mathbf{c}|^2 d\boldsymbol{\xi}. \quad (4.6d)$$

The macroscopic conservation equations, i.e., the continuity equation, momentum equation, and energy equation can be obtained by integrating the zeroth to second-order moments of the Boltzmann equation over the velocity space  $\boldsymbol{\xi}$ :

$$\frac{\partial \rho}{\partial t} + \frac{\partial \rho v_i}{\partial x_i} = 0, \quad (4.7a)$$

$$\frac{\partial \rho v_i}{\partial t} + \frac{\partial \rho v_i v_j}{\partial x_j} = -\frac{\partial \Pi_{ij}}{\partial x_j}, \quad (4.7b)$$

$$\frac{\partial \rho e}{\partial t} + \frac{\partial \rho v_j e}{\partial x_j} = -\Pi_{ij} \frac{\partial v_i}{\partial x_j} - \frac{\partial q_j}{\partial x_j}, \quad (4.7c)$$

where the stress tensor  $\mathbf{\Pi}$  and the heat flux  $\mathbf{q}$  are given as<sup>2</sup>

$$\mathbf{\Pi} = \int f \mathbf{c}^2 d\xi, \quad (4.8a)$$

$$\mathbf{q} = \frac{1}{2} \int f \mathbf{c}^3 d\xi. \quad (4.8b)$$

The tensors  $\mathbf{\Pi}$  and  $\mathbf{q}$  are not explicitly known but can be linked to the macroscopic variables through the so-called *Chapman-Enskog analysis* (Chapman and Cowling, 1970). Based on the Chapman-Enskog expansion, the distribution function is expanded as

$$f = f^{(0)} + \epsilon f^{(1)} + \epsilon^2 f^{(2)} + \dots, \quad (4.9)$$

where  $f^{(0)} = f^{eq}$  is the equilibrium distribution, and  $f^{(k)}$  represents the  $k$ th-order perturbation on top of equilibrium distribution when  $k \geq 1$ . The label  $\epsilon$  is a smallness label instead of a numerical parameter, and  $\epsilon^k$  indicates that  $f^{(k)}/f^{(0)} = \mathcal{O}(\text{Kn}^k)$ , where  $\text{Kn} = l_{\text{mfp}}/l$  is the Knudsen number defined as the ratio between the mean free path length  $l_{\text{mfp}}$  and the physical characteristic length  $l$ .

Different levels of momentum and energy equations can be recovered when the Chapman-Enskog expansion is truncated to different orders:

- zero-order ( $f \approx f^{eq}$ ): the Euler equation is recovered as it leads to  $\mathbf{\Pi} = p$  and  $\mathbf{q} = 0$ .
- first-order ( $f \approx f^{eq} + f^{(1)}$ ): the Navier-Stokes equation is recovered, where  $\mathbf{\Pi} = \mathbf{p}^3$  and  $\mathbf{q} = -\kappa \nabla T_e$  with the shear viscosity and thermal conductivity given as

$$\mu = \rho R T_e \tau, \quad (4.10a)$$

$$\kappa = \frac{5}{2} p R \tau. \quad (4.10b)$$

The Chapman-Enskog analysis is an important while complex topic. Its details are not expanded here but can be found in chapters like Krüger et al. (2017, Ch. 4) and Viggen (2014, Ch. 3.8).

---

<sup>2</sup>The power of a vector denotes the direct vector product such that  $\mathbf{c}^2 = \mathbf{c}\mathbf{c}$  presents an outer product, which should be distinguished from  $|\mathbf{c}|^2 = \mathbf{c} \cdot \mathbf{c}$ .

<sup>3</sup> $\mathbf{p}$  is the compressive stress tensor introduced in Ch. 3.1.2

### 4.1.3 Discretization in velocity space

The velocity space discretization was inherited from LGA and was not originally associated with the continuum Boltzmann equation. It was later connected to the Boltzmann equation using either the Mach number expansion (He and Luo, 1997) or Hermite series expansion (Shan and He, 1998). The latter method for velocity space discretization is illustrated here, in which the distribution function is projected into a space spanned by truncated Hermite series, with the Hermite coefficients directly related to macroscopic fluid variables. The Hermite coefficients are numerically evaluated using the Gauss-Hermite quadrature, which approximates the integral by adding up the weighted function values at abscissae, where the abscissae correspond to the discretized velocities in the velocity space.

#### 4.1.3.1 Projection of distribution functions on Hermite basis

Grad (1949a,b) recovered the Navier-Stokes equation from the Boltzmann equation using the Hermite series expansion, where the distribution function is expanded in terms of Hermite polynomials

$$f(\boldsymbol{\xi}) = \omega(\boldsymbol{\xi}) \sum_{n=0}^{\infty} \frac{1}{n!} \mathbf{a}^{(n)} : \mathbf{H}^{(n)}(\boldsymbol{\xi}), \quad (4.11a)$$

$$f^{eq}(\boldsymbol{\xi}) = \omega(\boldsymbol{\xi}) \sum_{n=0}^{\infty} \frac{1}{n!} \mathbf{a}^{(n),eq} : \mathbf{H}^{(n)}(\boldsymbol{\xi}), \quad (4.11b)$$

where the ‘:’ denotes full index contraction, and the coefficients are defined as

$$\mathbf{a}^{(n)} = \int f(\boldsymbol{\xi}) \mathbf{H}^{(n)}(\boldsymbol{\xi}) d\boldsymbol{\xi}, \quad (4.12a)$$

$$\mathbf{a}^{(n),eq} = \int f^{eq}(\boldsymbol{\xi}) \mathbf{H}^{(n)}(\boldsymbol{\xi}) d\boldsymbol{\xi} \quad (4.12b)$$

and the weight function is given as

$$\omega(\boldsymbol{\xi}) = \frac{1}{(2\pi)^{(D/2)}} e^{-\boldsymbol{\xi}^2/2}. \quad (4.13)$$

Taking the three lowest order Hermite polynomials as examples

$$\mathbf{H}^{(0)}(\boldsymbol{\xi}) = 1, \quad (4.14a)$$

$$\mathbf{H}^{(1)}(\boldsymbol{\xi}) = \boldsymbol{\xi}, \quad (4.14b)$$

$$\mathbf{H}^{(2)}(\boldsymbol{\xi}) = \boldsymbol{\xi}^2 - \boldsymbol{\delta}, \quad (4.14c)$$

the expansion coefficients are found to be directly related to hydrodynamic variables:

$$\mathbf{a}^{(0)} = \int f \, d\boldsymbol{\xi} = \rho, \quad (4.15a) \quad \mathbf{a}^{(0),eq} = \rho, \quad (4.15d)$$

$$\mathbf{a}^{(1)} = \int \boldsymbol{\xi} f \, d\boldsymbol{\xi} = \rho \mathbf{v}, \quad (4.15b) \quad \mathbf{a}^{(1),eq} = \rho \mathbf{v}, \quad (4.15e)$$

$$\mathbf{a}^{(2)} = \int (\boldsymbol{\xi}^2 - \boldsymbol{\delta}) f \, d\boldsymbol{\xi} = \boldsymbol{\Pi} + \rho(\mathbf{v}^2 - \boldsymbol{\delta}), \quad (4.15c) \quad \mathbf{a}^{(2),eq} = \rho \mathbf{v}^2, \quad (4.15f)$$

where  $\boldsymbol{\Pi} = \int f \mathbf{c}^2 \, d\boldsymbol{\xi}$ .

When the expansion is truncated to the finite order  $N$ , it implies that the distribution function is projected into the Hilbert space spanned by the leading  $N$  Hermite polynomials,

$$f^N(\boldsymbol{\xi}) \approx \omega(\boldsymbol{\xi}) \sum_{n=0}^N \frac{1}{n!} \mathbf{a}^{(n)} : \mathbf{H}^{(n)}(\boldsymbol{\xi}), \quad (4.16a)$$

$$f^{eq,N}(\boldsymbol{\xi}) \approx \omega(\boldsymbol{\xi}) \sum_{n=0}^N \frac{1}{n!} \mathbf{a}^{(n),eq} : \mathbf{H}^{(n)}(\boldsymbol{\xi}), \quad (4.16b)$$

Thanks to the orthogonality properties of the Hermite polynomials, the expansion coefficients  $\mathbf{a}^{(n)}$  for  $n \leq N$  can be expressed in terms of the truncated distribution function as follows

$$\mathbf{a}^{(n)} = \int f(\boldsymbol{\xi}) \mathbf{H}^{(n)}(\boldsymbol{\xi}) \, d\boldsymbol{\xi} = \int f^N(\boldsymbol{\xi}) \mathbf{H}^{(n)}(\boldsymbol{\xi}) \, d\boldsymbol{\xi}, \quad (4.17)$$

which indicates that velocity moments of  $f(\boldsymbol{\xi})$  up to  $N$ th order are preserved by  $f^N(\boldsymbol{\xi})$  and the corresponding conservation equation can be recovered<sup>4</sup>.

By keeping the expansion terms up to the second-order moment, the equilibrium distri-

---

<sup>4</sup>The Hermite expansion order  $n$  is directly related to hydrodynamic moment order such as the first-order coefficient  $\mathbf{a}^{(1)} = \rho \mathbf{v}$  is the same as the first-order hydrodynamic moment of the distribution function  $\int f \boldsymbol{\xi} \, d\boldsymbol{\xi} = \rho \mathbf{v}$ . It should be distinguished from the Chapman-Engskog expansion order  $k$  that is introduced in Sec. 4.1.2. Such two truncation orders work together in determining the hydrodynamic behavior of the discretized Boltzmann equations (Shan et al., 2006).

bution Eq. 4.16b is approximated as

$$f^{eq}(\boldsymbol{\xi}) \approx \omega(\boldsymbol{\xi})\rho \left[ 1 + \boldsymbol{\xi} \cdot \mathbf{v} + \frac{1}{2}(\boldsymbol{\xi} \cdot \mathbf{v})^2 - |\mathbf{v}|^2 \right] \quad (4.18)$$

#### 4.1.3.2 Discrete-velocity Boltzmann equation

The Gauss-Hermite quadrature is used to numerically evaluate an integral in the following form

$$\int \omega(\mathbf{x})P(\mathbf{x})d\mathbf{x} = \sum_{i=0}^{q-1} w_i P(\mathbf{x}_i), \quad (4.19)$$

when it satisfies  $Q \leq 2M - 1$ , where  $Q$  is the order of the polynomial  $P(\mathbf{x})$ , and  $\mathbf{x}_i$  are known as the abscissae, essentially the roots of the Hermite polynomial  $H^{(M)}(x)$  of order  $M$ . The total number of abscissae is given as  $q = M^D$  with  $D$  the dimension of the vector  $\mathbf{x}$ .  $\omega(\mathbf{x})$  are the weight function of Hermite polynomials shown in Eq. 4.13.

To discretize the velocity space, the expansion coefficients (Eq. 4.17) are first rewritten in the form of Eq. 4.19,

$$\mathbf{a}^{(n)} = \int \omega(\boldsymbol{\xi}) \frac{f^N(\boldsymbol{\xi})}{\omega(\boldsymbol{\xi})} \mathbf{H}^{(n)}(\boldsymbol{\xi}) d\boldsymbol{\xi} = \sum_{i=0}^{q-1} \frac{w_i f^N(\boldsymbol{\xi}_i) \mathbf{H}^{(n)}(\boldsymbol{\xi}_i)}{\omega(\boldsymbol{\xi}_i)}, \quad (4.20a)$$

$$\mathbf{a}^{(n),eq} = \int \omega(\boldsymbol{\xi}) \frac{f^{eq,N}(\boldsymbol{\xi})}{\omega(\boldsymbol{\xi})} \mathbf{H}^{(n)}(\boldsymbol{\xi}) d\boldsymbol{\xi} = \sum_{i=0}^{q-1} \frac{w_i f^{eq,N}(\boldsymbol{\xi}_i) \mathbf{H}^{(n)}(\boldsymbol{\xi}_i)}{\omega(\boldsymbol{\xi}_i)}, \quad (4.20b)$$

and the Gauss-Hermite quadrature is applied to convert the continuous integral to discrete summation in the above equation by assuming  $f^N(\boldsymbol{\xi})\mathbf{H}^{(n)}(\boldsymbol{\xi})/\omega(\boldsymbol{\xi})$  a polynomial of order  $Q = N + n \leq 2N$  when  $n \leq N$ . The abscissae  $\boldsymbol{\xi}_i$  of the Gauss-Hermite quadrature of a degree  $\geq 2N$  are equivalently the roots of Hermite polynomial of order  $M > N$  (Shan et al., 2006). For example, it requires that  $M \geq 3$  for Hermite expansion up to order  $N = 2$  (e.g., (Qian et al., 1992)). When  $M = 3$ , there are  $q = 3^D$  abscissae, i.e., 9 and 27 discrete velocities in two- and three-dimensional physical space, which corresponds to the classical D2Q9 and D3Q27 schemes as will be discussed in a later section.

The *discrete-velocity distribution functions*, also known as *particle populations*, are defined

as

$$f_i = w_i f(\boldsymbol{\xi}_i) / \omega(\boldsymbol{\xi}_i), \quad (4.21a)$$

$$f_i^{eq} = w_i f^{eq}(\boldsymbol{\xi}_i) / \omega(\boldsymbol{\xi}_i), \quad (4.21b)$$

and the corresponding discrete-velocity equilibrium distribution can be obtained by plugging Eq. 4.18 into Eq. 4.21b,

$$f_i^{eq} = w_i \rho \left[ 1 + \boldsymbol{\xi}_i \cdot \mathbf{v} + \frac{1}{2} (\boldsymbol{\xi}_i \cdot \mathbf{v})^2 - |\mathbf{v}|^2 \right]. \quad (4.22)$$

The zeroth and first moments of the (equilibrium) distribution function are shown to be

$$\rho = \sum_{i=0}^{q-1} f_i = \sum_{i=0}^{q-1} f_i^{eq}, \quad (4.23a)$$

$$\rho \mathbf{v} = \sum_{i=0}^{q-1} f_i \boldsymbol{\xi}_i = \sum_{i=0}^{q-1} f_i^{eq} \boldsymbol{\xi}_i. \quad (4.23b)$$

Finally, the *discrete-velocity Boltzmann equation* (DVBE) is obtained by projecting the force-free Boltzmann equation (Eq. 4.2 without  $F_\beta$ ) into the space spanned by the three lowest order Hermite polynomials and expressing it in terms of the discrete-velocity distribution function  $f_i$  and equilibrium distribution  $f_i^{eq}$

$$\frac{\partial f_i}{\partial t} + \xi_{i\alpha} \frac{\partial f_i}{\partial x_\alpha} = \Omega(f_i). \quad (4.24)$$

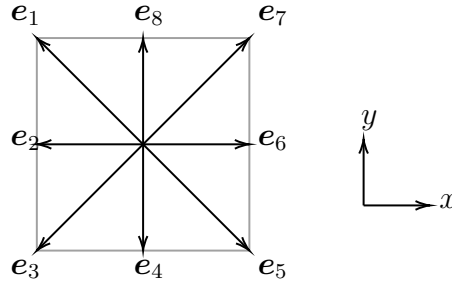
### 4.1.3.3 The velocity set

The discretization of particle velocity  $\boldsymbol{\xi}$  returns a discrete velocity set  $\{\boldsymbol{\xi}_i\}$  and the corresponding weights  $\{w_i\}$ . The size of the velocity set is determined by the dimension of the system as well as the Hermite polynomial truncation order<sup>5</sup>. Typically, the velocity set is denoted as  $DdQq$ , where  $d$  and  $q$  represent the system dimension and the number of discrete velocities, respectively. Taking  $D2Q9$  as an example, the velocity set is given in Table 4.1 and illustrated in Fig. 4.3.

<sup>5</sup>In-depth discussion can be found in the book (Krüger et al., 2017, A.4) or the paper by Shan et al. (2006)

**Table 4.1:** The D2Q9 velocity set.

<i>Position</i>	<i>i</i>	$\xi_i$	$e_i$	$w_i$
center	0	(0, 0)	(0, 0)	4/9
axial	1	$(-\sqrt{3}, \sqrt{3})$	(-1, 1)	1/36
	3	$(-\sqrt{3}, -\sqrt{3})$	(-1, -1)	1/36
	5	$(\sqrt{3}, -\sqrt{3})$	(1, -1)	1/36
	7	$(\sqrt{3}, \sqrt{3})$	(1, 1)	1/36
diagonal	2	$(-\sqrt{3}, 0)$	(-1, 0)	1/9
	4	$(0, -\sqrt{3})$	(0, -1)	1/9
	6	$(\sqrt{3}, 0)$	(1, 0)	1/9
	8	$(0, \sqrt{3})$	(0, 1)	1/9

**Fig. 4.3:** The D2Q9 velocity set.

It is worth noting that there is an additional column displaying the vector  $e_i$ , which is the “normalized” velocity  $e_i = \xi_i/\sqrt{3}$  obtained by extracting the common factor  $\sqrt{3}$  from the abscissae. Eqs. 4.22, 4.23, and 4.24 are reformulated in terms of  $e_i$

$$f_i^{eq} = w_i \rho \left( 1 + \frac{e_i \cdot \bar{v}}{c_s^2} + \frac{(e_i \cdot \bar{v})^2 - |\bar{v}|^2 \cdot c_s^2}{2c_s^4} \right), \quad (4.25)$$

$$\rho = \sum_{i=0}^{q-1} f_i = \sum_{i=0}^{q-1} f_i^{eq}, \quad (4.26a)$$

$$\rho \bar{v} = \sum_{i=0}^{q-1} f_i e_i = \sum_{i=0}^{q-1} f_i^{eq} e_i, \quad (4.26b)$$

$$\frac{\partial f_i}{\partial t} + e_{i\alpha} \frac{\partial f_i}{\partial x_\alpha} = \Omega(f_i), \quad (4.27)$$

where  $e_i = \xi_i c_s$  and  $\bar{v} = v c_s$  with  $c_s = 1/\sqrt{3}$  defined as the lattice sound speed. The

above equations in terms of “normalized velocities” are more commonly used in numerical applications of LBM, and the bar on top of the  $\bar{\mathbf{v}}$  is omitted hereafter for simplicity.

#### 4.1.4 Discretization in time and space

The *lattice Boltzmann equation* (LBE) is derived by further discretizing the discrete-velocity Boltzmann equation (DVBE) in time  $t$  and physical space  $\mathbf{x}$ . Considering DVBE (Eq. 4.27) as an inhomogeneous advection equation with characteristic equations expressed as

$$\frac{d\mathbf{x}}{dt} = \mathbf{e}_i, \quad (4.28a)$$

$$\frac{df_i}{dt} = \Omega(f_i), \quad (4.28b)$$

it can be solved using the method of characteristics, where particle populations  $f_i$  are considered to travel along the characteristic curves  $\mathbf{x} - \mathbf{e}_i t = \text{const.}$ , which are straight lines with the slope  $d\mathbf{x}/dt = \mathbf{e}_i$ . The solution is thus obtained by integrating the above equation over the time  $[t, t + \Delta t]$ ,

$$f_i(\mathbf{x} + \mathbf{e}_i \Delta t, t + \Delta t) - f_i(\mathbf{x}, t) = \int_t^{t+\Delta t} \Omega_i(\mathbf{x} + \mathbf{e}_i \Delta t, t + \Delta t) dt. \quad (4.29)$$

The approximation of the RHS by the trapezoidal rule gives

$$f_i(\mathbf{x} + \mathbf{e}_i \Delta t, t + \Delta t) - f_i(\mathbf{x}, t) = \Delta t \frac{\Omega_i(\mathbf{x}, t) + \Omega_i(\mathbf{x} + \mathbf{e}_i \Delta t, t + \Delta t)}{2}, \quad (4.30)$$

which is second-order accurate in space and time.

The above equation is transformed from the implicit form to an explicit form through a change of variable  $f_i \rightarrow \bar{f}_i$ , which gives the *lattice Boltzmann equation*

$$\bar{f}_i(\mathbf{x} + \mathbf{e}_i \Delta t, t + \Delta t) = \bar{f}_i(\mathbf{x}, t) + \Delta t \bar{\Omega}_i(\mathbf{x}, t), \quad (4.31)$$

where  $\bar{f}_i = f_i - \Omega_i \Delta t / 2$ . The new variables still satisfy the mass and momentum conservation, so that  $\sum_i \bar{f}_i = \rho$  and  $\sum_i \bar{f}_i \mathbf{e}_i = \rho \mathbf{v}$ .

For the BGK model, the lattice BGK equation is written as

$$\bar{f}_i(\mathbf{x} + \mathbf{e}_i \Delta t, t + \Delta t) = \bar{f}_i(\mathbf{x}, t) - \frac{\Delta t}{\bar{\tau}} [\bar{f}_i(\mathbf{x}, t) - f_i^{eq}(\mathbf{x}, t)], \quad (4.32)$$

where  $\bar{\tau} = \tau + \Delta t/2$  and is related to the lattice kinematic viscosity

$$\nu = c_s^2 \left( \bar{\tau} - \frac{\Delta t}{2} \right). \quad (4.33)$$

For the sake of clarity, the overlines will be omitted in the subsequent sections.

#### 4.1.5 Lattice Boltzmann method

The *lattice Boltzmann method* is essentially a numerical method for solving LBE, which is decomposed in two equations that correspond to the two steps:

1. collision

$$\begin{aligned} f_i^*(\mathbf{x}, t) &= f_i(\mathbf{x}, t) - \frac{\Delta t}{\tau} [f_i(\mathbf{x}, t) - f_i^{eq}(\mathbf{x}, t)] \\ &= \left( 1 - \frac{\Delta t}{\tau} \right) f_i(\mathbf{x}, t) + \frac{\Delta t}{\tau} f_i^{eq}(\mathbf{x}, t), \end{aligned} \quad (4.34)$$

2. streaming

$$f_i(\mathbf{x} + \mathbf{e}_i \Delta t, t + \Delta t) = f_i^*(\mathbf{x}, t), \quad (4.35)$$

where  $f_i^*(\mathbf{x}, t)$  is known as the post-collision distribution function.

The collision step will redistribute the populations that go along different directions, and the streaming process propagates post-collision populations to their neighbors as illustrated in Fig. 4.4.

#### 4.1.6 Unit Conversion

All the macroscopic variables in LBM simulation are presented in the “lattice unit”, such as density and momentum calculated using Eq. 4.26 or lattice sound speed defined as  $c_s = \sqrt{1/3} \approx 0.577$ . The simulation sometimes requires to convert the lattice unit back to physical unit or the other way round, for example, when dealing with the airflow-reed interaction in the mouthpiece modeling. A conversion factor  $C_{\text{var}} = \text{Var}_{\text{ph}}/\text{Var}_{\text{la}}$  is required for each macroscopic variable  $\text{Var}$ , where the subscripts *ph* and *la* indicate variables in physical and lattice units, respectively. This section defines a specific way of lattice-to-physical unit conversion that is later employed in the saxophone mouthpiece simulation. More general discussions on this topic can be found in the book by Krüger et al. (2017).

Primary conversion factors  $C_l$ ,  $C_t$  and  $C_\rho$  should be first determined using the following

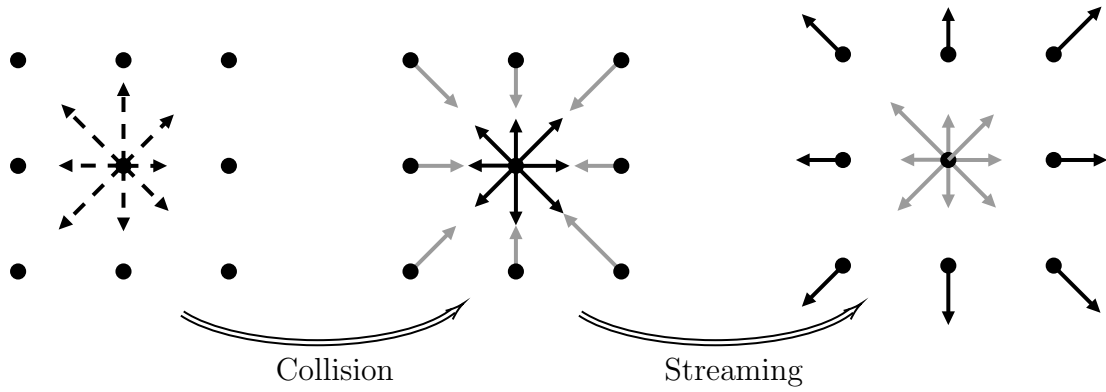


**Fig. 4.4:** The illustration of the collision and streaming processes of the center node. The solid and dashed arrows represent pre- and post-collision populations, respectively, and the arrow length indicates the population strength. During the streaming process, the black arrows represent the outgoing populations from the center node, while the gray arrows represent incoming populations from adjacent nodes. For clarity, the pre-collision populations of neighboring nodes are not displayed in the leftmost figure.

steps, and all the other conversion factors can be derived from primary conversion factors using the expressions shown in Table 4.2.

1. set the physical sound speed  $c_{s,\text{ph}}$ , density  $\rho_{\text{ph}}$  and kinematic viscosity  $\nu_{\text{ph}}$ ,
2. assume the lattice grid length and time step to be unity  $\Delta x_{\text{la}} = \Delta t_{\text{la}} = 1$ ,
3. determine  $C_l = \Delta x_{\text{ph}} = c_{s,\text{ph}} / (f_{\text{ppw}} N_{\text{ppw}})$  by setting point-per-wavelength  $N_{\text{ppw}}$  at a specific frequency  $f_{\text{ppw}}$ ,
4. determine  $C_v = \frac{c_{s,\text{ph}}}{c_{s,\text{la}}}$ , where  $c_{s,\text{la}} = \sqrt{1/3}$ ,
5. determine  $C_t = \Delta t_{\text{ph}} = \Delta x_{\text{ph}} / C_v$ ,
6. determine  $C_\rho = \rho_{\text{ph}} / \rho_{\text{la}}$ , where it normally assumes  $\rho_{\text{la}} = 1.0$ ,
7. determine  $\tau = \nu_{\text{la}} / c_{s,\text{la}}^2 + 1/2$  from Eq. 4.33, where  $\nu_{\text{la}} = \nu_{\text{ph}} / C_v$  is the lattice kinematic viscosity, and  $C_\nu = \Delta x^2 / \Delta t$  is the kinematic viscosity conversion factor,

<sup>6</sup>This chapter discusses the isothermal LBM, which is based on the isothermal equation of state (derived from the pressure-density relation in Eq. 3.18 by setting the isothermal condition  $\gamma = 1$ )

$$p = \rho c_s^2. \quad (4.36)$$

However, the pressure unit conversion only works for the pressure fluctuations  $p'$  but not necessarily for the ambient pressure  $p_0$  (Krüger et al., 2017, Ch. 7.2.1.2).

**Table 4.2:** List of conversion factors.

Variables	Conversion factor $C_{\text{Var}} = \text{Var}_{\text{ph}}/\text{Var}_{\text{la}}$
length	$C_l = C_t C_v = \Delta x_{\text{ph}}$
time	$C_t = C_l/C_v = \Delta t_{\text{ph}}$
velocity	$C_v = C_l/C_t = c_{s,\text{ph}}/c_{s,\text{la}}$
viscosity	$C_\nu = C_l^2/C_t$
density	$C_\rho = \rho_{\text{ph}}/\rho_{\text{la}}$
pressure <sup>6</sup>	$C_p = C_\rho C_v^2 = C_\rho (C_l/C_t)^2$

## 4.2 Recursive regularized lattice Boltzmann method

The BGK scheme is known to be unstable for high Reynolds number flow when  $\nu \rightarrow 0$  (or equivalently when  $\tau \rightarrow 1/2$ ). It is also known to suffer numerical noise that disturbs the simulated acoustic signals (Xu and Sagaut, 2011). To improve the stability of LBM, many advanced collision operators have been proposed, including the multirelaxation time (MRT) LBM (d’Humières, 2002), two-relaxation-times (TRT) LBM (Ginzburg et al., 2008a,b), cumulant LBM (Geier et al., 2015), regularized BGK (rBGK) (Latt and Chopard, 2005, 2006), and recursive regularized BGK (rrBGK) (Coreixas et al., 2017, Malaspinas, 2015). The recursive regularized BGK has been demonstrated to be effective and accurate in aeroacoustics applications (Brogi et al., 2017), so that it is applied in this research for aeroacoustic modeling of the mouthpiece.

The recursive regularized BGK was originally developed by Malaspinas (2015) to improve the stability and accuracy of BGK for isothermal and weakly compressible flow, and Coreixas et al. (2017) generalized it for thermal and fully compressible flow. The regularized BGK that forms the foundation of rrBGK is introduced in Sec. 4.2.1, following which the original rrBGK scheme proposed by Malaspinas (2015) is discussed in Sec. 4.2.2.

### 4.2.1 Regularized BGK

The regularized BGK (RBGK) was proposed by Latt and Chopard (2005, 2006), where the pre-collision population  $f_i$  is regularized as

$$f_i = f_i^{(0)} + f_i^{(1)}, \quad (4.37)$$

so that all the higher order terms ( $\mathcal{O}(\text{Kn}^k)$  when  $k \geq 2$ ) in the Chapman-Enskog expansion and their non-hydrodynamic contributions are filtered out<sup>7</sup>.

The collision equation Eq. 4.34 is modified correspondingly as

$$f_i^*(\mathbf{x}, t) = \left(1 - \frac{\Delta t}{\tau}\right) f_i^{(1)}(\mathbf{x}, t) + f_i^{eq}(\mathbf{x}, t). \quad (4.38)$$

While the equilibrium population is still calculated using Eq. 4.25,  $f_i^{(1)}$  needs to be approximated using the truncated Hermite expansion

$$f_i^{(1)} = w_i \sum_{n=0}^2 \frac{1}{c_s^{2n} n!} \mathbf{a}_1^{(n)} : \mathbf{H}_i^{(n)},$$

where  $\mathbf{H}_i^{(n)}$  is the discrete Hermite polynomials and the subscript of  $\mathbf{a}$  corresponds to the Chapman-Enskog expansion order  $k$  (Malaspinas, 2009, Appendix A).

The first three expansion coefficients are required to recover  $f_i^{(1)}$ . While the first two coefficients are trivial from Eq. 4.15  $\mathbf{a}_1^{(0)} = \mathbf{a}_1^{(1)} = 0$ ,  $\mathbf{a}_1^{(2)}$  is calculated as follows:

$$\mathbf{a}_1^{(2)} = \mathbf{\Pi}^{(1)} = -2\tau\rho\epsilon = \sum_{i=0}^{q-1} f_i^{(1)} \mathbf{e}_i^2, \quad (4.39)$$

where  $\epsilon = \frac{1}{2} (\nabla \mathbf{u} + \nabla \mathbf{u}^T)$ .

The regularized BGK assumes that  $f_i^{neq} \approx f_i^{(1)}$ , so that  $\mathbf{a}_1^{(2)}$  is approximated as

$$\mathbf{a}_1^{(2)} \approx \sum_{i=0}^{q-1} f_i^{neq} \mathbf{e}_i^2 = \sum_{i=0}^{q-1} (f_i - f_i^{eq}) \mathbf{e}_i^2 = \mathbf{\Pi}^{neq}, \quad (4.40)$$

which finally gives that

$$f_i^{(1)} = \frac{w_i}{2c_s^4} \mathbf{\Pi}^{neq} : \mathbf{H}_i^{(2)}, \quad (4.41)$$

where  $\mathbf{H}_i^{(2)} = \mathbf{e}_i^2 - c_s^2 \delta$ .

---

<sup>7</sup>The population is expanded as  $f_i = f_i^{(0)} + f_i^{(1)} + f_i^{(2)} + \dots$  before the regularization.

### 4.2.2 Recursive regularized BGK

While the same regularization scheme as in Eq. 4.37 was applied in rrBGK, the equilibrium and non-equilibrium distribution functions are calculated differently by reserving some higher order terms. For the D2Q9 scheme as an example, the Hermite polynomials up to the second order provide only six bases for the nine-dimensional velocity field. Three extra higher-order Hermite polynomials are introduced to complete the set of bases, and the particle population is written as

$$f_i = w_i \left[ \rho + \frac{\mathbf{e}_i \cdot \rho \mathbf{v}}{c_s^2} + \frac{1}{2c_s^4} \mathbf{a}^{(2)} : \mathbf{H}_i^{(2)} + \frac{1}{2c_s^6} \left( H_{ixxy}^{(3)} a_{ixxy}^{(3)} + H_{ixyy}^{(3)} a_{ixyy}^{(3)} \right) + \frac{1}{4c_s^8} H_{ixxyy}^{(4)} a_{ixxyy}^{(4)} \right], \quad (4.42)$$

and the corresponding equilibrium and non-equilibrium populations are given as

$$f_i^{(0)} = w_i \rho \left[ 1 + \frac{\mathbf{e}_i \cdot \mathbf{v}}{c_s^2} + \frac{1}{2c_s^4} \mathbf{a}_0^{(2)} : \mathbf{H}_i^{(2)} + \frac{1}{2c_s^6} \left( H_{ixxy}^{(3)} a_{0,ixxy}^{(3)} + H_{ixyy}^{(3)} a_{0,ixyy}^{(3)} \right) + \frac{1}{4c_s^8} H_{ixxyy}^{(4)} a_{0,ixxyy}^{(4)} \right], \quad (4.43)$$

$$f_i^{(1)} = w_i \left[ \frac{1}{2c_s^4} \mathbf{a}_1^{(2)} : \mathbf{H}_i^{(2)} + \frac{1}{2c_s^6} \left( H_{ixxy}^{(3)} a_{1,ixxy}^{(3)} + H_{ixyy}^{(3)} a_{1,ixyy}^{(3)} \right) + \frac{1}{4c_s^8} H_{ixxyy}^{(4)} a_{1,ixxyy}^{(4)} \right], \quad (4.44)$$

The zeroth and first order Hermite coefficients can be recursively determined using the following expressions

$$\mathbf{a}_0^{(n)} = \mathbf{a}_0^{(n-1)} \mathbf{v}, \text{ and } a_0^{(0)} = \rho \quad (4.45)$$

$$a_{1,\alpha_1 \dots \alpha_n}^{(n)} = a_{1,\alpha_1 \dots \alpha_n}^{(n-1)} u_{\alpha_n} + \frac{1}{\rho} \sum_{l=1}^{n-1} a_{0,\beta_l}^{(n-2)} a_{1,\alpha_l \alpha_n}^{(2)}, \quad \text{for } n \geq 3, \quad (4.46)$$

where  $\beta_l = \alpha_1 \dots \alpha_{l-1} \alpha_{l+1} \alpha_n$  denotes the omission of the index  $\alpha_l$ .

## 4.3 Boundary Conditions

Boundary conditions are employed differently in LBM than in Navier-Stokes solvers because LBM requires to define the particle populations, rather than macroscopic variable, at the

boundary. This section starts with general techniques applied in Dirichlet boundary conditions and then discusses the non-reflecting boundary condition for acoustic problems and the immersed boundary condition for fluid-structure interaction problems.

### 4.3.1 Dirichlet boundary condition

A Dirichlet boundary condition directly defines the macroscopic value at boundaries, giving

$$\mathbf{v}(\mathbf{x}_B, t) = \mathbf{V}_B(\mathbf{x}_B, t), \quad (4.47)$$

where  $\mathbf{V}_B$  represent the imposed boundary velocity along the boundaries defined at  $\mathbf{x}_B$ . It is called the non-slip boundary condition when  $\mathbf{V}_B = 0$ .

However, the macroscopic value might be insufficient for LBM boundaries because the populations  $f_i$  defined at the mesoscopic level need to be determined. The general problem of an LBM Dirichlet boundary condition is illustrated in Fig. 4.5. During the streaming process, the populations  $f_{2-6}$  of the boundary node at the center can be updated from its neighboring nodes. However, because there are no neighboring nodes in the corresponding directions, the populations  $f_{1,7,8}$  are left unknown after the streaming, and resolving these unknown populations to satisfy the macroscopic boundary condition is the kernel task of an LBM boundary condition.

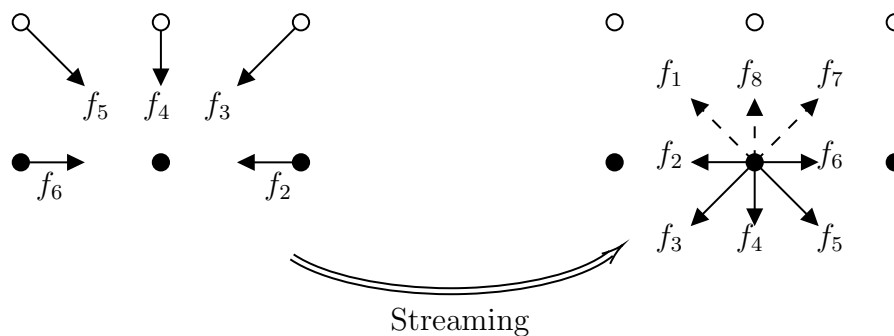


**Fig. 4.5:** The illustration of the general boundary problem. The empty and solid circles represent fluid and boundary nodes, respectively. The arrows represent the populations traveling at different directions, with the dashed ones indicating unknown populations after the streaming process.

The boundary nodes shown in Fig. 4.5 do not necessarily correspond to the actual location of the physical boundary wall, and the alignment of the boundary nodes and the boundary

wall depends on the type of the LBM boundary condition. In general, there are two types of boundaries conditions for straight boundaries as shown in Fig. 4.6, known as

- the *link-wise* boundary where the boundary wall lies on the link between solid and fluid nodes, and
- the *wet-node* boundary where the boundary nodes are considered to locate infinitely close to the boundary wall yet remain in the fluid as “wet-nodes”.

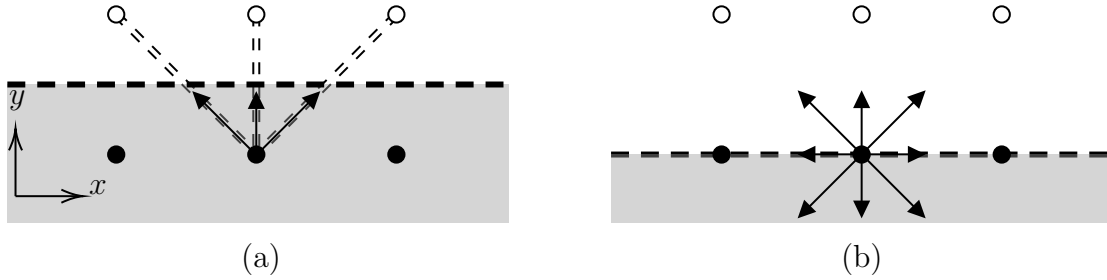


**Fig. 4.6:** The illustration of the (a) *link-wise* and (b) *wet-node* boundaries aligned with the  $x$ -axis. The gray and white area represent the solid and fluid regions, respectively, while the empty and solid nodes represent the fluid and boundary nodes, correspondingly. The thick dashed lines represent the wall, which locates across the lattice links (dashed double lines) or aligns with the boundary nodes for the *link-wise* and *wet-node* boundaries, correspondingly.

#### 4.3.1.1 Bounce-back boundary condition

The bounce-back boundary condition is a typical *link-wise* boundary, which is also the simplest method to implement a non-slip boundary condition. For a boundary node shown in Fig. 4.5, the unknown populations  $f_{1,7,8}$  are given

$$f_1 = f_5, \quad f_7 = f_3, \quad f_8 = f_4, \quad (4.48)$$

In general, it means that the incoming populations of the boundary nodes are bounced back in the opposite direction, resulting in

$$f_{\bar{i}} = f_i, \quad (4.49)$$

where index  $i$  and  $\bar{i}$  denote the incoming and bounced-back direction  $\mathbf{e}_i$  and  $\mathbf{e}_{\bar{i}}$ , respectively, and  $\mathbf{e}_{\bar{i}} = -\mathbf{e}_i$ . The rest of the populations on the boundary nodes are often left undefined, as is the macroscopic density as well.

### 4.3.1.2 Zou-He boundary condition

The Zou-He boundary condition, also known as the non-equilibrium bounce-back boundary condition, is a wet-node boundary condition proposed by Zou and He (1997). It first calculates the density for the Dirichlet velocity boundary with known populations. For the boundary node illustrated in Fig. 4.5, the density and the  $y$ -direction momentum are given as

$$\begin{aligned}\rho_B &= \sum_i^{q-1} f_i = f_{\text{unknown}} + f_0 + f_2 + f_3 + f_4 + f_5 + f_6, \\ \rho_B V_{B,y} &= \sum_i^{q-1} e_{iy} f_i = f_{\text{unknown}} - (f_3 + f_4 + f_5),\end{aligned}\tag{4.50}$$

where  $f_{\text{unknown}} = f_1 + f_7 + f_8$  is the sum of unknown populations, and the values of  $e_{iy}$  are given in Table 4.1. The two equations above are combined to derive a formula of  $\rho_B$ , which is expressed solely in terms of known populations

$$\rho_B = \frac{1}{1 - V_{B,y}} [f_0 + f_2 + f_6 + 2(f_3 + f_4 + f_5)].\tag{4.51}$$

To obtain the unknown populations, the equilibrium population is computed with the imposed velocity  $\mathbf{V}_B$  and the density  $\rho_B$  calculated using Eq. 4.51. The non-equilibrium part of the populations are updated using the bounce-back method, which, taking a resting wall ( $\mathbf{V}_B = 0$ ) as an example, is given as:

$$f_i^{neq} = f_i^{neq} = f_i - f_i^{eq}.\tag{4.52}$$

### 4.3.2 Non-reflecting boundary conditions

Modeling an unbounded physical domain in a finite computational domain is a common numerical challenge, and the non-reflecting boundary condition (NRBC) is a widely used technique to address such an issue in solving wave problems. NRBC is typically formulated on the Navier-Stokes level by defining macroscopic variables, and there have been multiple NRBCs that have been adapted to LBM by deriving a proper mesoscopic formulation, such as the characteristic boundary condition (CBC) (Izquierdo and Fuego, 2008), perfectly matching layers (Najafi-Yazdi and Mongeau, 2012, Tekitek et al., 2009), and absorbing boundary condition (ABC), also known as absorbing layers (Kam et al., 2006, Xu and Sagaut, 2013).

The ABC proposed by (Kam et al., 2006, 2007) will be introduced in this section, while CBC will be described in Ch. 5.

ABC introduces a buffer zone near the boundaries, inside which the collision process in Eq. 4.34 is modified as follows:

$$f_i^*(\mathbf{x}, t) = f_i(\mathbf{x}, t) - \frac{\Delta t}{\tau} [f_i(\mathbf{x}, t) - f_i^{eq}(\mathbf{x}, t)] - \sigma (f_i^{eq}(\mathbf{x}, t) - f_i^{eq,t}(\mathbf{x}, t)), \quad (4.53)$$

where  $f_i^{eq,t}(\mathbf{x}, t)$  is the target particle population that is calculated using Eq. 4.25 with a target density  $\rho^t$  and target velocity  $\mathbf{v}^t$ .  $\sigma = \sigma_m \delta_m^2$  is the absorbing coefficient, where  $\sigma_m$  is a constant that is typically set to 0.3, and  $\delta_m \in [0, 1]$  is a normalized distance that increases from 0 to 1, from the start to the end of the buffer zone. ABC provides a simple and efficient way of absorbing the outgoing waves as a NRBC. In addition, ABC can be used as sound sources by properly setting  $\rho^t$  and  $\mathbf{v}^t$  (da Silva et al., 2007), and this approach will be applied in Chs. 5 and 7 to define the inlet of the fluid domain.

### 4.3.3 Immersed boundary method

The immersed boundary method (IBM) was originally proposed by Peskin (1972) in the context of Navier-Stokes solvers. Since then, many IBM variations have been developed (Kim and Choi, 2019, Mittal and Iaccarino, 2005, Peskin, 2002). In LBM, IBM was first introduced by Feng and Michaelides (2004), which is known as the immersed-boundary lattice Boltzmann method (IB-LBM). This section will focus on the multi-direct-forcing IB-LBM, which is going to be employed in computational aeroacoustic modeling of the saxophone mouthpiece.

The multi-direct-forcing IBM was initially proposed by Wang et al. (2008), which was later combined with LBM by Inamuro (2012). The kernel concept of IBM is to represent solid walls as a series of Lagrangian markers  $\mathbf{x}_k(t)$  (also known as immersed boundary (IB) nodes), which are positioned among the Eulerian fluid grids. The motion and interaction of IB nodes with fluid grids are linked through *velocity interpolation* and *force spreading*, which are illustrated in Fig. 4.7.

The *velocity interpolation* process interpolates the velocity at the position of IB nodes

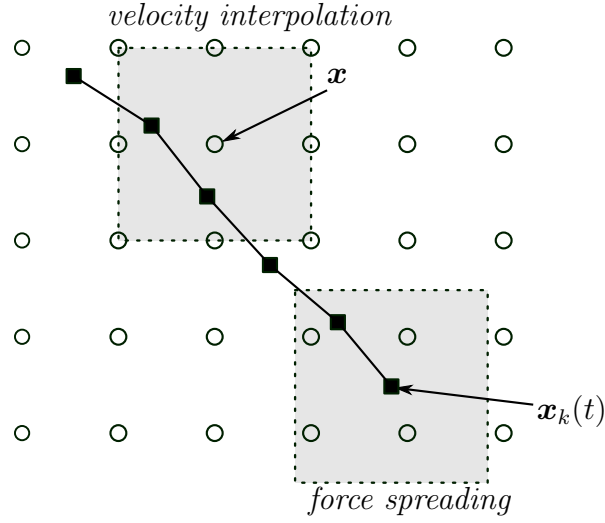


**Fig. 4.7:** Illustration of the *force spreading* and *velocity interpolation*. The open circles and filled squares represent the Eulerian fluid nodes and Lagrangian solid nodes, respectively. The gray squares represent the area covered by a kernel function.

$\mathbf{x}_k$  using velocities of neighboring Eulerian grids. This calculation is expressed as

$$\mathbf{v}(\mathbf{x}_k, t) = \sum_{\mathbf{x}} \mathbf{v}(\mathbf{x}, t) W(\mathbf{x}_k(t), \mathbf{x}) \Delta x^D, \quad (4.54)$$

where  $\mathbf{v}(\mathbf{x}_k, t)$  represents the interpolated velocity at the location of an IB node  $k$ . The interpolated velocity is expected to be equal to a known velocity of the IB node  $\mathbf{v}_k^b$  to enforce a non-slip boundary condition on the solid wall.

$W(\mathbf{x}_k(t), \mathbf{x}) = W(\mathbf{x}_k - \mathbf{x})$  is a kernel function proposed by Peskin (2002):

$$W(\mathbf{r}) = \frac{1}{\Delta x^D} \prod_{i=1}^D \phi(r_i/\Delta x), \quad (4.55)$$

with  $D$  representing the dimensionality, and the 1D kernel function defined as

$$\phi(r) = \begin{cases} \frac{1}{8} \left( 3 - 2|r| + \sqrt{1 + 4|r| - 4r^2} \right), & |r| \leq 1, \\ \frac{1}{8} \left( 5 - 2|r| + \sqrt{-7 + 12|r| - 4r^2} \right), & 1 \leq |r| \leq 2, \\ 0, & \text{otherwise.} \end{cases} \quad (4.56)$$

The *force spreading* process is governed by

$$\mathbf{F}(\mathbf{x}, t)\Delta x^D = \sum_k \mathbf{F}_k(t)W(\mathbf{x}_k(t), \mathbf{x})\Delta V_k, \quad (4.57)$$

where the force exerted on an Eulerian fluid node is obtained by spreading force from neighboring Lagrangian IB nodes. Here,  $\mathbf{F}(\mathbf{x}, t)$  and  $\mathbf{F}_k(t)$  represent the force densities of the LB grids and IB nodes, respectively. The term  $\Delta x^D$  on the left-hand side represents the volume of an LB grid, while  $\Delta V_k$  on the right-hand side is the volume on which the IB force is exerted. For evenly distributed IB nodes, this volume is given as  $\Delta V_k = S/N\Delta x$ , where  $S$  is the solid surface area, and  $N$  denotes the total number of IB nodes. For a two-dimensional problem, it is typically recommended to maintain a distance between IB nodes  $S/N$  within the range of  $(0.5\Delta x, \Delta x)$  (Krüger et al., 2017, 11.4.2.7).

Applying a direct-forcing IBM to LBM requires an LBM with a forcing scheme. The Shan-Chen forcing scheme (Shan and Chen, 1993) is utilized in the present study, which modifies the velocity calculation to incorporate the effect of external forces. Instead of being calculated with Eq. 4.26 in a force-free LBM, the LB velocity is updated with:

$$\mathbf{v}(\mathbf{x}) = \frac{1}{\rho} \sum_{i=0}^{q-1} f_i \mathbf{e}_i + \frac{\tau \mathbf{F}(\mathbf{x})}{\rho}. \quad (4.58)$$

This equation can be considered as a velocity correction procedure when an external force is present.

In an IB-LBM, after the collision and streaming at each time step (process as if there is no wall in the fluid field), LB velocities need to be corrected upon the presence of the solid nodes using Eq. 4.58. It requires force densities  $\mathbf{F}(\mathbf{x})$  on the fluid grids in the vicinity of IB nodes, which are obtained through the force spreading (Eq. 4.57) procedure, and this further relies on the known IB forces  $\mathbf{F}_k$  exerted on the solid nodes. The different ways of determining these IB forces distinguish various IB-LBMs from each other. The direct-forcing IB-LBM computes IB force directly from the flow field using a similar formula as Eq. 4.58:

$$\mathbf{F}_k = \rho \frac{\mathbf{v}_k^b - \mathbf{v}(\mathbf{x}_k)}{\tau}, \quad (4.59)$$

where the IB force corrects the interpolated velocity  $\mathbf{v}(\mathbf{x}_k)$  calculated using Eq. 4.54 to the

imposed wall velocity  $\mathbf{v}_k^b$ . It forms an implicit system in conjunction with Eqs. 4.54, 4.57 and 4.58, and the various methods to solve this implicit system result in further IB-LBM variations. The multi-direct-forcing IB-LBM solves this system iteratively, and the algorithm is shown as follows:

1. Compute  $\rho$  and  $\mathbf{v}^{(0)} = \frac{1}{\rho} \sum_i f_i \mathbf{e}_i$ , where a superscript in parentheses represents an iteration number.
2. Perform the velocity interpolation

$$\mathbf{v}^{(m)}(\mathbf{x}_k) = \sum_{\mathbf{x}} \mathbf{v}^{(m)}(\mathbf{x}) W(\mathbf{x}_k, \mathbf{x}) \Delta x^D,$$

and advance the iteration number  $m$  ( $m = m + 1$ )

3. Compute the IB force density using Eq. 4.59

$$\mathbf{F}_k^{(m)} = \rho \frac{\mathbf{v}_k^b - \mathbf{v}^{(m-1)}(\mathbf{x}_k)}{\tau}.$$

4. Perform the force spreading to obtain the force on LB grids

$$\mathbf{F}^{(m)}(\mathbf{x}, t) \Delta x^D = \sum_k \mathbf{F}_k^{(m)}(t) W(\mathbf{x}_k(t), \mathbf{x}) \Delta V_k.$$

5. Apply the force to correct the velocity

$$\mathbf{v}^{(m)}(\mathbf{x}) = \mathbf{v}^{(m-1)}(\mathbf{x}) + \frac{\tau \mathbf{F}^{(m)}(\mathbf{x})}{\rho}.$$

6. Go back to Step. 2 if  $m < m_{\max}$ .
7. Compute total correction force density

$$\mathbf{F}(\mathbf{x}) = \sum_{m=1}^{m_{\max}} \mathbf{F}^{(m)}(\mathbf{x}).$$

8. Perform the LB collision using  $\mathbf{F}(\mathbf{x})$  and then the streaming process.
9. Calculate  $\mathbf{F}_k$  and use it to update  $\mathbf{v}_k^b$  from the solid model.
10. Advect the Lagrangian nodes  $\mathbf{x}_k(t + \Delta t) = \mathbf{x}_k(t) + \mathbf{v}_k^b \Delta t$ .
11. Advance the time step and go back to Step. 1.

An essential step of coupling the solid model and the LB simulation is calculating of  $\mathbf{F}_k$ . In the present research, the IB force density is updated with a similar process as the *velocity interpolation* shown in Eq. 4.54, but only with LB nodes in the fluid volume (demonstrated in Fig. 4.8). Thus, the formula is expressed as follows:

$$\mathbf{F}_k(t) = \sum_{\mathbf{x} \in V} \mathbf{F}(\mathbf{x}, t) W(\mathbf{x}_k(t), \mathbf{x}) \Delta x^D, \quad (4.60)$$

where  $V$  represent the fluid volume.

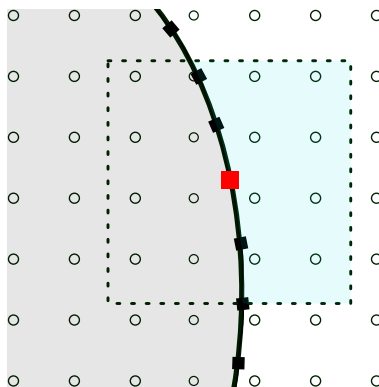


**Fig. 4.8:** Illustration of the IB force calculation. The open circles represent the fluid grids, whereas the filled squares represent the IB nodes. The gray and white regions represent the solid and fluid volumes, respectively. The dotted square denotes the kernel function range for a specific IB node (marked as the red square), and the light blue area encompasses the LB grids used to interpolate the IB force  $\mathbf{F}_k$ .

#### 4.4 Why LBM?

LBM and Navier-Stokes (NS) solvers are the two main options for computational aeroacoustic (CAA) modeling. Previous research by Marié et al. (2009) found that LBM-BGK is less dissipative than high-order finite difference schemes and less dispersive than a second-order scheme in space with a 3-step Runge-Kutta scheme in time. More recent studies by Suss et al. (2023) showed that rrBGK, the advanced collision model used in the present study, exhibits a higher numerical dissipation on shear modes than NS solvers (finite volume schemes), but much lower dissipation on the acoustic modes. The numerical efficiency of different models, when run with the same level of errors, also demonstrated that rrBGK is a better candidate

than finite volume schemes for acoustic problems. All these studies seemingly qualify the choice of LBM with rrBGK used in CAA modeling of the saxophone mouthpiece. However, it is important to note that these comparisons primarily focused on the bulk flow field. They did not consider the influence of boundary conditions, which is important in determining the numerical accuracy and efficiency of a CAA model. In addition, the accuracy of the NS solvers used in the above comparisons is between second- and third-orders, whereas higher-order NS solvers with lower numerical dispersion and dissipation can be employed in CAA models, such as the sixth-order accurate finite-difference applied in single-reed instrument modeling (Yokoyama et al., 2020, Yoshinaga et al., 2021). With that said, LBM was chosen in the present study not because it is a “more accurate” numerical method, but for a more practical reason, as discussed below.

There are three main options to develop a CAA model for a saxophone: developing an in-house numerical solver, using commercial software, or developing based on an open-source computational fluid dynamic (CFD) framework. An open-source framework was chosen as a compromise between the other two options. On one hand, it saves time from developing everything from scratch, allowing the focus to be on the research problem. On the other hand, open-source software is more extensible compared to commercial software, which allows users to implement and integrate their algorithms and models.

The available options are further narrowed down to the finite volume method (FVM)-based software OpenFOAM (Jasak, 2009), and the LBM-based software Palabos (Latt et al., 2021), and OpenLB (Krause et al., 2020). The choice of LBM over FVM is based on the analytical comparison by Marié et al. (2009), as discussed earlier, and numerical tests by Kühnelt (2016), who demonstrated the higher efficiency of LBM compared to a detached eddy simulation implemented in Ansys Fluent for a CAA model of a recorder. Palabos is chosen over OpenLB, mainly because it has implemented the rrBGK that I decided to use, which has been verified in CAA applications (Brogi et al., 2017).

Palabos (**Parallel Lattice Boltzmann Solver**) is an open-source LBM-based computational fluid dynamic framework. It is based on the multi-block concept and the message passing interface (MPI) for parallel computing, which supports both shared or distributed-memory architectures. Palabos provides a majority of algorithms used in this thesis such as rrBGK, Zou-He boundary condition and IBM, and also offers convenient interfaces for users to implement their own algorithms. Palabos is used for the LB simulation in Chs 5 and 7 and 8.

## Chapter 5

# Characteristic-based time-domain impedance boundary condition

In this chapter, the characteristic-based time-domain impedance boundary condition (C-TDIBC) is for the first time applied in lattice Boltzmann (LB) simulations. It is proposed for a later application in the aeroacoustic modeling of a saxophone mouthpiece to increase simulation efficiency and reduce computational cost by replacing the distributed LB modeling of the resonator with a local representation of the resonator as a boundary condition. In general, it is a combination of several existing techniques, including

- the characteristic boundary condition (CBC), or specifically, the local one-dimensional inviscid (LODI) model with transverse terms and transverse relaxation, which is referred to as LODI-T in this section (Wissocq et al., 2017, Yoo et al., 2005),
- the plane wave masking (PWM) technique, which is incorporated with CBC and external excitations to form the characteristic-based reflecting boundary condition (C-RBC) (Jaensch et al., 2016, Kaess et al., 2008, Polifke et al., 2006), and
- a time-domain representation of input impedance as a recursive parallel filter structure (Maestre et al., 2016, 2018), which can be considered as a variant of the time-domain impedance boundary condition (TDIBC).

This chapter starts with the general overview of CBC in Sec. 5.1, followed by a description of the PWM technique and the formulation of C-RBC in Sec. 5.2. TDIBC is addressed in Sec. 5.3. Finally, C-TDIBC implementation in an LB simulation is presented in Sec. 5.4 with various numerical validations in Sec. 5.5.

## 5.1 Characteristic boundary condition

The characteristic boundary condition (CBC) was first developed by (Thompson, 1987, 1990), which served as a non-reflecting boundary condition (NRBC) for the Euler equation system. Poinsot and Lele (1992) later generalized it for Navier-Stokes equations, resulting in the Navier-Stokes characteristic boundary conditions (NSCBC). They proposed the so-called local one-dimensional inviscid (LODI) model, which assumes an inviscid and one-dimension flow at the boundary and discards viscous and transverse terms in the Navier-Stokes equation. However, Yoo et al. (2005) and Yoo and Im (2007) discovered that incorporating the transverse and viscous terms in the boundary condition can help reduce the spurious reflection at the boundary, which results in a better performance of NRBC. Furthermore, Polifke et al. (2006) performed an analytical analysis of LODI and discovered that LODI is partially reflective instead of fully non-reflective. This is attributed to the linear relaxation term introduced in CBC to suppress the mean flow drift, and such a problem can be mitigated using the plane wave masking (PWM) technique proposed by Polifke et al. (2006) in the context of plane acoustic wave propagation with normal incidence to the boundary. PWM also allows the incorporation of external acoustic excitation by defining incoming acoustic sources at the boundary. Since the incoming acoustic source is typically a reflection of the outgoing acoustic wave at the boundary, such a boundary condition is named as the characteristic-based reflecting boundary condition (C-RBC) in this thesis. C-RBC provides an interface to couple CBC with the time-domain impedance boundary condition (TDIBC) (Jaensch et al., 2016, Kaess et al., 2008) and this combination is referred to in this thesis as the characteristic-based time-domain impedance boundary condition (C-TDIBC).

The next section provides a brief overview of the characteristic decomposition of a hyperbolic equation system, which serves as the mathematical foundation of the characteristic boundary condition. The NSCBC, including the original LODI as well as its variant LODI-T, will be introduced afterward.

### 5.1.1 Characteristic decomposition of hyperbolic systems

Consider a hyperbolic equation system of primitive variables  $\mathbf{U}$  in the form of

$$\frac{\partial \mathbf{U}}{\partial t} + \mathbf{A} \frac{\partial \mathbf{U}}{\partial x_1} + \mathbf{C} = 0, \quad (5.1)$$

the matrix  $\mathbf{A}$  is diagonalizable with real eigenvalues, resulting in  $\mathbf{S}^{-1}\mathbf{A}\mathbf{S} = \mathbf{\Lambda}$  (LeVeque, 2007, Ch. 10.10).  $\mathbf{S}$  and its inversion  $\mathbf{S}^{-1}$  are the matrices of right eigenvectors  $\mathbf{r}_i$  and left eigenvectors  $\mathbf{l}_i^T$  of  $\mathbf{A}$ , respectively, i.e.,

$$\mathbf{A}\mathbf{r}_i = \lambda_i\mathbf{r}_i, \quad (5.2a)$$

$$\mathbf{l}_i^T\mathbf{A} = \lambda_i\mathbf{l}_i^T, \quad (5.2b)$$

with  $\mathbf{\Lambda}$  the diagonal matrix of eigenvalues  $\lambda_i$ .

Equation 5.1 can be expressed in the characteristic variable formulation

$$\frac{\partial \mathbf{W}}{\partial t} + \mathbf{\Lambda} \frac{\partial \mathbf{W}}{\partial x_1} + \mathbf{S}^{-1}\mathbf{C} = 0, \quad (5.3)$$

where  $\mathbf{W} = \mathbf{S}^{-1}\mathbf{U}$  is known as the “characteristic variable” or “characteristic waves”, with each of its components given as

$$W_i = \mathbf{l}_i^T\mathbf{U}. \quad (5.4)$$

The second term of Eq. 5.3 is known as the wave amplitude variations, and is commonly denoted as

$$\mathcal{L} = \mathbf{\Lambda} \frac{\partial \mathbf{W}}{\partial x_1} = \mathbf{\Lambda}\mathbf{S}^{-1} \frac{\partial \mathbf{U}}{\partial x_1} = \mathbf{S}^{-1}\mathbf{A} \frac{\partial \mathbf{U}}{\partial x_1}, \quad (5.5)$$

with each of its elements given as

$$\mathcal{L}_i \equiv \lambda_i \mathbf{l}_i^T \frac{\partial \mathbf{U}}{\partial x_1}. \quad (5.6)$$

The wave amplitude variation  $\mathcal{L}$  is the most important concept in CBC, and it can be interpreted as the directional derivative of  $\mathbf{U}$  in the characteristic direction of  $\mathbf{l}_i^T$ .

The hyperbolic equation is then reformulated in terms of  $\mathcal{L}$  as

$$\frac{\partial \mathbf{U}}{\partial t} + \mathbf{S}\mathcal{L} + \mathbf{C} = 0, \quad (5.7)$$

or in the characteristic variable format as

$$\frac{\partial \mathbf{W}}{\partial t} + \mathcal{L} + \mathbf{S}^{-1}\mathbf{C} = 0. \quad (5.8)$$

### 5.1.2 Navier-Stokes characteristic boundary conditions

NSCBC is constructed based on the governing equation system (Eqs. 3.4, 3.8 and 3.16) of fluid dynamics, which is written below in three dimensions:

$$\frac{\partial \rho}{\partial t} + v_1 \frac{\partial \rho}{\partial x_1} + v_2 \frac{\partial \rho}{\partial x_2} + v_3 \frac{\partial \rho}{\partial x_3} + \rho \left( \frac{\partial v_1}{\partial x_1} + \frac{\partial v_2}{\partial x_2} + \frac{\partial v_3}{\partial x_3} \right) = 0, \quad (5.9a)$$

$$\frac{\partial p}{\partial t} + v_1 \frac{\partial p}{\partial x_1} + v_2 \frac{\partial p}{\partial x_2} + v_3 \frac{\partial p}{\partial x_3} + \gamma p \left( \frac{\partial v_1}{\partial x_1} + \frac{\partial v_2}{\partial x_2} + \frac{\partial v_3}{\partial x_3} \right) = (\gamma - 1) \tau_{ij} \frac{\partial v_i}{\partial x_j}, \quad (5.9b)$$

$$\frac{\partial v_1}{\partial t} + v_1 \frac{\partial v_1}{\partial x_1} + v_2 \frac{\partial v_1}{\partial x_2} + v_3 \frac{\partial v_1}{\partial x_3} + \frac{1}{\rho} \frac{\partial p}{\partial x_1} = \frac{1}{\rho} \frac{\partial \tau_{1j}}{\partial x_j}, \quad (5.9c)$$

$$\frac{\partial v_2}{\partial t} + v_1 \frac{\partial v_2}{\partial x_1} + v_2 \frac{\partial v_2}{\partial x_2} + v_3 \frac{\partial v_2}{\partial x_3} + \frac{1}{\rho} \frac{\partial p}{\partial x_2} = \frac{1}{\rho} \frac{\partial \tau_{2j}}{\partial x_j}, \quad (5.9d)$$

$$\frac{\partial v_3}{\partial t} + v_1 \frac{\partial v_3}{\partial x_1} + v_2 \frac{\partial v_3}{\partial x_2} + v_3 \frac{\partial v_3}{\partial x_3} + \frac{1}{\rho} \frac{\partial p}{\partial x_3} = \frac{1}{\rho} \frac{\partial \tau_{3j}}{\partial x_j} \quad (5.9e)$$

Considering a boundary with its normal parallel to the  $x_1$  direction, the equation system is written in the matrix equation form as in Eq. 5.1:

$$\frac{\partial \mathbf{U}}{\partial t} + \mathbf{A} \frac{\partial \mathbf{U}}{\partial x_1} + \mathbf{T} = \mathbf{V}, \quad (5.10)$$

where  $\mathbf{U} = [\rho, p, v_1, v_2, v_3]^T$ , and

$$\mathbf{A} = \begin{bmatrix} u_1 & 0 & \rho & 0 & 0 \\ 0 & v_1 & \gamma p & 0 & 0 \\ 0 & 1/\rho & v_1 & 0 & 0 \\ 0 & 0 & 0 & v_1 & 0 \\ 0 & 0 & 0 & 0 & v_1 \end{bmatrix}, \quad (5.11)$$

The matrices  $\mathbf{V}$  and  $\mathbf{T}$  include all the inviscid transverse terms and the viscous terms,

respectively, shown as

$$\mathbf{T} = \begin{bmatrix} T_\rho \\ T_p \\ T_{v1} \\ T_{v2} \\ T_{v3} \end{bmatrix} = \begin{bmatrix} v_2 \frac{\partial \rho}{\partial x_2} + v_3 \frac{\partial \rho}{\partial x_3} + \rho \left( \frac{\partial v_2}{\partial x_2} + \frac{\partial v_3}{\partial x_3} \right) \\ v_2 \frac{\partial p}{\partial x_2} + v_3 \frac{\partial p}{\partial x_3} + \gamma p \left( \frac{\partial v_2}{\partial x_2} + \frac{\partial v_3}{\partial x_3} \right) \\ v_2 \frac{\partial v_1}{\partial x_2} + v_3 \frac{\partial v_1}{\partial x_3} \\ v_2 \frac{\partial v_2}{\partial x_2} + v_3 \frac{\partial v_2}{\partial x_3} + \frac{1}{\rho} \frac{\partial p}{\partial x_2} \\ v_2 \frac{\partial v_3}{\partial x_2} + v_3 \frac{\partial v_3}{\partial x_3} + \frac{1}{\rho} \frac{\partial p}{\partial x_3} \end{bmatrix} \quad (5.12)$$

$$\mathbf{V} = \begin{bmatrix} V_\rho \\ V_p \\ V_{v1} \\ V_{v2} \\ V_{v3} \end{bmatrix} = \begin{bmatrix} 0 \\ (\gamma - 1)\tau_{ij} \frac{\partial v_i}{\partial x_j} \\ \frac{1}{\rho} \frac{\partial \tau_{1j}}{\partial x_j} \\ \frac{1}{\rho} \frac{\partial \tau_{2j}}{\partial x_j} \\ \frac{1}{\rho} \frac{\partial \tau_{3j}}{\partial x_j} \end{bmatrix} \quad (5.13)$$

The eigenvalues of  $\mathbf{A}$  are

$$\lambda_1 = v_1 - c, \quad \lambda_2 = \lambda_3 = \lambda_4 = v_1, \quad \lambda_5 = v_1 + c, \quad (5.14)$$

with the corresponding left eigenvectors written as

$$\begin{aligned} \mathbf{l}_1^T &= (0, 1, -\rho c, 0, 0), \\ \mathbf{l}_2^T &= (c^2, -1, 0, 0, 0), \\ \mathbf{l}_3^T &= (0, 0, 0, 1, 0), \\ \mathbf{l}_4^T &= (0, 0, 0, 0, 1), \\ \mathbf{l}_5^T &= (0, 1, \rho c, 0, 0), \end{aligned} \quad (5.15)$$

where  $c = \sqrt{\gamma p / \rho}$  is the speed of sound as given in Eq. 3.18.

The ‘‘characteristic variables’’ defined in Eq. 5.4 are given as

$$\mathbf{W} = \begin{bmatrix} W_1 \\ W_2 \\ W_3 \\ W_4 \\ W_5 \end{bmatrix} = \begin{bmatrix} p - \rho c v_1 \\ \rho c^2 - p \\ v_2 \\ v_3 \\ p + \rho c v_1 \end{bmatrix}, \quad (5.16)$$

and the wave amplitude variations defined in Eq. 5.6 are given as

$$\mathcal{L}_1 = \frac{\partial W_1}{\partial x_1} = \lambda_1 \left( \frac{\partial p}{\partial x_1} - \rho c \frac{\partial v_1}{\partial x_1} \right), \quad (5.17a)$$

$$\mathcal{L}_2 = \frac{\partial W_2}{\partial x_1} = \lambda_2 \left( c^2 \frac{\partial \rho}{\partial x_1} - \frac{\partial p}{\partial x_1} \right), \quad (5.17b)$$

$$\mathcal{L}_3 = \frac{\partial W_3}{\partial x_1} = \lambda_3 \frac{\partial v_2}{\partial x_1}, \quad (5.17c)$$

$$\mathcal{L}_4 = \frac{\partial W_4}{\partial x_1} = \lambda_4 \frac{\partial v_3}{\partial x_1}, \quad (5.17d)$$

$$\mathcal{L}_5 = \frac{\partial W_5}{\partial x_1} = \lambda_5 \left( \frac{\partial p}{\partial x_1} + \rho c \frac{\partial v_1}{\partial x_1} \right), \quad (5.17e)$$

Each  $W_i$  represents a different traveling wave, with the eigenvalues  $\lambda_i$  representing the corresponding wave speeds.  $W_1$  and  $W_5$  represent left- and right-traveling acoustic waves, respectively, with corresponding traveling speeds of  $v_1 - c$  and  $v_1 + c$ .  $W_2$  and  $W_{3,4}$  are related to the entropy wave and vorticity waves, which are convected by the mean flow velocity  $v_1$ .

The equation system Eq. 5.9 can be rewritten in the characteristic variable form of Eq. 5.8 as

$$\begin{bmatrix} \frac{\partial W_1}{\partial t} \\ \frac{\partial W_2}{\partial t} \\ \frac{\partial W_3}{\partial t} \\ \frac{\partial W_4}{\partial t} \\ \frac{\partial W_5}{\partial t} \end{bmatrix} + \begin{bmatrix} \mathcal{L}_1 \\ \mathcal{L}_2 \\ \mathcal{L}_3 \\ \mathcal{L}_4 \\ \mathcal{L}_5 \end{bmatrix} = \begin{bmatrix} \mathcal{T}_1 \\ \mathcal{T}_2 \\ \mathcal{T}_3 \\ \mathcal{T}_4 \\ \mathcal{T}_5 \end{bmatrix} + \begin{bmatrix} \mathcal{V}_1 \\ \mathcal{V}_2 \\ \mathcal{V}_3 \\ \mathcal{V}_4 \\ \mathcal{V}_5 \end{bmatrix}, \quad (5.18)$$

which is normally used to define the boundary condition with

$$\mathcal{T} = \begin{bmatrix} -(T_p - \rho c T_{v_1}) \\ -(c^2 T_\rho - T_p) \\ -T_{v_2} \\ -T_{v_3} \\ -(T_p + \rho c T_{v_1}) \end{bmatrix} \quad (5.19a)$$

$$\mathcal{V} = \begin{bmatrix} V_p - \rho c V_{v_1} \\ c^2 V_\rho - V_p \\ V_{v_2} \\ V_{v_3} \\ V_p + \rho c V_{v_1} \end{bmatrix}. \quad (5.19b)$$

Equation 5.9 is also rewritten in the form of Eq. 5.7 as

$$\frac{\partial}{\partial t} \begin{bmatrix} \rho \\ p \\ v_1 \\ v_2 \\ v_3 \end{bmatrix} + \begin{bmatrix} \frac{1}{2c^2} \left[ \mathcal{L}_2 + \frac{1}{2}(\mathcal{L}_5 + \mathcal{L}_1) \right] \\ \frac{1}{2}(\mathcal{L}_5 + \mathcal{L}_1) \\ \frac{1}{2\rho c}(\mathcal{L}_5 - \mathcal{L}_1) \\ \mathcal{L}_3 \\ \mathcal{L}_4 \end{bmatrix} + \begin{bmatrix} T_\rho \\ T_p \\ T_{v1} \\ T_{v2} \\ T_{v3} \end{bmatrix} = \begin{bmatrix} V_\rho \\ V_p \\ V_{v1} \\ V_{v2} \\ V_{v3} \end{bmatrix}, \quad (5.20)$$

which is used to update macroscopic variables  $\rho$ ,  $p$ , and  $\mathbf{v}$  at the boundaries in the time domain.

Consider an outflow boundary on the right surface of a computational domain, as shown in Fig. 5.1, the time derivatives  $\partial/\partial t$  in Eq. 5.20 can be approximated using the Runge-Kutta or Euler method, and the transverse terms  $\partial/\partial x_2$  and  $\partial/\partial x_3$  in  $\mathbf{T}$  and  $\mathbf{V}$  are approximated using finite difference schemes with information on the boundary.  $\mathcal{L}_{2,3,4,5}$  correspond to right-traveling wave amplitude variables that leave from the computational domain, which allows their  $\partial/\partial x_1$  terms to be approximated using a one-sided finite difference with upstream variables within the computational domain.  $\mathcal{L}_1$  corresponds to the left-traveling acoustic wave that enters the domain through the boundary so that it cannot be approximated using an upwind scheme and becomes the only term that remains unknown to solve the equation system on the boundary. However, based on the boundary condition defined in Eq. 5.18,  $\mathcal{L}_1$  can be defined with other terms in the first row of the equation:

$$\mathcal{L}_1 = -\frac{\partial W_1}{\partial t} + \mathcal{T}_1 + \mathcal{V}_1. \quad (5.21)$$

The primary goal of CBC is to define the outgoing wave amplitude variables  $\mathcal{L}_i$  that cannot be approximated with known variables in the computational domain by using proper boundary conditions. The boundary conditions specified here focus on the subsonic non-reflecting outflow boundaries. One can refer to the papers by Poinsot and Lele (1992) and Lodato et al. (2008) for the CBC formulations of other types of boundary conditions.

For non-reflecting boundary conditions, the incoming characteristic waves are constant

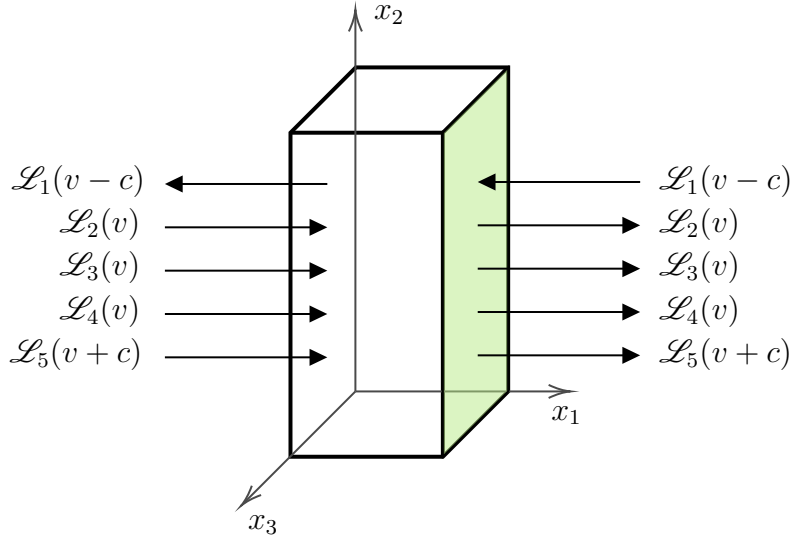


**Fig. 5.1:** Illustration of the computational domain with NSCBC applied on the right surface (green) perpendicular to the  $x_1$ -axis.  $\mathcal{L}_i$  represents wave amplitude variations and the arrows indicate the characteristic wave traveling direction.

in time at the boundaries, which gives (Hedstrom, 1979)

$$\partial W_1 / \partial t = 0, \quad (5.22)$$

so that Eq. 5.21 is simplified as

$$\mathcal{L}_1 = \mathcal{T}_1 + \mathcal{V}_1. \quad (5.23)$$

The LODI proposed by Poinso and Lele (1992) further dropped the viscous and transverse terms  $\mathcal{T}_1$  and  $\mathcal{V}_1$ , which leads to the so-called “perfectly non-reflecting” CBC (Poinso and Lele, 1992).

$$\mathcal{L}_1 = 0. \quad (5.24)$$

However, such a condition is ill-posed and can lead to mean flow drift. A simple way to ensure well-posedness is to introduce a pressure relaxation term (Poinso and Lele, 1992, Rudy and Strikwerda, 1980)

$$\mathcal{L}_1 = K_p(p - p_\infty), \quad (5.25)$$

where

$$K_p = \sigma(1 - \text{Ma}^2)c/L \quad (5.26)$$

is the relaxation frequency,  $Ma$  is the Mach number of the mean flow,  $L$  is the characteristic size of the domain in the  $x_1$  direction, and  $\sigma$  is a chosen constant.  $p_\infty$  is a target pressure that is normally set to the far field pressure. This boundary condition is obtained by substituting Eq. 5.25 back into Eq. 5.21

$$\frac{\partial W_1}{\partial t} = -K_p(p - p_\infty).$$

This boundary condition is known to be partially reflective since it violates the ideal non-reflecting boundary condition in Eq. 5.22. The plane wave masking is proposed as a remedy in the context of a plane wave propagation problem and will be presented in the next section.

Yoo et al. (2005) improved LODI by including the transverse term  $\mathcal{T}$  and an additional relaxation of the transverse term toward a reference value  $\mathcal{T}_\infty$ . The incoming acoustic wave variation is modified as

$$\mathcal{L}_1 = K_p(p - p_\infty) - K_T(\mathcal{T}_1 - \mathcal{T}_{1,\infty}) + \mathcal{T}_1, \quad (5.27)$$

with the transverse relaxation parameter typically set as  $K_T = 2M$ . The corresponding boundary condition is denoted as

$$\frac{\partial W_1}{\partial t} = -K_p(p - p_\infty) + K_T(\mathcal{T}_1 - \mathcal{T}_{1,\infty}) + \mathcal{V}_1, \quad (5.28)$$

which is referred to as LODI-T, and will be primarily applied in the present study.

## 5.2 Plane wave masking

Polifke and Wall (2002) and Polifke et al. (2006) proved that LODI with the pressure relaxation term provided in Eq. 5.25 is partially reflective and that the amplitude of the reflection coefficient  $R$  of the boundary condition approaches unity at low frequencies. Polifke et al. (2006) proposed the plane wave masking (PWM) to overcome the problem when applying CBC in plane acoustic wave propagation with normal incidence to the boundary. This section will first present PWM for non-reflecting boundary conditions, then discuss the formulation of the characteristic-based reflecting boundary condition (C-RBC) by applying PWM in CBC with external excitations.

### 5.2.1 PWM for non-reflecting boundary conditions

The essential of PWM is to identify the outgoing acoustic wave  $p'_{out}$  from the pressure  $p$  at the boundary and mask its contribution to the incoming acoustic wave by modifying  $\mathcal{L}_1$

$$\mathcal{L}_1 = K_p(p - p'_{out} - p_\infty). \quad (5.29)$$

Considering the same boundary as shown in Fig. 5.1, the acoustic pressure wave traveling along the  $x_1$ -axis is decomposed into the right-traveling  $p^+ = p^+(x - (\bar{v}_1 + c)t)$  and left-traveling waves  $p^- = p^-(x - (\bar{v}_1 - c)t)$ , where  $\bar{v}_1$  is the mean flow velocity in the  $x_1$  direction. The right-traveling pressure  $p^+$  corresponds to the one that leaves the domain, so that the above equation is rewritten as

$$\mathcal{L}_1 = K_p(p - p^+ - p_\infty). \quad (5.30)$$

For LODI-T,  $\mathcal{L}_1$  defined in Eq. 5.27 can also be modified correspondingly as

$$\mathcal{L}_1 = K_p(p - p^+ - p_\infty) - K_T(\mathcal{T}_1 - \mathcal{T}_{1,\infty}) + \mathcal{T}_1. \quad (5.31)$$

Acoustic pressure and velocity are considered as small fluctuations on top of the mean value such that  $p = \bar{p} + p'$  and  $v_1 = \bar{v}_1 + v'_1$ . In order to calculate  $p^+$  to complete the boundary condition, PWM assumes a plane wave at the boundary, where the acoustic pressure and velocity are uniform across the transverse plane and can be approximated with

$$\begin{aligned} p' &\approx \langle p - \bar{p} \rangle, \\ v'_1 &\approx \langle v_1 - \bar{v}_1 \rangle, \end{aligned} \quad (5.32)$$

where  $\langle \cdot \rangle$  represents the spatial average along the boundary.

With the known acoustic pressure  $p'$  and velocity  $v'_1$  on the boundary, the right-traveling and left-traveling waves are calculated with

$$p^+ = \frac{1}{2}(p' + \rho c v'_1), \quad (5.33a)$$

$$p^- = \frac{1}{2}(p' - \rho c v'_1). \quad (5.33b)$$

### 5.2.2 PWM for reflecting boundary conditions

The characteristic boundary condition relies on the definition of  $\mathcal{L}_1$  based on Eq. 5.21, which is rewritten here:

$$\mathcal{L}_1 = -\frac{\partial W_1}{\partial t} + \mathcal{T}_1 + \mathcal{V}_1.$$

The non-reflecting boundary condition is based on Hedstrom (1979)'s boundary condition in Eq. 5.22 which set  $\partial W_1/\partial t = 0$ . However,  $\partial W_1/\partial t$  does not equal zero when there is an external excitation.

By combining the definition of  $W_1 = p - \rho cv_1$  with PWM assumption in Eq. 5.32, the approximation of  $\partial W_1/\partial t$  gives

$$\frac{\partial W_1}{\partial t} = \frac{\partial(p - \rho cv_1)}{\partial t} \approx \frac{\partial(p' - \rho cv_1')}{\partial t} = 2\frac{\partial p^-}{\partial t}, \quad (5.34)$$

The definitions of  $\mathcal{L}_1$  in LODI (Eq. 5.30) and LODI-T (Eq. 5.31) for non-reflecting boundary conditions are extended by including the non-zero  $\partial W_1/\partial t$ , and are expressed correspondingly as

$$\mathcal{L}_1 = K(p - (p^+ + p^-) - p_\infty) - 2\frac{\partial p^-}{\partial t}, \quad (5.35)$$

and

$$\mathcal{L}_1 = K(p - (p^+ + p^-) - p_\infty) - K_T(\mathcal{T}_1 - \mathcal{T}_{1,\infty}) + \mathcal{T}_1 - 2\frac{\partial p^-}{\partial t}. \quad (5.36)$$

It is important to note that the pressure relaxation target includes not only the outgoing acoustic pressure  $p^+$  as in NRBC, but also the incoming acoustic pressure  $p^-$ , so that the total acoustic pressure  $p' = p^+ + p^-$  is masked.

The above boundary condition in Eqs. 5.35 and 5.36 is named as characteristic-based reflecting boundary condition (C-RBC) in this thesis which needs to be completed with user-defined excitation terms  $p^-$  and  $\partial p^-/\partial t$ . C-RBC is commonly applied at the end of the computational domain to help couple an acoustic component to the numerical system. A time-domain reflection function  $r(t)$  can be used to model the acoustic component so that the incoming acoustic wave  $p^-$  can be calculated by convolving  $r(t)$  with the outgoing acoustic wave  $p^+$

$$p^-(t) = (p^+ * r)(t). \quad (5.37)$$

Different acoustic models, such as the digital waveguide method, wave digital filters,

and TDIBC, can be integrated with C-RBC by taking  $p^+$  at the boundary as an input to the acoustic model and calculate the output  $p^-$ , which is fed back to the computational domain. In the present research, TDIBC is primarily used in the aeroacoustic modeling of the saxophone mouthpiece, and the next sections will cover the TDIBC formulation, its integration with C-RBC, as well as its implementation in LB simulations.

### 5.3 Time-domain impedance boundary condition

The time-domain impedance boundary condition (TDIBC) can be divided into two groups depending on the mean flow direction relative to the wall orientation. The majority of TDIBCs have been proposed based on the Ingard-Myers boundary condition (Ingard, 1959, Myers, 1980) and are commonly applied for grazing flows passing along acoustic liners, with the wall being parallel to the flow direction. In this thesis, TDIBC is meant to be applied at the end of a pipe to implement an acoustic load connected to the computational domain. In such a circumstance, the flow travels perpendicular to the boundary, and it usually requires to separate the mean flow from the acoustic flow using numerical filters (Schuermans et al., 2005) or the characteristic boundary condition (Kaess et al., 2008, Polifke et al., 2006). Despite the different flow directions to the boundary, the framework of TDIBC is the same and is generally composed of two processes: *modeling* and *implementation*.

The *modeling* focuses on establishing a proper representation of the frequency-domain impedance or reflection coefficients. Early TDIBC models, such as the first TDIBC model (Tam and Auriault, 1996) that implemented a single frequency impedance and the first “broadband” impedance model (Özyörük et al., 1998), are based on a rational function representation of the impedance. Taking the impedance in the continuous frequency domain as an example, it can be approximated by a rational function of  $j\omega$  (Dragna et al., 2015):

$$Z(\omega) \approx Z_p(\omega) = Z_\infty + \frac{a_0 + \dots + a_{P-1}(j\omega)^{P-1}}{1 + \dots + b_P(j\omega)^P}, \quad (5.38)$$

where all coefficients  $a_i$  and  $b_i$  are real, and can be obtained by fitting the frequency response to a known impedance. The rational representation can be built in the continuous frequency domain and then transformed to the  $z$ -domain (Özyörük et al., 1998), or immediately fit in the  $z$ -domain (Huber et al., 2008).

The multipole model is another extensively used representation (Fung and Ju, 2001, Li

et al., 2012, Reymen et al., 2007). It is based on the partial fraction expansion of the rational representation (Eq. 5.38), which yields

$$Z_p(\omega) = Z_\infty + \sum_n \frac{C_n}{j\omega - s_n}, \quad (5.39)$$

where  $s_n$  and  $C_n$  correspond to the poles and residues, respectively.

The *implementation* of TDIBC is primarily concerned with the transformation of a frequency-domain representation to a time-domain representation so that the boundary condition can be applied in a time-domain simulation. Widely applied implementations include the recursive convolution (Fung and Ju, 2001, Li et al., 2012, Reymen et al., 2007), auxiliary differential equation method (Dragna et al., 2015), state-space representation (Jaensch et al., 2016, Schuermans et al., 2005, Zhong et al., 2016) to name a few.

In this thesis, the input impedance  $Z(z)$  is modeled as a recursive parallel filter structure in the  $z$ -domain (Maestre and Scavone, 2016, Maestre et al., 2017). Akin to a discretized modal expansion, resonant behavior of the impedance is conveyed by a number of parallel two-pole resonators:

$$Z(z) = \sum_{n=1}^N (b_{0,n} + b_{1,n}z^{-1})H_n(z), \quad (5.40)$$

where

$$H_n(z) = \frac{1 - z^{-1}}{(1 - p_n z^{-1})(1 - \bar{p}_n z^{-1})}, \quad (5.41)$$

with  $p_n$  and  $\bar{p}_n$  being a pair of complex conjugate poles of the  $n$ -th resonator, which guarantees the realness of the coefficients.  $b_{0,n}$  and  $b_{1,n}$  are real coefficients to control the amplitude and phase of each individual resonator.

As described by Maestre et al. (2018), the impedance digital filter  $Z(z)$  can be transformed into a linear form

$$Z(z) = B_0 + z^{-1}Q(z), \quad (5.42)$$

where

$$Q(z) = z^{-1}B_1 + z^{-1}H^0(z) + z^{-2}H^1(z), \quad (5.43)$$

$$B_0 = \sum_{n=1}^N b_{0,n}, \quad B_1 = \sum_{n=1}^N b_{1,n}, \quad (5.44)$$

$$H^0(z) = \sum_{n=1}^N b_{0,n}H_n^p(z), \quad H^1(z) = \sum_{n=1}^N b_{1,n}H_n^p(z), \quad (5.45)$$

and

$$H_n^p(z) = \frac{c_{0,n} + c_{1,n}z^{-1}}{1 + a_{1,n}z^{-1} + a_{2,n}z^{-2}}, \quad (5.46)$$

with  $c_{0,n} = -1 - a_{1,n}$  and  $c_{1,n} = -a_{2,n}$ .

In order to be coupled with C-RBC, the input impedance model is transformed to a reflection coefficient representation using the approach proposed by Maestre et al. (2017, 2018), which helps retain the parallel structure of the filter during the transformation.

Making use of the fact that  $P(z) = Z(z)U(z)$  and  $U^\pm = \pm P^\pm Y_c$  with  $Y_c = 1/Z_c$  the characteristic admittance, the following expression of the volume flow rate  $U(z)$  can be derived

$$U(z) = \frac{2Y_c P^+(z)}{1 + Y_c Z(z)}, \quad (5.47)$$

which can then be reformulated by substituting it in Eq. 5.42:

$$U(z) = \frac{2Y_c P^+(z) - z^{-1}Y_c Q(z)U(z)}{1 + Y_c B_0}. \quad (5.48)$$

The pressure is then updated as

$$P(z) = B_0 U(z) + z^{-1}Q(z)U(z), \quad (5.49)$$

with which the reflected acoustic pressure is calculated

$$P^-(z) = P(z) - P^+(z). \quad (5.50)$$

Equations. 5.48-5.50 make it possible to take the outgoing acoustic wave  $P^+$  as an input and return the incoming wave  $P^-$ , which hence can be coupled with C-RBC. The corre-

sponding discrete-time domain expressions are written as

$$u[n] = \frac{Y_c}{1 + Y_c B_0} (2p^+[n] - q[n]), \quad (5.51)$$

$$p[n] = B_0 u[n] + q[n], \quad (5.52)$$

$$p^-[n] = p[n] - p^+[n]. \quad (5.53)$$

where  $q[n]$  only depends on the history of  $u[n]$ , i.e., on  $u[n - k]$  with  $k \geq 1$ . It should be noted that the volume flow rate  $u[n]$  is a temporary variable of the recursive parallel filter, which is independent of the flow velocity  $v_1$  in the LB domain at the boundary.

## 5.4 Implementation of C-TDIBC in LBM

The characteristic boundary conditions are defined at the macroscopic level. To implement it in LB simulations at the mesoscopic level, an LB boundary condition, such as the Zou-He boundary condition introduced in Sec. 4.3.1, should be used to update the particle population at each time step with the macroscopic variables determined from CBC.

Izquierdo and Fueyo (2008) were the first to apply CBC in the LB simulation by integrating the LODI with the LBM non-equilibrium bounce back boundary condition. Heubes et al. (2014) later proposed a modified Thompson boundary condition that combines Thompson's original CBC for Euler equations (Thompson, 1987) with LODI and uses a single parameter to control the contribution of the transverse terms. The non-equilibrium extrapolation method is used to complete the boundary condition at the LB level. Jung et al. (2015) incorporated Yoo and Im (2007)'s scheme into LB simulations, which includes viscous and transverse terms, as well as a transverse relaxation into the boundary condition. More recently, Wissocq et al. (2017) proposed the regularized CBC and investigated the combinations of the regularized boundary condition with several CBC variants including the LODI, the LODI with transverse terms and transverse relaxation (LODI-T) and the local streamline LODI.

The implementation of C-TDIBC in LB simulation is detailed in this section. It is essentially a combination of the C-RBC, the TDIBC, and the LB boundary condition, which are introduced in Sec. 5.2.2, Sec. 5.3, and Sec. 4.3.1, respectively. To summarize, the implementation of C-TDIBC in LB simulations involves the following steps:

1. compute  $\mathcal{L}_{2-5}$  defined in Eq. 5.17 using one-sided finite difference with upstream macroscopic variables inside the computational domain and compute the transverse terms  $\mathcal{T}$  using the finite difference to approximate the spatial derivatives in Eqs. 5.19a and 5.12,
2. using a low-pass filter (LPF) to separate the mean flow  $\bar{v}_1$  from acoustic flow  $v_1'$  as well as the mean pressure  $\bar{p}$  from acoustic pressure  $p'$ , and update the mean flow Mach number  $\text{Ma} = \bar{v}_1/c_s$ , and relaxation parameters  $K_p$  and  $K_T$ ,
3. compute  $p^+$  using Eq. 5.33a,
4. compute  $p^-$  and  $\partial p^-/\partial t$  with Eqs. 5.51-5.53 using TDIBC ( $p^-$  and  $\partial p^-/\partial t$  are set to zero for the non-reflecting boundary condition),
5. compute  $\mathcal{L}_1$  using Eq. 5.36 (the reference pressure and transverse terms are problem-dependent and initialized at the start of the simulation, and the relaxation coefficients  $K_p$  and  $K_T$  have been updated in Step 2),
6. update  $\rho$ ,  $p$ ,  $\mathbf{v}$  from Eq. 5.20, with the forward Euler method to approximate the time derivatives,
7. update LBM particle populations  $f_i$  with equilibrium particle distribution based on the macroscopic variables calculated in the previous step,
8. forward in time and go back to Step 1.

The LPF used in Step 2 is designed using the filter designer in Matlab. Specifically, an infinite impulse response (IIR) elliptic filter is constructed, which has a stopband starting at 100 Hz with an attenuation of 80 dB. The frequency response is shown in Fig. 5.2.

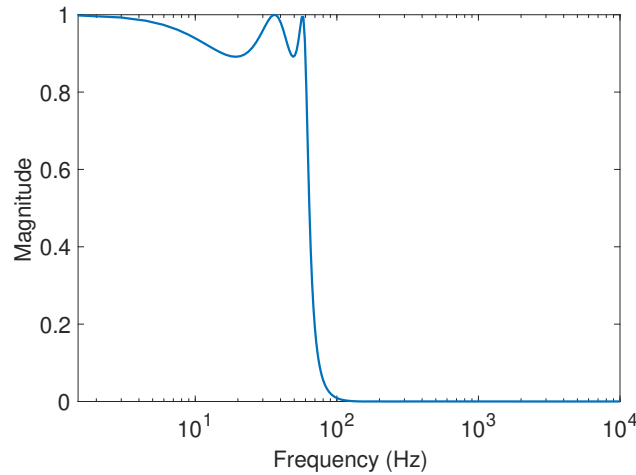


**Fig. 5.2:** The frequency response of the infinite impulse response low-pass filter.

## 5.5 Validations of characteristic-based boundary conditions

### 5.5.1 Non-reflecting boundary condition

#### 5.5.1.1 Free field wave propagation

The vortex convection test case, where a single vortex is convected by the uniform mean flow, is used to demonstrate the efficacy of the characteristic boundary condition as a non-reflecting boundary condition (NRBC). Three different NRBCs are tested including the absorbing boundary condition discussed in Sec. 4.3.2, LODI, as well as LODI-T.

The density and velocities are initialized as

$$\begin{cases} \rho = \rho_\infty - \rho \frac{C^2}{c_s^2 R_c^2} \exp\left(-\frac{r^2}{2R_c^2}\right) \\ v_1 = v_{1,\infty} + \frac{C}{\rho_\infty} \exp\left(-\frac{r^2}{2R_c^2}\right) \left(\frac{-(y-y_0)}{R_c^2}\right) \\ v_2 = 0 - \frac{C}{\rho_\infty} \exp\left(-\frac{r^2}{2R_c^2}\right) \left(\frac{-(x-x_0)}{R_c^2}\right) \end{cases} \quad (5.54)$$

where  $C = 25c_s N_x / 10^4$  is the vortex strength,  $R_c = N_x / 10$  is the vortex radius, and  $(x_0, y_0)$  is the vortex center that is located at the center of the domain  $(N_x/2, N_y/2)$ , and  $v_{1,\infty}$  is the mean flow velocity in the  $x_1$ -direction with Mach number equal to 0.1.  $N_x = N_y = 100$  is the number of grid points in  $x$ - and  $y$ -directions, correspondingly. The rrBGK is used for LBM simulation with the relaxation frequency  $\omega = 1/\tau = 1.993$ .

Figures 5.3 and 5.4 display the isocontours of the  $y$ -directional velocity and pressure, respectively, simulated by ABC, LODI and LODI-T, which show that LODI-T has the best performance in absorbing the outgoing wave with minimum disturbance in the upstream field.

#### 5.5.1.2 Wave propagation in pipe

To further validate the performance of CBC, the wave propagation in a two-dimensional pipe is simulated and the simulation setup is shown in Fig. 5.5. The inlet boundary condition is applied to the left of the pipe, which generates both the mean flow and the acoustic impulse. The impulse response of a finite impulse response low-pass filter is used as the sound source, which has a cut-off frequency of 10000 Hz. CBC is applied to the right of the pipe as a

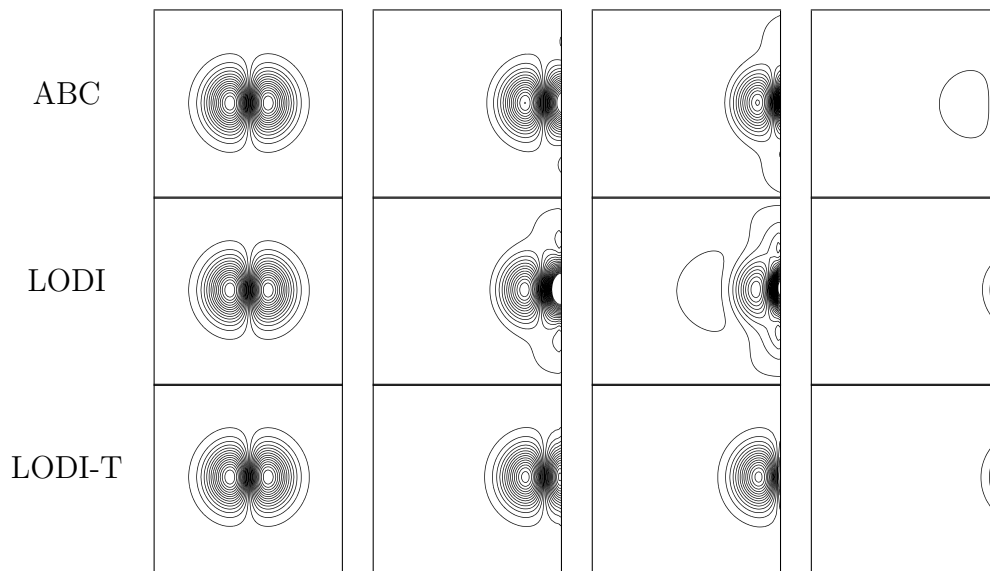


**Fig. 5.3:** Isocontours of the y-directional velocity at four different time steps.

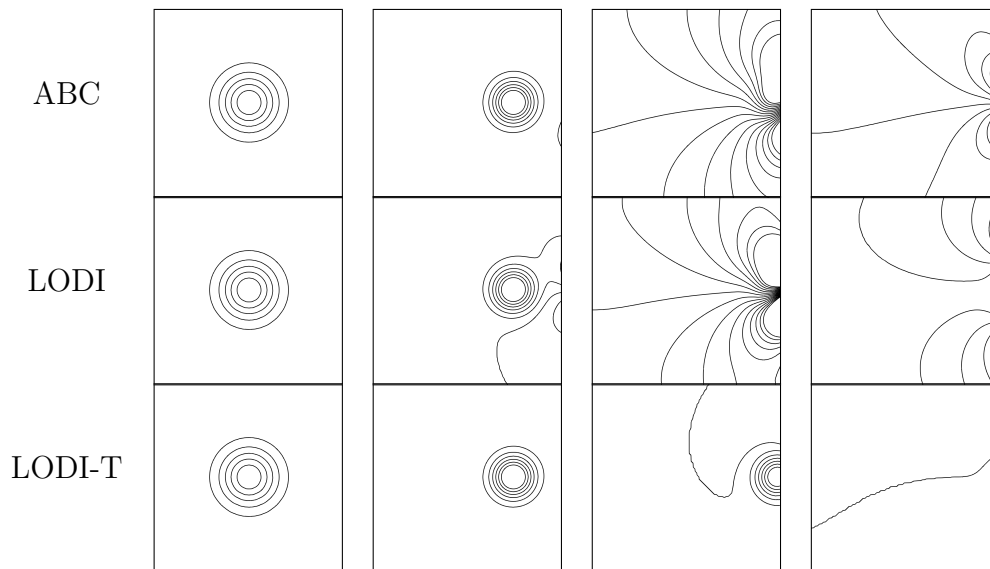
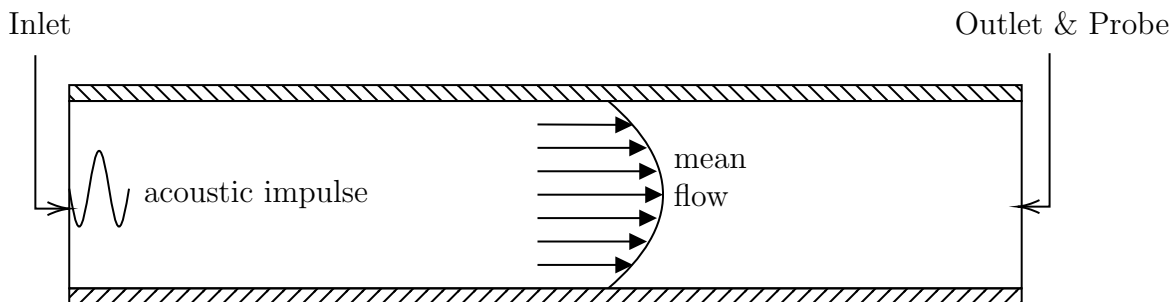


**Fig. 5.4:** Isocontours of pressure at four different time steps.

non-reflecting boundary condition, which indicates that the simulation can be considered as an acoustic impulse traveling in an infinite-long uniform pipe. Two different CBCs are tested including the LODI-T either with or without PWM, which correspond to the two different definitions of  $\mathcal{L}_1$  in Eq. 5.27 and Eq. 5.31, respectively. A probe is set at the right boundary to measure the acoustic pressure and velocity, which are Fourier-transformed to

the frequency domain and used to calculate the impedance  $Z$  as defined in Eq. 3.39, and reflection coefficients  $R$  using Eq. 3.42. Non-slip boundaries are applied to the top and bottom walls.

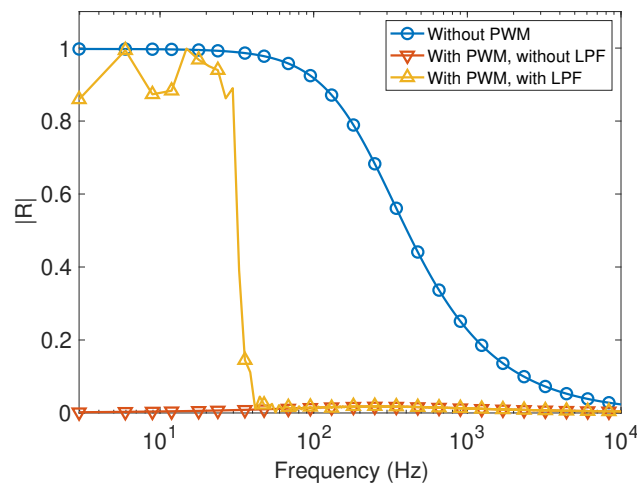
The pipe has a length of 8 mm and a width of 1.6 mm, which are selected based on the dimension of the saxophone mouthpiece. The acoustic sound speed is 343 m/s and the kinetic viscosity is set as  $1.51e^{-4}$  m<sup>2</sup>/s, which is an order of magnitude larger than that of the air to guarantee the stability of the simulation. The spatial resolution is set so that there are 180 grid points per wavelength at 10000 Hz.



**Fig. 5.5:** The schematic of the setup of wave propagation in a two-dimensional pipe.

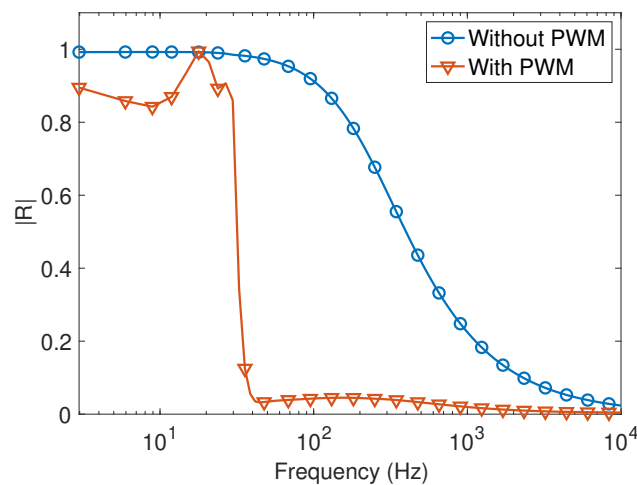
The simulation is first run under a quiescent flow. The acoustic impulse is triggered as soon as the simulation starts. Since there is no mean flow, there is no need to use the low-pass filter (IIR-LPF discussed in Sec. 5.4) to separate the mean values and acoustic fluctuations of the pressure and the velocity. However, simulations are computed both with and without the IIR-LPF, which are used to study the influence of the IIR-LPF on the performance of the non-reflecting boundary condition.

Figure 5.6 displays the measured magnitudes of the reflection coefficients using different CBC models. It demonstrates that the LODI-T without PWM is partially reflective and the reflectance goes toward unity at low frequencies as discussed in Sec. 5.2. PWM demonstrates its efficacy in improving the performance of NRBC, especially at low frequencies. An ideal NRBC should have zero reflection coefficient magnitudes at all frequencies. However, in reality, the wave can never be perfectly planar because of the acoustic boundary layer formulated due to the non-slip boundaries. In addition, the IIR-LPF is shown to degrade the CBC performance and the influence is found to mainly fall in the frequency range within the LPF passband by comparing results in Fig. 5.6 with the frequency response of the LPF shown in Fig. 5.2.



**Fig. 5.6:** The comparison of measured reflection coefficients for various CBCs under quiescent flow.

The simulation with the presence of mean flow runs through a few different phases. The velocity in the pipe is first initialized as zero and the inlet velocity then starts to increase from zero to the target mean flow velocity within 0.5 s. The acoustic impulse is finally triggered after the velocity field is stable. The measured reflection coefficients under the mean flow with Mach number 0.1 is shown in Fig. 5.7. A similar result as that of the quiescent flow simulation is found which further confirms the efficacy of PWM in improving the performance of the CBC as an NRBC.



**Fig. 5.7:** The comparison of measured reflection coefficients for various CBCs under mean flow (Ma=0.1).

### 5.5.2 Characteristic-based time-domain impedance boundary condition

In this section, the characteristic-based time-domain impedance boundary condition (C-TDIBC) is validated using the same simulation setup as shown in Fig. 5.5. Instead of deploying an NRBC to simulate an infinite pipe, the measured input impedance of a saxophone (the note C4 (written)) is imposed at the boundary with the help of C-TDIBC. The numerical measurement of the impedance is conducted both with and without mean flow with the same simulation parameters as used for NRBC validation. Figure 5.8 compares the imposed impedance with the probed ones under quiescent and mean flow ( $Ma = 0.1$ ), and Figure 5.9 compares the corresponding reflection coefficients. A good overall agreement is achieved for both cases while the main discrepancies lie around the first two anti-resonances of the impedance. This is consistent with the study of the non-reflecting characterization of the boundary condition, where the CBC is subject to larger fictitious reflections at low frequencies as shown in Figs. 5.6 and 5.7.

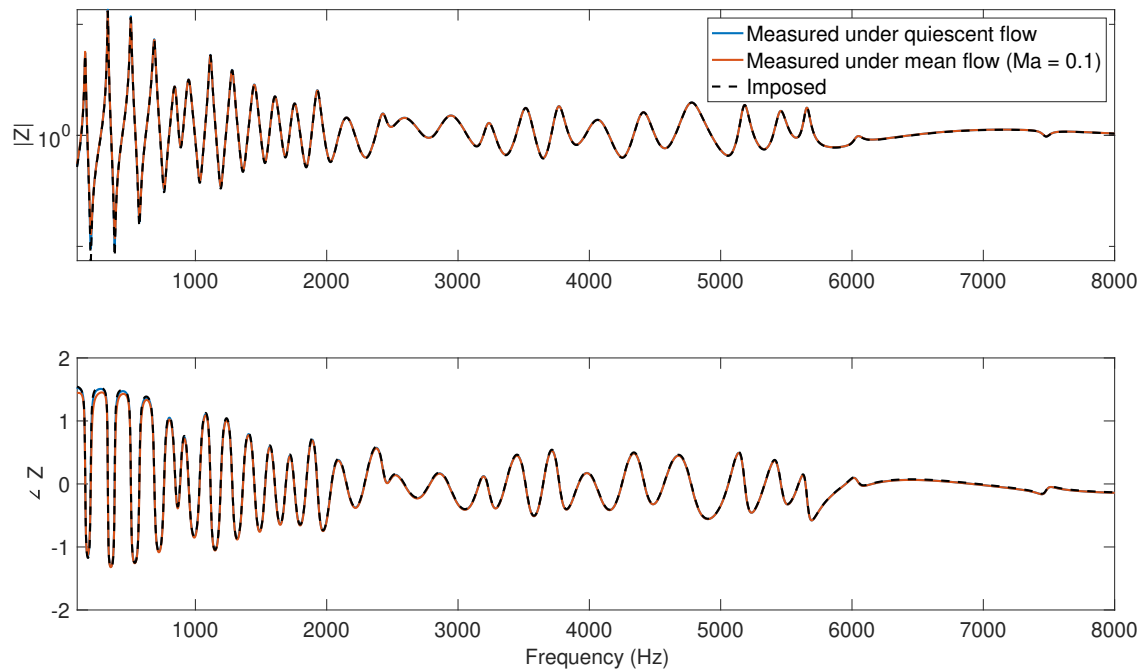


**Fig. 5.8:** The comparison between the imposed impedance and the measured ones under quiescent flow and mean flow ( $Ma=0.1$ ).

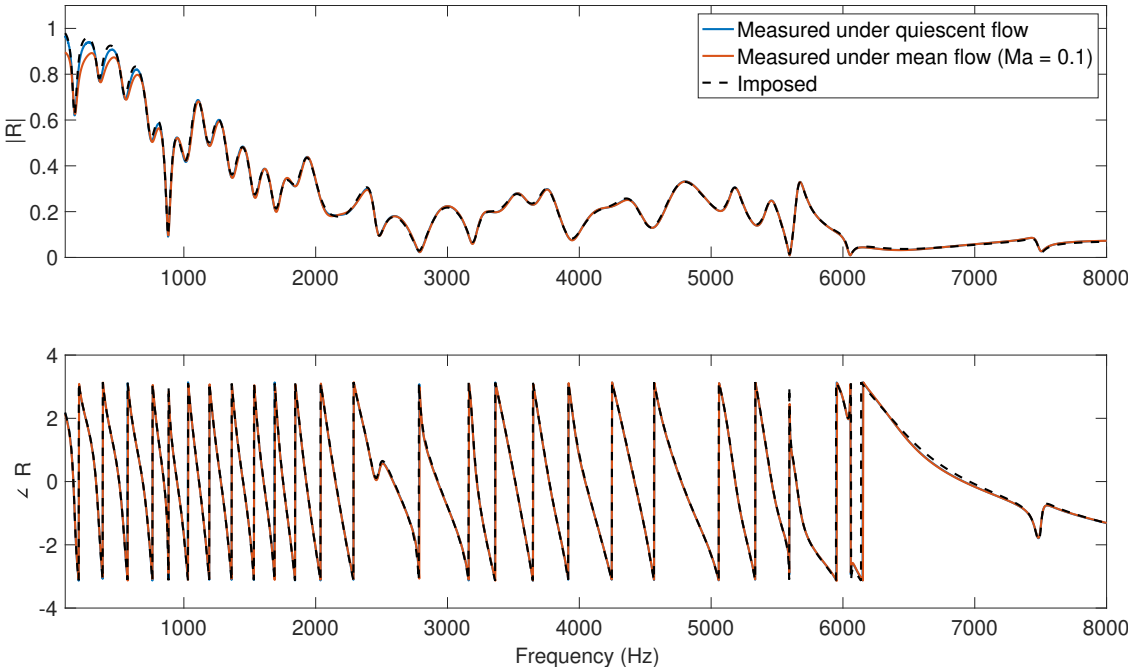


**Fig. 5.9:** The comparison between the imposed reflection coefficients and the measured ones under quiescent flow and mean flow (Ma=0.1).

## Chapter 6

# Acoustical Modeling of the Saxophone Mouthpiece

### 6.1 Introduction

In this chapter, the saxophone mouthpiece acoustics and its influence on the oscillation characteristics are investigated by treating the mouthpiece as a linear acoustic resonator. There are two main objectives in the present chapter. The first is to find a proper way to acoustically characterize the mouthpiece, and evaluate the mouthpiece's acoustic contribution to the saxophone. The input impedance of the mouthpiece is chosen as the primary feature for the acoustic characterization, and its definition is thoroughly discussed with an emphasis on determining the optimal place to define the mouthpiece acoustic input. The acoustic contribution of the mouthpiece is explored by comparing the measured input impedance of a conical pipe with and without a mouthpiece.

The second objective focuses on the acoustical modeling of the mouthpiece, with the goal of achieving a more accurate and flexible representation of a saxophone mouthpiece that can be applied both to sound synthesis and to investigate mouthpiece design variations. The saxophone body is a truncated conical air column with modal frequencies that are not harmonically related (Ayers et al., 1985). The mouthpiece completes the conical frustum by providing the volume equivalent to that of the missing part of the cone so that the fundamental frequency and the harmonics are better tuned (Benade, 1990, pp. 469-472). For the low-frequency range, where the wavelength is considerable in comparison to the dimen-

sion of the mouthpiece, the mouthpiece can be modeled as a parallel acoustic compliance that is determined only by the volume of the mouthpiece (Chen et al., 2009, Kergomard et al., 2016). However, such a lumped model is less accurate at high frequencies where the admittance of the parallel acoustic compliance overwhelms that of the resonator. Another way to represent the mouthpiece is as a cylindrical section, sometimes referred to as the “cyclone” model (Scavone, 2002). Similar to the lumped mouthpiece model, the volume of the cylinder is the same as that of the missing part of the cone. The cylindrical mouthpiece is coupled to the saxophone body based on mass conservation and pressure continuity at the junction between the cylinder and the conical frustum. Kergomard et al. (2016) extended the cylindrical mouthpiece model by allowing a cross-section discontinuity. It is shown that the behavior of the cylindrical mouthpiece model, including the resulting mouthpiece internal pressure waveform and the inharmonicity of the complete instrument, highly depends on the mouthpiece length and diameter. While the cylindrical model with a short length resembles the lumped model, more and more higher frequency components are introduced as the mouthpiece becomes longer. The dependence of the acoustic behavior on the variable length of the cylindrical mouthpiece model might bring about uncertainties when used in a sound synthesis scheme. A cylinder-cone mouthpiece model was proposed by van Walstijn and Campbell (2003) for the clarinet. It approximates the mouthpiece as a cylindrical section followed by a conical section. However, the structure near the tip of a real mouthpiece is more like a cone and the remaining part of the mouthpiece is more cylindrical so that the neck of the saxophone can be easily attached. Considering the mouthpiece is a non-reciprocal acoustic unit, reversing the order of the cone and the cylinder can lead to a totally different behavior. A more precise model of the saxophone mouthpiece was proposed by Andrieux et al. (2014, 2016) using the finite element (FE) method. The FE model was validated by the measured mouthpiece input impedance and was coupled to a measured input impedance of the saxophone body to study the mouthpiece geometry’s influence on the instrument. To the authors’ knowledge, this is the only work that has considered a more accurate geometry of a mouthpiece. However, the FE model is time-consuming to develop and compute, making it inappropriate for sound synthesis and the analysis of transient behaviors.

To overcome the limitations of the above-mentioned models, the transfer matrix model (TMM) of the mouthpiece is derived from the FE mouthpiece model so that the acoustic properties contributed by the complex mouthpiece geometry are intrinsically retained. For this reason, TMM is more accurate than the cylindrical and lumped mouthpiece models, as

shown by comparing the measured input impedance of a system composed of a mouthpiece coupled to a truncated cone (the mouthpiece-cone system), with that calculated using different mouthpiece models. As well, TMM provides a compact mouthpiece representation that can be used for real-time sound synthesis. In this chapter, the sound of the saxophone with different mouthpiece models is synthesized using the framework proposed by Maestre and Scavone (2016), Maestre et al. (2018). The differences in the sound, as well as the dynamics, among different mouthpiece models, are explored and discussed.

Finally, the transmission line mouthpiece model is proposed, which provides a slightly less accurate but more flexible representation than TMM. It is applied in the construction of the mouthpiece design interface, which will be discussed in the Appendix C.

In this study, a custom-designed alto saxophone mouthpiece with a medium round chamber and a straight baffle is employed for acoustic measurement and various acoustic modeling.

## 6.2 Acoustic characterization of the mouthpiece

### 6.2.1 Definition of the Mouthpiece Input Impedance

The input impedance is one of the most widely applied concepts in wind instrument acoustic study. It is defined as the ratio of the frequency-domain pressure to the volume flow rate at the system input (Eq. 3.40). One of the most challenging aspects of using the input impedance to study the mouthpiece is properly locating the input. When taking the mouthpiece-pipe system as a linear acoustic resonator, the airflow serves as the input of the system. As discussed in Ch. 2, the pressure-driven flow that enters through the tip window and the side slits, as well as the reed-induced flow produced by the reed motion, all contribute to the airflow that enters the mouthpiece. This implies a distributed input to the mouthpiece, which requires to be localized to simplify the problem.

There exist two choices in the literature for localizing the input. Chen (2009) and Andrieux et al. (2014) defined the input right at the mouthpiece window as shown in Fig. 6.1(a), and the mouthpiece acoustic cavity is the same as the mouthpiece inner cavity ①. It is assumed that the pressure-driven flow and the reed-induced flow have mixed with each other and enter together into the mouthpiece through the window. The input impedance defined on the window implicitly assumes an evenly distributed pressure field despite the curvature of the surface. Furthermore, the input is typically defined at a circular sub-area on the win-

dow rather than the complete window to facilitate the input impedance measurement (Chen, 2009). Andrieux et al. (2016) defined a different input plane that sits at the mouthpiece tip window as shown in Fig. 6.1(b). Such a definition extends the acoustic cavity of the mouthpiece by including the wedge-shaped complement to fill the space between the reed and the mouthpiece window, and the mouthpiece acoustic cavity is composed of both the mouthpiece inner cavity ① and the wedge-shape complement ②. In addition, the curved tip contour is also replaced with a flat tip window, where the mouthpiece input is defined.

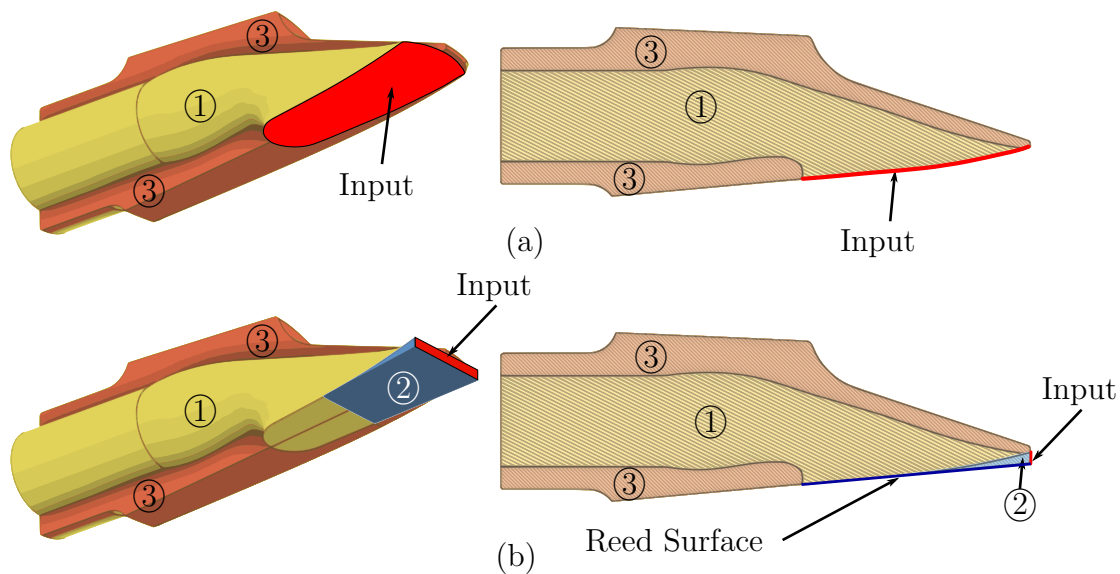


**Fig. 6.1:** The illustration of the mouthpiece input and acoustic cavity, where ①, ② and ③ represent the mouthpiece inner cavity, the wedge-shaped complement, and a half of the mouthpiece, respectively.

The second definition is employed in this chapter to build acoustic models because of the following two reasons. First, the input is defined on a flat surface where a planar wave can be assumed to make it easier to define the input impedance. In addition, defining the acoustic input at the tip window assumes a localized fluid-acoustic-structure interaction at the tip of the reed, which is consistent with the assumptions applied to the mathematical framework as discussed in Ch. 2.1.1, making it more straightforward to apply to sound synthesis.

In summary, the use of the second definition is based on the following assumptions. First of all, the acoustic system must be linear and passive. This is only true when the sound source of the saxophone is decoupled from the mouthpiece. Even though the reed is treated as part of the boundaries in the mouthpiece, its vibration is not. In this way, the

excitation and the nonlinearity of the system can be modeled separately, and the mouthpiece can be viewed as a linear and passive acoustic system. Second, the input is assumed to be localized at the tip window, and the acoustic cavity is completed by closing the side slits with hard walls and replacing the boundary confined by the vibrational reed with a solid wall corresponding to the equilibrium position of the reed. Another assumption is that only the propagating mode is considered on both the input and the output surfaces. At the input surface, this assumption is satisfied by assuming a plane wave sound source. On the output side, it is assumed that the discontinuity between the mouthpiece and the connected resonator is small enough that any excited evanescent modes decay sufficiently within the mouthpiece and do not interact with other discontinuities. Furthermore, it is also assumed that the discontinuities within the mouthpiece are sufficiently distant from the output plane.

### 6.2.2 Input Impedance Measurements

The acoustic impedance measurements were performed with a custom-built multi-microphone system (Lefebvre and Scavone, 2011) consisting of six microphones along a cylindrical pipe of 6.5 mm radius, providing a cutoff frequency slightly greater than 15 kHz. Three resonance-free calibration loads were used similar to the ones described by Dickens et al. (2007), including a quasi-infinite impedance, an almost purely resistive impedance and an unflanged pipe radiation load. For this work, the input impedances of an alto saxophone mouthpiece, a 40 cm-long truncated cone made of carbon fiber ( $3^\circ$  taper angle), and the combination of the mouthpiece and the truncated cone (the mouthpiece-cone system) were measured. To connect the mouthpiece to the impedance head, an adapted structure having the same inner geometry as the mouthpiece was designed and 3D-printed for the measurement. The surface of the reed and the side slits were closed by the walls in the adapter, with only a small rectangular tip window open to the impedance head.

When measuring the input impedance of the mouthpiece alone, the mouthpiece was closed by a 3D-printed block that shortened the mouthpiece inner length by 1 cm. For consistency, the truncated cone was inserted the same distance into the mouthpiece when measuring the mouthpiece-cone system.

The input impedances of the truncated cone, closed mouthpiece, and the mouthpiece-cone system are shown in Fig. 6.2. Compared to the truncated cone, the frequencies of the first few impedance peaks of the mouthpiece-cone system are lower because the mouthpiece lengthens

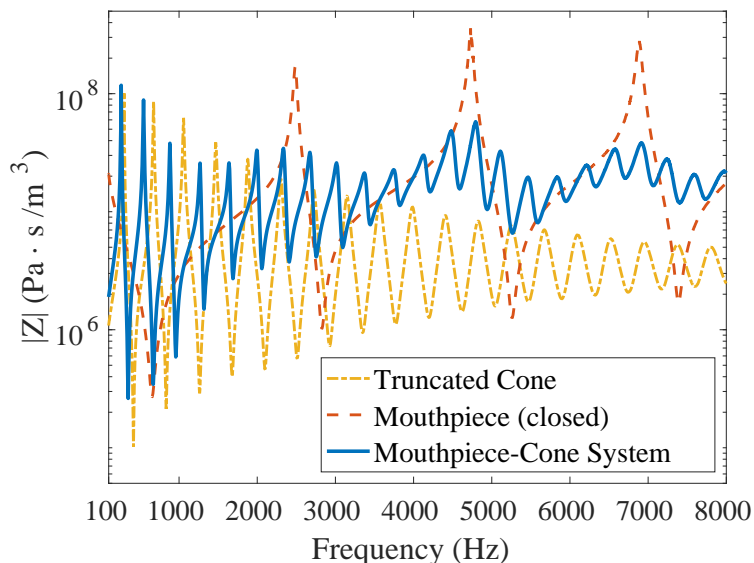


**Fig. 6.2:** The measured input impedances of the truncated cone, the closed mouthpiece, and the mouthpiece-cone system.

the instrument. The mouthpiece also modulates the input impedance of the resonator by amplifying it around the mouthpiece's resonance frequencies. This indicates a similar role as that played by a trumpet mouthpiece (Caussé et al., 1984), which helps explain the brightness contributed by the mouthpiece.

### 6.3 Finite element modeling of the mouthpiece

The mouthpiece cavity shown in Fig. 6.1(b) was imported into COMSOL Multiphysics<sup>®</sup> for the finite element simulation. A plane wave pressure source was set as the inlet boundary condition at the tip window of the mouthpiece and impedance boundary condition was applied to the rest of boundaries, which includes the viscothermal losses at the walls by an imposed acoustic admittance defined as (Chaigne and Kergomard, 2016)

$$Y_{\text{wall}} = \frac{1}{\rho c} \sqrt{jk} \left[ \sin^2 \theta \sqrt{l_v} + (\gamma - 1) \sqrt{l_t} \right], \quad (6.1)$$

with  $\rho$  the fluid density,  $c$  the speed of the sound,  $k$  the wavenumber,  $\theta$  the angle of the incidence of the wave,  $l_v = \mu/\rho c$  the vortical characteristic length,  $l_t = l_v/Pr$  the thermal characteristic length,  $\gamma$  the ratio of specific heats,  $\mu$  the fluid dynamic viscosity and  $Pr$  the

Prandtl number. The mesh of the FE model was constructed with a maximum element size of 6 mm, which allows the model to have at least 7-8 nodes per wavelength at 8 kHz.

### 6.3.1 Validation of the finite element model

The FE model of the mouthpiece was validated by comparing the simulated closed mouthpiece input impedance with the measured one, as shown in Fig. 6.3. A frequency-domain phase correction was applied to the measured data to compensate for sub-sample time delay discrepancies. Good agreement is achieved up to 15 kHz with maximum discrepancies of 1.8 dB in the magnitudes and 0.5% in the frequencies between the resonance peaks of the measured and simulated input impedances. There are relatively larger discrepancies around the anti-resonant frequencies than the resonant frequencies, which is mainly attributed to the discontinuity between the impedance head and the mouthpiece tip window, and might be potentially mitigated by taking into account the influence of higher-order modes using the multimodal method (van Walstijn et al., 2005). The onset of the higher order mode can be observed around 14 kHz in both the measured and FE-modeled input impedances. This corresponds to the cutoff frequency of the mouthpiece, above which non-planar modes are observed in the pressure iso-surface plot in COMSOL. It is worth noting that the cutoff frequency of the mouthpiece is larger than 12.7 kHz, the cutoff frequency of an ideal cylindrical pipe with a radius equal to that of the mouthpiece bore (the cylindrical part of the mouthpiece into which a resonator is inserted).

## 6.4 Transfer matrix modeling of the mouthpiece

The transfer matrix (TM) method has been widely applied to the study of the wind instrument resonator, including the effects of the tonehole (Keefe, 1990, Lefebvre, 2010) and the cutoff frequency (Petersen et al., 2019), to name a few. It is based on the acoustical two-port theory that assumes a linear acoustical system with two terminals (Pierce, 2019). The black-box region between terminals can be characterized by a  $2 \times 2$  matrix written as

$$\mathbf{T} = \begin{bmatrix} T_{11} & T_{12} \\ T_{21} & T_{22} \end{bmatrix}, \quad (6.2)$$

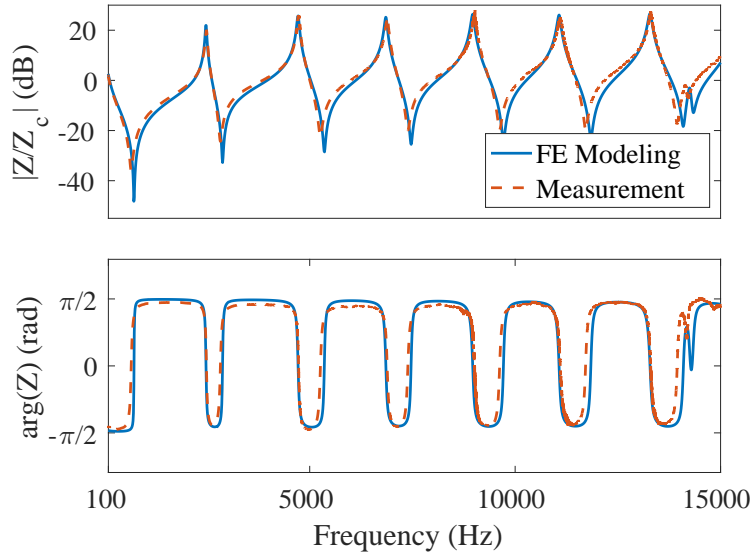


**Fig. 6.3:** The measured input impedance of the closed mouthpiece and that simulated using the FE model.

with all the matrix elements as functions of frequency. It defines the relationship of the acoustic pressure and volume velocity between the input and the output of the acoustic system:

$$\begin{bmatrix} P_o \\ Z_o^c U_o \end{bmatrix} = \mathbf{T} \begin{bmatrix} P_i \\ Z_i^c U_i \end{bmatrix}, \quad (6.3)$$

where  $Z_c = \rho c/S$  is the characteristic acoustic impedance and  $S$  the cross-section area. The subscripts  $i$  and  $o$  represent the input and the output side of the acoustic system, respectively.

To derive the transfer matrix of the mouthpiece, the two-load method was used by running the FE simulation twice with two different output boundary conditions (Lefebvre, 2010). With the simulated pressure and volume velocity at both the input and the output, the following linear equation system can be solved to obtain the four elements of the transfer matrix:

$$\begin{bmatrix} p_o^1 & Z_o^c U_o^1 & 0 & 0 \\ 0 & 0 & p_o^1 & Z_o^c U_o^1 \\ p_o^2 & Z_o^c U_o^2 & 0 & 0 \\ 0 & 0 & p_o^2 & Z_o^c U_o^2 \end{bmatrix} \begin{bmatrix} T_{11} \\ T_{12} \\ T_{21} \\ T_{22} \end{bmatrix} = \begin{bmatrix} p_i^1 \\ Z_i^c U_i^1 \\ p_i^2 \\ Z_i^c U_i^2 \end{bmatrix} \quad (6.4)$$

The superscripts 1 and 2 represent two different simulations with the loads set as a theoretical unflanged radiation impedance and the characteristic impedance, respectively.

The closed mouthpiece input impedance can be calculated as  $Z_{\text{closed}} = T_{11}/T_{21}$ , which agrees well with that calculated by the FE model as shown in Fig. 6.4. Comparing the input impedance calculated by TMM to that calculated by the FE model, the largest discrepancies in the resonance peak magnitudes and frequencies are 0.7 dB and 0.2%, respectively. Since the wall admittance is applied to the solid boundaries of the FE model, viscothermal losses are intrinsically included in the derived TMM. However, because TMM is derived from the FE simulation with specific temperature and corresponding physical variables, viscothermal losses are immutable once the transfer matrix is derived.

To enable the application of TMM to other studies, the transfer matrix is approximated with four 10th-order polynomials to fit all complex matrix elements  $T_{mn}$  up to 8 kHz<sup>1</sup>. The estimation errors, defined as  $E_{mn} = \|T_{mn} - T_{mn}^{\text{poly}}\|_2 / \|T_{mn}\|_2$ , for all elements are less than 0.5%, where  $T_{mn}^{\text{poly}}$  are approximated matrix elements. The polynomial approximation is available online.<sup>2</sup>

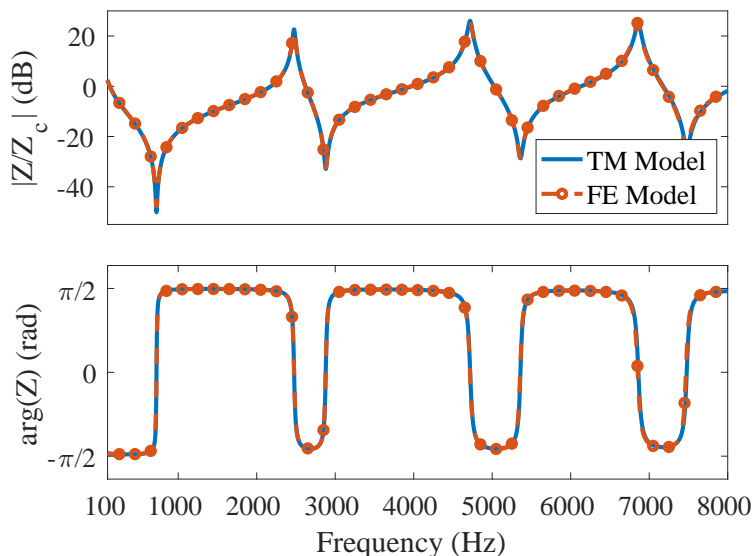


**Fig. 6.4:** The comparison of the modulus (top) and argument (bottom) of mouthpiece input impedances computed by the FE model and TMM.

<sup>1</sup>TMM derived from the FE model can reach to as high as the mouthpiece's cutoff frequency around 14 kHz, while only the part below 8 kHz was validated in this chapter.

<sup>2</sup><http://www.music.mcgill.ca/caml/doku.php?id=projects:adsm>

### 6.4.1 Validation of the transfer matrix model

The mouthpiece-cone system was used to validate TMM derived in Sec. 6.4. The measured input impedance of the conical frustum  $Z_{\text{cone}}$  was coupled to the transfer matrix (TM) mouthpiece as a load impedance. Since the diameter of the cone is different from that of the mouthpiece bore, there exists a discontinuity at the interface. Because the diameter difference is small, the influence of the non-propagating modes on the propagating mode is neglected and the acoustic impedances on the two sides of the junction are assumed equal to each other. However, the discontinuity, as illustrated in Fig. 6.5, should be carefully treated when using the normalized acoustic impedance  $\tilde{Z} = Z/Z_c$  in the calculations. The normalized impedance on the right of the junction is written as  $\tilde{Z}_2 = \tilde{Z}_1 S_2/S_1$ , where  $S_1$  and  $S_2$  are the cross-section areas on the left and right of the junction, respectively.

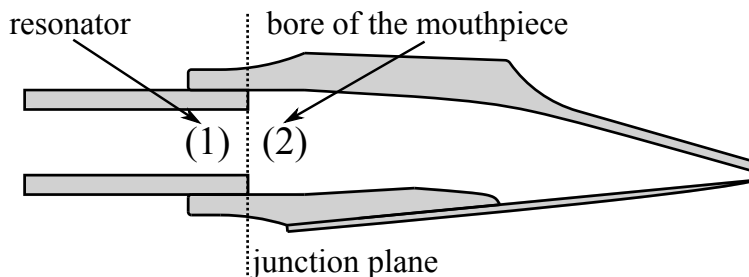


**Fig. 6.5:** An illustration of the junction between the mouthpiece and the resonator.

The input impedance of the mouthpiece-cone system can then be calculated with the following equation

$$\tilde{Z}_{\text{mc}} = \frac{T_{11} + T_{12}/\tilde{Z}_2}{T_{21} + T_{22}/\tilde{Z}_2}. \quad (6.5)$$

The comparison between the measured and calculated input impedances is shown in Fig. 6.6. The calculated input impedance generally matches the measured one, with the largest peak magnitude discrepancy of 1.8 dB and the largest peak frequency deviation less than 1%. As mentioned before, the discrepancies around the anti-resonances are relative larger, which is due to the measurement error caused by the discontinuity between the impedance head and the mouthpiece tip window.

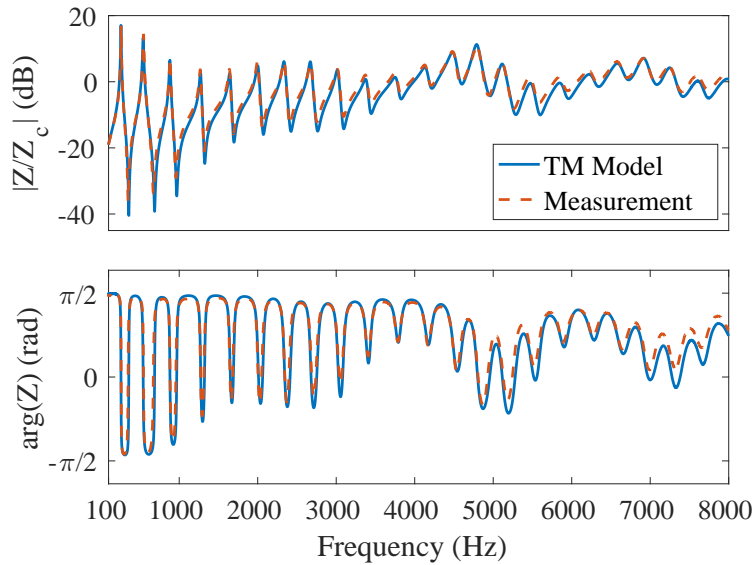


**Fig. 6.6:** The measured input impedance of the mouthpiece-cone system and that calculated with TMM using Eq. 6.5.

## 6.4.2 Acoustic comparison between different mouthpiece models

### 6.4.2.1 Mouthpiece coupled to a truncated cone

TMM can be compared to two previously reported mouthpiece representations, i.e., the cylindrical mouthpiece model and the lumped mouthpiece model. For each of the mouthpiece representations, the input impedance of a combined mouthpiece-cone system is calculated using the input impedance of the truncated cone measured in Sec. 6.2.2 as the load impedance.

The cylindrical mouthpiece model takes the mouthpiece as a pure cylinder that has the same volume  $V_m^{\text{eq}}$  as the missing part of the truncated cone. In this chapter, the cylindrical mouthpiece is modeled based on its TM representation (see Sec. 3.2.5), which is expressed as

$$\mathbf{T}_{\text{cyl}} = \begin{bmatrix} \cosh(\Gamma L) & Z_c \sinh(\Gamma L) \\ Z_c^{-1} \sinh(\Gamma L) & \cosh(\Gamma L) \end{bmatrix}, \quad (6.6)$$

where  $\Gamma$  depends on the acoustic constants of the air (Chaigne and Kergomard, 2016) and includes the wall losses due to viscothermal effects.

For consistency, the radius of the cylinder is chosen to be equal to that of the mouthpiece bore  $S_2$  so that the length of the mouthpiece  $L = V_m^{\text{eq}}/S_2$  is fixed. The input impedance of

the mouthpiece-cone system  $\tilde{Z}_{\text{mc}}$  is calculated using Eq. 6.5 by substituting  $\mathbf{T}$  with  $\mathbf{T}_{\text{cyl}}$ .

The lumped mouthpiece model approximates the mouthpiece as an acoustic compliance  $C_m = V_m^{\text{eq}}/(\rho c^2)$  in parallel with the impedance of the resonator. This lumped representation is often sufficient for low frequencies, where the wavelength is large compared to the characteristic length of the mouthpiece. Taking the same load impedance  $Z_2$  used with the other mouthpiece models, the input impedance of the mouthpiece-cone system with a lumped mouthpiece is calculated as

$$Z_{\text{mc}}^{\text{lumped}} = \frac{1}{\frac{1}{Z_2} + j\omega C_m}. \quad (6.7)$$

The input impedances of mouthpiece-cone systems with different mouthpiece models are compared with the measurement in Fig. 6.7. The calculations with TMM result in the best match to the measured input impedance compared to the other two mouthpiece representations. Because all three mouthpiece models have the same mouthpiece volume, they have a similar behavior at low frequencies where the lumped model assumption is valid. However, the performance of the lumped mouthpiece degrades quickly as it shunts high-frequency components. The high-frequency characteristics of the cylindrical mouthpiece model show significant discrepancies from the measured and TMM responses because of the oversimplified geometric approximation. Derived from the FE model, the TM mouthpiece intrinsically contains the complex geometry information of the mouthpiece, which provides advantages in preserving the high-frequency structure over the other models.

#### 6.4.2.2 Mouthpiece coupled to an alto saxophone

Previous input impedance ( $Z(\omega) = P(\omega)/U(\omega)$ ) and radiation transfer function ( $E(\omega) = P_{\text{rad}}(\omega)/U(\omega)$ ) measurements of an alto saxophone (without mouthpiece) made by Maestre et al. (2018) were used to investigate the coupling of the different mouthpiece models with an alto saxophone.  $P(\omega)$  and  $P_{\text{rad}}(\omega)$  are the frequency-domain mouthpiece pressure and radiated pressure, respectively, and  $U(\omega)$  is the volume flow rate at the entrance of the resonator in the frequency domain. As with the mouthpiece-cone system, coupled responses were obtained with the measurements as load impedances. In the junction between the bore of the mouthpiece and the neck of the saxophone, there is a discontinuity that was accounted for by multiplying the measured saxophone body input impedance by the cross-section area

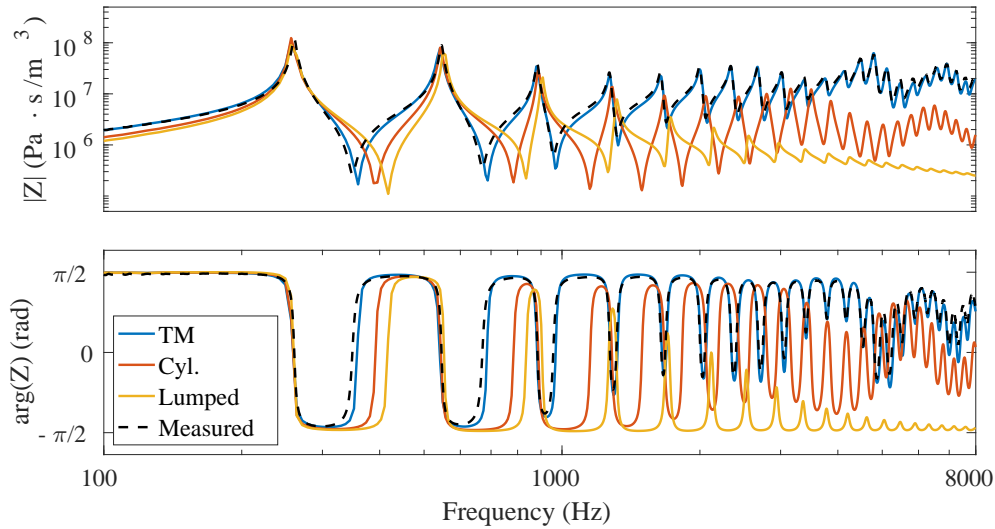


**Fig. 6.7:** The measured input impedance of the mouthpiece-cone system and that calculated using TMM, cylindrical mouthpiece model (Cyl.) and the lumped mouthpiece model (Lumped).

ratio  $S_2/S_1$ , so that we were able to obtain the impedance on the mouthpiece side of the junction  $\tilde{Z}_2 = \tilde{Z}_1 S_2/S_1$ . Similarly, the radiation transfer function was also multiplied by the same factor so that  $\tilde{E}_2 = \tilde{E}_1 S_2/S_1$ . Input impedances of the entire instrument can be calculated using either Eq. 6.5 for the TM mouthpiece and cylindrical mouthpiece, or Eq. 6.7 for the lumped mouthpiece. For the cylindrical mouthpiece and the TM mouthpiece, the radiation transfer function can be derived as follows using the transfer matrix elements:

$$\tilde{E}_{\text{sax}} = \frac{\tilde{E}_2}{T_{21}\tilde{Z}_2 + T_{22}}, \quad (6.8)$$

For the lumped mouthpiece, the radiation transfer function is calculated as

$$\tilde{E}_{\text{sax}}^{\text{lumped}} = \frac{\tilde{E}_2 \tilde{Z}_{\text{sax}}^{\text{lumped}}}{\tilde{Z}_2}. \quad (6.9)$$

As an example, the input impedances and the radiation transfer functions with and without the TM mouthpiece are shown in Fig. 6.8 for the note B<sup>b</sup>4 (written).

The mouthpiece helps tune the fundamental frequency and the harmonics by completing the truncated cone of the saxophone body. To compare the influence of the different mouth-

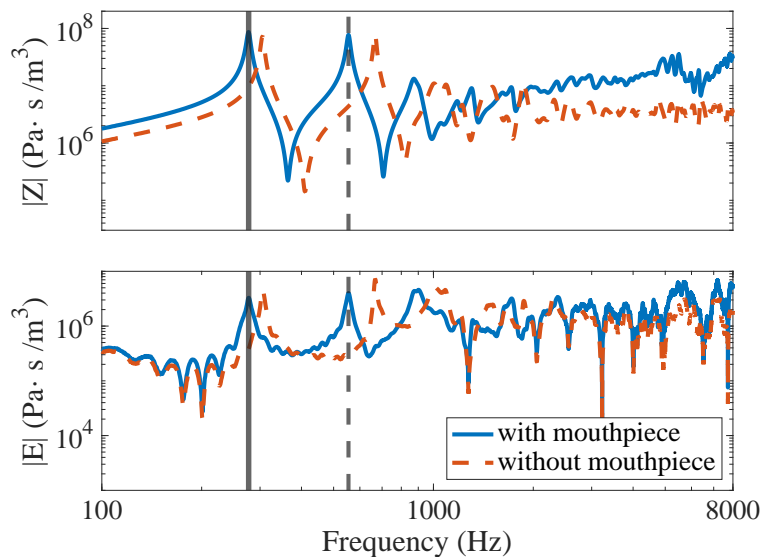


**Fig. 6.8:** Comparisons of the input impedance and radiation transfer function with (solid lines) and without (dashed lines) the TM mouthpiece for the note  $B^b_4$  (written). The vertical solid and dashed lines correspond to the equal-tempered scale frequencies of the first and second harmonics of the note, respectively. The input impedance and radiation transfer function with the TM mouthpiece are calculated using Eqs. 6.5 and 6.8, respectively.

piece representations on the alignment of the impedance peaks across the entire playing range, each mouthpiece model was tuned separately when coupled with the measurement for the  $F_4$  (written) fingering by adjusting the mouthpiece volume to align the first input impedance peak to the corresponding equal-tempered scale frequency.

As shown in Fig. 6.9, the deviation (in cents) between the frequency of the first or second peak of the input impedance and the equal-tempered scale frequency of each note are compared among different fingerings with and without different mouthpiece models. Comparisons are made to the first input impedance peak for first register notes (below  $D_5$ ) and to the second peak for the remaining (second register) notes. For the body of the saxophone alone (without mouthpiece), the deviation is large and generally increases with the fundamental frequency within each register. All the mouthpiece models help reduce such a deviation, though the tuning performance varies from note to note. The TM mouthpiece performs similarly to the other two mouthpiece models in the first register, while it shows the least deviation in the second register.

Following the definition of the inharmonicity parameter used by Gilbert et al. (2019),

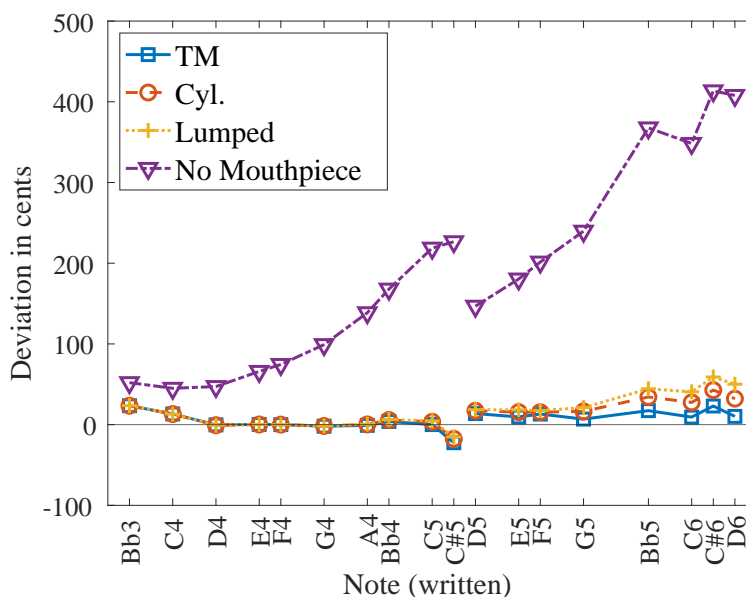


**Fig. 6.9:** The deviation in cents between the first or second input impedance peak and the equal-tempered scale frequency of different notes.

the inharmonicity for the notes of the first register was characterized as  $I = (f_2 - 2f_1)/2f_1$ , where  $f_1$  and  $f_2$  are the two lowest resonance frequencies of the input impedance. The comparison of the inharmonicities between the saxophone with different mouthpiece models is displayed in Fig. 6.10, showing that the input impedance peaks of the saxophone with the TM mouthpiece are more harmonically aligned than the others.

More comparisons between the saxophones with different mouthpiece models for the note B<sup>b</sup>4 (written) are shown in Fig. 6.11, including the input impedance, normalized input impedance, reflection function, and the radiation transfer function. All mouthpieces have the same volume in this comparison, and as expected, they have similar behavior in the lower-frequency range. The magnitude and the frequency of the first peak match each other very well, while the difference between the second peak is more significant. Comparing the normalized input impedances, magnitude differences are readily apparent. This is because the impedance is normalized by values of  $Z_c$  that are calculated with different cross-section areas for different mouthpiece models. For the cylindrical and lumped mouthpieces, the mouthpiece bore cross-section area is used (see Fig. 6.5). However, the TM mouthpiece results are normalized by the cross-section area at the mouthpiece tip, which is much smaller than the bore area. At higher frequencies, the input impedance magnitudes of the TM

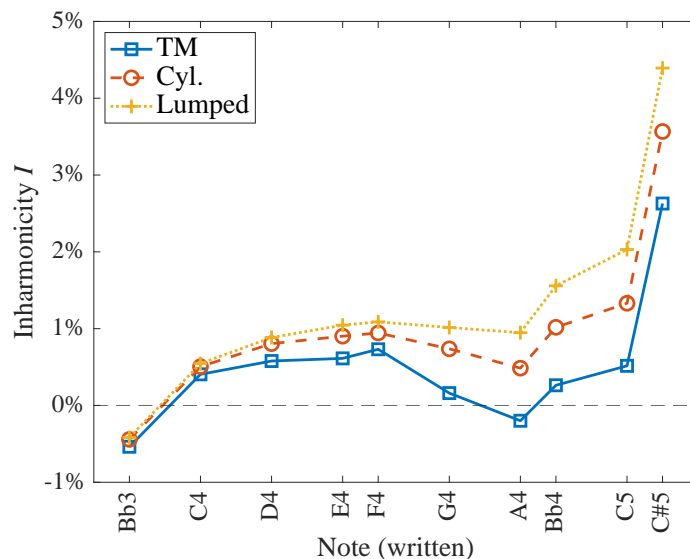


**Fig. 6.10:** Input impedance peak inharmonicities for the different mouthpiece representations.

mouthpiece and the cylindrical mouthpiece converge toward the specific impedance (or a normalized value of one). However, due to the increase of the acoustic admittance used in the lumped model, the input impedance magnitude continues to decrease, which causes the reflection function to approach one as the frequency increases. Such a behavior can be especially problematic in the context of sound synthesis, as mentioned by Kergomard et al. (2016), so a preprocessing must be applied to force the reflection function towards zero, as discussed in the following section.

The differences in the magnitude level of the normalized input impedance also leads to differences in the magnitudes of the reflection function  $R = (\tilde{Z} - 1)/(\tilde{Z} + 1)$ . As can be seen from its definition, the magnitude of the reflection function will have minima around frequencies where  $\tilde{Z} \approx 1$ . Because the input impedance magnitude of the TM mouthpiece system is generally lower than that of the other two mouthpiece models and the magnitudes of the first two peaks are just above one, the  $|R|$ -plot of the TM mouthpiece has extra dips around 2000 - 4000 Hz and their positions do not correspond with those of the other two models.

Finally, the comparison of the radiation transfer function shows that all three different mouthpiece models have a similar behavior at the low-frequencies and the high-frequency characteristics of TM mouthpiece are more significant compared to those of the other mouth-

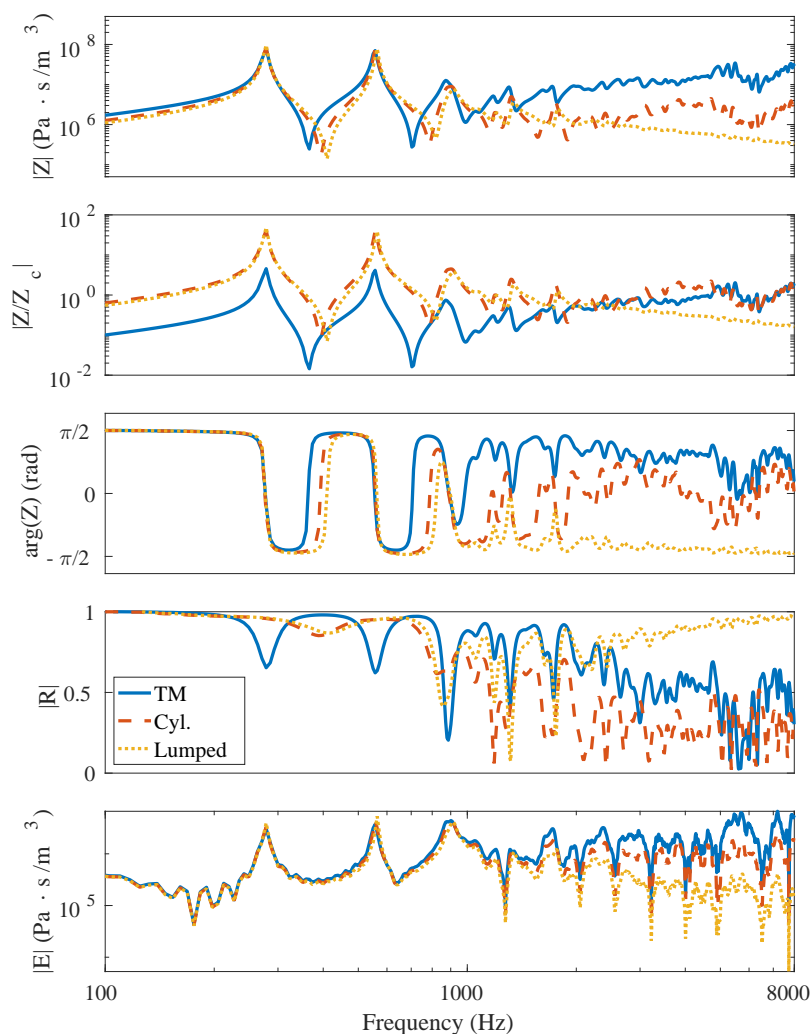


**Fig. 6.11:** Comparisons (from top to bottom) of the modulus of the physical input impedances, the modulus of the normalized input impedances, the argument of the normalized input impedances, the reflection functions, and the radiation transfer functions between the TM mouthpiece (solid lines), cylindrical mouthpiece (dashed lines) and the lumped mouthpiece (dotted lines) coupled with the measured impedance of the alto saxophone resonator for the note B<sup>b</sup>4 (written).

piece models. This is consistent with the discussion about the input impedance comparison.

### 6.4.3 Sound and dynamics comparison between different mouthpiece models

This section describes the synthesis of alto saxophone sounds using different mouthpiece models and measured saxophone impedances in order to analyze the influence of differ-

ent mouthpiece models on the nonlinear dynamics and properties of the rendered sound. Based on the work by Maestre et al. (2018), the saxophone was represented by the classic three-equation single-reed instrument model (Chaigne and Kergomard, 2016), which was discretized based on a combination of three different schemes (Guillemain et al., 2005, Maestre and Scavone, 2016, Scavone and Smith, 2006). As previously described, the different mouthpiece models were coupled to measured input impedance and radiation transfer functions of an alto saxophone. From this frequency-domain data, we fit recursive parallel filters that jointly represented the mouthpiece and the resonator as an efficient digital filter that was used for audio synthesis for a subsequent analysis of dynamics and sound properties. The results of the note B<sup>b</sup>4 (written) were taken as an example to quantitatively compare the performances of different mouthpiece models with the discussion of possible explanations for their differences in sound characteristics and dynamics behavior.

#### 6.4.3.1 The synthesis model

The standard three-equation single-reed instrument model comprises three unknowns: the mouthpiece pressure  $p$ , the volume velocity  $u$  and the reed tip displacement  $y$  away from the equilibrium position. Dimensionless variables are used in the governing equations as

$$\tilde{p} = \frac{p}{p_M}, \quad \tilde{u} = Z_c \frac{u}{p_M}, \quad \tilde{y} = \frac{y}{H}, \quad (6.10)$$

where  $p_M$  is the mouth pressure at which the reed channel is closed,  $Z_c$  is the characteristic impedance at the input of the resonator, and  $H$  is the distance at equilibrium from the tip of the reed to the lay of the mouthpiece. For the sake of simplicity, all the tildes are subsequently omitted.

The pressure-controlled reed is modeled by a single-degree-of-freedom damped oscillator that is governed by the following equation:

$$\frac{1}{\omega_r^2} \frac{d^2 y}{dt^2} + \frac{q_r}{\omega_r} \frac{dy}{dt} + y = -\Delta p, \quad (6.11)$$

where  $\omega_r = 2\pi f_r$  with  $f_r$  being the reed resonance frequency, and  $q_r$  is the reed damping coefficient. The variable  $\Delta p = \gamma - p$  is the pressure difference between the mouth pressure  $\gamma$  and the pressure in the mouthpiece  $p$ .

The linear resonator, composed of the mouthpiece and the saxophone, is modeled based

on the input impedance of the entire system,

$$Z(\omega) = \frac{P(\omega)}{U(\omega)}. \quad (6.12)$$

The nonlinearity of the saxophone is governed by the Bernoulli flow equation:

$$u = \begin{cases} \zeta(1+y)\text{sign}(\gamma-p)\sqrt{|\gamma-p|}, & 1+y \geq 0, \\ 0, & 1+y < 0, \end{cases} \quad (6.13)$$

where  $\zeta = Z_c w H \sqrt{2/(\rho p_M)}$ , with  $w$  the reed channel width.

Equations 6.11, 6.12 and 6.13 compose the governing equations of the saxophone model, which need to be discretized for the time-domain sound synthesis.

The discretization of the reed model is performed by way of the bilinear transform (Scavone and Smith, 2006), leading to

$$\frac{Y(z)}{\Delta P(z)} = \frac{-4\omega_r^2 z^{-1}}{a_0 + 2(\omega_r^2 - \alpha^2)z^{-1} + (\alpha^2 - g_r \alpha + \omega_r^2)z^{-2}}, \quad (6.14)$$

where  $g_r = q_r/\omega_r$ ,  $a_0 = \alpha^2 + g_r \alpha + \omega_r^2$  and  $\alpha = \omega_r/\tan(\omega_r/2f_s)$  is the bilinear transform constant that controls the frequency warping and is defined to match the reed resonance frequency between the continuous and discrete domains.

The input impedance  $Z(\omega)$  is modeled as a recursive parallel filter (Maestre and Scavone, 2016, Maestre et al., 2017) as discussed in Sec. 5.3. It ultimately gives a time-domain expression in Eq. 5.52, which is rewritten here:

$$p[n] = B_0 u[n] + q[n], \quad (6.15)$$

where  $p[n]$  and  $u[n]$  represent the discrete-time pressure and volume flow rate, respectively, and  $q[n]$  only depends on the history of  $u[n]$ , i.e., on  $u[n-k]$  with  $k \geq 1$ .

By substituting Eq. 6.15 into the discrete version of Eq. 6.13, the volume flow rate  $u[n]$  can be solved explicitly as (Guillemain et al., 2005)

$$u[n] = \begin{cases} \frac{1}{2}\text{sign}(\gamma - q[n])(-B_0 w[n]^2 + w[n]\sqrt{(B_0 w[n])^2 + 4|\gamma - q[n]|}) & 1+y[n] \geq 0, \\ 0, & 1+y[n] < 0, \end{cases} \quad (6.16)$$

where  $w[n] = \zeta(1 + y[n])$ . Afterward,  $p[n]$  can be updated using Eq. 6.15.

To obtain the radiated sound, we employed again the scheme proposed by Maestre et al. (2018), which jointly approximates the input impedance  $Z(\omega)$  and the radiation transfer function  $E(\omega)$  as a single set of recursive digital filters in parallel form. As in the case of the impedance, this leads to a time-domain expression for the radiated sound pressure as

$$p_{\text{rad}}[n] = D_0 u[n] + g[n]. \quad (6.17)$$

where  $D_0$  is constant and  $g[n]$  only depends on  $u[n - k]$ , with  $k \geq 1$ .

Thus, to summarize, the acoustic pressure  $p[n]$ , flow rate  $u[n]$ , and the radiated sound pressure  $p_{\text{rad}}[n]$  were computed as follows:

1. update the reed position  $y[n]$  use Eq. 6.14.
2. update  $q[n]$  and  $g[n]$  in Eq. 6.15 and Eq. 6.17, correspondingly, based on previous samples of the flow rate  $u[n - k]$  with  $k \geq 1$ .
3. explicitly solve the flow rate in the mouthpiece  $u[n]$  using Eq. 6.16.
4. calculate the mouthpiece pressure  $p[n]$  and the radiated pressure  $p_{\text{rad}}[n]$  using Eq. 6.15 and Eq. 6.17, respectively.
5. go back to the step 1.

The number of parallel sections  $N$  depends on the fingerings and the mouthpiece models, and was manually selected. A higher-note fingering normally has a smaller  $N$  than that of a lower-note fingering for it involves less prominent modes. For a resonator with  $N = 32$  parallel sections and a sampling frequency of 48 kHz, this model ran at a speed more than 30 times faster than real-time on one logical core of a laptop computer.

#### 6.4.3.2 Fitting of the input impedance and the radiation transfer function

To design the digital filters corresponding to the impedance model and the radiation model, we employed the nonlinear optimization described by Maestre et al. (2018). The sound synthesis model was designed to run at a standard audio sample rate of 48 kHz. Some preprocessings was performed before fitting the digital filter coefficients. For the cases of TM mouthpiece and cylindrical mouthpiece representations, the target normalized input impedance magnitude above 8 kHz was set to one, with a cross-fade region from 7 to 8 kHz. This assumes that no sound is reflected from the end of the instrument above 8 kHz. For the lumped mouthpiece representation, the target normalized input impedance magnitude

was cross-faded to one in the region from 2 to 3 kHz, for reasons noted in Sec. 6.4.2. For all three mouthpiece models, the magnitude of the radiation transfer function was set to -40 dB above 8 kHz, as this response exhibited some noise at higher frequencies due to limitations of the measurement space.

The fittings of the input impedance and the radiation transfer function are shown in Fig. 6.12. For the lumped mouthpiece model,  $N = 14$  parallel sections were used, while  $N = 32$  for the cylindrical and TMMs.

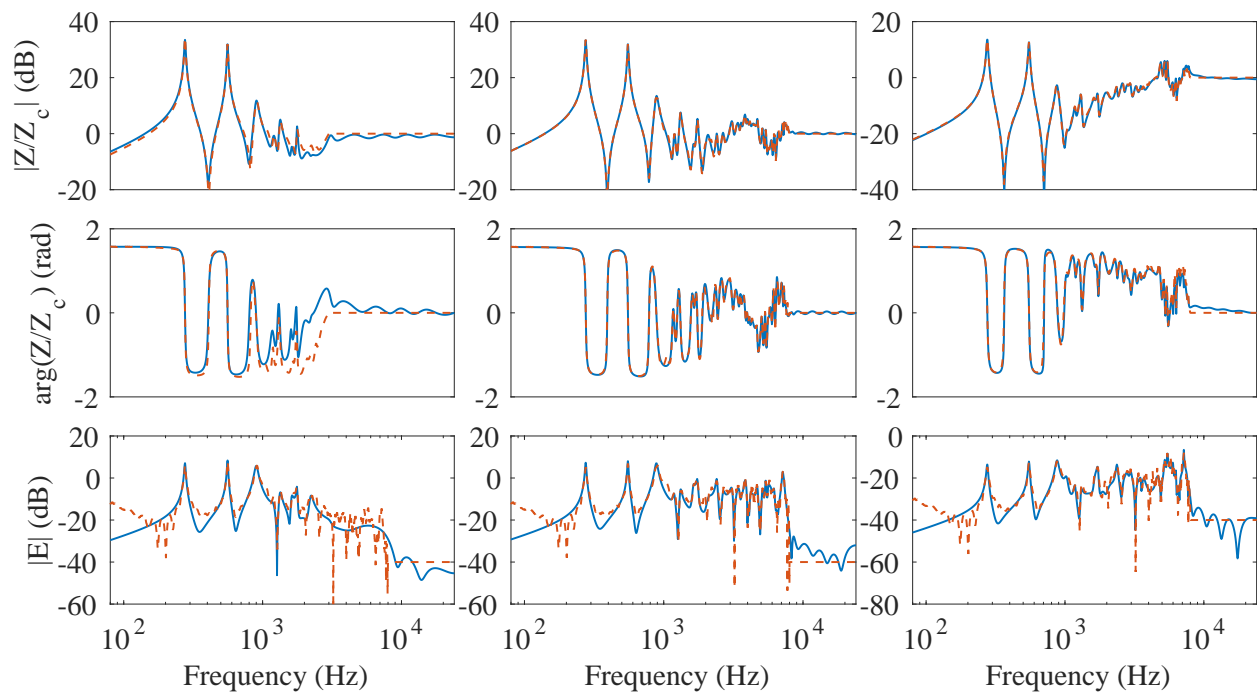


**Fig. 6.12:** The fitting of the modulus (top) and argument (middle) of the impedance and the radiation transfer function (bottom) of the lumped mouthpiece (left), cylindrical mouthpiece (center), and TM mouthpiece (right). In each plot, dashed lines (red) and solid lines (blue) are used to represent the original data and the model, respectively.

### 6.4.3.3 Analysis of nonlinear dynamics and sound properties

The sound of the saxophone was synthesized at the sampling frequency 48 kHz for the note B<sup>b</sup>4 with different mouthpiece models. The resonance frequency of the reed was  $f_r = 1500$  Hz, the damping factor was  $q_r = 1.5$ , the stiffness of the reed was  $k_r = 8 \times 10^6$  Pa/m, the density was  $\rho = 1.18$  kg/m<sup>3</sup> and the speed of sound was defined as 347.23 m/s. The width of

the mouthpiece tip window was  $w = 12$  mm and the equilibrium height of the reed channel was  $H_0 = 0.8$  mm. The reed parameters were initially chosen based on values provided in the literature (Colinot et al., 2020, Petersen et al., 2019), though they were subsequently modified so that the synthesized sounds of different mouthpiece models were in the same regimes. These values correspond to values of  $\zeta = 0.3$  in Eq. 6.13 for the lumped and cylindrical mouthpiece models, falls into the typical range  $\zeta \in [0.1, 1]$  (Kergomard et al., 2016).

The synthesis was performed using a linearly varying mouth pressure with a fixed slope  $k = 0.01$ . The normalized mouth pressure  $\gamma$  either increased from 0 to 3, or decreased from 1.2 to 0. The comparisons of the bifurcation diagrams, fundamental frequencies and spectral centroids exhibited by different mouthpiece models are shown in Fig. 6.13 for the increasing and decreasing mouth pressure profiles.

Unlike the traditional bifurcation diagram generated by solving a non-linear system theoretically (Dalmont et al., 2000) or numerically (Colinot et al., 2020), the one shown at the top of Fig. 6.13 was obtained by extracting the envelope of the synthesized mouthpiece pressure  $p$ , as has been used by Colinot et al. (2019). Though it cannot show all bifurcation branches nor types, this diagram presents the stable solutions from which it is possible to identify the different dynamics thresholds, including the oscillation threshold, extinction threshold, inverse oscillation threshold and the inverse extinction threshold, and compare them between different mouthpiece models. In addition, one may notice the sudden jump taking place in the bifurcation diagram along the lower envelope around  $\gamma = 1.5$ , which corresponds to the point that the oscillation changes from the Helmholtz motion to the inverted Helmholtz motion, as discussed by Dalmont (2007). While the overall characteristics remain similar, the main differences between mouthpiece models revolve around the extinction threshold identified in the bifurcation diagram. The thresholds where the regime changes from Helmholtz motion to inverted Helmholtz motion also vary among different mouthpiece models. The difference in thresholds is partially explained by the inharmonicity difference as shown in Fig. 6.10. However, though inharmonicity of impedance peaks has been shown to influence dynamics (Dalmont et al., 1995, Doc and Vergez, 2015, Gilbert et al., 2019), its impact on different oscillation thresholds is still unclear.

The playing frequency  $f_p$  was also compared based on its deviation from the frequency

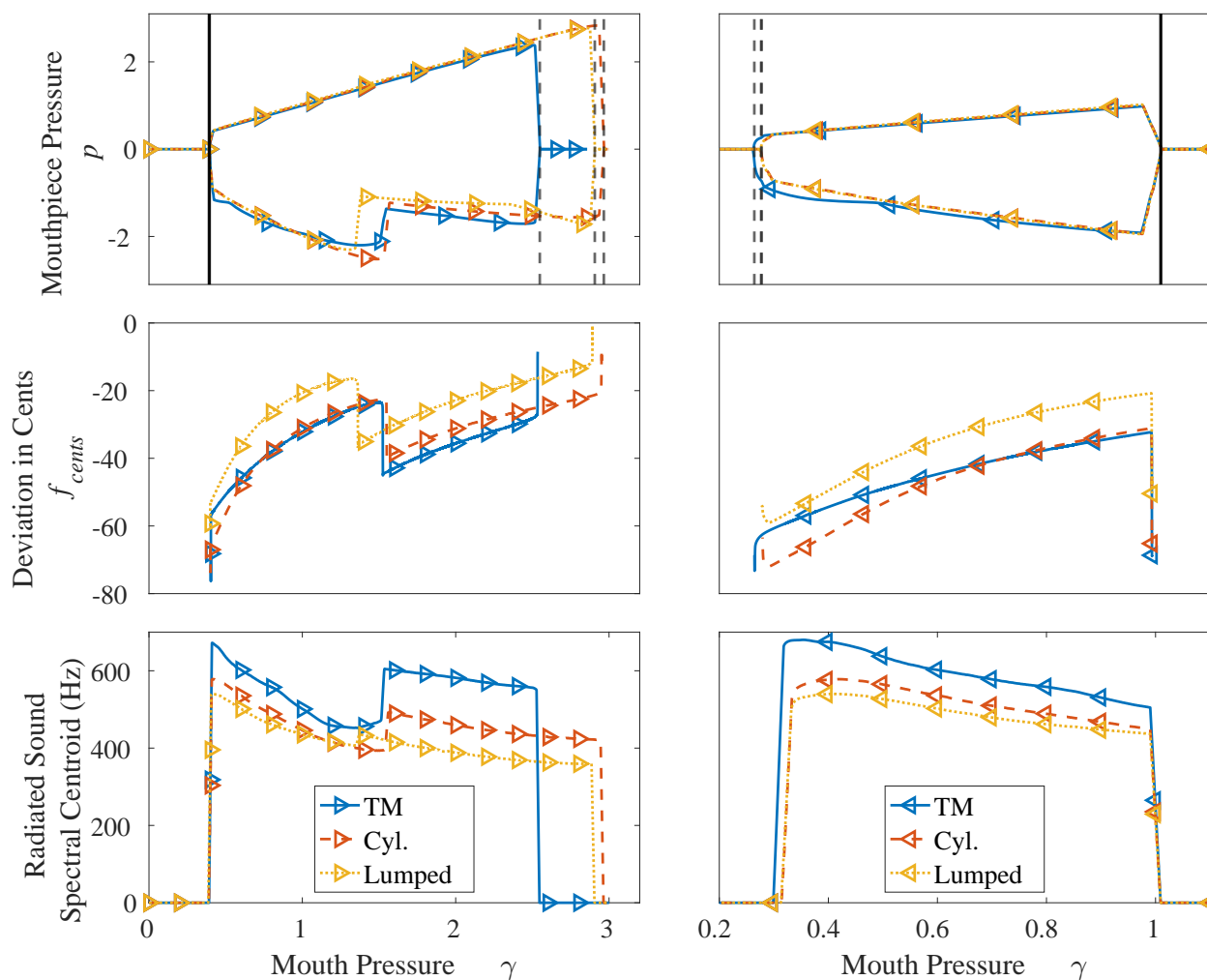


**Fig. 6.13:** Comparisons of the bifurcation diagrams (top), playing frequencies (middle) and radiated sound spectral centroid (bottom) for increasing (left) and decreasing (right) mouth pressure profiles. The (inverse) oscillation thresholds and (inverse) extinction thresholds are shown in the bifurcation diagrams as vertical solid and dashed lines, correspondingly.

of the first peak of the input impedance  $f_1$

$$f_{cents} = 1200 \log_2 \left( \frac{f_p}{f_1} \right), \quad (6.18)$$

and the difference can be as large as 15 cents between mouthpiece models. Such differences are partially contributed by the inharmonicity among different mouthpiece models as discussed in Section 6.4.2.2 (Coyle et al., 2015, Dalmont et al., 1995, Gilbert et al., 2019).

The spectral centroids of the radiated sound were compared as well. As shown at the bottom of Fig. 6.13, the TM mouthpiece has the highest spectral centroid, mainly due to its more accurate representation of higher-frequency characteristics as indicated in the input impedance and the radiation transfer function.

The waveforms of the pressure inside the mouthpiece of two different regimes are shown in Fig. 6.14. The mouthpiece pressure waveforms for the three different models are generally similar to each other, though the TM mouthpiece result displays the largest fluctuation, especially when the reed is closed (around the valleys of the pressure waveform). This can be traced to the discontinuity in the flow model as the reed channel starts to close and the fact that TMM reflects more high-frequency components.

When  $\gamma = 2$ , the saxophone is oscillating under the inverted Helmholtz motion. It is interesting to see that the cylindrical mouthpiece has a more similar waveform to the TM mouthpiece than to the lumped mouthpiece model. This could indicate that under the inverted Helmholtz motion, where the closing phase of the reed channel is longer than the opening phase, the inertance of the mouthpiece plays an important role in determining the waveform. However, such an assumption needs to be further tested before a conclusion can be drawn.

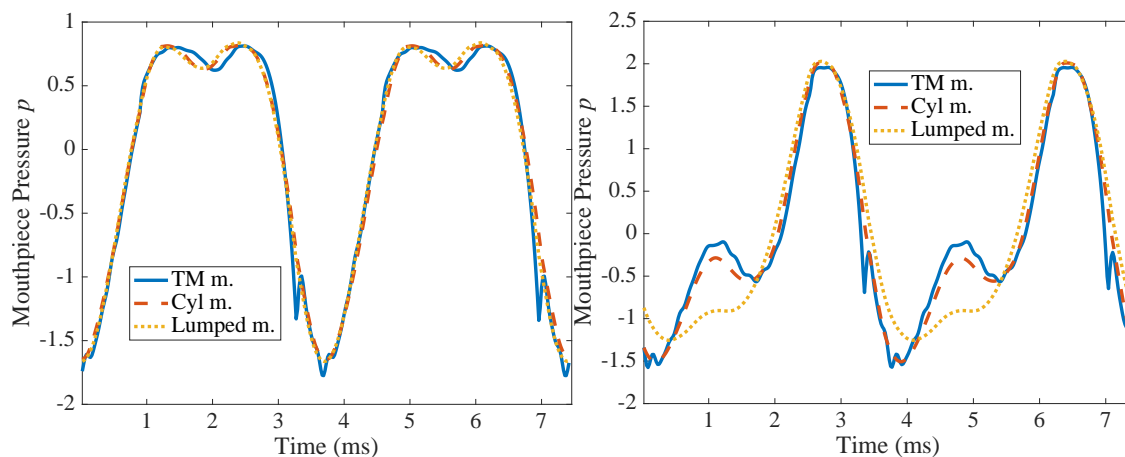


**Fig. 6.14:** The comparison of the waveforms among three mouthpiece models when a)  $\gamma = 0.8$  and b)  $\gamma = 2$ .

Finally, the so-called bifurcation delay was quantitatively compared among different mouthpiece models. The bifurcation delay was first proposed in the context of the clarinet by Bergeot et al. (2014), which is defined by the difference between the theoretical

oscillation threshold and the dynamic threshold simulated under dynamic conditions (as in our experiments). In practice, the bifurcation delay is calculated as  $BD = P_{\text{mdt}} - P_{\text{mst}}$ .  $P_{\text{mst}}$  is the minimum value of a static blowing pressure above which an instability can emerge. The  $P_{\text{mdt}}$  is the dynamic oscillation threshold where the periodic oscillation occurs when the mouth pressure increases. However, the theoretical oscillation threshold is nearly impossible to estimate for a real instrument. As shown in the results by Bergeot et al. (2014), decreasing the mouth pressure changing rate  $k$  will make the measured inverse extinction threshold closer to the theoretical static oscillation threshold. Based on this,  $P_{\text{mst}}$  was set to the inverse extinction threshold with the smallest pressure change rate of  $k = 0.01$ . The comparison of  $BD$  and its changes with  $k$  are displayed in Fig. 6.15. For a better sense of the difference, the pressure is shown in Pascals rather than dimensionless pressure in this figure.

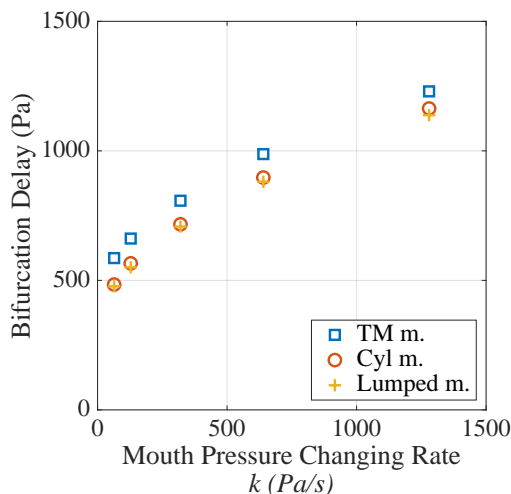


**Fig. 6.15:** The comparison of the bifurcation delays with different mouth pressure changing rate  $k$ .

## 6.5 Transmission line modeling of the mouthpiece

The transmission line mouthpiece model (TLM) is proposed in this section. The model represents the mouthpiece as a series of cascaded acoustic cylinders of varying cross-section area, each modeled with a transmission line matrix. The one-dimensional cross-section area function is created by slicing the 3D mouthpiece acoustic cavity along a longitudinal path

from the tip of the mouthpiece to the end of the bore. There are two possible ways of defining the guiding path as shown in Fig. 6.16. The first path follows a longitudinal straight line perpendicular to the mouthpiece tip window (TLM-Perp), while the second path follows the center line of the acoustic cavity of the mouthpiece (TLM-CL). Fig. 6.17 illustrates a comparison of the two area functions by slicing the mouthpiece into 80 segments, indicating a minor difference between the two slicing methods.

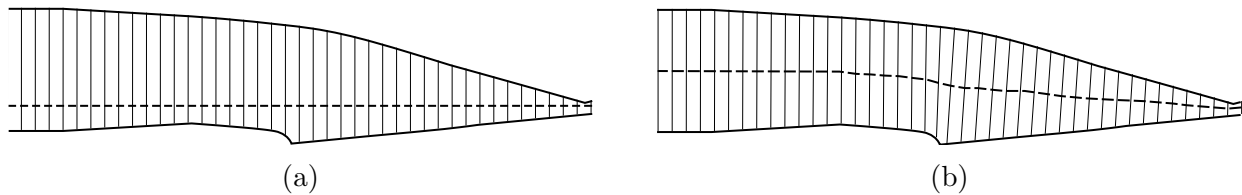


**Fig. 6.16:** The illustration of the mouthpiece slices (vertical thin solid lines) following (a) the path (horizontal dashed lines) perpendicular to the tip window and (b) the path through the center line of the mouthpiece acoustic cavity.

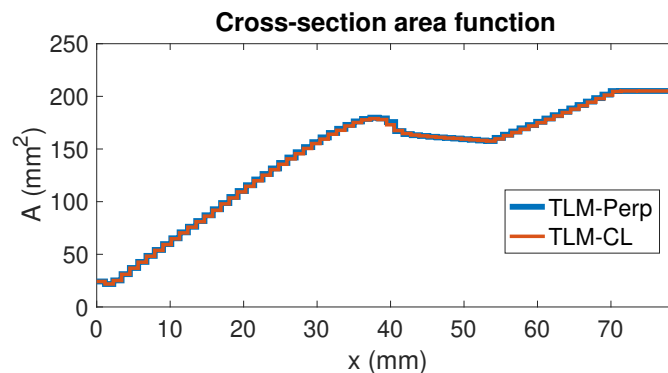


**Fig. 6.17:** The area functions built based on two different paths.

In Fig. 6.18, the input impedances of the closed mouthpiece calculated by two different TLMs are compared with that calculated with the finite element method (FEM) in Ch. 6.3. Both TLMs perform well at low frequencies where the acoustic capacitance plays a more important role. However, the discrepancies increase with frequency, which could be attributed mainly to the geometry simplification when converting the 3D acoustic cavity into a 1D area function, particularly in the front part from of the mouthpiece from the tip to the throat where the cross-section resembles more of a rectangular pipe. Representing this front part of the mouthpiece with cylindrical segments results in underestimated damping, which ex-

plains the overestimated resonance amplitude in the TLM results. TLM-CL is shown to have slightly lower resonant frequencies than TLM-Perp. This is due to the fact that the center line guiding path is slightly longer than the straight guiding path of TLM-Perp, resulting in a larger overall length, and lower resonant frequencies for TLM-CL.

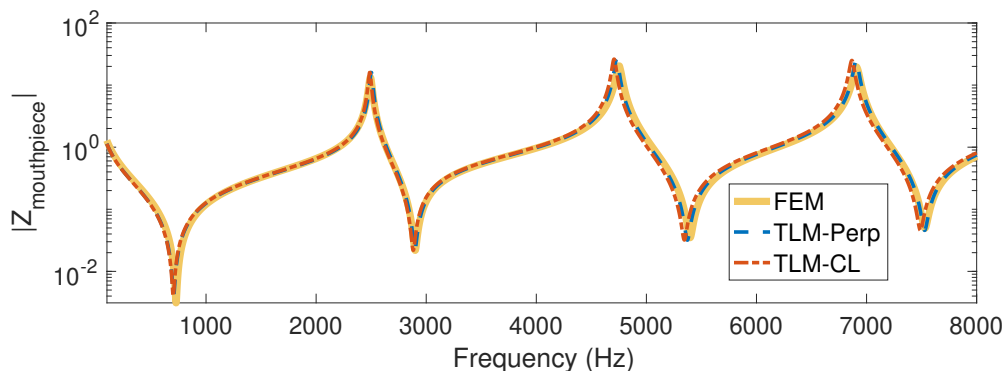


**Fig. 6.18:** The input impedance of a closed mouthpiece calculated by TLMs and FEM.

The simulated input impedance of the saxophone (connecting the saxophone body to the mouthpiece) by TLMs and TMM are shown in Fig. 6.19. The input impedances calculated with TLMs agree well with that calculated by TMM in general, and the discrepancy is relatively larger around the resonances and anti-resonances of the closed mouthpiece.

In summary, TLM provides a way of modeling the mouthpiece using a series of cylindrical pipes, with accuracy comparable to TMM for the frequencies below the second resonance of the mouthpiece. TLM makes it convenient to customize and characterize the mouthpiece by modifying the cross-section area function and calculating the corresponding input impedance. A TLM-based interactive mouthpiece design interface is built and discussed in Appendix C.

## 6.6 Discussion

The present chapter begins with the definition of the mouthpiece input impedance. By adding the wedge-shaped space between the reed surface and the mouthpiece window, the acoustic cavity of the mouthpiece is extended to the tip window, where the input is defined. Such a definition makes it easier to measure and calculate the input impedance of the mouthpiece, and the measured input impedances are used for the acoustic characterization of the mouthpiece. It shows that when a mouthpiece is connected to a truncated cone, the

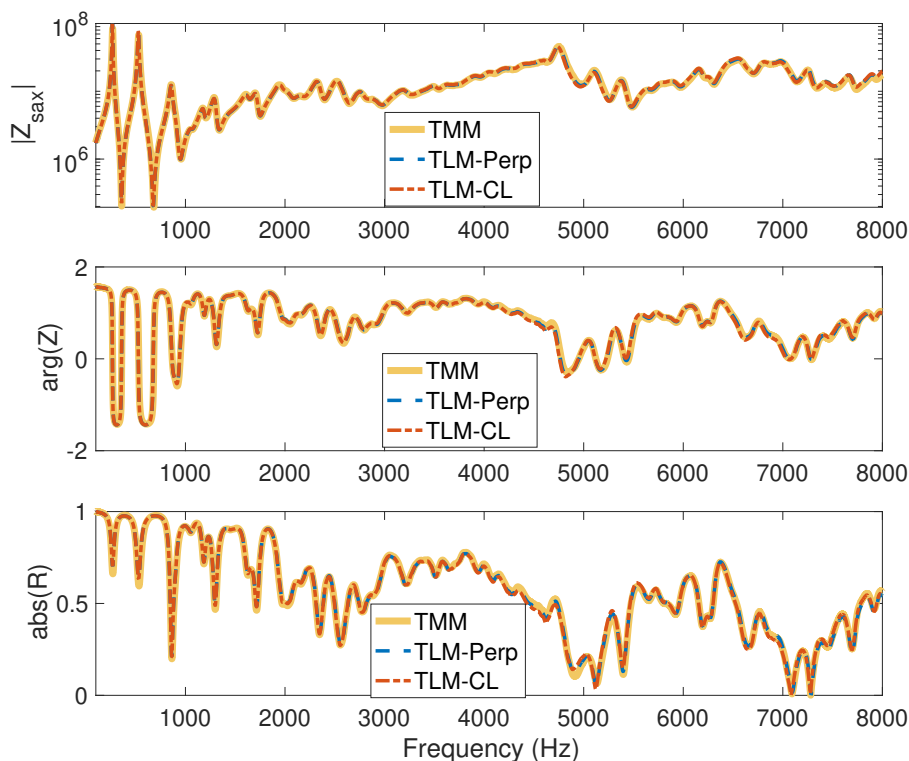


**Fig. 6.19:** The input impedance of the saxophone for the note  $B^b4$  (written) simulated with TLMs and TMM.

resonator’s harmonic frequencies are shifted down due to the increase of the overall pipe length, and the mouthpiece resonant frequencies shape the “formants” of the overall input impedance.

The transfer matrix mouthpiece model was derived from a finite element mouthpiece model, which represents the mouthpiece as a  $2 \times 2$  matrix. The modeling was validated by comparing the calculated input impedance of a mouthpiece-cone system with measurements. The same measured input impedance was also used to compare calculated results using lumped and cylindrical mouthpiece models. TMM was shown to be the most accurate representation among all three models, providing the highest degree of fidelity in the high-frequency region.

Using a sound synthesis model based on recursive parallel filters, the three different mouthpiece models were coupled to the same alto saxophone and a comparison was per-

formed in terms of the fundamental frequency, inharmonicity, dynamics threshold, playing frequency, spectral centroid, pressure waveform, and the bifurcation delay. Different mouthpiece models clearly show varying behaviors that can be explained by differences in their inharmonicity and high-frequency characteristics. In this chapter, basic comparisons were aimed at demonstrating differences in terms of a number of acoustical and dynamical features in simulated played conditions, and we leave a detailed analysis of other features, such as the influence of inharmonicity or higher modes on the dynamics, for future studies.

Because the transfer matrix provides an efficient way to represent the mouthpiece while being accurate enough to retain the complex mouthpiece geometry information, the proposed TMM is adaptable and ideal for different applications. TMM, which could be applied to other instruments such as the clarinet, can be connected to different resonators by taking either the measured or calculated resonator input impedance as the load impedance, which is useful for instrument prototyping purposes. It should also be straightforward to apply TMM to a variety of sound synthesis schemes, leading to a more accurate simulation of both high- and low-frequency regions.

The TLM built in this chapter is based on a one-dimensional cross-section function representation of the mouthpiece geometry. Despite the simplification in geometry from 3D to 1D, the input impedance calculated using TLM closely matches the TMM-simulated results. Unlike TMM, which requires running the more expensive FE model twice for a modified mouthpiece geometry, updating the mouthpiece geometry is a trivial task for TLM. The cross-section area function can be directly edited or updated by re-slicing the modified 3D CAD model, which is an efficient process in either case. Though not covered in this chapter, TLM can also be used for sound synthesis. The synthesis can be based on either the recursive parallel filter representation as used for TMM, or a time-domain scattering representation such as those used with digital waveguide models (Scavone, 1997, van Walstijn, 2002).

All three acoustic models developed in this chapter will be used for the acoustic analysis of mouthpieces in Ch. 8, and TLM is applied to build the interactive mouthpiece design interface in Appendix C.

## Chapter 7

# Aeroacoustical Modeling of the Saxophone Mouthpiece

A two-dimensional (2D) computational aeroacoustic model of the saxophone mouthpiece is developed in this chapter to investigate the fluid-structure-acoustic interaction (FSAI) during saxophone sound generation. The objective is to explore the role of the mouthpiece in sound generation using aeroacoustic analyses.

The chapter begins with a comprehensive overview of the computational model in Sec. 7.1. The lattice Boltzmann method (LBM) is used to simultaneously resolve fluid and acoustic fields in the mouthpiece, which is commonly known as the direct method in computational aeroacoustics (Wagner et al., 2007, Sec. 1.2.4). The mouthpiece solid walls and the one-dimensional beam model of the moving reed are incorporated with the LB simulation using the immersed boundary method (IBM), as detailed in Sec. 4.3.3. The characteristic-based time-domain impedance boundary condition (C-TDIBC) is utilized to represent the acoustic resonator at the end of the mouthpiece. While C-TDIBC was validated in Ch. 5 in simple flows, it will be further validated in the context of self-sustained sound generation in Sec. 7.2. Finally, in Sec. 7.3, the Ffowcs Williams and Hawkings (FW-H) acoustic analogy is employed for the aeroacoustic analysis based on the LB simulation, which helps characterize the sound generation process by investigating different sound sources distributed in the mouthpiece.

## 7.1 Lattice Boltzmann aeroacoustic model of the mouthpiece

### 7.1.1 Mouthpiece Model

The schematic of the mouthpiece model is shown in Fig. 7.1. A Meyer 5M alto saxophone mouthpiece is used in this chapter, which has a tip opening of 1.8 mm, and a round medium-size chamber. The 2D mouthpiece geometry is represented by a series of B-splines, which are obtained by projecting the three-dimensional (3D) mouthpiece onto its sagittal plane. To provide the mouth pressure that drives the instrument, the absorbing boundary condition (ABC) described in Sec. 4.3.2 is applied with a layer thickness of 30 grid points at the computational domain's inlet. C-TDIBC introduced in Ch. 5 is applied to the end of the mouthpiece to represent the acoustic resonator. The immersed boundary method (IBM) presented in Sec. 4.3.3 is used to model the mouthpiece and reed walls. IBM is only applied to the complex geometry of the mouthpiece before the throat, whereas the Zou-He boundary condition (Sec. 4.3.1.2) is applied to the rest of the solid walls, including the cylindrical bore of the mouthpiece and the walls in the mouth. The immersed boundary (IB) nodes and Zou-He boundaries are represented by dotted and solid lines in the diagram, respectively. The IB nodes of the mouthpiece walls are created every  $0.8\Delta x$  along B-splines, where  $\Delta x$  represents a grid size of the LB simulation. For the top of the reed, discretized IB nodes are initially placed on the  $x_{\text{reed}}$ -axis of the reed coordinate  $(x_{\text{reed}}, y_{\text{reed}})$ . The reed coordinate sets the origin at the tip of the mouthpiece ramp, and the  $x_{\text{reed}}$ -axis is placed along the mouthpiece table, with its positive direction pointing toward the tip of the mouthpiece. The  $y_{\text{reed}}$ -axis is set perpendicular to  $x_{\text{reed}}$ -axis, with its positive direction pointing into the mouthpiece. The bottom reed curve is determined by the reed thickness  $b(x)$ , along which the IB nodes were created.

The upstream length (measured from the tip of the mouthpiece to the upstream boundary) is 3 cm, and the mouthpiece bore length depends on simulations and will be defined separately.

The sound speed is set to 343 m/s. The kinetic viscosity is set to  $1.51e^{-4} \text{ m}^2/\text{s}$ , which is approximately an order of magnitude larger than that of the air. This is a numerical tradeoff to help allow a coarser grid while ensuring the simulation stability. A larger viscosity corresponds to a smaller Reynolds number, which will yield a more laminar flow in the mouthpiece reed channel. However, previous research (Wang and Scavone, 2019) has shown

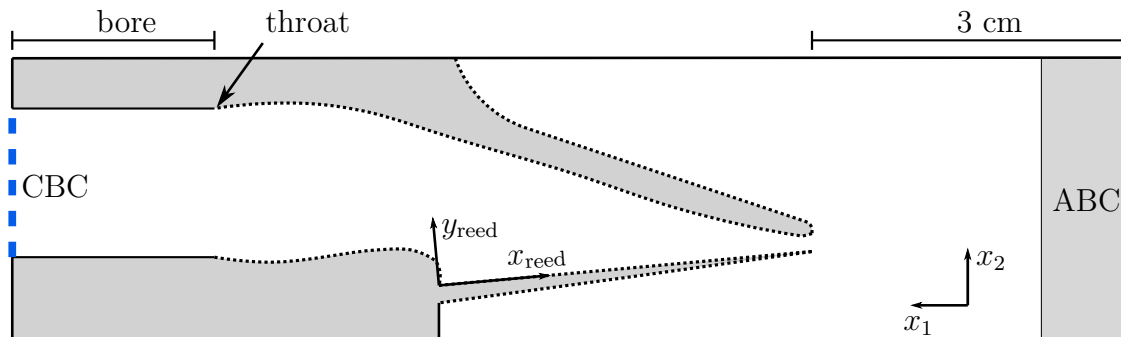


**Fig. 7.1:** The schematic of the simulation setup.

that LB simulations with larger viscosities are accurate enough to model the quasi-static flow in a saxophone mouthpiece. In addition, although a larger viscosity can introduce greater dissipation on acoustic waves, it has demonstrated good performance in solving aeroacoustic problems, as will be discussed in Appendix B. All simulations use a grid size of  $\Delta x \approx 9.53e^{-5}$  m and a time step of  $\Delta t \approx 1.60e^{-7}$  s, which guarantees 360 grid points per wavelength at 10 kHz.

Both the pressure and velocity are initialized as zero in the computational domain. The ABC pressure also starts at zero and then increases linearly to reach the target pressure  $p^t$  within a short amount of time  $t_r$ . The ramping-up period is typically 5 ms for the saxophone playing frequencies studied in the present research (from around 200 to 600 Hz). The short pressure ramping time is not set to match a realistic playing condition but is rather a numerical tradeoff to help faster achieve a steady-state signal and to save computational time. However, it is important to note that a short ramping-up duration may not be suitable for playing lower notes, such as fingering B<sup>b</sup>3 on a saxophone, as it may result in an unintended higher register note.

The total simulation duration is selected to be long enough for the system to reach a steady state, which is typically between 0.1 s and 0.2 s.

### 7.1.2 Reed Model

The mouthpiece-reed-lip model developed by Avanzini and van Walstijn (2004) is used in this research, where the reed is modeled as a one-dimensional bar clamped to the mouthpiece at one end and free at the other. The reed's interaction with the fluid, mouthpiece, and lip is achieved by applying corresponding external forces along the reed.

A schematic view of the mouthpiece-reed-lip model is displayed in Fig. 7.2. The reed is modeled in a separated coordinate  $(x_{\text{reed}}, y_{\text{reed}})$  in the LB simulation, as illustrated in Fig. 7.1. However, the reed coordinate subscripts are omitted in this section for clarity.

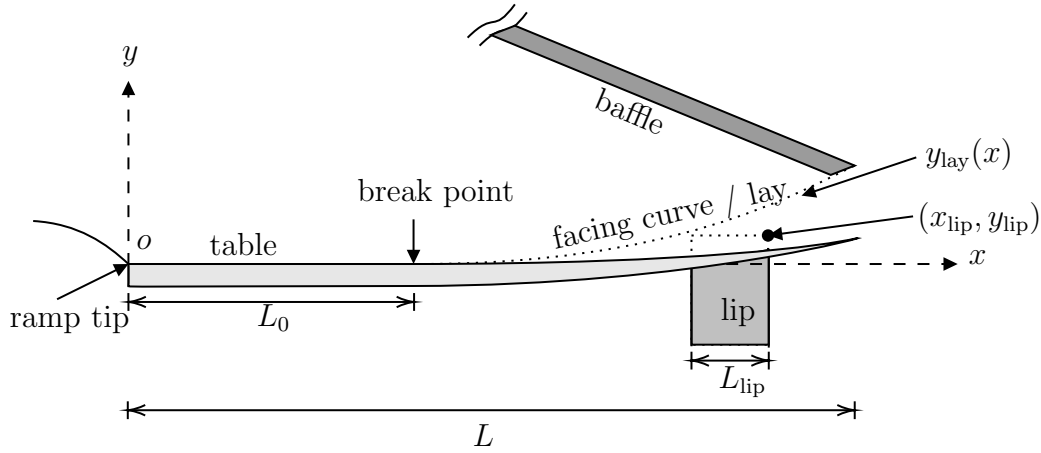


**Fig. 7.2:** The schematic view of the mouthpiece-reed-lip interaction.

The transverse oscillation amplitude of the reed  $y(x, t)$  is governed by the Euler-Bernoulli equation:

$$\frac{\partial^2}{\partial x^2} \left[ YI(x) \left( 1 + \eta \frac{\partial}{\partial t} \right) \frac{\partial^2 y}{\partial x^2} \right] + \rho_r S(x) \left[ \frac{\partial^2 y}{\partial t^2} + \gamma_B \frac{\partial y}{\partial t} \right] = F(x, t), \quad (7.1)$$

where  $\rho_r$  represents the reed density, while  $Y$  and  $\eta$  denote Young's modulus and magnitude of the internal viscoelastic losses, respectively. In addition,  $I(x) = S(x)\kappa^2(x)$  represents the moment of inertia about the longitudinal axis with  $\kappa(x)$  being the radius of gyration of the cross-section  $S(x) = wb(x)$ , where  $w$  and  $b(x)$  denote the width and thickness of the reed, respectively.

The time discretization of the equation uses the same time step as the LB simulation, and the spatial discretization is based on the discretized IB nodes with a grid size of  $0.8\Delta x$ , where  $\Delta x$  denotes the grid size of the LB simulation. The finite difference method is used to solve the reed model and details can be found in the original paper by Avanzini and van Walstijn (2004). The reed IB nodes are constrained to move solely along the  $y$ -axis, with their  $x$ -axis positions fixed. At each time step, the node velocity is updated using the backward Euler method  $dy^n(x)/dt = (y^n(x) - y^{n-1}(x))/\Delta t$  before being transformed from the reed coordinate to the LB coordinate.

The external force acting on the reed is expressed as a sum of three forces: lip force  $F_{\text{lip}}$ , lay force  $F_{\text{lay}}$ , and fluid force  $F_{\text{fluid}}$ , written as  $F(x, t) = F_{\text{lip}}(x, t) + F_{\text{lay}}(x, t) + F_{\text{fluid}}(x, t)$ .

The lip distributes both elastic force and additional damping along its contact area with the reed, which is defined over the range of  $x \in (x_{\text{lip}} - L_{\text{lip}}, x_{\text{lip}})$ , where  $L_{\text{lip}}$  represents the length of the lip, and  $x_{\text{lip}}$  indicates the position of the front edge of the lip. The elastic force is exerted on the reed when  $\Delta y_{\text{lip}} > 0$ , where  $\Delta y_{\text{lip}} = y_{\text{lip}} - y(x, t) + b(x)$  denotes the lip compression with  $y_{\text{lip}}$  representing the vertical position of the top of the uncompressed lip, as illustrated in Fig. 7.2. This force is given by  $F_{\text{lip}} = -k_{\text{lip}}\Delta y_{\text{lip}}$ , where  $k_{\text{lip}}$  represents the stiffness of the lip. Meanwhile, to account for the damping effect, the damping coefficient  $\gamma_B$  in Eq. 7.1 is defined as

$$\gamma_B = \begin{cases} \gamma_{\text{air}} + \gamma_{\text{lip}}, & x \in (x_{\text{lip}} - L_{\text{lip}}, x_{\text{lip}}), \\ \gamma_{\text{air}} & \text{otherwise.} \end{cases} \quad (7.2)$$

The contact force  $F_{\text{lay}}$  between the reed and mouthpiece lay can be decomposed into the elastic and dissipative components. The elastic force is given as

$$F_{\text{el}} = \begin{cases} -k_{\text{lay}}\Delta y_{\text{lay}}(x, t) & \Delta y_{\text{lay}} > 0, \\ 0 & \text{otherwise,} \end{cases} \quad (7.3)$$

where  $\Delta y_{\text{lay}} = y(x, t) - y_{\text{lay}}(x)$  is the distance that the reed “penetrates” into the lay. The dissipative force is defined as

$$[F_{\text{dis}}(x, t)dx]\Delta t = \dot{y}(x, t)dm, \quad (7.4)$$

where the reed mass is given as  $dm(x) = \rho_r b(x)w dx$ . The dissipative force is present only when the reed collides with the lay (i.e., the reed position  $y(x)$  crosses through  $y_{\text{lay}}(x)$ ) during  $\Delta t$ .

The aerodynamic force on each IB node of the reed is determined in the LB domain using IBM as discussed in Sec. 4.3.3. It is then projected to the reed coordinate to achieve  $F_{\text{fluid}}(x)$ .

A fourth-order polynomial is utilized to fit the reed thickness profile of a plastic reed measured by (Avanzini and van Walstijn, 2004). The original polynomial was designed

specifically for a reed with a length of  $34 \cdot 10^{-3}$  m, however, it is adapted to arbitrary reed length  $L$  using the following formula:

$$b(x) = \begin{cases} \sum_{n=0}^4 b_n (x - L + 34 \cdot 10^{-3})^n, & x > (L - 34 \cdot 10^{-3}), \\ b_0, & \text{otherwise.} \end{cases} \quad (7.5)$$

with  $b_{0,\dots,4} = [2.263 \cdot 10^{-3}, -4.9483 \cdot 10^{-2}, -4.444, 2.0126 \cdot 10^2, -2.4385 \cdot 10^3]$ .

The profile of the lay is obtained from the 3D mouthpiece geometry, which is also fitted by a fourth-order polynomial, shown as

$$y_{\text{lay}}(x) = \begin{cases} \sum_{n=0}^4 l_n (x - L_0)^n, & x > L_0, \\ 0, & x \leq L_0. \end{cases} \quad (7.6)$$

## 7.2 Validation of C-TDIBC in aeroacoustic modeling of single-reed mouthpieces

### 7.2.1 Validation procedure

Section 5.5.2 presents the validation of C-TDIBC in a 2D uniform pipe with and without mean flow. This section explores and validates the application of C-TDIBC in the aeroacoustic modeling of single-reed instruments. The validation procedure is presented below, which includes three separate simulations as illustrated in Fig. 7.3:

1. simulate the wave propagation in a 2D pipe with a length of 30 cm and diameter of 1.5 cm. C-TDIBC and the unflanged radiation impedance  $Z_{\text{rad}}$  are applied at its outlet. The pressure and velocity at the inlet are spatially averaged to calculate the input impedance of the pipe  $Z_{\text{pipe}}$ .
2. simulate the mouthpiece-reed system, coupled with the 30 cm pipe used in step 1. The same C-TDIBC and unflanged radiation impedance  $Z_{\text{rad}}$  are applied at the outlet of the pipe.
3. simulate the mouthpiece-reed system with C-TDIBC applied at the end of the mouthpiece. The impedance  $Z_{\text{pipe}}$  measured in step 1 is applied at the boundary.
4. The results obtained in steps 2 and 3 are compared to assess the accuracy and reliability of C-TDIBC in modeling the sound generation in single-reed instruments.

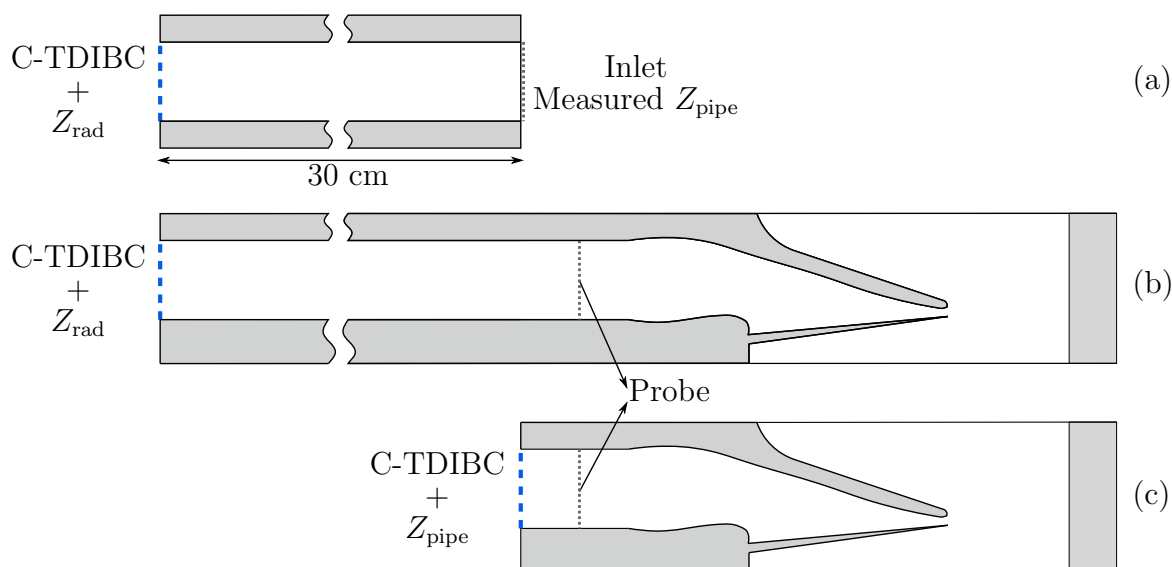


**Fig. 7.3:** The illustration of simulation setups in (a) step 1, (b) step 2, and (c) step 3.

### 7.2.2 Simulation details

While Sec. 7.1 describes the general setup for the LB modeling of the mouthpiece, this section provides specific details on several simulations conducted in different steps.

The mouthpiece has a bore length of 1 cm and a diameter of 1.5 cm. In step 3, the cylindrical part includes both the 30 cm pipe and the 1 cm mouthpiece bore, making its total length to 31 cm. The probe is consistently placed 8 mm away from the mouthpiece throat in both simulations, as shown by dashed gray lines in Fig. 7.3

The simulation lasts for 0.1 s in both steps 2 and 3. The mouth pressure increases from 0 to 6000 Pa within 5 ms and remains constant until the simulation ends. The reed parameters shown in Table 7.1 are based on research on clarinets (Avanzini and van Walstijn, 2004, da Silva et al., 2007, Yoshinaga et al., 2021), but have been adjusted to account for the saxophone mouthpiece's larger tip opening.

The unflanged pipe radiation impedance employed in steps. 1 and 2 is derived from reflection coefficients using Eq. 3.43. A rational function approximation of the reflection coefficients proposed by Silva et al. (2009) is employed to model the unflanged opening of the pipe:

$$R(\omega) = \frac{-1 + n_1 jka}{1 + m_1 jka + m_2 (jka)^2}, \quad (7.7)$$

**Table 7.1:** Reed and lip parameters used in steps 2 and 3.

Component	Parameter	Value
Reed	Density	$\rho_r = 1000 \text{ kg/m}^3$
	Young's Modulus	$Y = 4 \cdot 10^9 \text{ Pa}$
	Viscoelastic constant	$\eta = 6 \cdot 10^{-7} \text{ s}$
	Fluid damping coefficient	$\gamma_{\text{air}} = 1000 \text{ s}^{-1}$
	horizontal position	$x_{\text{lip}} = 12.25 \text{ mm}$
Lip	vertical position	$y_{\text{lip}} = 10.85 \text{ mm}$
	contact length	$L_{\text{lip}} = 9 \text{ mm}$
	additional damping	$\gamma_{\text{lip}} = 1.6 \cdot 10^4 \text{ s}^{-1}$
	stiffness per unit length	$k_{\text{lip}} = 6.5 \cdot 10^4 \text{ N/m}^2$
Lay	contact stiffness per unit length	$k_{\text{lay}} = 10^8 \text{ N/m}^2$

where values of  $n_1 = 0.167$ ,  $m_1 = 1.393$ , and  $m_2 = 0.457$  are used as specified in the original paper for the unflanged case<sup>1</sup>.

The bilinear transform is applied to obtain a model in the discrete-time domain, which essentially is a two-zero, two-pole numerical filter. Figure 7.4 presents a comparison of reflection coefficients calculated using Eq. 7.7 in the  $s$ -domain, the bilinear transformed version in the  $z$ -domain, and Levine and Schwinger (1948)'s (L&S) analytical expression. Although the bilinear transform is known to cause frequency warping, the high sampling rate of the LB simulation ( $f_s \approx 6.25 \cdot 10^6 \text{ Hz}$ ) renders its effect negligible. Furthermore, while there are relatively larger deviations between the approximation and the L&S analytical reflection coefficients at high frequencies, these discrepancies will not affect the efficacy of the C-TDIBC validation if the same  $Z_{\text{rad}}$  is used in steps 1 and 2.

The same low-pass filter as described in Sec. 5.4 is used for C-TDIBC. It has a stopband that starts at 100 Hz, which is set lower than an alto saxophone's lowest note (around 138.6 Hz).

### 7.2.3 Results and discussion

Figure 7.5 presents a comparison of the time-domain tip opening measured in steps 2 and 3. Furthermore, Figs. 7.6 and 7.7 present comparisons for the probed pressure and velocity,

<sup>1</sup>It should be noted that while the  $e^{j\omega t}$  convention is used here, Silva et al. (2009)'s original paper used  $e^{-j\omega t}$ . As a result, there is a sign difference between Eq. 7.7 and the corresponding equation described in the original paper.

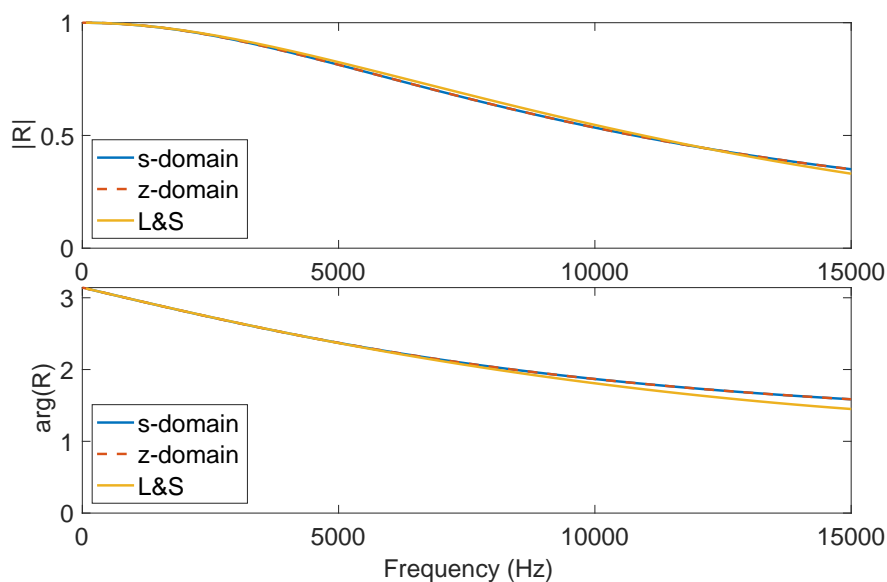


**Fig. 7.4:** A comparison of the approximated unflanged pipe radiation coefficients in the s- and z-domains with the analytical expression proposed by Levine and Schwinger (1948).

respectively. The single-period steady-state signals are compared in Fig. 7.8.

In general, the comparison shows good agreement in the steady-state signal and the initial onset of the simulation, but there exist larger discrepancies during the intermediate transient stage from around 0.005 to 0.035 s.

To better evaluate the performance of C-TDIBC, the tip opening amplitude spectra are compared at the top of Fig. 7.9, with their amplitude deviation in dB shown at the bottom. The “period synchronized sampling” technique (Grothe, 2013, Sec. 5.1.3) is used to obtain a clean spectrum of the steady-state signal by assuming that the harmonic frequencies of the signals are integer multiples of the fundamental frequency. It first extracts a single-period steady-state signal to calculate the fundamental frequency  $f_0$ , and the single-period signal is resampled under a new sampling frequency, which is set as an integer multiple of  $f_0$ . The discrete Fourier transform is applied to the resampled signal and the harmonic frequencies are ensured to be aligned with the frequency of each bin.

The frequency-domain comparison demonstrates a good overall performance of C-TDIBC below 2 kHz, with a maximum deviation of less than 3 dB. However, discrepancies get larger at higher frequencies. Several sources can account for these deviations, although the primary factor is that C-TDIBC generates spurious reflections that cause the resonator impedance to deviate from the imposed one at the boundary. The envelope of deviations shown in Fig. 7.9

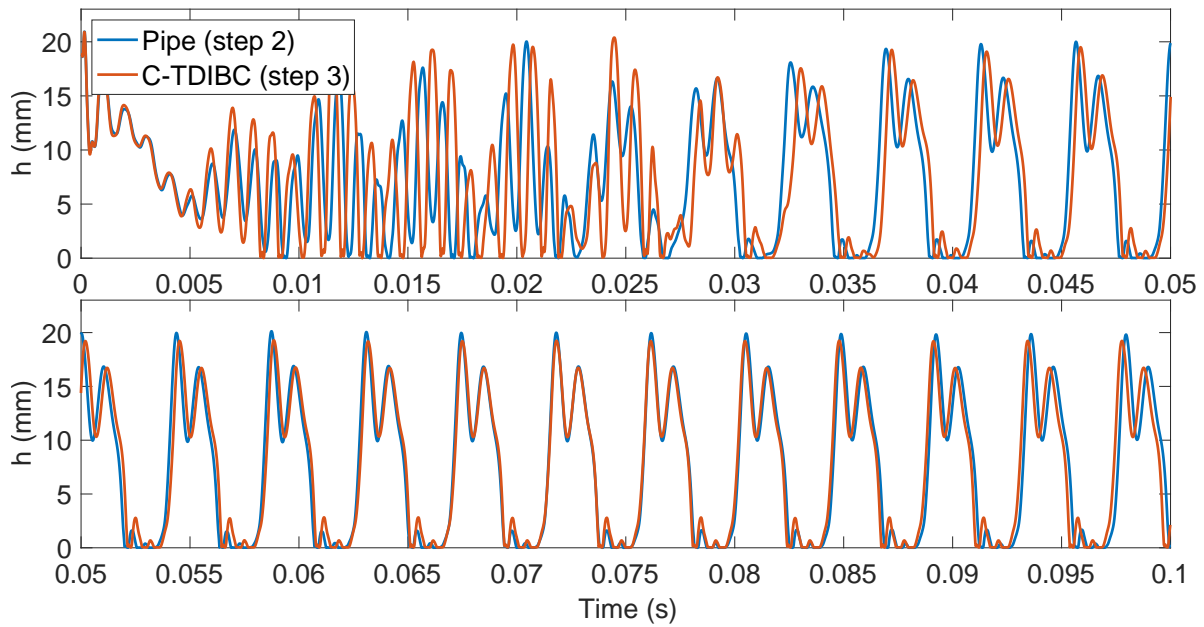


**Fig. 7.5:** The comparison of tip opening in the time domain, with the two rows showing the first and last 0.05 s of signal.

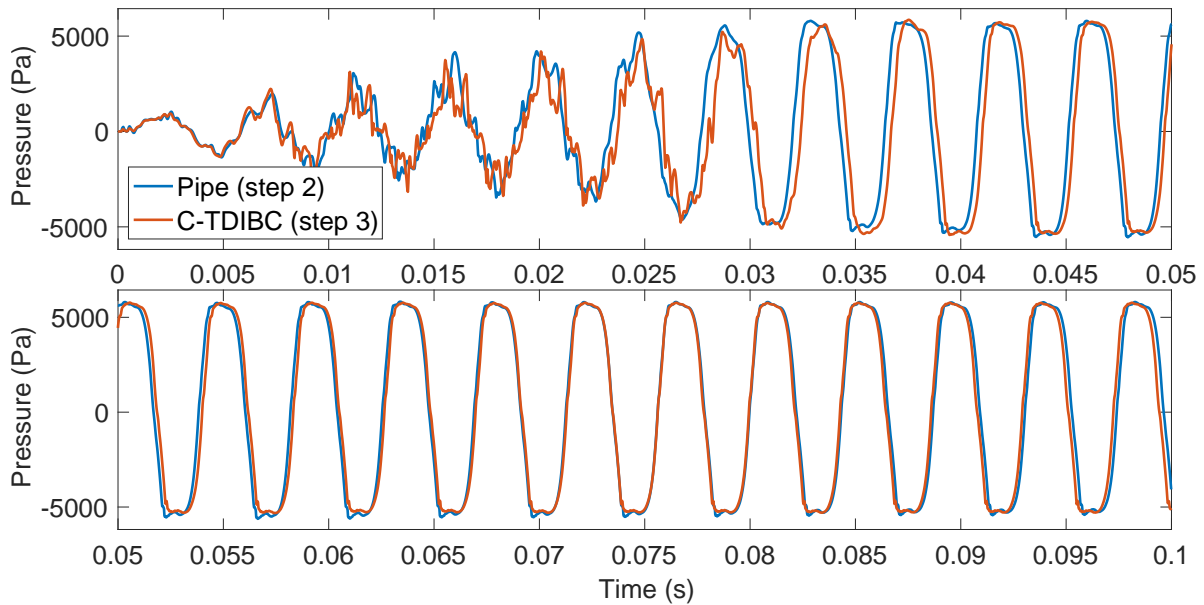


**Fig. 7.6:** The comparison of probed pressure in the time domain.

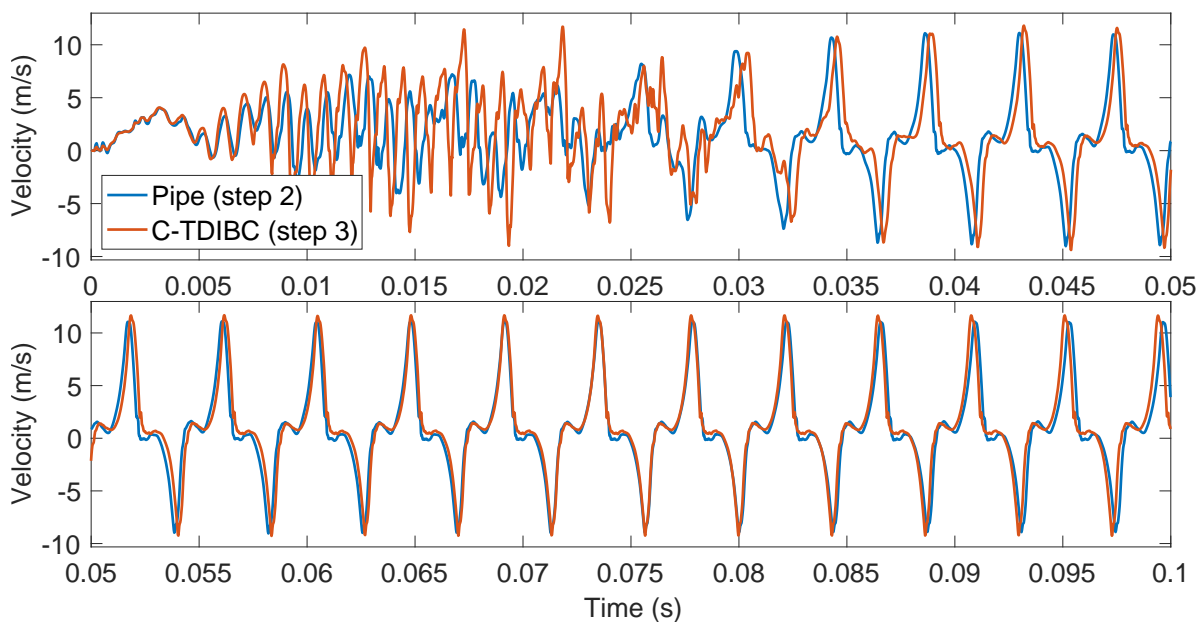


Fig. 7.7: The comparison of probed velocity in the time domain.

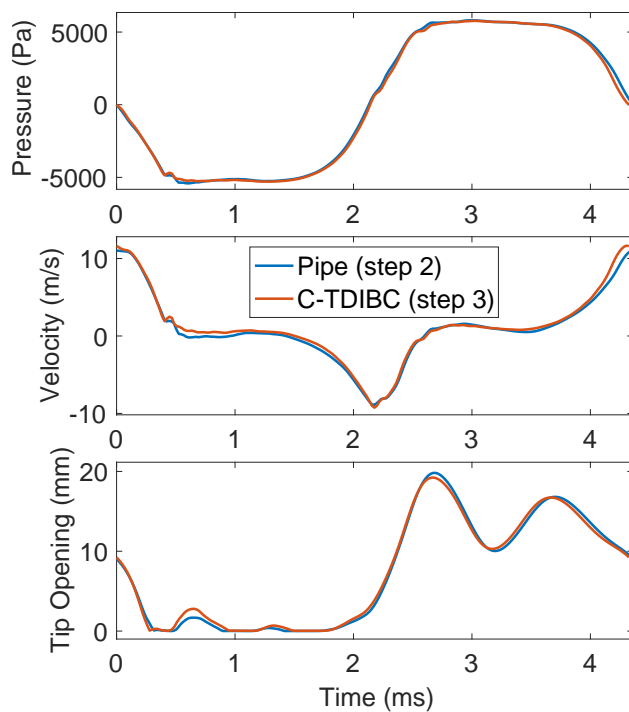
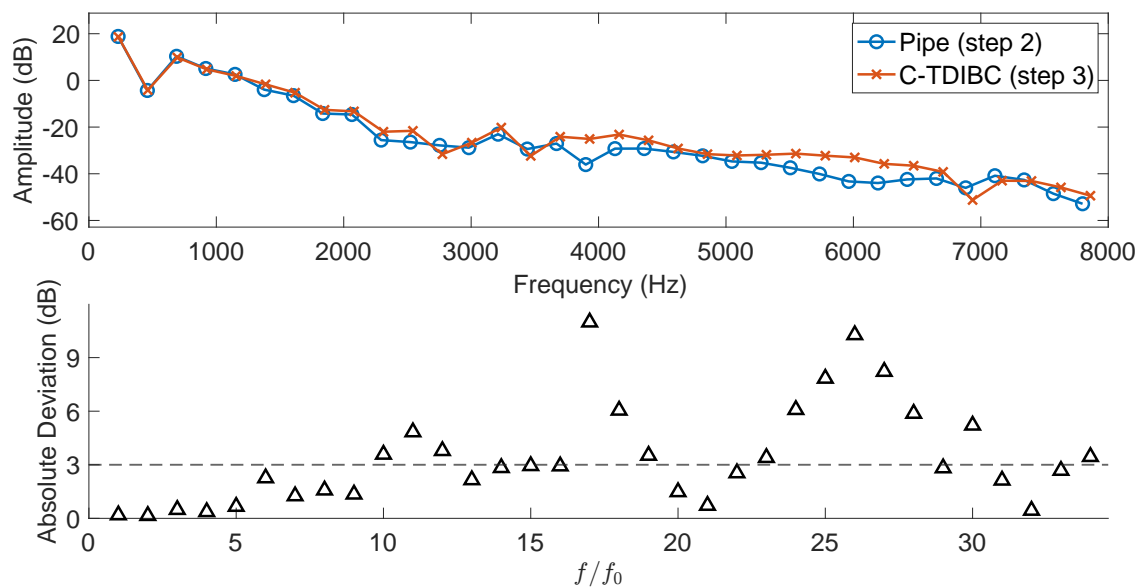


Fig. 7.8: The comparison of single-period time-domain signals.



**Fig. 7.9:** The frequency-domain comparison between the measured tip openings in steps 2 and 3 (top), and the absolute amplitude deviations in dB of harmonics below 8 kHz (bottom). The +3 dB is shown as a reference in the bottom figure by the horizontal dashed line.

presents a resonance-like structure in the frequency domain with several “resonances”, such as the 26th harmonic around 6000 Hz. This structure arises due to the amplification of the spurious reflections around the mouthpiece’s resonance frequency<sup>2</sup> when these reflections travel back and forth within the mouthpiece.

C-TDIBC is essentially a combination of the characteristic boundary condition (CBC) and time-domain impedance boundary condition (TDIBC). The spurious reflection generated by CBC is a well known problem that arises when applying it as a non-reflecting boundary condition. CBC applied in the present research relies on the local one-dimensional inviscid model with transverse terms and transverse relaxation (LODI-T), and the plane wave masking (PWM) technique. On one hand, LODI-T exhibits spurious reflection, particularly when stronger vortices are present in the system (Sec. 5.5.1.1). On the other hand, the PWM technique assumes a planar wave at the boundary, which is not ideally representative of higher-frequency acoustic waves due to the disturbed fluid fields and the presence of higher-order modes in the mouthpiece. Consequently, the performance of C-TDIBC can be degraded if the outgoing acoustic wave cannot be perfectly resolved in such cases.

<sup>2</sup>One can refer to Fig. 6.2 about the resonance structure of a closed mouthpiece.

In addition to the amplitude deviation, the fundamental frequency of the steady-state signal measured in step 3 (with C-TDIBC applied) is about 2 Hz higher than that measured in step 2 (with a pipe), and all the harmonics also shift correspondingly. This is likely another artifact due to the spurious reflection from C-TDIBC but requires further study to confirm it. Another factor that may contribute to this discrepancy is that the pipe input impedance applied in step 3 is measured under a quiescent flow in step 1, while in step 2, it experiences a non-zero mean flow velocity in the pipe. Consequently, the imposed input impedance in step 3 has higher resonance frequencies, which is consistent with trend of the observed discrepancies. However, the convective effect is known to introduce a multiplicative factor of  $1 - \text{Ma}^2$  of the resonant frequencies (Rodriguez et al., 2012) with  $\text{Ma}$  denoting the Mach number. Considering that the mean flow measured at the end of the mouthpiece in step 2 is only about 2 m/s, the convective effect is too weak to have a significant influence on the playing frequency.

Additionally, the pressure amplitude spectra are displayed in Fig. 7.10, which shows a similar behavior as that of the tip opening spectra with a good accuracy at low frequencies.

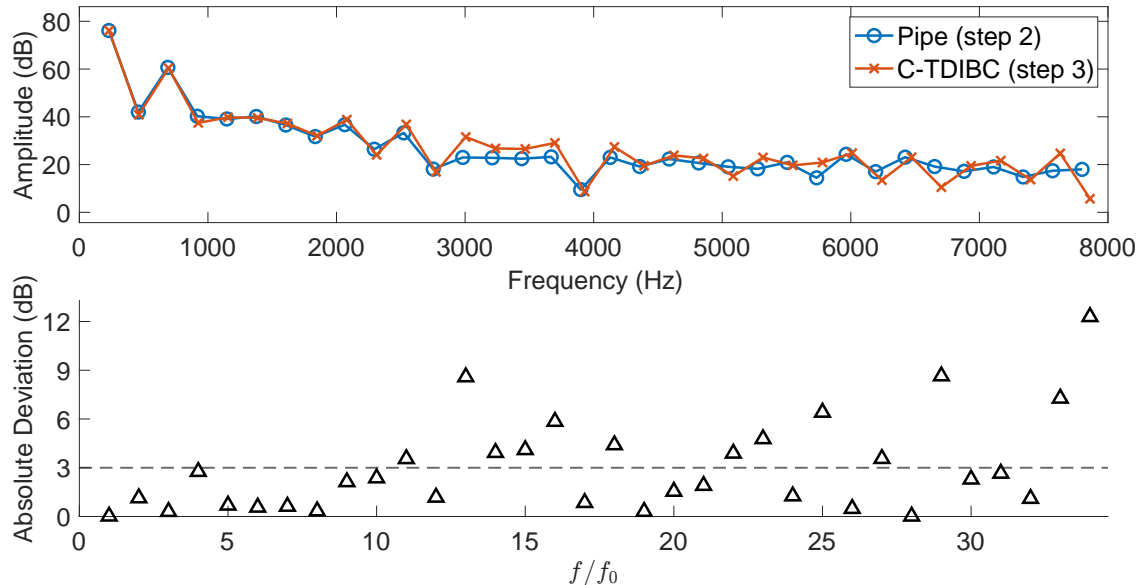


**Fig. 7.10:** The frequency-domain comparison between the measured pressure in steps 2 and 3 (top), and the absolute amplitude deviations in dB of harmonics below 8 kHz (bottom). The +3 dB is shown as a reference in the bottom figure by the horizontal dashed line.

### 7.2.4 Conclusion

This section presents the first application of C-TDIBC in computational aeroacoustic modeling of the saxophone. The results demonstrate that C-TDIBC can model the acoustic resonator in a self-sustained system, with accurately simulated steady-state signals up to 2 kHz. The main limitation of C-TDIBC is the spurious reflection it generates at the boundary, which contributes to discrepancies at high frequencies and the transient signal. This is, however, not only an issue for the present research, but a well-known problem for all non-reflecting boundary conditions. Further improvements are necessary, especially in addressing high-frequency wave absorption and strong vortices at the boundaries, to enhance its performance.

C-TDIBC is proposed to reduce computation costs and improve modeling efficiency. In the application presented in this section, the utilization of C-TDIBC in step 3 has resulted in a computational domain size that is only one-quarter of that used in step 2. This reduction in domain size has led to a 60% reduction in the total simulation runtime (155.9 mins for step 3 and 393.8 mins for step 2). It is worth mentioning that even step 2 itself benefits from C-TDIBC by using  $Z_{\text{rad}}$  to model the radiation domain. This means that the simulation efficiency improvement by C-TDIBC can be larger than 60% in the model demonstrated here. The simulation efficiency improvement by C-TDIBC also depends on other factors and the reduction in simulation runtime may not be linearly proportional to the number of LB grids. The IBM is used to model the mouthpiece and reed, which deploys a series of IB nodes in the mouthpiece region and requires more computations at each time step. Truncating the computational domain and applying C-TDIBC do not help reduce the computation cost by IBM. In addition, other strategies can be applied to improve the simulation efficiency such as grid refinement. Yoshinaga et al. (2021) applied a finer grid around the reed channel and used a coarser grid to resolve the resonator and the radiation domain. However, no grid refinement is applied in the present model in order to avoid potential spurious reflection at the interface between different grid resolutions.

### 7.3 Sound generation characterization using Ffowcs-Williams and Hawkings acoustic analogy

This section presents an analysis of saxophone sound generation using the Ffowcs Williams-Hawkings acoustic analogy. The present work is inspired by research on confined flow, especially in the context of flow passing through vocal folds (Zhao et al., 2001, 2002) and orifice (Hofmans, 1998). Ffowcs Williams (1969) first introduced the application of an acoustic analogy in internal flow by utilizing the one-dimensional Green's function for an infinite pipe. Hofmans (1998) used the same Green's function in Curle's formulation of Lighthill's equation to examine aeroacoustic problems in confined flows. Later, Zhao et al. (2001) and Zhang (2002) developed a corresponding solution for the Ffowcs-Williams and Hawkings equation, which helps incorporate the effect of moving vocal folds in the aeroacoustic study of human phonation.

The objective of this study is to investigate the sound generation characteristics of the saxophone, with a specific focus on understanding the role of the mouthpiece in saxophone sound generation. A methodology similar to that used in other confined flow research is employed to achieve this goal. To this end, a hybrid method (Wagner et al., 2007, Sec. 1.2.4) is used, which combines LB simulation and FW-H acoustic analogy. The LB simulation resolves the near-field sound generation, while the FW-H acoustic analogy serves as an analytical transport method to estimate far-field acoustics based on the near-field simulation results. As the LB model of the mouthpiece has already been detailed in previous sections, this section focuses on adapting the FW-H acoustic analogy to the saxophone mouthpiece and its implementation based on LB simulation.

The FW-H acoustic analogy is based on the FW-H formulation, which takes the form of either Eq. 3.58 or Eq. 3.59. The definitions of the integral domain, Green's function, and the values of hydrodynamic variables are required to evaluate the integral in the formulation, which will be addressed in Secs. 7.3.1, 7.3.2, and 7.3.3, respectively.

#### 7.3.1 Definition of the integral domain

The integral domain and integral surface must be defined in order to evaluate the integral in an FW-H formulation. For confined flows passing through orifices or vocal folds, the integral domain spans the entire computational domain, with integral surfaces distributed

on both sides of the confined region, as illustrated in Fig. 3.2<sup>3</sup>. In the saxophone mouthpiece, an analogous integral domain and integral surface can be defined by considering the reed channel as an orifice and the player's mouth and the inner mouthpiece as the upstream and downstream regions, respectively. The corresponding integral volume  $V'$  is bounded by dashed lines, and the associated integral surface is shown as dotted lines in Fig. 7.11(a). This acoustic system can be abstracted as a simplified acoustic model, illustrated in Fig. 7.11(b), which consists of four connected pipes to represent the mouth cavity above the mouthpiece beak  $V_b$ , the mouth cavity below the reed  $V_r$ , the inner mouthpiece cavity  $V_{mp}$ , and the upstream mouth cavity  $V_m$ .

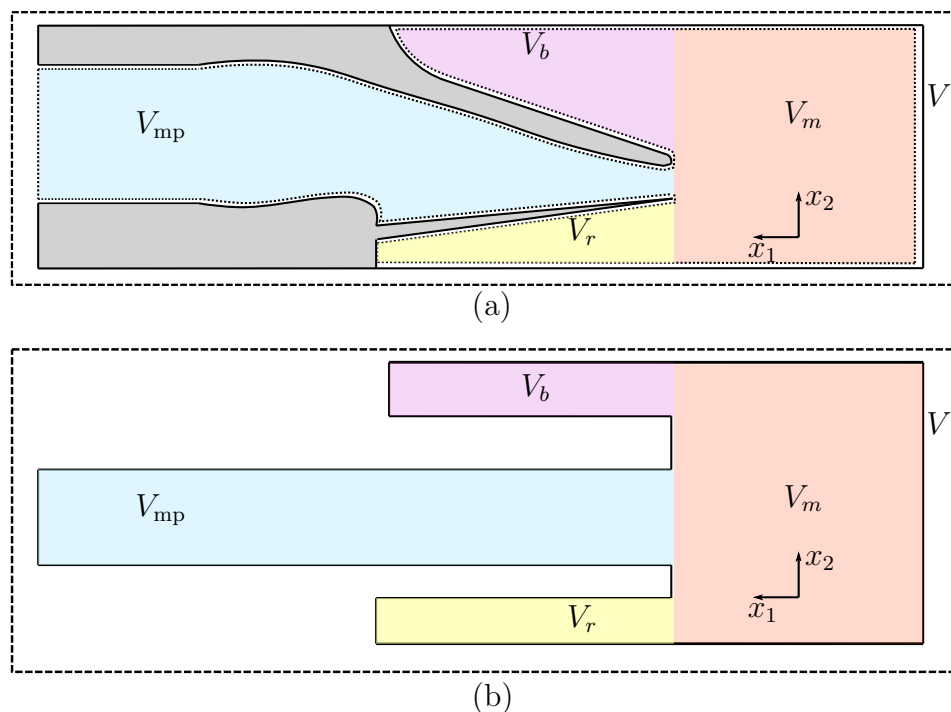


**Fig. 7.11:** The illustration of (a) the definition of an integral domain based on research in confined flows, and (b) a simplified acoustic system comprising four interconnected pipes.

However, to focus on the sound generation in the mouthpiece, an alternative definition of the integral surfaces is proposed, which excludes the mouth cavity represented by the sum of three volumes  $V_b + V_r + V_m$ , and restricts the integral volume to  $V_{mp}$ . This definition is justifiable when the mouth cavity is viewed as a pressure reservoir, and the effect of the

<sup>3</sup>To maintain the consistency with the FW-H derivation in Sec. 3.3, the coordinate is denoted as  $(x_1, x_2)$  instead of  $(x, y)$ .

vocal tract is neglected. Furthermore, the area in the reed channel (the area between the mouthpiece tip rail and the reed) is removed from the integral volume, and the inlet is placed at the end of the mouthpiece reed channel. This simplification is made to eliminate the potential for an unclear definition of the integral surface in the reed channel during the beating of the reed with the mouthpiece.

The integral surface and domain for the FW-H formulation in a saxophone mouthpiece are illustrated in Fig. 7.12. The integral surface is composed of the inlet  $S_{\text{in}}$ , outlet  $S_{\text{out}}$ , and solid walls  $S_w = S_{\text{mp}}^{\text{upper}} + S_{\text{mp}}^{\text{lower}} + S_r + S_{\text{bore}}$  that includes the upper  $S_{\text{mp}}^{\text{upper}}$ , lower  $S_{\text{mp}}^{\text{lower}}$ , and bore  $S_{\text{bore}}$  parts of the mouthpiece as well as the reed surface  $S_r$ . The normal  $\mathbf{n}$  of the integral surface is pointing into the mouthpiece.

In contrast to external flow applications, the observer in wind instruments like the saxophone cannot be placed in the acoustic far field due to the presence of standing waves inside the instrument. Therefore, the observer has to be placed in the acoustic near field, which is one of the primary differences between the present FW-H application in the saxophone and previous research in human phonation, where the vocal tract was replaced with an infinite pipe without acoustic feedback.

The observer is placed between the throat and outlet of the mouthpiece, and should be as far away from any abrupt geometric discontinuity as possible to minimize the influence of higher-order modes on the planar wave.

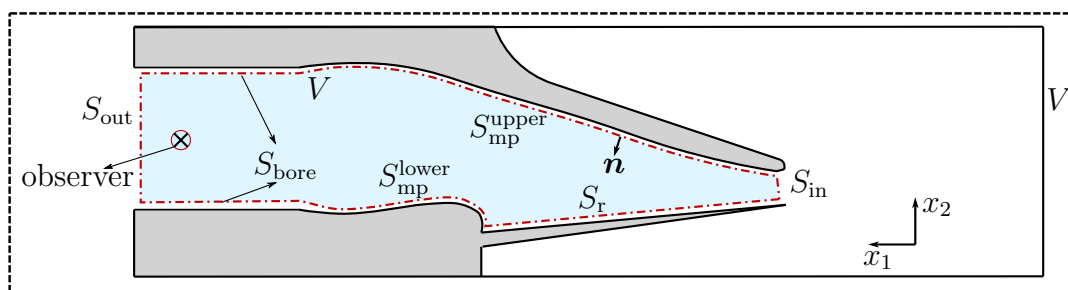


**Fig. 7.12:** The integral domain for FW-H acoustic analogy in a saxophone mouthpiece.

### 7.3.2 Choices of Green's function

This section provides three different Green's functions, including:

- 2D free-field Green's function,
- 1D Green's function for an infinite pipe, and

- the 1D Green's function for a semi-infinite pipe terminated at the inlet.

All of these Green's functions are viable options in the FW-H formulation, while the latter two 1D Green's functions are employed in the present study.

### 7.3.2.1 2D Green's function

The 2D free-field Green's function for the wave equation is given as:

$$G(\mathbf{x}, t | \mathbf{y}, \tau) = \frac{c}{2\pi} \frac{H(c(t - \tau) - r)}{\sqrt{c^2(t - \tau)^2 - r^2}}, \quad (7.8)$$

where  $r = |\mathbf{x} - \mathbf{y}|$  is the distance between the observer and the source, and  $H$  is the Heaviside function. The 2D Green's function is similar to the 3D version denoted in Eq. 3.31, but becomes singular at the observer due to the infinite denominator of Eq. 7.8 at the retarded time  $\tau = t^*$  with  $t^* = t - r/c$ . Additionally, the Green's function involves a time integral with a long tail due to the presence of the Heaviside function, which can be computationally expensive in certain applications. To overcome these issues, FW-H formulations in the frequency domain are typically used, with different formulations proposed for different scenarios depending on whether the source is moving and whether the source is in a moving medium (Bozorgi et al., 2017, Guo, 2000, Lockard, 2000, Zhou et al., 2023).

### 7.3.2.2 1D Green's function for an infinite pipe

The 1D Green's function for an infinite pipe is presented in Eq. 3.61, which is rewritten here

$$G(x_1, t | y_1, \tau) = \frac{c}{2S} H(t - \tau - |x_1 - y_1|/c).$$

It has been used in confined flows as introduced in Sec. 3.3.3, which assumes a planar wave and zero mean flow velocity at the observer placed outside of the source region,

Based on the integral domain specified in Fig. 7.12, the FW-H formulation in Eq. 3.64 is

modified as follows:

$$\begin{aligned} \rho'(x_1, t)c_\infty^2 &= \frac{1}{2c_\infty S} \frac{\partial}{\partial t} \int_V [T_{11}]_{t^*} dV & \text{(I)} \\ &+ \frac{1}{2S} \int_{S_w} [p_{1j}n_j]_{t^*} dS & \text{(II)} \\ &+ \frac{c_\infty}{2S} \int_{S_r} [\rho_\infty \bar{v}_j n_j]_{t^*} dS & \text{(III)} \\ &+ \frac{1}{2S} \int_{S_{in}} [(\rho v_1 v_1 + p_{11}) + \rho c_\infty v_1]_{t^*} dS & \text{(IV)} \\ &+ \frac{1}{2S} \int_{S_{out}} [(\rho v_1 v_1 + p_{11}) - \rho c_\infty v_1]_{t^*} dS. & \text{(V)} \end{aligned} \quad (7.9)$$

In this formulation, the term (I) corresponds to the quadrupole sound source, which arises due to the Lighthill stress tensor in the control volume. Term (II) represents the dipole sound source contributed by the force exerted on the fluid by the solid walls, while term (III) accounts for the monopole sound source produced by the induced displacement flow of the moving reed. Theoretically, terms (IV) and (V) are combinations of the dipole contribution by  $\rho v_1 v_1 + p_{11}$  and the monopole contribution by  $\rho v_1$ . However, these terms can also be treated as equivalent monopoles produced by the mass flux across the inlet and outlet surfaces  $\rho v_1 M_1 + \rho v_1^\pm$ , where  $M_1 = v_1/c_\infty$  is the Mach number in  $x_1$ -direction, and  $v_1^\pm = p_{11}/\rho c \pm v_1$  represents the incoming acoustic velocities. It should be noted that both  $S_{out}$  and  $S_{in}$  are defined perpendicular to the  $x_1$ -axis, so that their normal vectors  $n_j$  are correspondingly replaced with  $(-1, 0)$  and  $(1, 0)$  during the derivation.

The above formulation can be further simplified by omitting the quadrupole term (I), since its magnitude is typically two orders lower than that of the dipole (Zhao et al., 2002). Additionally, the dipole contribution from the bore  $S_{bore}$  is zero, owing to the wall's parallel orientation with respect to the  $x_1$ -axis. Consequently, sound source terms (II)-(IV) are all located upstream of the observer so that they only contribute to the left-going pressure  $p^+(x_1, t)$  at the observer's position. On the other hand, the term (V) represents the only sound source located downstream of the observer and contributes exclusively to the right-going pressure  $p^-(x_1, t)$ .

Given that the present study focuses on sound generation within the mouthpiece, the final FW-H formulation is as follows, which evaluates the left-going pressure at the observer

using a surface integral over a region located upstream of the observer:

$$p^+(x_1, t) = \frac{1}{2S} \int_{S_{w'}} [p_{1j} n_j]_{t^*} dS \quad (\text{II}')$$

$$+ \frac{c_\infty}{2S} \int_{S_r} [\rho_\infty \bar{v}_j n_j]_{t^*} dS \quad (\text{III}) \quad (7.10)$$

$$+ \frac{1}{2S} \int_{S_{\text{in}}} [(\rho v_1 v_1 + p_{11}) + \rho c_\infty v_1]_{t^*} dS \quad (\text{IV}),$$

where the total wall surface area is defined as  $S_{w'} = S_{\text{mp}}^{\text{upper}} + S_{\text{mp}}^{\text{lower}} + S_r$ . Terms (II'), (III) and (IV) are referred to as the dipole, reed monopole, and inlet monopole, respectively, in later discussions.

### 7.3.2.3 1D Green's function for a semi-infinite pipe terminated at inlet

The resonator of the saxophone can be modeled as a close-open pipe, with the closed end placed at the instrument's inlet. In this case, an alternative Green's function can be used in FW-H formulation - the 1D Green's function for a semi-infinite pipe terminated at the inlet  $x_1^{\text{in}}$ :

$$G_T(x_1, t|y_1, \tau) = \frac{c}{2S} \left[ H \left( t - \tau - \frac{|x_1 - y_1|}{c} \right) + H \left( t - \tau - \frac{x_1 + y_1 - 2x_1^{\text{in}}}{c} \right) \right]. \quad (7.11)$$

This Green's function  $G_T$  is defined as a sum of two terms. The first term represents the direct wave from the source at  $y_1$  to the observer at  $x_1$ , and is equivalent to the Green's function for an infinite pipe  $G$ , which was introduced in the previous section. The second term in  $G_T$  corresponds to the reflected wave by the closed end at  $x_1^{\text{in}}$  with  $x_1 > x_1^{\text{in}}$ . It can be also considered as an image source placed at  $2x_1^{\text{in}} - y_1$  in an infinite pipe, which has the same amplitude with an opposite sign with the direct sound source placed at  $y_1$ .

$G_T$  can be considered as a 1D tailored Green's function that satisfies the boundary condition of an ideally closed pipe at the inlet:

$$\left( \frac{\partial G_T}{\partial y_1} \right)_{y_1=x_1^{\text{in}}} = 0. \quad (7.12)$$

The corresponding spatial- and time-derivatives of the Green's function are given as

$$\frac{\partial G_T}{\partial \tau} = -\frac{c}{2S} \left[ \delta\left(t - \tau - \frac{|x_1 - y_1|}{c}\right) + \delta\left(t - \tau - \frac{x_1 + y_1 - 2x_1^{\text{in}}}{c}\right) \right]. \quad (7.13)$$

and

$$\frac{\partial G_T}{\partial y_1} = \frac{1}{2S} \left[ \text{sign}(x_1 - y_1) \delta\left(t - \tau - \frac{|x_1 - y_1|}{c}\right) - \delta\left(t - \tau - \frac{x_1 + y_1 - 2x_1^{\text{in}}}{c}\right) \right] \quad (7.14)$$

The equivalent of Eq. 7.10 using  $G_T$  is given as follows

$$\begin{aligned} p^+(x_1, t) &= \frac{1}{2S} \int_{S_w} [p_{1j} n_j]_{t_1^*} - [p_{1j} n_j]_{t_2^*} dS & (\text{II}'') \\ &+ \frac{c_\infty}{2S} \int_{S_r} [\rho_\infty \bar{v}_j n_j]_{t_1^*} + [\rho_\infty \bar{v}_j n_j]_{t_2^*} dS & (\text{III}'') \\ &+ \frac{1}{2S} \int_{S_{\text{in}}} [2\rho c_\infty v_1]_{t_1^*} dS & (\text{IV}'') \\ &+ \frac{1}{2S} \int_{S_{\text{out}}} [(\rho v_1 v_1 + p_{11}) - \rho c_\infty v_1]_{t_2^*} dS, & (\text{V}'') \end{aligned} \quad (7.15)$$

where  $t_1^* = t - |x_1 - y_1|/c$  and the  $t_2^* = t - (x_1 + y_1 - 2x_1^{\text{in}})/c$  are the two retarded times, corresponding to the direct and reflected sound, respectively.

Equations 7.10 and 7.15 provide two different interpretations of the sound generation inside the mouthpiece. Comparing these representations can provide a better understanding of the results obtained from the FW-H acoustic analogy as will be discussed in subsequent sections.

In general, applying  $G_T$  to the FW-H means placing all the sound sources in Eq. 7.10 by the closed end at the inlet. Assuming the dipole in the mouthpiece consists of two horizontally aligned monopoles with opposite signs  $(-, +)$ , it creates a quadrupole  $(+ - - +)$  sound source when combined with its image (Rienstra and Hirschberg, 2004, Ch. 6), which is known to be less efficient in radiation compared to an acoustic dipole. Meanwhile, all the monopoles are typically strengthened when being placed by the wall.

Compared to the dipole term (II') in Eq. 7.10, the corresponding term (II'') in Eq. 7.15 includes an additional component  $-[p_{1j} n_j]_{t_2^*}$ , which accounts for the image dipole placed on the opposite side of the inlet.

The reed monopole (III) in Eq. 7.10 is strengthened by the additional image monopole  $[\rho_\infty \bar{v}_j n_j]_{t_2^*}$  in Eq. 7.15.

For the sound source located at the inlet, the dipole component  $\rho v_1 v_1 + p_{11}$  of the term (IV) is canceled by its counterpart from the image dipole, while the monopole component contributed by  $[\rho c_\infty v_1]_{t_1^*}$  is doubled.

Finally, there is an extra term (V'') in Eq. 7.15, which corresponds to the reflection of the incoming wave from the outlet by the closed end at the inlet. This term should have the same amplitude but with an opposite sign as the sum of all other image sources, so that Eqs. 7.10 and 7.15 are equivalent to each other.

$$(V'') = - \{ [(II'') - (II')] + [(III'') - (III)] + [(IV'') - (IV)] \}. \quad (7.16)$$

### 7.3.3 Simulation details

The simulation setup is the same as that described in Sec. 7.1, and the playing parameters are presented in Table 7.2. By applying the measured input impedance to the end of the mouthpiece through C-TDIBC, four different fingerings of a saxophone are simulated, including B<sup>b</sup>4, D5, G5, and B<sup>b</sup>5.

**Table 7.2:** The playing parameters used in this section.

Component	Parameter	Value
Reed	Density	$\rho_r = 900 \text{ kg/m}^3$
	Young's modulus	$Y = 5.6 \times 10^9 \text{ Pa}$
	Viscoelastic constant	$\eta = 6 \times 10^{-7} \text{ s}$
	Fluid damping coefficient	$\gamma_{\text{air}} = 4000 \text{ s}^{-1}$
Lip	Horizontal position	$x_{\text{lip}} = 6 \text{ mm}$
	Vertical position	$y_{\text{lip}} = 1.5 \text{ mm}$
	Contact length	$L_{\text{lip}} = 9 \text{ mm}$
	Additional damping	$\gamma_{\text{lip}} = 1.6 \times 10^4 \text{ s}^{-1}$
	Stiffness per unit length	$k_{\text{lip}} = 6.5 \times 10^4 \text{ N/m}^2$
Lay	Contact stiffness per unit length	$k_{\text{lay}} = 10^8 \text{ N/m}^2$
Mouth	Target mouth pressure	$P_m = 8000 \text{ Pa}$
	Ramp up time	$t_r = 5 \text{ ms}$

To evaluate the FW-H formulations, hydrodynamic variables are sampled at discrete time  $k\Delta t$ , where  $k$  is a non-negative integer, and  $\Delta t$  is the sampling period. The sampling frequency is set to 48000 Hz, which is lower than that of the LB simulation in order to save on storage and computation time.

In order to compute the outgoing pressure  $p^+(x_1, k\Delta t)$  using the FW-H formulation of Eq. 7.10 or Eq. 7.15, it is necessary to evaluate the corresponding integrands at the retarded time  $t^* = t - |x - y|/c$ . However, in practice, the calculation is performed by evaluating each integrand at its own sampled time  $m\Delta t$  and subsequently adding it to the outgoing pressure  $p^+$  at the time  $(m + n)\Delta t$ , where  $n = \lfloor \frac{|x - y|/c}{\Delta t} \rfloor$ .

The compressive stress  $p_{1j}$  and normal vector  $n_j$  on the solid walls are necessary for the computation of dipole terms. While  $p_{1j}$  is calculated using the immersed boundary method,  $n_j$  is initialized based on the B-splines of solid walls and is updated in real-time for the moving-reed immersed boundary (IB) nodes. The reed velocity, i.e.,  $\bar{v}_j$  in term (III), is obtained by projecting the reed velocity in the reed model onto the LB coordinate, as discussed in Sec. 7.1.2. Measuring the pressure and velocity on the inlet surface  $S_{\text{in}}$  at the end of the reed channel is necessary to evaluate the inlet term (IV). As this area varies over time, different sets of LB nodes are involved in the calculation at each time step, and a zoomed-in view of the area around the reed channel is shown in Fig. 7.13 for illustration. The pressure  $p$  is calculated by simply averaging the pressure on the LB nodes (red circles). To compute the velocity, intersection points (black squares) between the inlet surface and both the mouthpiece and the reed must be identified. These intersection points assume a zero velocity based on the non-slip boundary condition on the wall. The inlet velocity  $v_1$  is computed as  $v_1 = \frac{1}{S_{\text{in}}} \sum_{n=1}^{N-1} \frac{v_1^{n+1} + v_1^n}{2} \Delta S_n$  using the set of velocities  $\{v_n^n\}$  composed of the LB nodes and the intersection points, where  $\Delta S_n = x_2^{n+1} - x_2^n$  and  $S_{\text{in}} = x_2^N - x_2^1$ ,  $v_1^n$  represents the  $x_1$ -direction velocity, and  $x_2^n$  represents the  $x_2$ -axis position of the  $n$ -th node in the set.

### 7.3.4 Results and discussion

#### 7.3.4.1 Validation of the FW-H acoustic analogy

Figure 7.14 presents a comparison of the outgoing pressure waveforms for fingering B<sup>b</sup>4 obtained from the LB simulation and those estimated using the FW-H acoustic analogy with

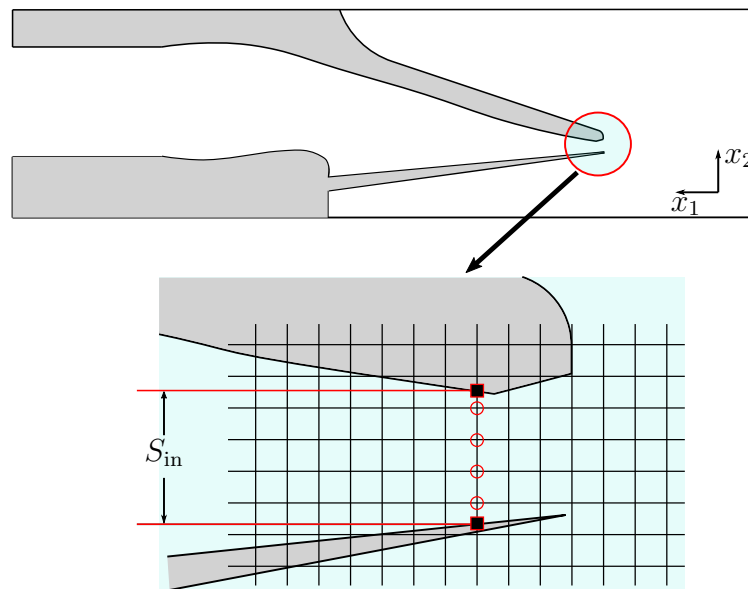


**Fig. 7.13:** The illustration of the nodes utilized for measuring inlet velocity and pressure. LB nodes on the inlet surface are shown in red circles, while the black squares represent the two additional intersection points of the inlet surface with the mouthpiece and the reed.

the 1D Green's function for an infinite pipe  $G$ . Both transient and steady-state signals exhibit good overall agreement between the FW-H and LB simulation. The frequency spectra of steady-state signals are obtained using the period synchronized sampling technique described in Sec. 7.2 and are compared in Fig. 7.15. This further demonstrates the efficacy of the FW-H acoustic analogy's application in saxophone sound generation, with the largest discrepancy being less than 3 dB.

The observed discrepancy between the FW-H and LB simulation is mainly because the assumptions made during the FW-H formulation's derivation are not strictly fulfilled. One of the main assumptions made when using the 1D Green's function in FW-H is that the sound wave propagation from the source to the observer is planar. However, in reality, the acoustic wave in the mouthpiece travels through a complex geometry and is influenced by vortices, higher-order acoustic modes, and the spurious reflection from C-TDIBC. As a result, it cannot be assured that the wave will remain planar while traveling toward the observer. On the other hand, the convection effect is neglected when deriving the FW-H formulation in this research, hence both the sources and the observer are assumed to be located in a region free of background mean flow. Such a convection effect is small enough

to be neglected at the observer with the measured mean flow around 2 m/s for the studied fingerings. However, the mean flow velocity varies across the axial direction and is higher when it is closer to the inlet.

The FW-H estimation of the outgoing pressure using  $G_T$  is compared with the LB simulation result in the time- and frequency-domain, which are shown in Figs. 7.16 and 7.17,

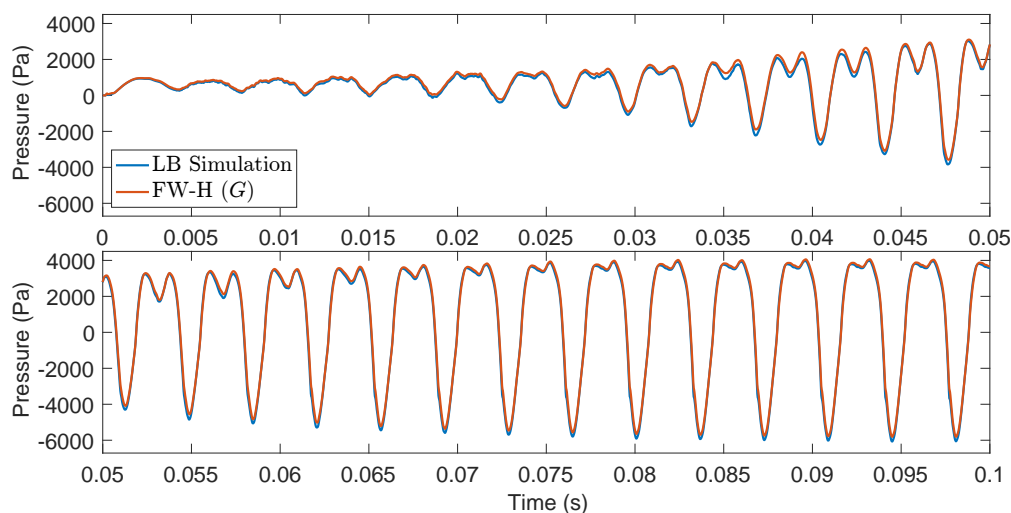


**Fig. 7.14:** The time-domain comparison of the outgoing pressure between the LB simulation and FW-H with  $G$  (fingering  $B^b4$ ).

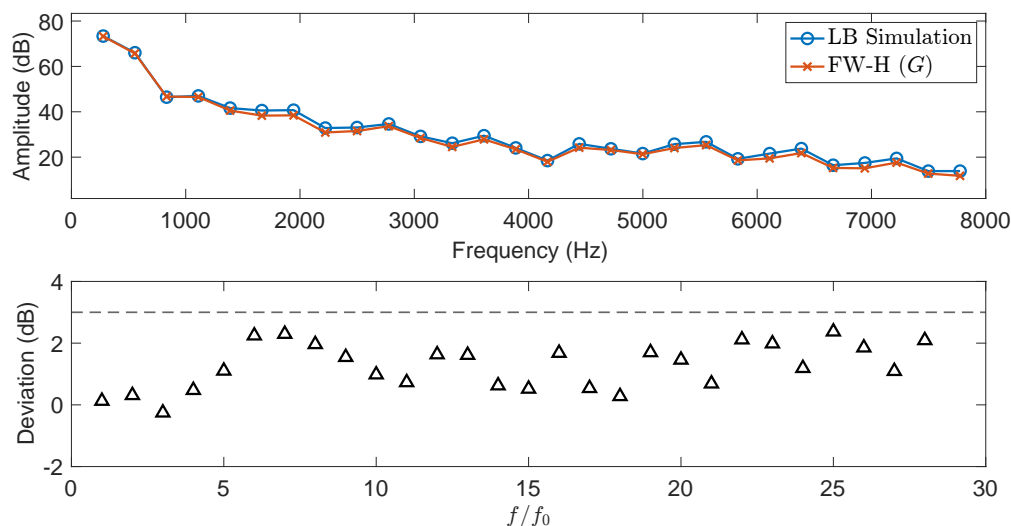


**Fig. 7.15:** The comparison of the outgoing pressure spectra between the LB simulation and FW-H with  $G$  (top), and the deviation in dB (bottom) (fingering  $B^b4$ ).

respectively. The FW-H with  $G_T$  shows a larger discrepancy compared to FW-H with  $G$ . This is because FW-H with  $G_T$  involves extra assumed planar traveling waves from image sources to the observer, which results in a larger deviation from the actual wave traveling in the LB simulation.

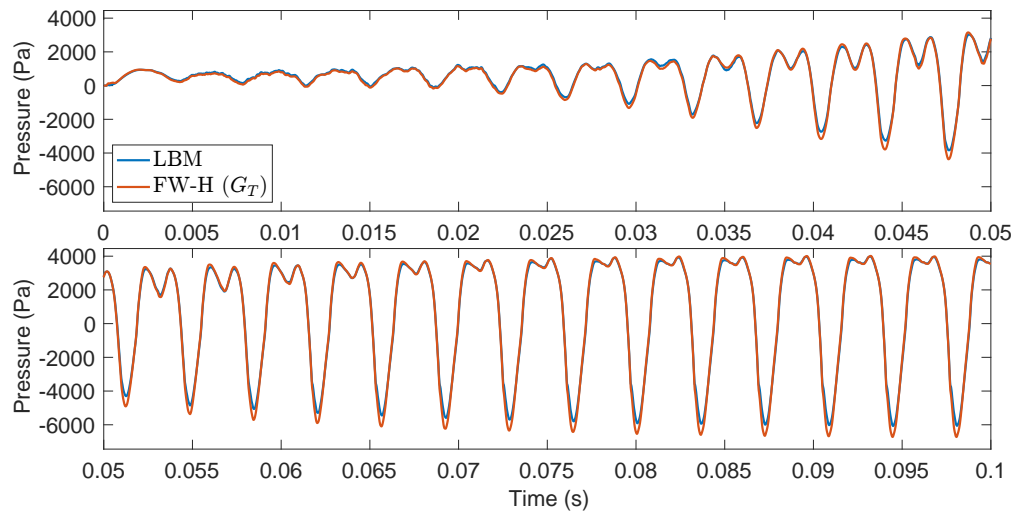


**Fig. 7.16:** The time-domain comparison of the outgoing pressure between the LB simulation and FW-H with  $G_T$  (fingering B<sup>b</sup>4).

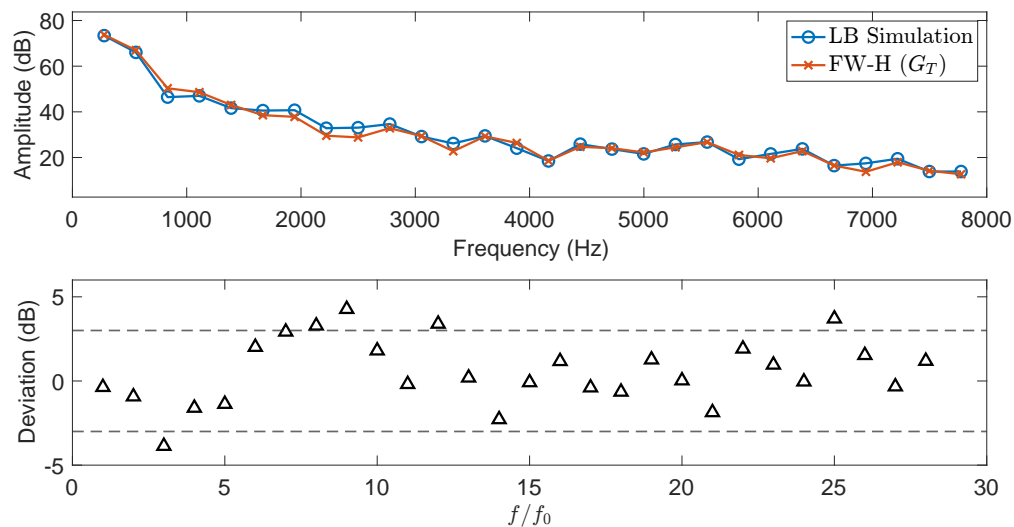


**Fig. 7.17:** The comparison of the outgoing pressure spectra between the LB simulation and FW-H with  $G_T$  (top), and the deviation in dB (bottom) (fingering B<sup>b</sup>4).

### 7.3.4.2 Comparison of different sound generation mechanisms

One of the main benefits of using the FW-H acoustic analogy is its ability to decompose the sound into contributions from various sound generation mechanisms. The equivalent sound level  $L_{\text{eq}}$  is used to measure the strength of different sound sources:

$$L_{\text{eq}} = 10 \log \frac{1}{T} \int \frac{p(t)^2}{p_0^2} dt, \quad (7.17)$$

where  $p$  is the sound pressure signal,  $p_0 = 20 \mu\text{Pa}$  is the reference pressure, and  $T$  is the period of the signal.

For the FW-H with  $G$ , the sound sources are decomposed into the dipole, reed monopole, and inlet monopole, corresponding to the terms (II'), (III) and (IV) in Eq. 7.10, respectively. Their time-domain signals are compared in Fig. 7.18, and the  $L_{\text{eq}}$  of steady-state signals are 184.1 dB, 170.4 dB, and 152.3 dB, correspondingly. It is clear that the dipole, which is generated by the unsteady-force exerted by the solid walls to the fluid, dominates the sound generation. This seems paradoxical because one may assume that the modulated jet flow through the reed channel to be the main source in the saxophone sound generation. Such a contrary finding comes from the fact that the fluctuating force that contributes to the dipole in FW-H with  $G$  is not only composed of the fluctuation in rotational fluid fields such as the vortices, but also the acoustic fluctuation, which is essentially the acoustic response of the mouthpiece solid walls' to the incoming wave from the resonator. In other words, the dipole presented in term (II') not only accounts for the presence of solid walls in the fluid, but also for the interaction of reflected sound from the resonator with the solid walls (Howe, 2003, Sec. 2.3.2). The interaction with the reflected sound reveals the role of the mouthpiece as an acoustic resonator as discussed in Ch. 6.

The acoustic response of the mouthpiece solid walls is excluded from the dipole when using FW-H with  $G_T$ , because the reflection of the incoming acoustic wave appears in a separate term (V'') in Eq. 7.15. The comparison of different contributions in FW-H with  $G_T$  is shown in Fig. 7.19, and the sound level  $L_{\text{eq}}$  of the dipole term (II'')<sup>4</sup>, reed monopole term (III''), and the inlet monopole (IV'') are 171.2 dB, 158.3 dB, and 173.3 dB, respectively. Additionally, the term (V'') that comes from the reflection of the incoming wave at the inlet

---

<sup>4</sup>Although the term (II'') is equivalently a quadrupole composed of the dipole and image dipole, it is called dipole sound source here to keep the consistency with that in FW-H with  $G$ .

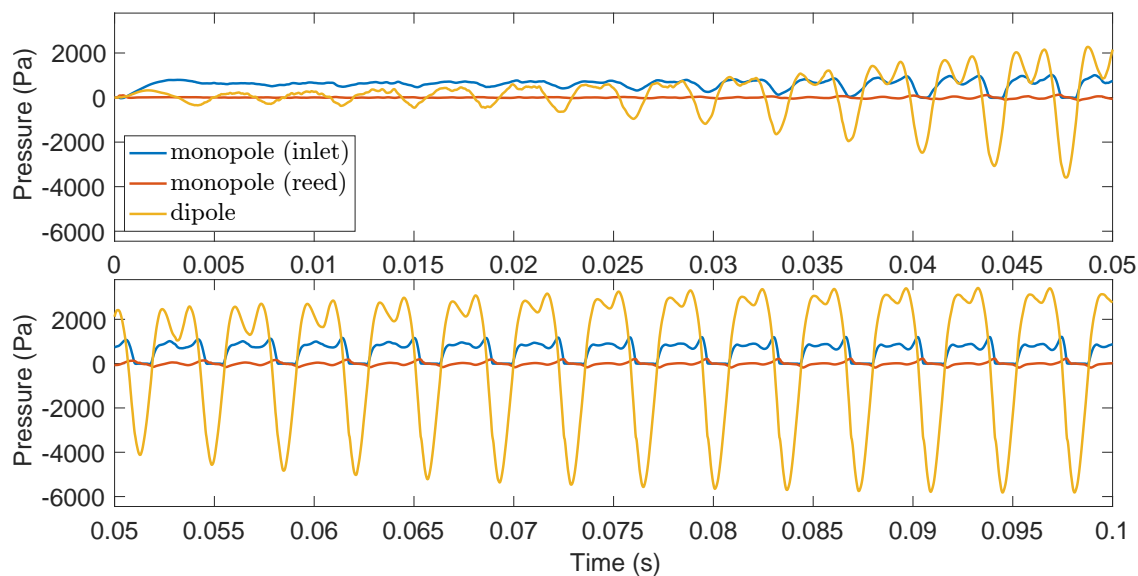


**Fig. 7.18:** The comparison between different contributions to the outgoing pressure at the observer using FW-H with  $G$ .

contributes 184.5 dB, which dominates the outgoing pressure sound level at the observer.

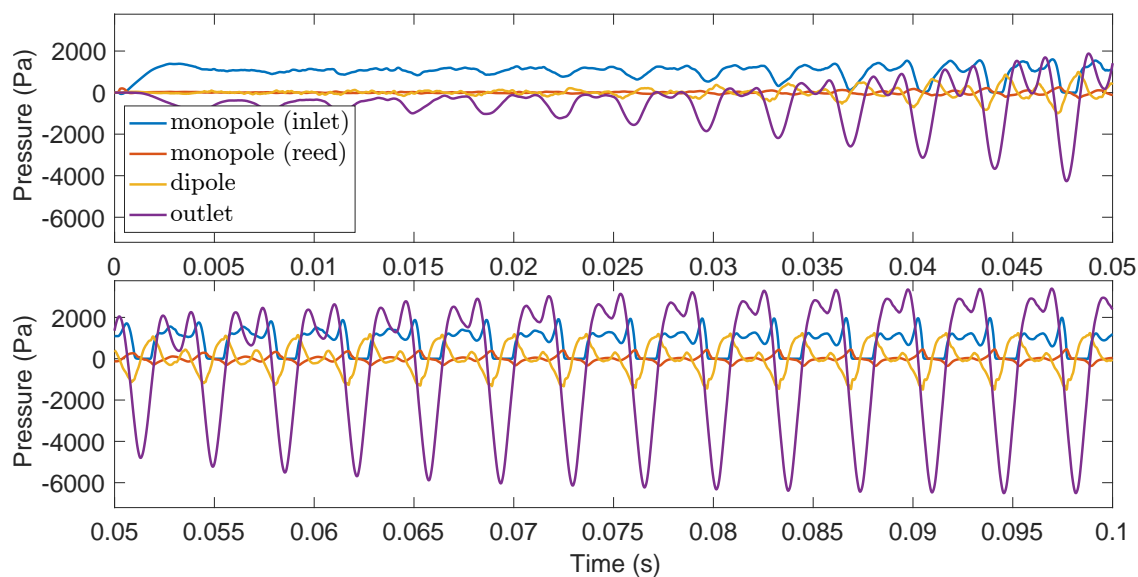


**Fig. 7.19:** The comparison between different contributions to the outgoing pressure at the observer using FW-H with  $G_T$ .

### 7.3.4.3 Effect of playing frequency

The effect of playing frequency is examined by comparing the relative contribution of monopoles to dipoles at different playing frequencies. The FW-H with  $G$  is used in this analysis.

The root-mean-square of the pressure signal is used to represent the strength of the sound source

$$p_{\text{rms}} = \sqrt{\frac{1}{T} \int_0^T p(t)^2 dt}. \quad (7.18)$$

The dependency of monopole-dipole  $p_{\text{rms}}$  ratios on playing frequency is shown in Fig. 7.20, and it shows that the relative contribution of monopoles increases with the playing frequency. This is due to the nature of the sound source, where the monopole is contributed by the  $\partial Q/\partial t$  term in the Ffowcs Williams-Hawkings equation, Eq. 3.57, while the dipole is contributed by  $\partial F_i/\partial x_i$ . The frequency dependency of the monopole is better illustrated in the frequency domain, where  $\partial \hat{Q}/\partial t = i\omega \hat{Q}$ , with  $\hat{Q}$  being the Fourier transform of  $Q$ . The dipole term, on the other hand, is not supposed to vary much with the playing frequency.

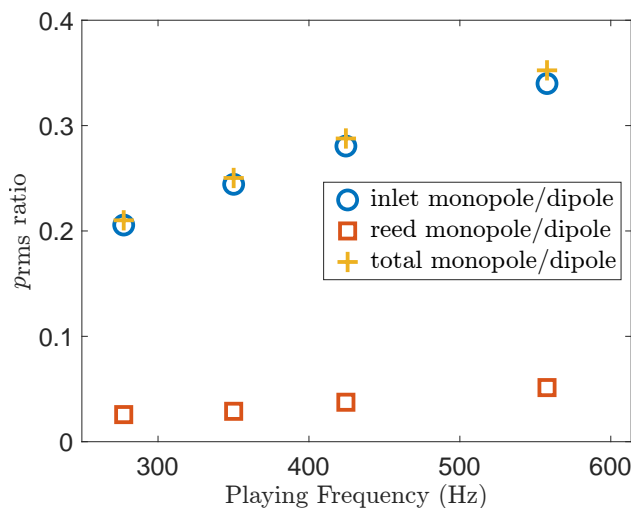


**Fig. 7.20:**  $p_{\text{rms}}$  ratio between different monopole and dipole sound sources at different playing frequencies.

In addition, the sound source at the inlet is considered as an equivalent monopole  $\rho v_1 M_1 + \rho v_1^+$  as discussed in Sec. 7.3.1, and the  $p_{\text{rms}}$  ratio between the  $\rho v_1 M_1$  contribution and the total inlet monopole is displayed in Fig. 7.21, and the contribution by the momentum flux  $\rho v_1 M_1$  at the inlet is found to increase over playing frequencies.

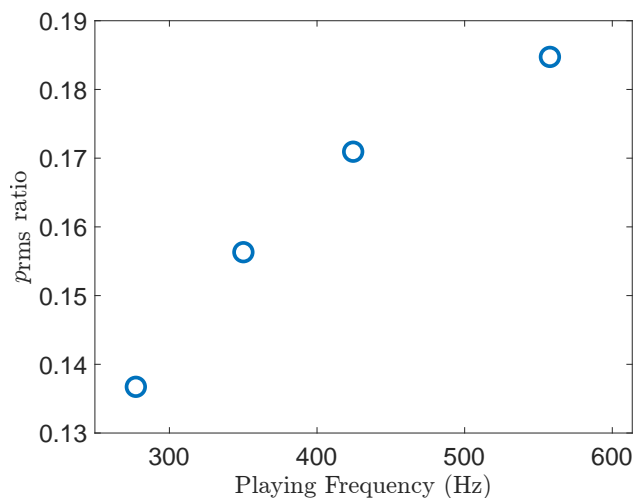


**Fig. 7.21:**  $p_{\text{rms}}$  ratio between the  $\rho v_1 v_1$  contribution and inlet monopole at different playing frequencies.

#### 7.3.4.4 Dipole characterizations

The dipole sound source is further decomposed into contributions by different solid walls, including the upper mouthpiece  $S_{\text{mp}}^{\text{upper}}$ , the lower mouthpiece  $S_{\text{mp}}^{\text{lower}}$ , and the reed surface  $S_r$ . The time-domain pressure signals are compared in Fig. 7.22. It shows that the upper mouthpiece contributes the strongest dipole compared to other walls. This is primarily attributed to the long inclined baffle connecting the tip rail to the mouthpiece throat. The reed dipole is roughly in phase with the upper mouthpiece dipole, but is out of phase with the lower mouthpiece dipole. This is because the upper mouthpiece and the reed are oriented in the positive direction of  $x_1$ , while the ramped wall of the lower mouthpiece is facing in the opposite direction, resulting in a different sign of the axial component normal vectors  $n_1$  when computing the dipole contribution, and hence a  $180^\circ$  phase difference. The root-mean-square compressive stress ( $(p_{1j}n_j)_{\text{rms}}$ ) distribution on solid walls is plotted in Fig. 7.23, together with the mouthpiece geometry shown at the bottom. Because the reed is moving over time, its time-averaged position is used in the plot. Figure 7.24 shows the same compressive stress distribution and the mouthpiece geometry as Fig. 7.23 and superimposes the absolute value of the solid wall slope  $|dy/dx|$  on the compressive stress plot. The range of the  $|dy/dx|$  plot is scaled so that the peak value of the two plots are aligned. The well-overlapped curves of the  $[p_{1j}n_j]_{\text{rms}}$  and  $|dy/dx|$  demonstrate the dependency of the dipole sound source on the mouthpiece geometry.

If  $[p_{1j}n_j]_{\text{rms}}$  can be assumed as a linear function of  $|dy/dx|$  for a specific period simulated, the amplitude contributed by the upper mouthpiece will mainly depend on the height difference in  $x_2$ -axis between the bore and the reed channel, and is less influenced by the shape of the wall. It also means the sound level in the mouthpiece is almost uniform along the wall, especially for the signal that has a dominant fundamental. This is also why the mouthpiece can be modeled using the lumped model as discussed in Ch. 6. However, the  $[p_{1j}n_j]_{\text{rms}}$  curve deviates from the  $|dy/dx|$  curve when it is closer to the tip of the mouthpiece. The area that extends from the end of the reed channel is known as the baffle of the mouthpiece, whose shape is known to have a significant influence on sound generation. This is also the area that the jet tends to reattach to after the initial separation at the entrance of the reed channel. In addition, the two curves on the reed misalign with each other, which is mainly because the reed movement creates a more complex pressure distribution along the reed.

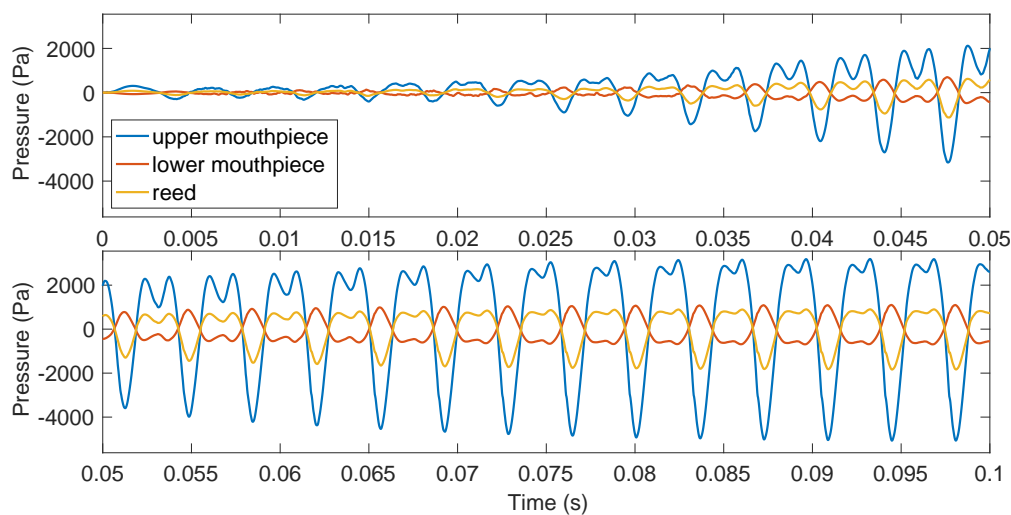


**Fig. 7.22:** The time-domain comparison of dipole sound sources contributed by different solid walls (fingering  $B^b4$ ).

### 7.3.5 Conclusion

In this section, the FW-H acoustic analogy is used to analyze the saxophone sound generation. It relies on the FW-H equation and makes use of the LBM-based computational aeroacoustic model of the saxophone mouthpiece to characterize the sound generation within the mouthpiece. The FW-H acoustic analogy provides a distinct perspective on the role of

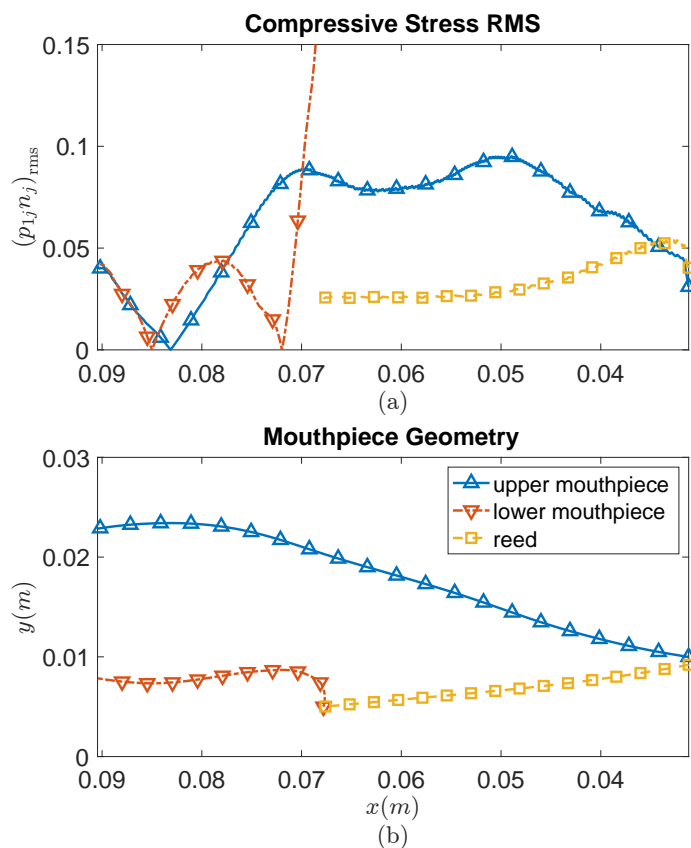


**Fig. 7.23:** (a) The  $(p_{1j}n_j)_{\text{rms}}$  distribution along solid walls, and (b) the mouthpiece geometry.

the mouthpiece by taking it as part of the sound generator with sound sources distributed inside. This is in contrast to the mouthpiece acoustic modeling in Ch. 6, where the mouthpiece is viewed as a passive acoustic resonator. The FW-H acoustic analogy improves the understanding of sound generation inside the mouthpiece by distinguishing between various sound generation mechanisms contributed by different parts of the mouthpiece. The application of different Green's functions in FW-H formulations leads to different interpretations of the sound generation mechanisms. When the 1D Green's function for an infinite pipe  $G$  is chosen, the sound at the observer is decomposed as the equivalent monopole source contributed by the pulsating jet through the reed channel, the monopole due to reed-induced flow, and the dipole arising from the unsteady force exerted on fluid by solid walls. The dipole sound source involves the interactions of the wall with fluid aerodynamic force and the reflected wave from the acoustic resonator, which together make it the dominant sound source in the

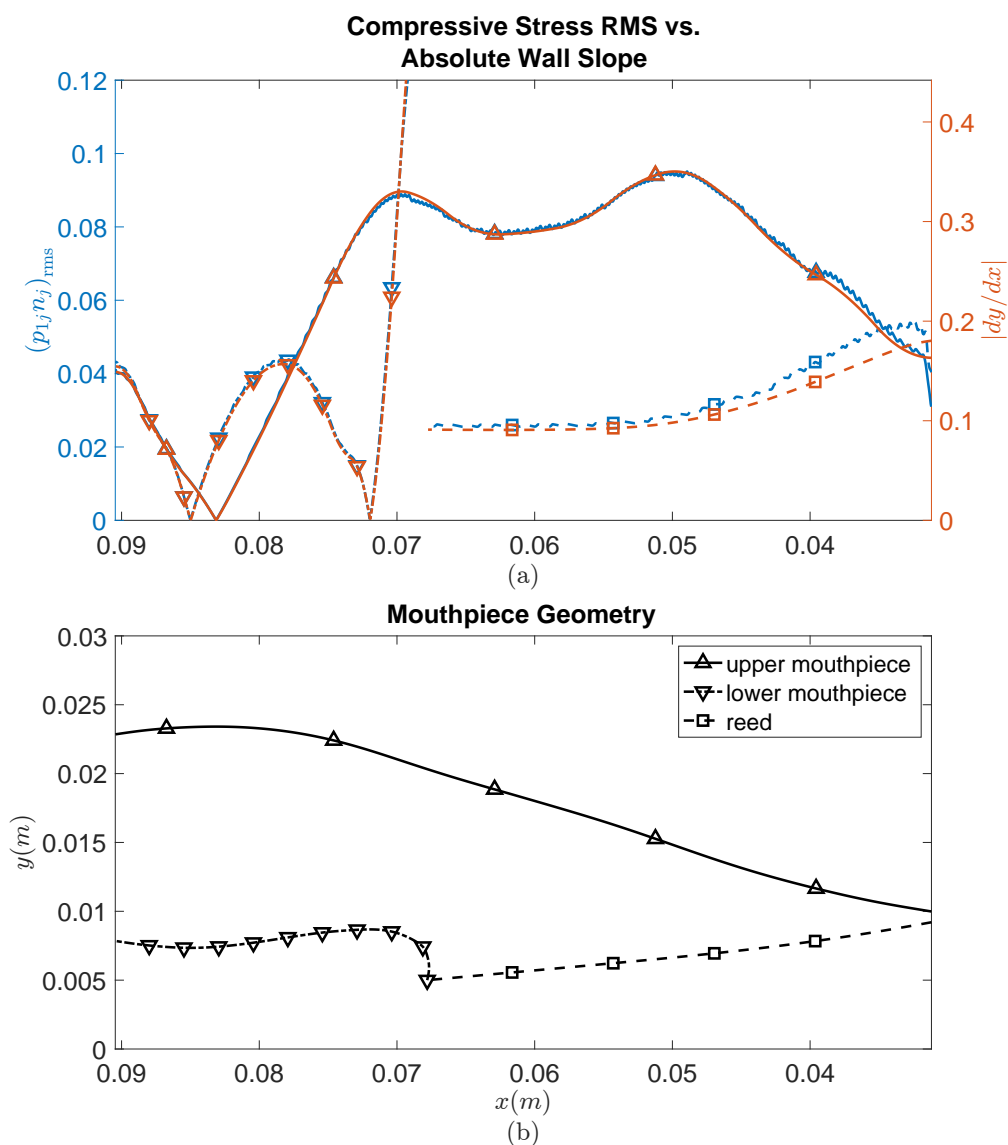


**Fig. 7.24:** (a) The  $(p_{1j}n_j)_{\text{rms}}$  distribution along solid walls shown in left  $y$ -axis, in compare to the absolute values of solid wall slopes  $|dy/dx|$  in right  $y$ -axis (a) and the mouthpiece geometry (b).

mouthpiece. When using the 1D Green's function for a semi-infinite pipe terminated at the inlet  $G_T$ , the monopoles are strengthened when being placed by the closed end of the pipe, while the dipole sound source turns into a quadrupole, which has less contribution to the outgoing pressure at the observer.

There exist discrepancies between LB-simulated and FW-H estimated pressure at the

observer, which can be attributed to two main factors. On the one hand, the spurious reflection from C-TDIBC disturbs the upstream acoustic fields, which makes it difficult to assume a planar wave at the observer and affects the calculation of spatially-averaged pressure in the LB domain. On the other hand, the application of a 1D Green's function to solve the FW-H equation assumes a planar wave traveling in a uniform pipe from a sound source to the observer. However, this assumption is violated due to the complex geometry of the mouthpiece. In addition, a larger discrepancy is observed when the tailored 1D Green's function  $G_T$  is applied. This extra discrepancy arises primarily from the ideally-assumed closed wall at the inlet, which in reality presents a finite impedance due to the periodically opening reed channel. Further investigation is required to find a better Green's function to account for the geometry's influence on the traveling wave from the sources to the observer. One potential option is to adapt the 1D Green's function for an infinite pipe with a contraction (Ffowcs Williams and Howe, 1975) to the pipe with expansion. In addition, it is possible to calculate an impulse response for each point along the axial direction of the mouthpiece using methods such as digital waveguide. This gives an equivalent 1D Green's function for a mouthpiece with a fixed reed position, which can be used to solve the FW-H equation.

## Chapter 8

# Aeroacoustic study of the influence of saxophone mouthpiece design

Designing a saxophone mouthpiece requires in-depth knowledge of how different geometric parameters affect oscillation characteristics. Research investigating the relationship between the mouthpiece geometry and oscillation features can be broadly classified into two groups, as illustrated in Fig. 8.1. The first group aims at building a direct connection between design parameters and sound characteristics by measuring and analyzing the sound of a variety of commercial or customized mouthpieces (Fig. 8.1(a)). Wyman (1972) was one of the first researchers to explore such direct links. He classified mouthpieces into five categories, and investigated how different mouthpiece design factors, such as chamber length, baffle shape, window length and tip opening, influence the tone quality, intonation, and mouthpiece resistance. The oscillation characteristics are extracted from either recorded audio or subjective surveys completed by saxophone players. Pipes (2018) conducted a similar study, but with a focus on the timbre of the instrument. Both Wyman (1972) and Pipes (2018) utilized commercially available mouthpieces. The main problem with using such mouthpieces is that there are various design changes amongst mouthpieces, making it difficult to explore the impact of a single design parameter. To address this issue, Wyman (1972) created four sets of mouthpieces, each of which changed a single design parameter to investigate the effects of the ramp shape, bore-to-table angle, beak shape, and window length. A more recent research by Ozdemir et al. (2021) utilized a computer-aided design (CAD) mouthpiece model and 3D printing technique to generate 27 mouthpieces with customized geometries, which involved

nine design parameters with three different levels. Furthermore, an artificial blowing machine was employed to play the saxophone, which helps quantitatively control the playing parameters and enables a more reliable comparison between measurements.

The second group introduces an intermediate layer between sound and geometric parameters to better understand why and how a design parameter is associated with a specific oscillation characteristic (Andrieux et al., 2016, Lorenzoni et al., 2013). The intermediate layer is concerned with the physics of the saxophone sound generation, which essentially is the fluid-structure-acoustics interaction (FSAI) within the mouthpiece. The study in this chapter falls into the second category by applying acoustic and aeroacoustic modeling techniques provided in Chapters 6 and 7 to explore the influences of the chamber size and baffle height on sound and playability. The objective of this chapter is to demonstrate the application of the models developed in the previous two chapters, and discuss their potential and limitations.

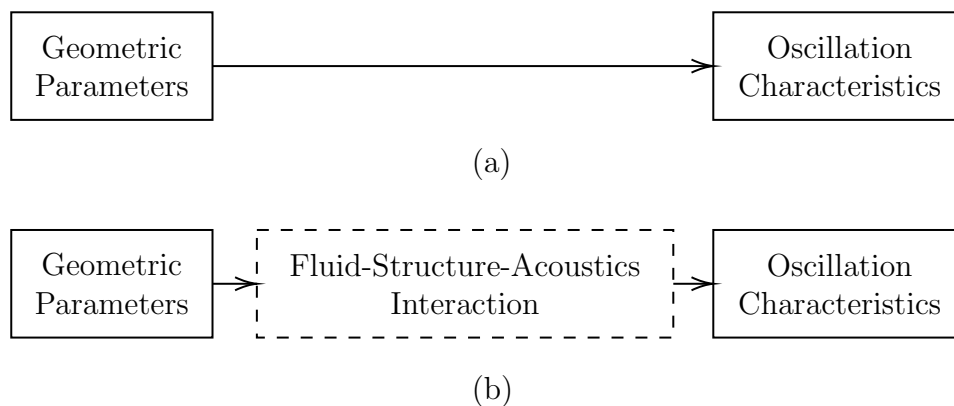


**Fig. 8.1:** Illustration of two different research categories.

## 8.1 Analysis procedures

The analysis procedure is shown in Fig. 8.2 and consists of three main processes: preprocessing, acoustic modeling, and aeroacoustic modeling.

### 8.1.1 Preprocessing

The preprocessing step prepares mouthpieces with various geometries and converts them into formats that will be used in acoustic and aeroacoustic modeling. It begins with the

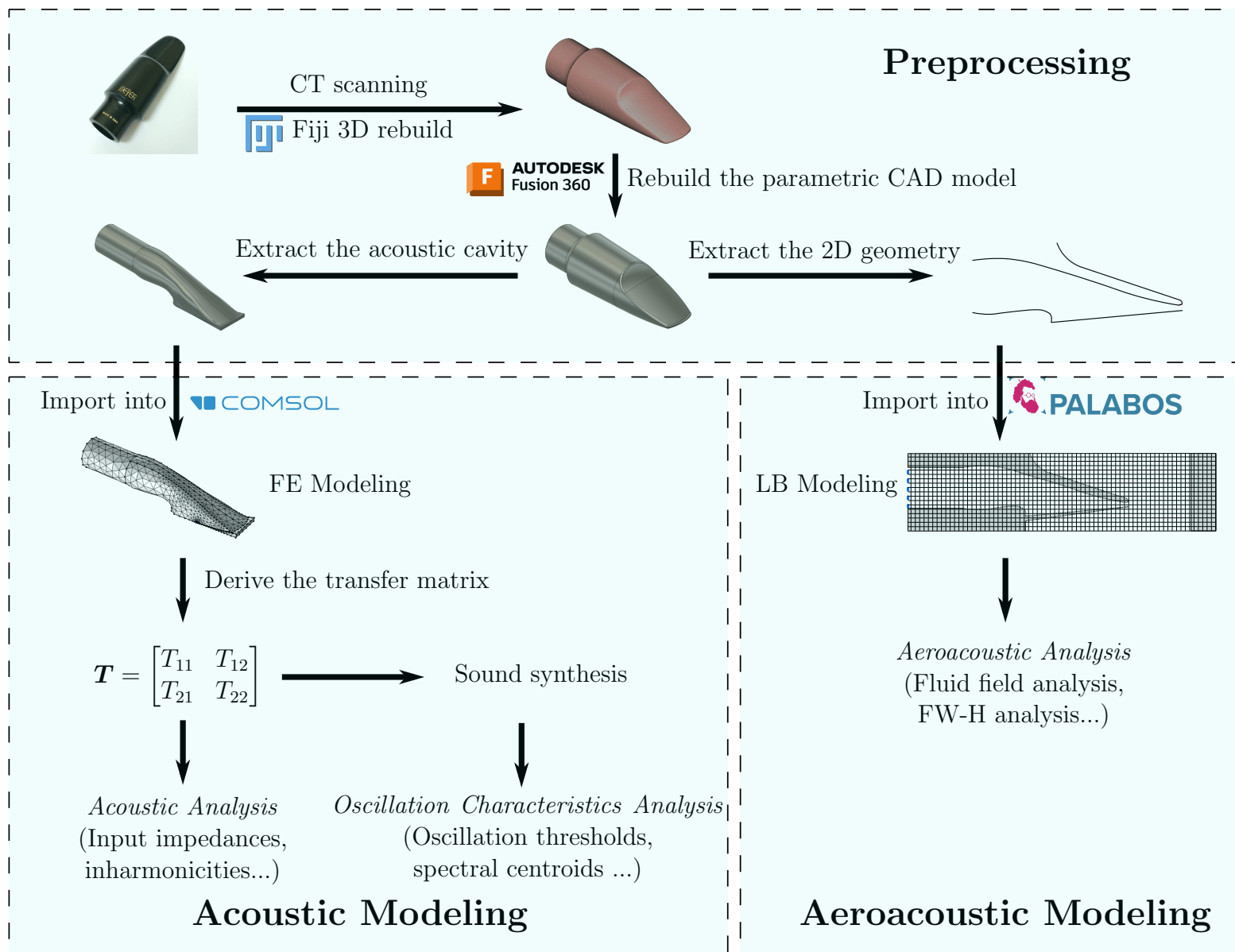


Fig. 8.2: The analysis procedures.

selection of commercial mouthpieces as reference models for developing a series of mouthpieces with a single design parameter modified. The Meyer 5M and Vandoren A45 Jumbo Java mouthpieces are used as reference models to study the effects of the chamber size and baffle height, respectively. The mouthpieces are first scanned using computed tomography (CT), and then the open-source software Fiji (Schindelin et al., 2012) is used to reconstruct the 3D mouthpiece from the image stacks. Autodesk Fusion 360 is used to create a 3D parametric CAD model based on the definitions of a series of sketches and mouthpiece design parameters. The scanned mouthpiece is imported into Fusion 360, and the parameters of the CAD model are manually adjusted to match the scanned one. A single design parameter, either the baffle height or the chamber size, is modified to develop a succession of mouthpiece variants. The inner cavities are obtained based on the definition in Sec. 6.2.1, and imported into COMSOL for the finite element (FE) modeling. The two-dimensional (2D) mouthpiece geometries are derived by projecting the mouthpiece onto its mid-sagittal plane, and they will be imported into Palabos for the lattice Boltzmann (LB) simulation.

### 8.1.2 Acoustic modeling

The acoustic modeling of a saxophone mouthpiece is described in Chapter 6. For a certain mouthpiece, its inner cavity is first imported into COMSOL for FE modeling, and the two-load method is applied to derive the transfer matrix representation of the mouthpiece:

$$\mathbf{T} = \begin{bmatrix} T_{11} & T_{12} \\ T_{21} & T_{22} \end{bmatrix}.$$

Two analyses are performed: the **acoustic analysis** primarily based on the input impedance, and the **oscillation characteristics analysis** relying on synthesized sound using the model specified in Sec. 6.4.3.1.

The **acoustic analysis** compares mouthpieces with the following acoustic characteristics:

- the *input impedance of a closed mouthpiece* calculated with the transfer matrix as  $Z_{\text{closed}} = T_{11}/T_{21}$ , with the volume of each mouthpiece set to the same value.
- the *input impedance of a complete saxophone*, where a complete saxophone consists of a mouthpiece and a saxophone body. The input impedance of the saxophone body  $\tilde{Z}_1$  is applied as an acoustic load to the mouthpiece, and the complete saxophone input

impedance is calculated using Eq. 6.5, which is rewritten here

$$\tilde{Z}_{\text{sax}} = \frac{T_{11} + T_{12}/\tilde{Z}_2}{T_{21} + T_{22}/\tilde{Z}_2},$$

where the tilde indicates a normalized input impedance. As discussed in Sec. 6.4.1 and illustrated in Fig. 6.5,  $\tilde{Z}_2 = \tilde{Z}_1 S_2 / S_1$  is used to account for the discontinuity between the mouthpiece and the saxophone neck in the above equation. The mouthpiece volume is separately adjusted for different mouthpieces and fingerings such that the frequency of the impedance peak aligns with the corresponding equal-tempered scale frequency. The first-register notes below D5 (written) use the frequencies of the first peak of the input impedance  $f_1$  to adjust the volume, while the second-register notes use the frequencies of the second peak  $f_2$ .

- the *radiation transfer function of a complete saxophone* that is calculated using Eq. 6.8,

$$\tilde{E}_{\text{sax}} = \frac{\tilde{E}_2}{T_{21}\tilde{Z}_2 + T_{22}},$$

where  $\tilde{E}_2$  represents the radiation transfer function of the saxophone body on the mouthpiece side of the mouthpiece-neck discontinuity.

- the *frequency deviation* in cents between  $f_1$  or  $f_2$  of the input impedance and the equal-tempered scale frequency for each note of an alto saxophone. Different mouthpiece volumes are tuned independently so that  $f_1$  corresponds to the equal-tempered scale frequency for the F4 (written) fingering.
- the *inharmonicicity*, which is defined as  $I = (f_2 - 2f_1)/2f_1$ . The same volume is used as for the frequency deviation.

The sound of the saxophone is synthesized for the **oscillation characteristics analysis**, and the following features are extracted to compare different mouthpieces:

- the *bifurcation diagram*, which is generated by extracting the envelope of the dimensionless mouthpiece pressure  $p$  and plotting it as a function of the dimensionless mouth pressure  $\gamma$ :
- the *oscillation thresholds* that include
  - the *oscillation threshold*  $p_{m,\text{osc}}$ ,
  - the *extinction threshold*  $p_{m,\text{ext}}$ ,

- the *inverse extinction threshold*  $p_{m,\text{ext}}^{\text{inv}}$ ,
- the *mouth pressure range*  $\Delta p_m = p_{m,\text{ext}} - p_{m,\text{ext}}^{\text{inv}}$ .

All the thresholds are chosen when the dimensionless mouthpiece pressure hits 0.02. Comparisons are made between dimensional mouth pressure  $p_m = \gamma P_M$  in Pascals for a better sense of the difference, where  $P_M = k_r H$  is the mouth pressure at which the reed closes, and  $k_r$  and  $H_0$  represent the reed stiffness and equilibrium tip opening, respectively. Because the inverse oscillation threshold should always be equal to  $P_M$ , it is not included in the comparison.

- the *deviation of the playing frequency from the equal-tempered scale frequency*,
- the *spectral centroid of the radiated sound* that is calculated within the frequency range of [100, 8000] Hz. The radiated pressure is computed in the frequency domain as  $P_{\text{rad}}(\omega) = E(\omega)U(\omega)$ , where  $U(\omega)$  represents the synthesized mouthpiece velocity. It is worth noting that the direct synthesis of radiated sound in the time domain using the recursive parallel filter is not employed in the analysis to avoid the potential influence of fitting errors.
- the *radiated sound energy* that is calculated using

$$\frac{1}{N_{\text{FFT}}} \sum_{k=K_1}^{K_2} |P_{\text{rad}}[k]|^2,$$

where  $P_{\text{rad}}[k]$  is the discrete Fourier transformed radiated pressure,  $N_{\text{FFT}}$  is the number of points used to calculate the discrete Fourier transform, and  $K_1$  and  $K_2$  correspond to the frequency bins that define the boundaries of the frequency range [100, 8000] Hz.

### 8.1.3 Aeroacoustic modeling

The aeroacoustic modeling of the mouthpiece is based on the LB model, which is described in Ch. 7. The 2D mouthpiece is obtained by projecting the 3D mouthpiece onto its mid-sagittal plane, and the lay profile is fitted by a fourth-order polynomial, as shown in Eq. 7.6. The length of the mouthpiece bore is adjusted so that the 2D mouthpiece area is consistent across all mouthpiece variants.

The **aeroacoustic analysis** utilizes LB simulation and the Ffowcs-Williams and Hawkins (FW-H) acoustic analogy to compare sound generation mechanisms in different mouthpiece designs. This analysis is applied to investigate only the influence of the baffle height

rather than chamber size since the aeroacoustic modeling is more effective in exploring flow-related phenomena that are highly sensitive to an upstream geometry change near the reed channel.

## 8.2 Influence of the chamber size

In this section, a comparison is made between three mouthpieces with different chamber sizes. The inner cavities of these mouthpieces are illustrated in Fig. 8.3. The Meyer 5M alto saxophone mouthpiece is employed as the reference model. A CAD sketch is created on a plane positioned 5 mm away from the throat, and the cross-sectional area of the inner cavity on this plane is used to define the chamber size. To facilitate easy control and comparison of chamber sizes, the cross-sectional area is defined as a circle. The circle radii are set to 6.5 mm, 8 mm and 9.5 mm, corresponding to the “small chamber”, “medium chamber”, and “large chamber” mouthpieces, respectively.

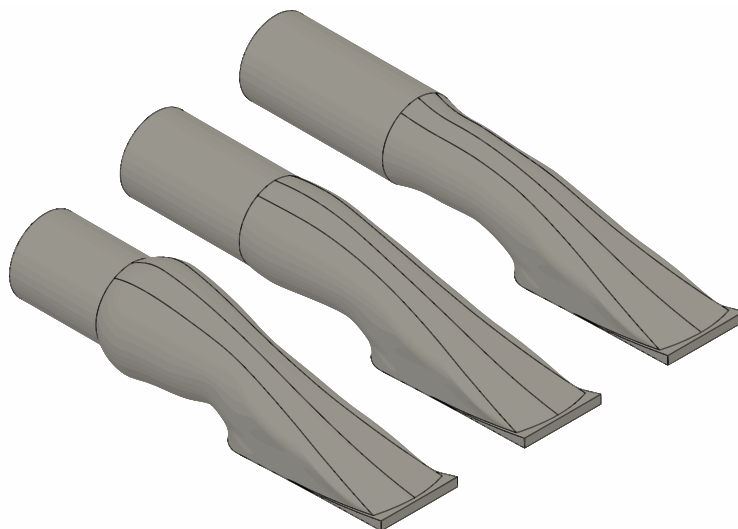


**Fig. 8.3:** Comparison between inner cavities of mouthpieces with different chamber sizes. The chamber size increases from right to left.

The closed mouthpiece input impedances are compared in Fig. 8.4, clearly demonstrating that the mouthpiece resonance frequency increases with the chamber size. Despite the mouthpiece’s complex geometry, its resonance frequencies are primarily influenced by the length of the mouthpiece. In mouthpieces with the same volume, a larger chamber mouth-

piece has a shorter length, resulting in higher resonance frequencies.

To compare complete saxophones, the alto saxophone bodies with fingerings B<sup>b</sup>3, B<sup>b</sup>4, and B<sup>b</sup>5 are taken as examples. Their input impedances are applied to the mouthpiece transfer matrix as load impedances, and the overall input impedances of complete saxophones are compared in Fig. 8.5. It shows that a larger chamber exhibits a slightly higher resonance frequency and a smaller magnitude for impedance peaks below 1000 Hz. The performance of intermediate to high frequencies is closely linked to the closed mouthpiece input impedance, as different mouthpieces emphasize different frequency components corresponding to the resonances of the mouthpiece itself.

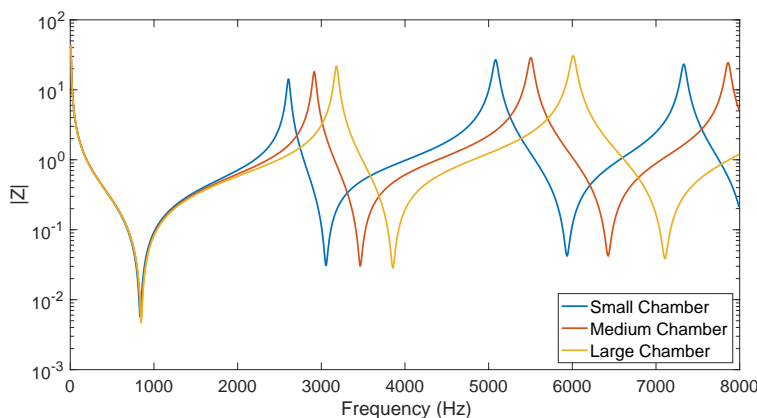


**Fig. 8.4:** Comparison of input impedances between closed mouthpieces with different chamber sizes.

The deviations in cents between the frequency of the input impedance peak and the equal-tempered scale frequency of each note are compared in Fig. 8.6(a). A larger chamber is shown to have higher resonance frequencies, which leads to a larger deviation, particularly noticeable in the second register. The inharmonicities are compared in Fig. 8.6(b) and it is observed that a larger chamber mouthpiece corresponds to a greater value of the inharmonicity  $I$ .

The sound is synthesized for different mouthpieces with two fingerings B<sup>b</sup>4 and B<sup>b</sup>5, which respectively represent notes in the first and second registers. The same synthesizing parameters as described in Sec. 6.4.3.1 are used in this analysis. The bifurcation diagram, deviation of playing frequencies from the equal-tempered scale frequencies, radiated sound spectral centroids, and radiated sound energy are compared among different mouthpieces in Figs. 8.7 and 8.8 for the two fingerings.

Different mouthpieces exhibit similar bifurcation characteristics, and the corresponding

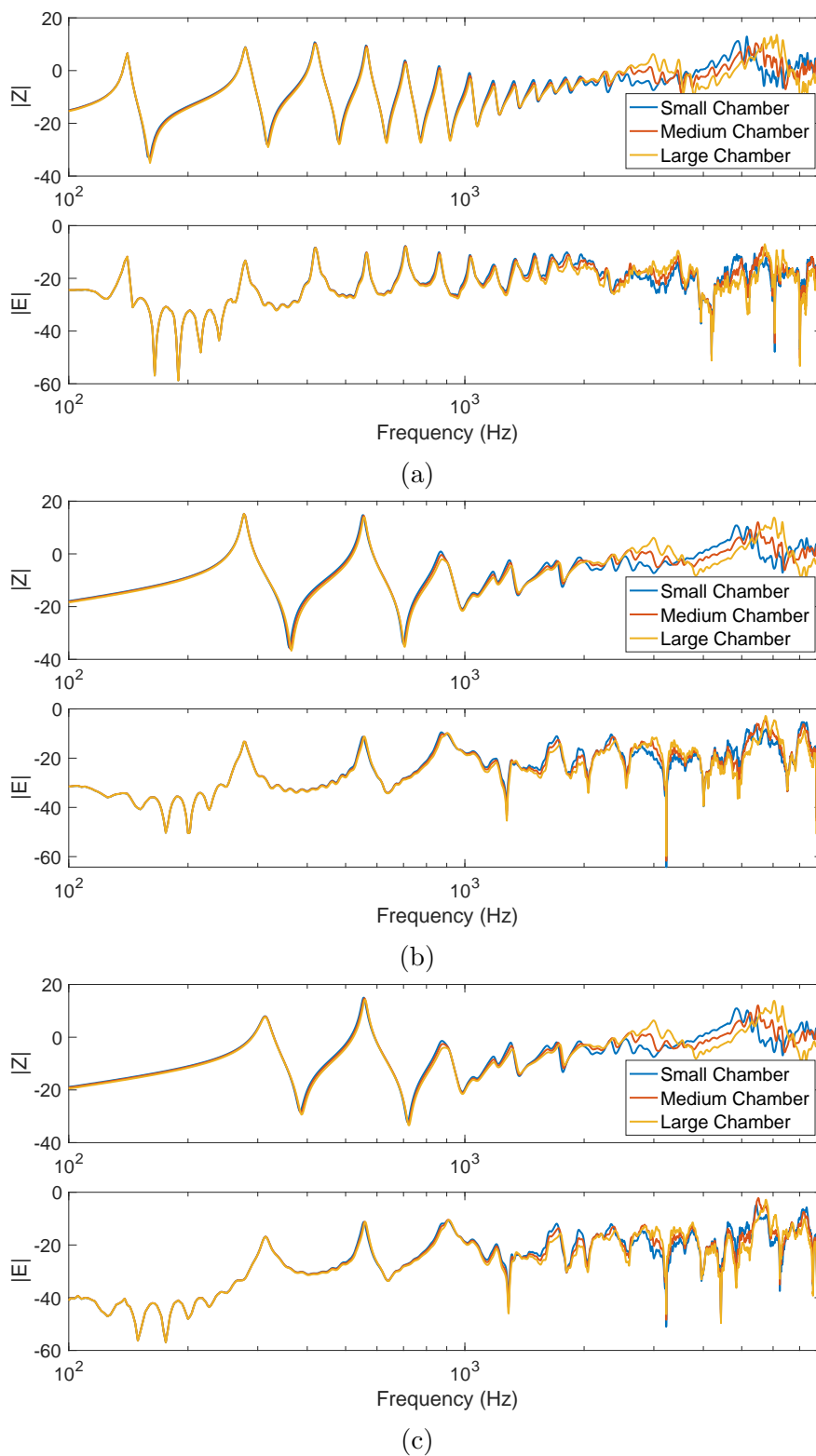


**Fig. 8.5:** Comparison of input impedances between saxophones consisting of mouthpieces with varying chamber sizes, and saxophone bodies with the fingering (a) B<sup>b</sup>3, (b) B<sup>b</sup>4, and (c) B<sup>b</sup>5 (written).

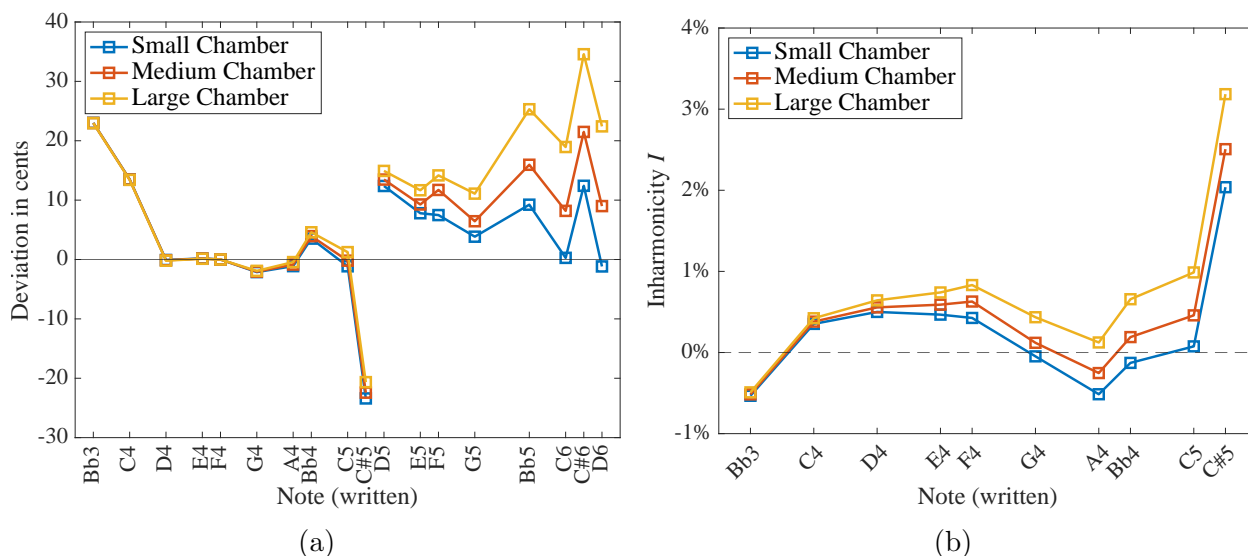


**Fig. 8.6:** Comparison of (a) frequency deviations of input impedance peaks from the equal-tempered scale frequency and (b) inharmonicities of different notes between mouthpieces with different chamber sizes.

mouth pressure thresholds are presented in Table 8.1. The chamber size has little influence on the oscillation thresholds in both registers, whereas it has a notable impact on the direct extinction thresholds. The influence is shown to be dependent on the register, with  $p_{m,ext}$  increasing with the chamber size for a high-register note ( $B^b5$ ) and decreasing with the chamber size for a low-register note ( $B^b4$ ). The dynamics characteristics are typically interpreted to provide information about the playability of an instrument (Fréour et al., 2020), and the comparison of the mouth pressure range  $\Delta p_m$  can be interpreted together with the comparison of the radiated sound energy. For a large chamber mouthpiece and a low-register note (Fig. 8.7), the instrument generates a less loud radiated sound and less dynamic range, but involves a larger mouth pressure range  $\Delta p_m$ . It indicates that a saxophonist needs to blow harder to play at a same dynamic level as a smaller chamber. For a high-register note (Fig. 8.8), a large chamber mouthpiece supports both a smaller dynamic range and mouth pressure range. It is also shown that the slope of the radiated sound energy (as a function of the mouth pressure) decreases with a larger chamber size, which means that a large chamber mouthpiece make it harder to crescendo for this fingering, which makes it a mouthpiece with a larger resistance (Wyman, 1972)<sup>1</sup>.

<sup>1</sup>It should be noted that the "resistance" is sometimes connected to the direct oscillation thresholds  $p_{m,osc}$

The playing frequencies, represented by their deviation from the equal-tempered scale frequencies, increase with the chamber size. This can be attributed to the increasing inharmonicity associated with larger chambers, as discussed in Sec. 2.2.2. The large chamber mouthpiece is shown to have a smaller range of the playing frequencies, which might indicate less flexibility to bend the pitch (Ozdemir et al., 2021).

Finally, a larger chamber results in a lower spectral centroid and reduced energy of radiated sound. This observation is consistent with previous studies, which have shown that larger chambers typically produce a darker and softer sound (Ozdemir et al., 2021, Pipes, 2018, Wyman, 1972). Such a result seems to contradict the comparison of input impedance and radiation transfer function spectra, in which a larger chamber has a higher resonance frequency, implying a higher spectral centroid. However, the spectra of the input impedance and radiation transfer function are different from the radiated sound spectra, where in the latter spectrum, the harmonic amplitudes decrease with the frequency so that the calculated spectral centroids are dominated by harmonics at low frequencies. Taking the fingering B<sup>b</sup>4 as an example, the first impedance peak of different mouthpieces is shown to have comparable amplitudes in Fig. 8.5, whereas a larger chamber has smaller amplitudes for the second and third impedance peaks. At low frequencies, the larger chamber is presented like an expansion in a pipe, which is known to act as a low-pass filter (Kinsler et al., 1999, Sec. 10.11), and this explains why it has a lower spectral centroid <sup>2</sup>.

---

(Ozdemir et al., 2021), which infers a different playability feature.

<sup>2</sup>It is worth mentioning that a constriction in a pipe also works as a low-pass filter at low frequencies. However, the “small chamber” mouthpiece used in this section does not present an obvious constriction area.

**Table 8.1:** Oscillation thresholds for mouthpieces with different chamber sizes.

Fingering	Chamber Size	$p_{m,osc}$ (Pa)	$p_{m,ext}$ (Pa)	$p_{m,ext}^{inv}$ (Pa)	$p_{m,ext} - p_{m,ext}^{inv}$ (Pa)
B <sup>b</sup> 4	Small	2532.8	17896.9	1888.7	16008.2
	Medium	2534.0	18353.9	1912.0	16441.8
	Large	2540.6	18477.8	1943.8	16534.0
B <sup>b</sup> 5	Small	2763.2	14171.3	2577.6	11593.7
	Medium	2775.4	13866.2	2607.9	11258.3
	Large	2789.2	13403.6	2621.3	10782.2

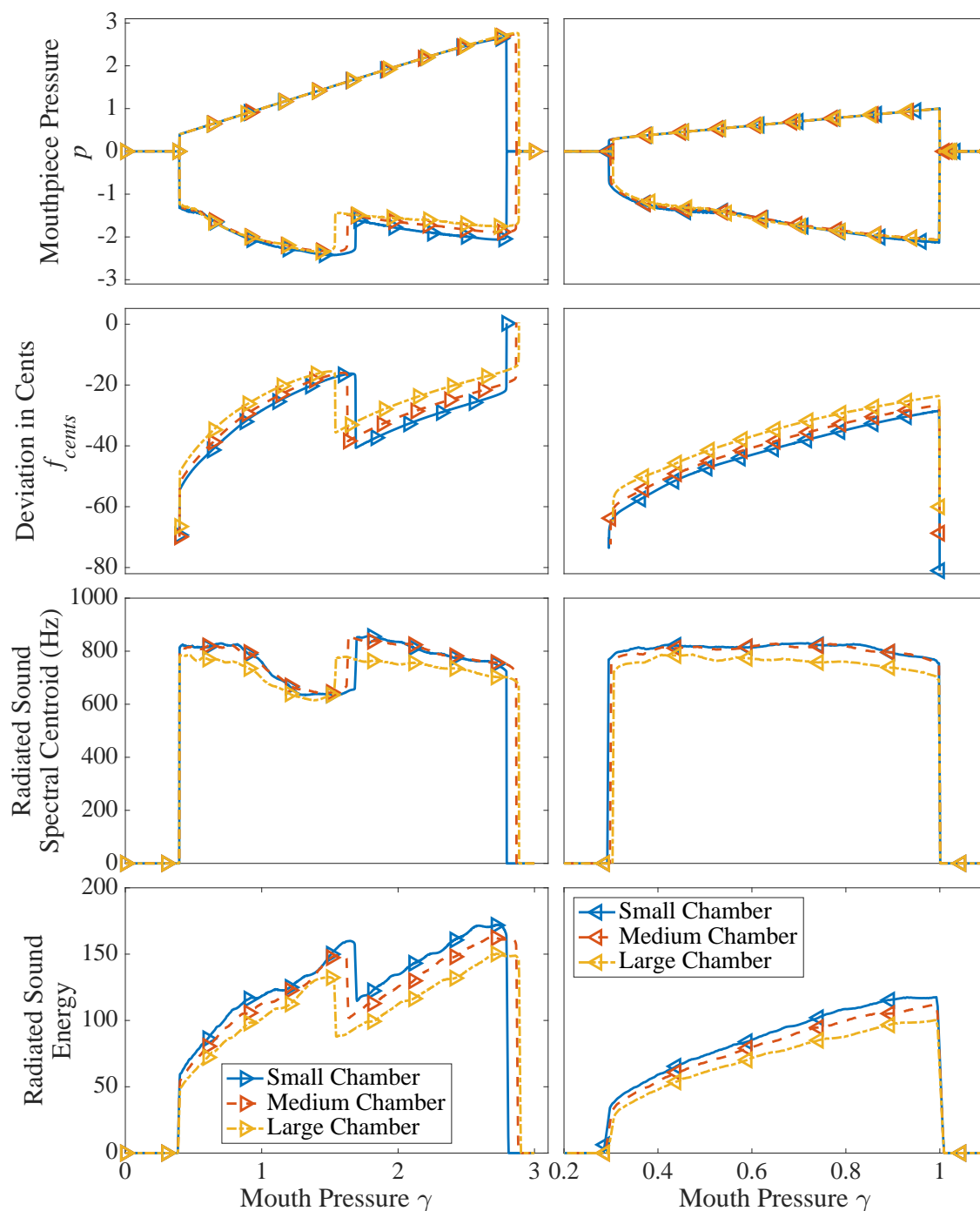


**Fig. 8.7:** Comparisons of the bifurcation diagrams, playing frequencies, radiated sound spectral centroid, and radiated sound energy for linearly increasing (left) and decreasing (right) mouth pressure profiles between mouthpieces with different chamber sizes attach to an alto saxophone (fingering B<sup>b</sup>4).

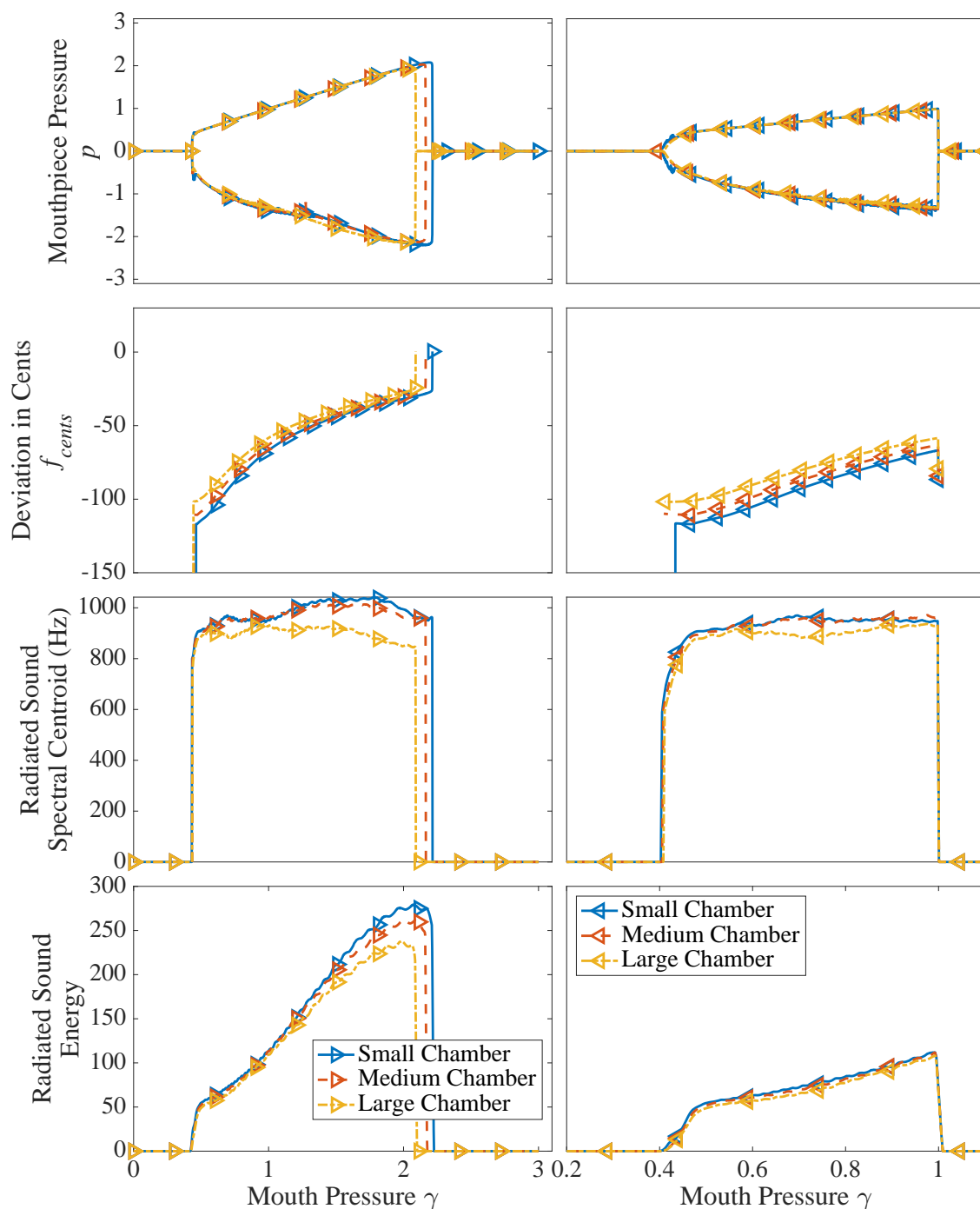


**Fig. 8.8:** Comparisons of the bifurcation diagrams, playing frequencies, radiated sound spectral centroid, and radiated sound energy for linearly increasing (left) and decreasing (right) mouth pressure profiles between mouthpieces with different chamber sizes attached to an alto saxophone (fingering  $B^b5$ ).

### 8.3 Influence of the baffle height

The baffle height is known to be another important factor in determining the sound of a saxophone, and it is determined by the distance between the baffle and the reed in the rest position (table plane). In this section, four mouthpieces with varying baffle heights are compared. They are denoted as “Baffle 1” through “Baffle 4”, with an increasing baffle-to-reed distance, and the sagittal view of the inner mouthpiece cavities is illustrated in Fig. 8.9<sup>3</sup>. This set of mouthpieces is developed based on the Vandoren A45 Jumbo Java mouthpiece, which itself corresponds to the mouthpiece “Baffle 1”.

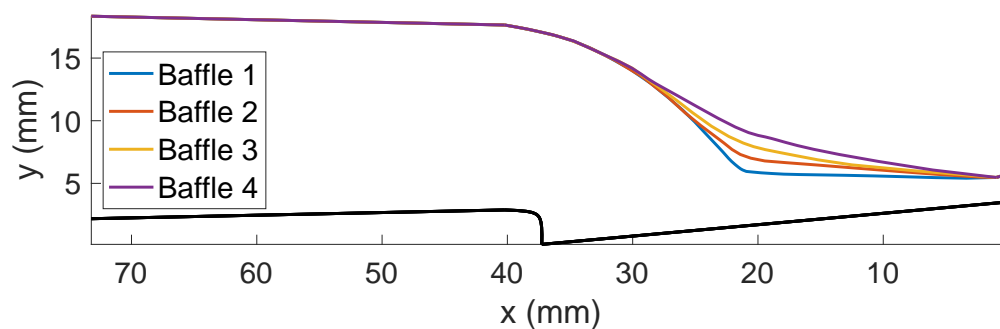


**Fig. 8.9:** Comparison of mouthpiece inner geometries with different baffle heights in the sagittal view.

#### 8.3.1 Acoustics modeling

The closed mouthpiece input impedances are compared in Fig. 8.10, and the resonance frequencies exhibit similar behavior as those observed in Fig. 8.4 for the chamber size comparison. A larger baffle-to-reed distance necessitates a shorter mouthpiece to maintain the same volume. This leads to an increase in resonance frequencies from “Baffle 1” to “Baffle 4”. Figure 8.11 compares the input impedances of complete saxophones, and it is shown that the impedance curves reflect the resonance structure of closed mouthpieces. While the baffle height has minimal influence on the first two impedance peaks, higher-frequency impedance peaks (below 1 kHz) tend to have slightly higher frequencies and smaller magnitudes. The

<sup>3</sup>It is worth noting that the conventional terminology in the literature refers to “high baffle” or “low baffle,” where a “high baffle” typically indicates a smaller baffle-to-reed distance due to the mouthpiece being positioned with the window facing upward. This is, however, the opposite of the mouthpieces shown in Fig. 8.9, where a smaller baffle-to-reed distance results in a “low” baffle. To prevent any potential confusion, a numerical system is adopted to represent the baffle heights.

baffle height shows a more pronounced influence in the intermediate frequencies from 1 kHz to 5 kHz, where a smaller baffle-to-reed distance results in larger amplitudes.

In addition, the baffle height has a minor impact on intonation and inharmonicity, as illustrated in Fig. 8.12.

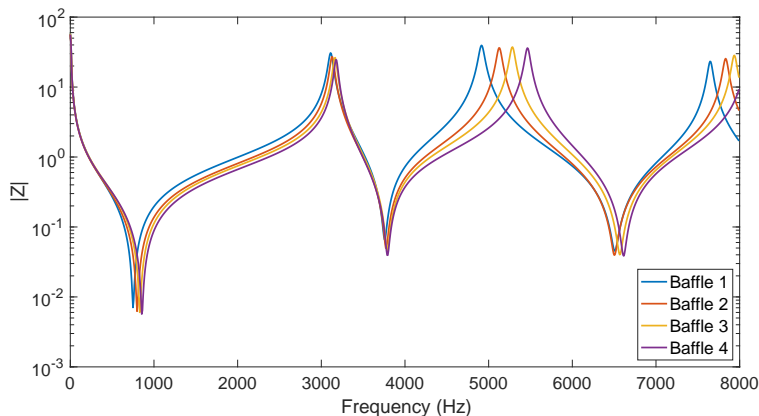


**Fig. 8.10:** Comparison of input impedances between closed mouthpieces with different baffle heights.

The dynamics characteristics are compared in Figs. 8.13 and 8.14, and the oscillation thresholds are presented in Table 8.2. Among all the oscillation characteristics, the baffle height appears to have the most significant influence on the radiated sound spectral centroid. A smaller baffle-to-reed distance is shown to result in a larger spectral centroid, which aligns with the findings from the analysis of the saxophone input impedances. This observation is also consistent with previous studies. For instance, Wyman (1972) stated that “the angle between the baffle surface and the plane of the table is inversely proportional to the brightness of the tone”. In this study, the baffle-to-reed angle serves as an alternative metric for the baffle height and is directly proportional to the mentioned angle. In addition, Ozdemir et al. (2021) identified the baffle height as an effective parameter influencing the spectral centroid, despite some unexpected trends found in their investigation of three baffle levels.

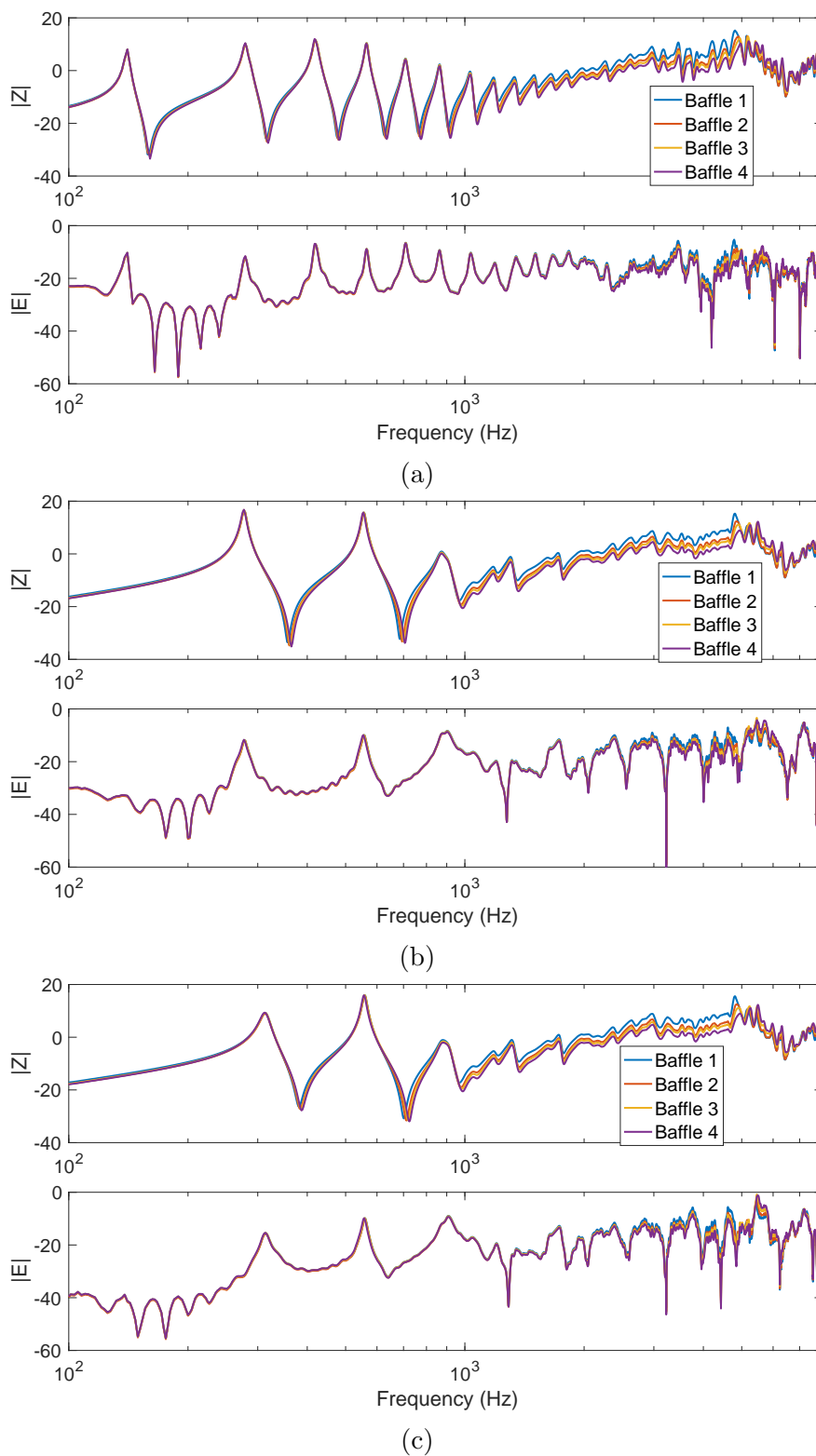


**Fig. 8.11:** Comparison of input impedances between saxophones consisting of mouthpieces with varying baffle heights, and saxophone bodies with the fingering (a) B<sup>b</sup>3, (b) B<sup>b</sup>4, and (c) B<sup>b</sup>5 (written).

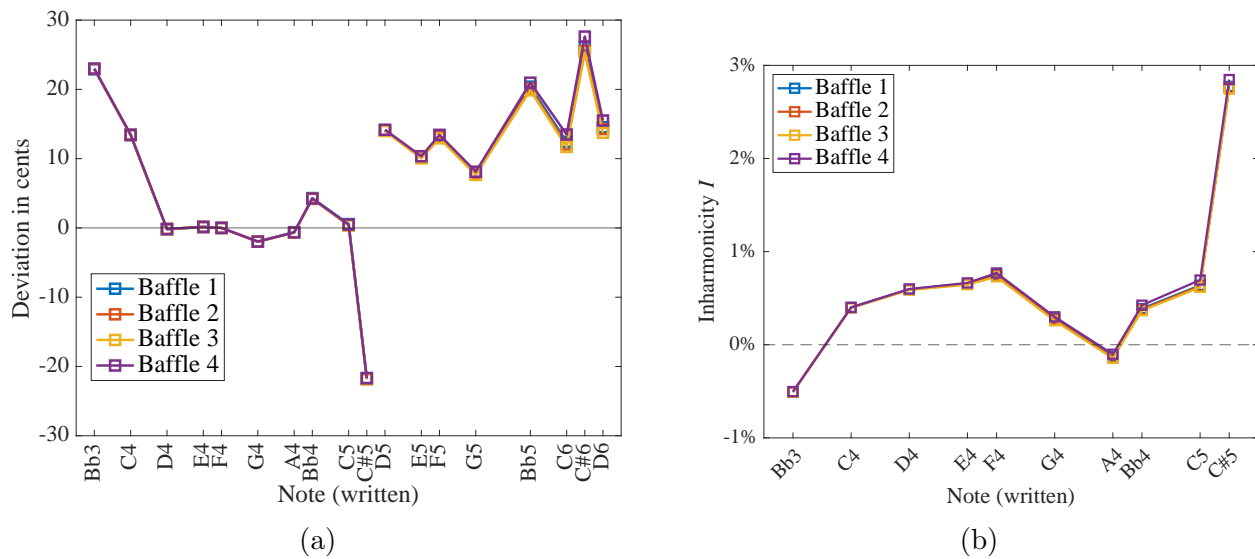


**Fig. 8.12:** Comparison of (a) frequency deviations of input impedance peaks from the equal-tempered scale frequency and (b) inharmonicities of different notes between mouthpieces with different baffle sizes.

**Table 8.2:** Oscillation thresholds for mouthpieces with different baffle heights.

Fingering	Chamber Size	$p_{m,osc}$ (Pa)	$p_{m,ext}$ (Pa)	$p_{m,ext}^{inv}$ (Pa)	$p_{m,ext} - p_{m,ext}^{inv}$ (Pa)
B <sup>b</sup> 4	Baffle 1	2565.0	16995.4	1907.8	15087.6
	Baffle 2	2575.6	16646.5	1946.2	14700.3
	Baffle 3	2570.7	17037.4	1952.3	15085.2
	Baffle 4	2569.3	17128.4	1973.8	15154.6
B <sup>b</sup> 5	Baffle 1	2807.0	12540.2	2628.7	9911.4
	Baffle 2	2830.8	12338.9	2647.8	9691.1
	Baffle 3	2824.8	12616.6	2633.6	9983.0
	Baffle 4	2839.1	12654.8	2626.8	10028.1

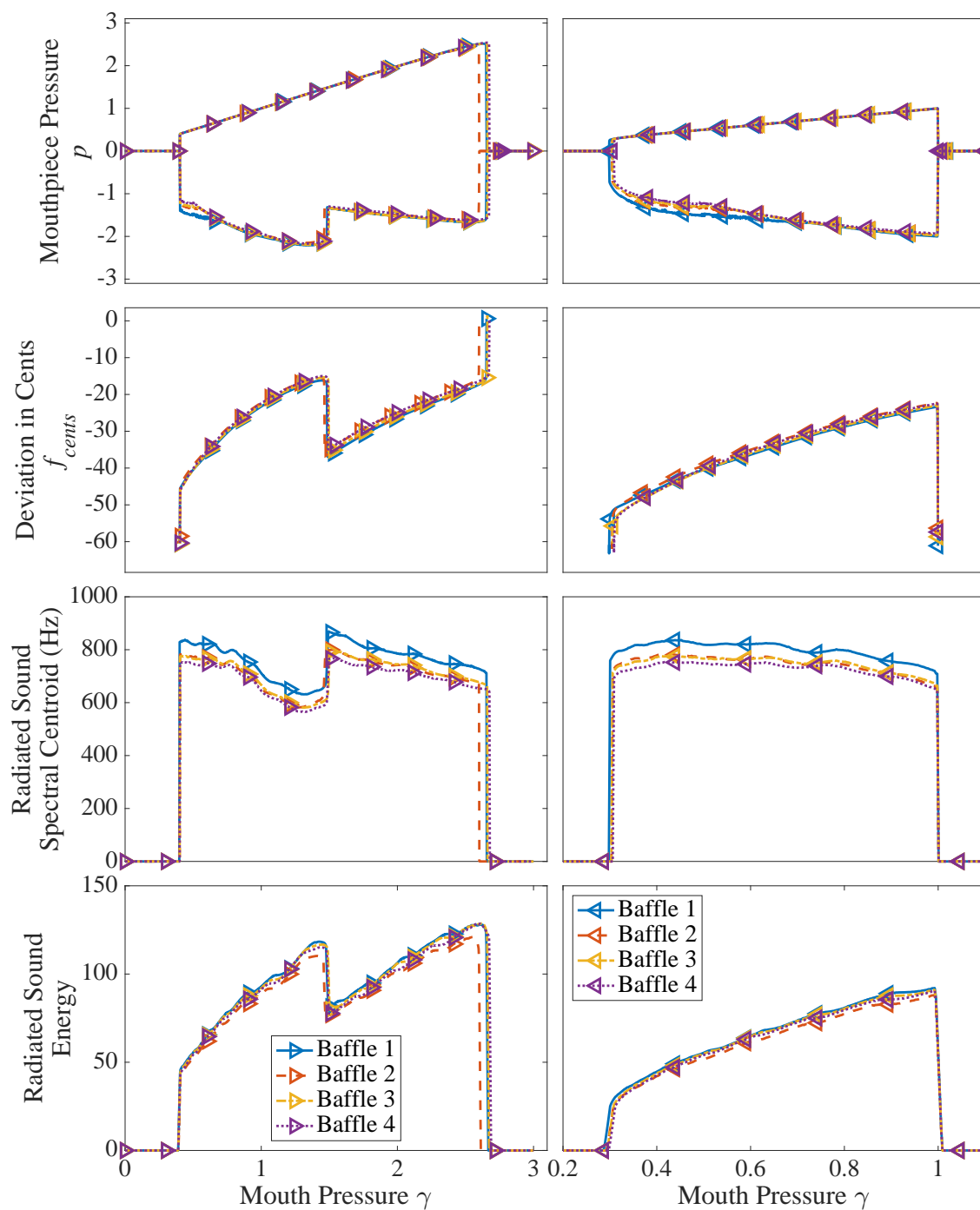


**Fig. 8.13:** Comparisons of the bifurcation diagrams, playing frequencies, radiated sound spectral centroid, and radiated sound energy for linearly increasing (left) and decreasing (right) mouth pressure profiles between mouthpieces with different baffle heights attach to an alto saxophone (fingering B<sup>b</sup>4).

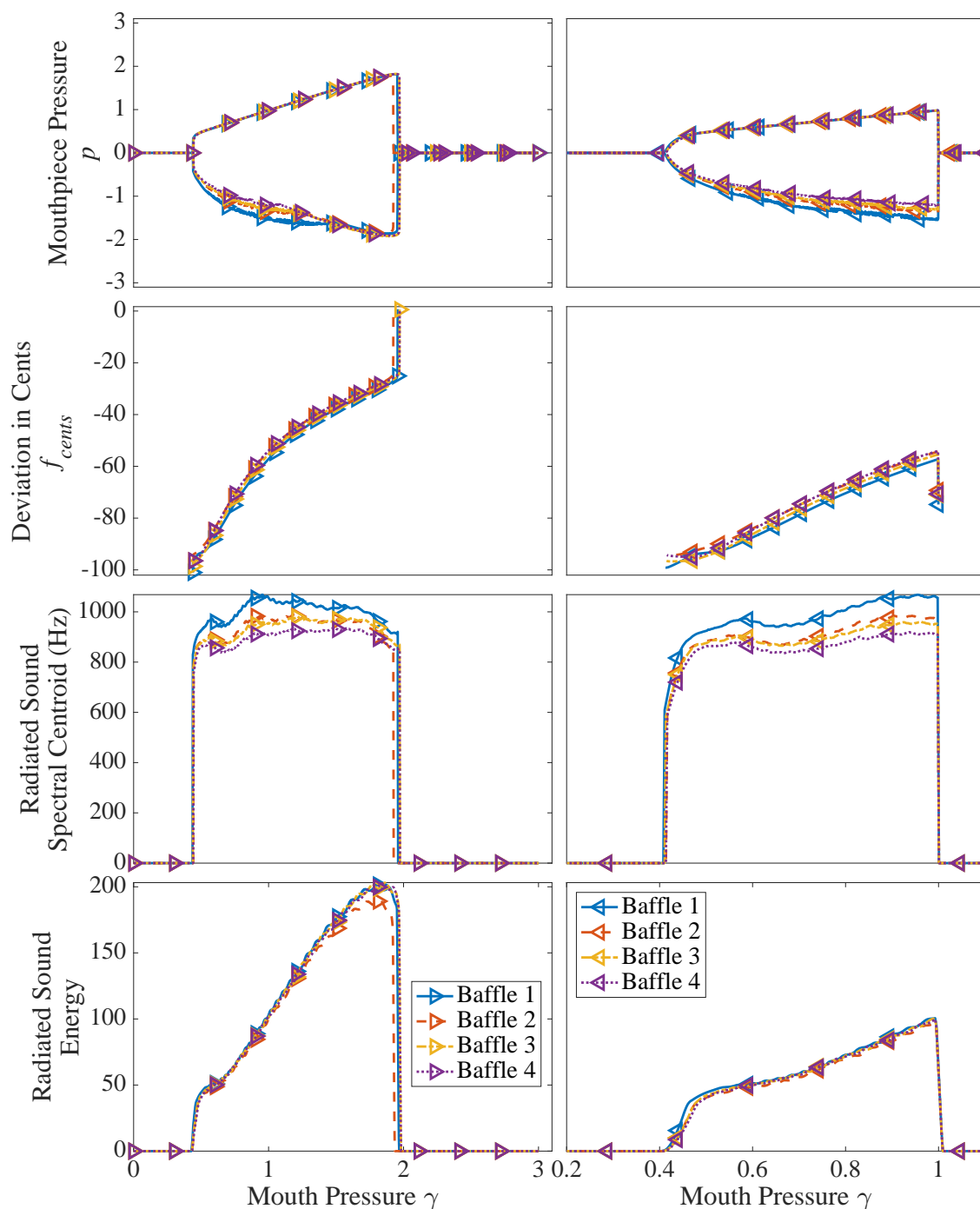


**Fig. 8.14:** Comparisons of the bifurcation diagrams, playing frequencies, radiated sound spectral centroid, and radiated sound energy for linearly increasing (left) and decreasing (right) mouth pressure profiles between mouthpieces with different baffle heights attach to an alto saxophone (fingering B<sup>b</sup>5).

### 8.3.2 Aeroacoustic modeling

In the aeroacoustic simulation, the 2D mouthpiece geometries are imported into the LB model, using the same simulation and playing parameters as described in Secs. 7.1 and 7.3.3. The input impedance of the saxophone body with the fingering B<sup>b</sup>4 is employed at the end of the mouthpiece.

The FW-H acoustic analogy with one-dimensional Green's function for an infinite pipe  $G$  is applied for the aeroacoustic analysis. An observer is located close to the end of the mouthpiece, and the outgoing pressure is decomposed into contributions from the monopole source at the inlet  $P_{\text{inlet}}$ , the monopole source due to the reed-induced flow  $P_{\text{reed}}$ , and the dipole sources arising from the force exerted by the solid walls on the fluid  $P_{\text{dipole}}$ . The spectra of the FW-H estimated outgoing pressure and its different contributions are obtained using the period synchronized sampling technique introduced in Sec. 7.2.2, and are compared between mouthpieces in Fig. 8.15. The corresponding spectral centroids are compared in Fig. 8.16. It is shown that all the spectral centroids decrease with an increase in the baffle-to-reed distance, which is consistent with the findings from the acoustic analysis in the previous section.

In addition, the frequency-domain comparison reveals that the baffle height has a more significant influence in 3-4 kHz range on the dipole source, while it affects higher frequencies for the inlet and reed monopoles. The difference can be attributed to the nature of the different sound sources. As discussed in Sec. 7.3.4, when using FW-H with  $G$ , the dipole contribution composes the acoustic response of the mouthpiece to the incoming wave. This acoustic response is related to the acoustic modeling of the mouthpiece, and the input impedance comparison in Fig. 8.11 also demonstrates that the influence of the baffle height is stronger around 3 kHz. On the other hand, the monopole sources are less sensitive to the acoustic resonance of the mouthpiece itself. Instead, they are directly influenced by the reed displacement and velocity, which are more affected by the tip opening and the lay profile of the mouthpiece.

The velocity fields of “baffle 1” and “baffle 4” within one single period are compared in Fig. 8.17. It can be observed that a smaller baffle-to-reed distance creates a more confined channel after the reed channel exit, which delays the development of jet instability. It also leads to a slightly higher jet velocity, which results in a smaller pressure above the reed and accelerates the reed when it moves toward the tip rail. This observation partially explains

the higher spectral centroid of “baffle 1”.

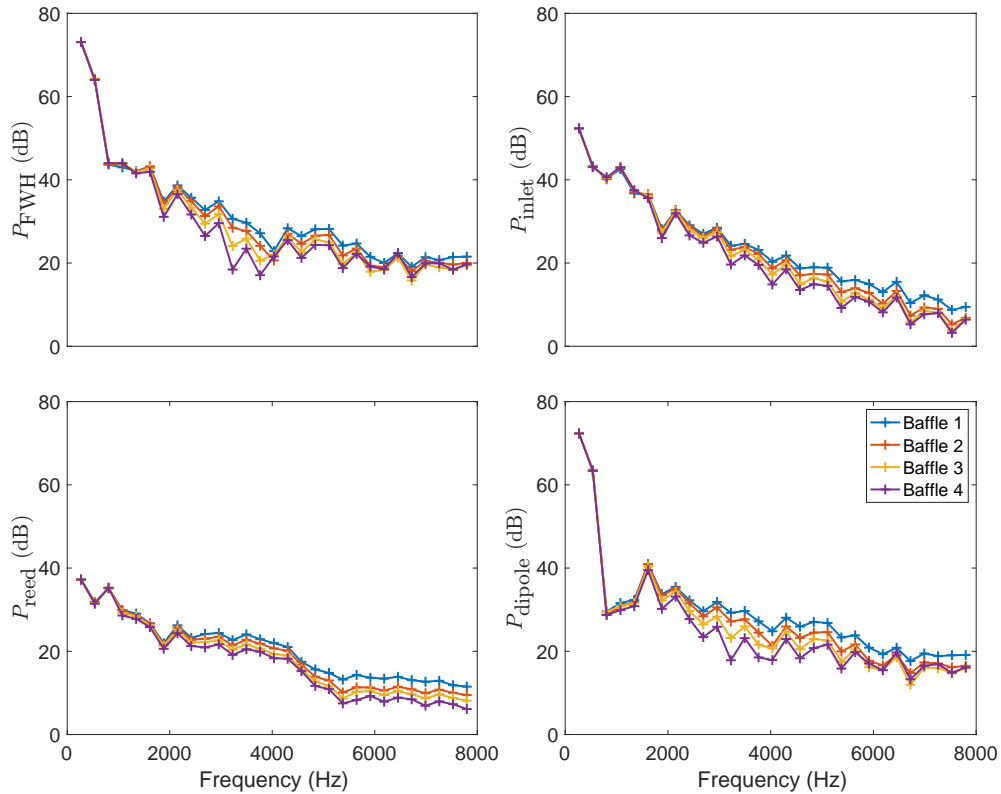


**Fig. 8.15:** Comparisons of spectra of FW-H estimation and different sound sources between mouthpieces with different baffle heights.

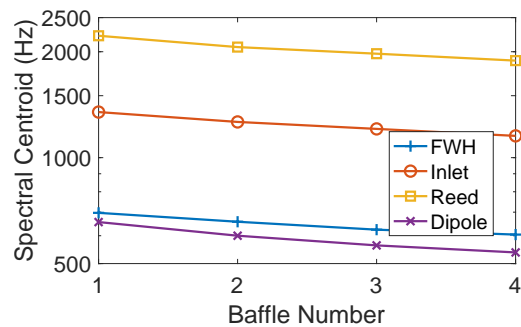


**Fig. 8.16:** Comparisons of the spectral centroid of different sound sources between mouthpieces with different baffle heights.

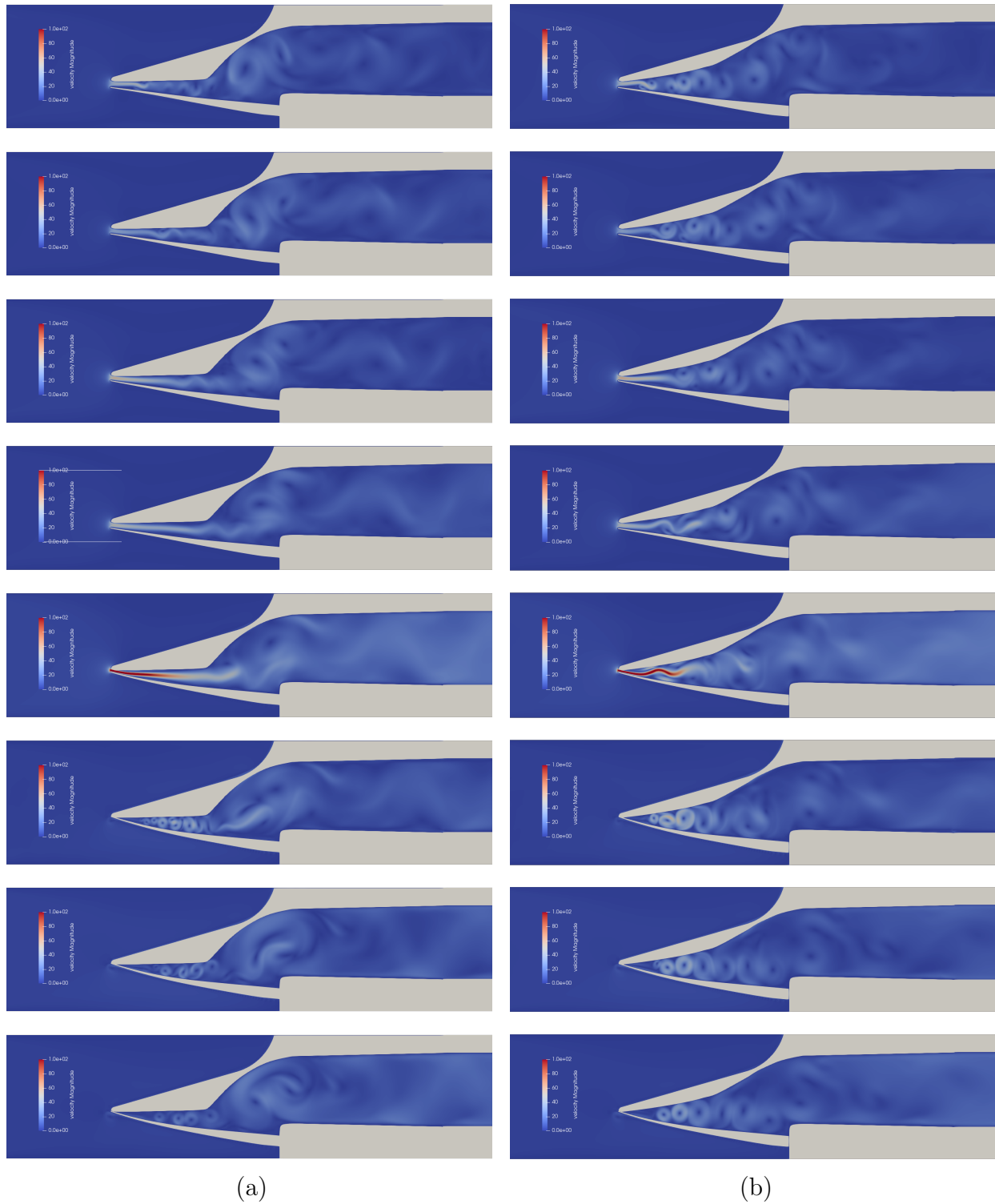


**Fig. 8.17:** Comparison of eight uniformly sampled snapshots of the velocity field within a single period between mouthpieces (a) “baffle 1” and (b) “baffle 4”.

## 8.4 Discussion

This chapter applies the acoustic and aeroacoustic models proposed in the previous two chapters to investigate the influence of mouthpiece design parameters on oscillation characteristics.

The acoustic modeling of the mouthpiece can be used to analyze both acoustic and oscillation characteristics of the mouthpiece, which relies respectively on the input impedance and the synthesized sound. The input impedances of the mouthpiece, with and without a saxophone body, provide an efficient way of comparing mouthpieces at the rest condition of the instrument, which helps factor out the influence of players and focus on the mouthpiece itself. It provides information on the intonation, timbre, and inharmonicity of the instrument, and the inharmonicity further implies potential influences of different design parameters on the playability and intonation (see Sec. 2.2.2). The synthesized sound, on the other hand, helps explore the incorporation of different mouthpieces with a player, and quantifies the effects of a design parameter on oscillation characteristics such as the oscillation thresholds and spectral centroids. Compared to the physical measurement and analysis, the present acoustic analysis procedure circumvents the problem of repeatability, and enables efficient tests with a larger number of mouthpieces and playing conditions using automated synthesizing and analyzing scripts. The main limitation of the oscillation characteristics analysis comes from the sound synthesis model. The synthesizer used in this research is based on the three-equation model discussed in Sec. 2.1.1, and that has involved a series of assumptions and simplifications. One of the most important simplifications made is that the reed is modeled as a single-degree-of-freedom oscillator. This makes it impossible to study certain design parameters such as the lay profile. In addition, the fluid model is simplified as the Bernoulli flow model, where the flow pattern is independent of the tip opening. This also introduces difficulties in investigating the influence of the geometry near the tip of the mouthpiece, such as the reed channel length and the tip opening.

The aeroacoustic modeling of the mouthpiece relies on the LB simulation and the FW-H acoustic analogy. On one hand, the LB model resolves the limitation of the acoustic modeling by representing the reed as a 1D distributed beam, and including the interaction of the reed with the lay. On the other hand, it provides a detailed modeling of the FSAI within the mouthpiece, which involves not only the acoustics and the solid, but also the complex fluid field. The sound pressure simulated in the LB mouthpiece model can be used in the oscillation

characteristics analysis. It is similar to that of acoustic modeling, except that it is not easy to obtain the oscillation thresholds because ramping up or down the mouth pressure with slow changing rates is too expensive to simulate. The FW-H characterizes saxophone sound generation by decomposing the sound into contributions from different sound sources. This provides a better understanding of how a design parameter influences sound by connecting a design parameter to each sound generation mechanism. In general, design parameters that influence the mouthpiece acoustic response have a stronger effect at the frequencies around the resonance frequencies of the mouthpiece itself (typically between 2 - 3 kHz). The design parameters that directly influence the reed motion, such as the tip opening and the lay profile, will have stronger contributions at higher frequencies. Such speculations are based on the characteristics of different sound sources but it requires further study of various mouthpiece design parameters to validate.

There are a few limitations to consider in the aeroacoustic study of the mouthpiece. First, the use of a 2D LB model restricts the ability to directly compare certain design parameters, such as the chamber shape and chamber width. The 2D nature of the model oversimplifies the geometry and may not fully capture the intricacies of the airflow and sound production in 3D space. Additionally, certain 3D effects, such as turbulent flow, side slits, and the effect of the side rail<sup>4</sup>, are either simplified or omitted in the 2D model. Another limitation is the expensive computational cost. In the present study, it took approximately 2.5 hours to simulate only 0.1 seconds of sound on an Intel Core i9-10900K CPU 3.70 GHz. Although the performance can be improved with more powerful processors, the computational overhead should be carefully calculated and the geometry variations should be selectively generated when designing numerical experiments.

In conclusion, both acoustic modeling and aeroacoustic modeling have advantages and disadvantages when studying the mouthpiece design parameters. By combining the insights gained from both methodologies, a more comprehensive understanding of the mouthpiece design and its impact on sound production can be achieved, which allows for a more thorough exploration of the design space while optimizing computational resources.

---

<sup>4</sup>While the collision between the reed and the lay is implemented in the reed model, a 2D model does not distinguish the window and the side rails of the mouthpiece.

## Chapter 9

# Conclusions and perspectives

This research focused on the acoustic and aeroacoustic analyses of the saxophone mouthpiece in order to gain a better understanding of its role in saxophone sound generation and to reveal the connection between the mouthpiece geometry and oscillation characteristics.

The mouthpiece is an essential component of the saxophone, serving as both a linear passive resonator and a nonlinear active resonator. These two roles of the mouthpiece were examined separately through acoustic modeling in Chapter 6 and aeroacoustic modeling in Chapter 7.

Chapter 6 focused on the characterization of the mouthpiece's linear acoustic properties using its input impedance. The study involved measurements of the input impedance, and using the finite element (FE) model, transfer matrix model (TMM), and transmission line model (TLM) to investigate the acoustic characteristics of the mouthpiece. TMM was derived from the FE mouthpiece model and was validated by input impedance measurements. It provided a more accurate mouthpiece representation compared to the lumped mouthpiece model and cylindrical mouthpiece model, and can be used in comparative acoustic studies of mouthpieces with different designs. It was also incorporated with sound synthesis, which helped analyze the oscillation characteristics of the instrument. TLM modeled the mouthpiece as piecewise cylinder segments, which provided a less accurate but more flexible mouthpiece representation. A mouthpiece design interface was prototyped in Appendix C based on TLM.

Chapter 7 focused on the aeroacoustic analysis of the sound generation of the mouthpiece-reed system. A two-dimensional computational aeroacoustic mouthpiece model was devel-

oped using the lattice Boltzmann method. A characteristic-based time-domain impedance boundary condition (C-TDIBC) was proposed in Chapter 5, and it was applied at the end of the mouthpiece to provide a localized representation of the saxophone body as a boundary condition using the saxophone body's input impedance. The Ffowcs Williams and Hawkings acoustic analogy was employed to analyze the sound generation in the mouthpiece-reed system, and the outgoing acoustic pressure at a downstream observer was decomposed into the inlet monopole, reed monopole, and dipole sound sources. The interpretation of various sound sources was demonstrated to be dependent on the choice of the Green's function. When the one-dimensional Green's function for an infinite pipe was used, the dipole source dominated monopoles because it involved the response of mouthpiece walls to both the aerodynamic force and acoustic fluctuations, where the latter contribution is connected to the acoustic characteristics of the mouthpiece as a linear acoustic filter. The dipole source intensity was reduced to a comparable level as the inlet monopole when the one-dimensional Green's function for a semi-infinite pipe was applied, and a new monopole source contributed by the outlet emerged and dominated all the other contributions to the outgoing pressure at the observer.

Finally, the acoustic and aeroacoustic analysis routines were employed to study the influence of two design parameters, specifically the chamber size and the baffle height, on acoustic and oscillation characteristics in Chapter 8. It was demonstrated that a larger chamber size leads to a lower spectral centroid and less sound energy in the radiated sound. It also resulted in a larger resistance of the mouthpiece, which made it harder to crescendo. A baffle height was found to mainly influence the spectral centroid, with a smaller baffle-to-reed distance tending to produce a larger spectral centroid.

## 9.1 Contributions

The present research has contributed to original knowledge from multiple aspects, including:

- A comprehensive discussion on the definition of the mouthpiece input impedance, covering different choices for the input plane and necessary assumptions to define the input impedance. Impedance measurements were conducted, and a finite element model was built to validate the concept.
- A quantitative illustration of the acoustic effect of the mouthpiece through input impedance measurements, revealing the presence of a “formant” structure in the in-

strument's input impedance due to the resonances of the mouthpiece.

- A transfer matrix model (TMM) for the mouthpiece, representing the mouthpiece acoustic cavity as a transfer matrix. TMM was validated through input impedance measurements, and was proved to be an accurate acoustic model by comparing it with the FE model, lumped mouthpiece model, and cylindrical mouthpiece model. It also showed its strength in the acoustic and oscillation characterization of the mouthpiece.
- A transmission line model (TLM) of the mouthpiece, representing the mouthpiece as piecewise cylindrical segments. It provides greater flexibility for mouthpiece acoustic modeling and serves as the base for the mouthpiece design interface prototype.
- A characteristic-based time-domain impedance boundary condition (C-TDIBC), which is a TDIBC variant based on the characteristic boundary condition (CBC), plane wave masking (PWM), and a time-domain representation of the input impedance as a recursive parallel filter structure.
- A novel two-dimensional lattice Boltzmann computational aeroacoustic (CAA) model that is unique in comparison with other single-reed instrument CAA models by using C-TDIBC to model the resonator. C-TDIBC was applied for the first time in a self-sustained system and a single-reed instrument study.
- The first application of the Ffowcs Williams and Hawkings acoustic analogy in the context of single-reed instrument sound generation, which provided a new insight of the sound generation characteristics based on the mechanisms of various sound sources.
- Investigations of the influence of mouthpiece chamber size and baffle height on the acoustics and oscillations through acoustic and aeroacoustic analyses.

## 9.2 Suggestions for future work

A number of avenues for future work are possible from this research, including:

- Given the reasonable acoustic approximation of the mouthpiece provided by TLM, it is worthwhile to revisit the model proposed by Stewart and Strong (1980). A one-dimensional distributed reed model was employed in the model, and the mouthpiece was represented by a cross-area function and modeled with an equivalent circuit of the transmission line. It allows a distributed interaction between the reed, flow and mouthpiece, which will provide features that have been omitted by a single-degree-of-freedom representation of the reed.

- The TLM-based mouthpiece design interface provides basic functionality for interactive mouthpiece design with real-time feedback on acoustic and sound properties. It can be improved by incorporating optimization algorithms so that users can create mouthpieces by directly defining and tuning acoustic and oscillation characteristics, such as the “formant” of the mouthpiece or even a desired sound spectrum.
- A main limitation of the present aeroacoustic analysis is the two-dimensional nature of the computational aeroacoustic model, which cannot replicate certain phenomena observed in a real single-reed instrument such as turbulent flow and the influence of side slits in the mouthpiece-reed system. The present model shall be extended to three dimensions with the simulation and analysis results compared with the findings presented in this thesis. The extension shall be straightforward, as C-TDIBC can be readily applied to three-dimensional problems using the framework proposed in Chapter 5, and along with the same Green’s function employed in the thesis, a similar aeroacoustic analysis can be conducted using the FW-H acoustic analogy.
- Another limitation of the aeroacoustic analysis comes from the large kinematic viscosity employed in the lattice Boltzmann model. The larger value was chosen in the present thesis to ensure the stability of the simulation, but it is worthwhile to use the air viscosity and compare the results of the simulation and FW-H analysis to those found in Ch. 7.
- In this thesis, FW-H analysis was performed with two different one-dimensional Green’s functions. It would be valuable to conduct a FW-H analysis using a two-dimensional free-field Green’s function in the frequency domain, and compare the results to those provided in this study.
- The performance of C-TDIBC has been shown to degrade when strong vortices are present near the boundary. It is worth investigating alternative boundary conditions to mitigate spurious reflection in such scenarios. The key to improving the C-TDIBC performance relies on the effectiveness of the boundary condition as a non-reflecting boundary condition. The C-TDIBC scheme proposed in this thesis made use of a local one-dimensional inviscid (LODI) model with transverse terms and transverse relaxation, but its performance may be improved by including viscous terms in the boundary condition formulation, as discussed by Yoo et al. (2005). In addition, the use of a zonal characteristic boundary condition (Gill et al., 2017, Sandberg and Sandham, 2006) deserves further investigation.

- 
- Since C-TDIBC was built based on the characteristic-based reflecting boundary condition, a digital waveguide method can be used to represent the resonator.
  - While this thesis primarily focuses on the aeroacoustics analysis of sound generation, further exploration of the aerodynamics, particularly the hysteresis effects as discussed in Section 2.1.3, is necessary.
  - Regarding the influence of mouthpiece design parameters, it is possible to investigate more design parameters using the same analysis process proposed in Chapter 8. In addition, it is worthwhile to print the mouthpieces using a 3D printer for physical measurement and subjective evaluations.

# Appendix A

## Review on artificial blowers

This appendix serves as a supplement to Sec. 2.3.2 and aims to provide a focused review on artificial blowers for single-reed instruments.

As mentioned in Sec. 2.3.2, measurements of a single-reed instrument under playing conditions can provide valuable insights into the oscillation characteristics and their relationship with both the instrument and its interactions with the player.

Taking measurements while the instrument is playing requires the incorporation of a player, which can be either a human or a machine. While a human player provides a more realistic playing condition, it is more challenging to quantitatively control the instrument and guarantee the experiment repeatability. In addition, the use of sensors is constrained due to the limited space within the player's mouth. Artificial blowers are employed to address such problems by providing precise control over the playing parameters using electronic or mechanical systems, and flexibility in integrating different sensors for measurement purposes.

The early development of artificial blowers can be traced back to the work by McGinnis and Gallagher (1941), where an artificial blower was designed to study the motion of a clarinet reed. In the pioneering research conducted by Backus (1961, 1963), an artificial blower was employed to investigate the sound generation mechanisms of a clarinet, which helped advance our early understanding of the underlying physics (Sec. 2.1.1). Numerous research groups have been actively involved in developing artificial players or artificial blowers, including Laboratory of Mechanics and Acoustics (LMA - Laboratoire de Mécanique et d'Acoustique) at Aix-Marseille University (Ferrand and Vergez, 2008), Laboratory of acoustics at University of Le Mans (LAUM - Laboratoire d'Acoustique de l'Université du Mans) (Dalmont et al.,

2003, Gazengel et al., 2007, Muñoz Arancón, 2017), Music Acoustic Group at University of New South Wales (Almeida et al., 2010, 2017, Li et al., 2016b), Department of Musical Acoustics Wiener Klangstil (IWK - Institut für Musikalische Akustik - Wiener Klangstil) at University of Music and Performing Arts Vienna (Chatziioannou et al., 2017, Mayer, 2003), Computational Acoustic Modeling Laboratory (Kemp et al., 2019) and others. Artificial blower designs are subject to change depending on different applications, and different designs may employ different methods to control the embouchure and different sensors to measure the signal. The overall development of the artificial blower can be roughly divided into two parts, namely the control and the measurement, which will be separately discussed in Secs. A.1 and A.2, respectively.

## A.1 Control

The present discussion on the control of the instrument focuses on the embouchure, which involves the mouth cavity, lips, and the tongue.<sup>1</sup>

### A.1.1 Blowing pressure

As introduced in Sec. 2.1, the mouth pressure drives the airflow into the instrument and largely influences the oscillation characteristics. It creates pressure differences across the reed, which is a crucial factor in sound generation. When using an artificial player, there are two options for creating the desired pressure difference.

The first option is to construct an artificial mouth that is placed upstream of the instrument to blow the air into it. In most applications, the influence of the vocal tract is typically ignored, making the shape and the volume of the artificial mouth less critical. A rectangular box or a cylindrical tube, typically made of plexiglass with occasional metal reinforcement, is generally used to represent the “oral cavity”. The volume of the mouth box varies a lot depending on the specific applications. For example, Ferrand and Vergez (2008) used a mouth box with a volume of  $30 \text{ cm}^3$ , which corresponds to the average volume of an actual mouth, while Lorenzoni and Ragni (2012) used a much larger mouth box with a

---

<sup>1</sup>The control of fingers and other gestures will not be addressed in this review since they are less included in previous research. To the author’s best knowledge, Almeida et al. (2010) may have built the only automated clarinetist that has been used in scientific research, and readers interested in fingering control may refer to that paper for more details.

volume of 1300 cm<sup>3</sup> for particle image velocimetry (PIV) measurements. An air compressor or air pump is commonly used as the air source, and a muffler can be installed between the air source and the artificial mouth to suppress source noise. A regulator is necessary to control the mouth pressure. Manual regulators are typically used for simplicity, although there have been attempts to achieve automatic and precise control of the mouth pressure, such as the use of proportional servo-valves combined with proportional-integral-derivative (PID) controller schemes by Bergeot et al. (2014), Ferrand and Vergez (2008) and Chatziioannou et al. (2017). Almeida et al. (2010) and Li et al. (2016b) also implemented a PID loop to control air leakage from the system using a shaker to achieve the desired mouth pressure.

The second option involves placing a vacuum downstream of the instrument to aspirate the air out of the instrument. A vacuum cleaner (Backus, 1985, Muñoz Arancón et al., 2018) or a pump (Almeida et al., 2017) can be applied at the end of the instrument. A reservoir and a muffler need to be installed between the instrument and the aspiration system to minimize the influence of the aspiration system on the radiation impedance of the instrument. The choice of the pressure driving system depends on specific experiment requirements. In the case of Muñoz Arancón (2017)'s experiment, the aspiration system enables convenient in-place reed calibration and testing. It also allows a human player to play the instrument while the aspiration system is off, which enables direct comparisons between different playing conditions.

### A.1.2 Lip

When constructing an artificial lip for an artificial blower, there are several important considerations, including the choice of material, and means of controlling the lip position and exerting force on the reed.

There are two main types of materials commonly used as an artificial lip. The first option is rubber foam, which can be either polyester (Chatziioannou et al., 2017), polyurethane (Li et al., 2016b), neoprene (Backus, 1961) and silicone rubber (Idogawa et al., 1993, McGinnis and Gallagher, 1941). Another option is a latex tube filled with liquid (water or glycerin) or liquid-saturated foam (Dalmont et al., 2003, Ferrand and Vergez, 2008, Lorenzoni and Ragni, 2012). While Gazengel et al. (2007) demonstrated that a glycerin-filled artificial lip performs better than a water-filled one, further comparative investigations between different materials are still needed.

To control the lip force and lip position, a mechanical structure is necessary. The lip is normally assumed to be applied perpendicularly to the reed, and the lip force can be controlled by adjusting the height of the lip. The simplest approach to implement a lip force is by using screws to control the vertical position of a bar or plate with the artificial lip attached. This type of structure has been widely employed due to its simplicity (Backus, 1961, Dalmont et al., 2003, Idogawa et al., 1993, Lorenzoni and Ragni, 2012, McGinnis and Gallagher, 1941). However, quantitatively controlling the lip force with a screw can be challenging. Alternative methods for lip force control have been proposed, such as using a hanging mass (Li et al., 2016b), a translation stage (Chatziioannou et al., 2017), or servos (Almeida et al., 2010). It should be noted that the lip force control is closely related to lip force measurement, and it sometimes requires incorporating force sensors like load cells.

The lip position of an artificial player is mostly assumed to be fixed, which is located approximately 1 to 1.5 cm from the tip of the reed. However, certain clarinet artificial blowers, which hold the mouthpiece through an external integrated barrel, allow for adjusting the relative lip position by sliding the mouthpiece in and out while keeping the lip position fixed (Dalmont et al., 2003, Idogawa et al., 1993).

### A.1.3 Tonguing

Tonguing is important in studies of articulations. In the work of Chatziioannou et al. (2017, 2019), an electric-controlled shaker was used to mimic the action of the tongue, and a cellular polyethylene foam was attached to the shaker as tongue material. Other options include the use of a servo to provide a binary control of the tongue (Almeida et al., 2010), and a system composed of two beams and two masses to control the tonguing with an adjustable acceleration (Li et al., 2016b).

## A.2 Measurements

### A.2.1 Mouth and mouthpiece pressure

When measuring mouth pressure in artificial players, a uniform static pressure is normally assumed within the mouth box. This allows to employ a manometer for the pressure measurement, which can be placed at an arbitrary position in the box.

It is the opposite when measuring the mouthpiece pressure, where static pressure is

usually assumed to be zero so that only the dynamic pressure is measured. A pressure sensor is typically placed after the mouthpiece baffle (Almeida et al., 2017, van Zon et al., 1990), and it requires to modify the mouthpiece to flush mount the transducer.

A differential pressure sensor can be used to measure the pressure difference between the mouth and mouthpiece (Dalmont et al., 2003). It can also be applied in the experiment with an aspiration system, where the “mouth pressure” is always equal to the atmosphere pressure (Muñoz Arancón, 2017).

### A.2.2 Reed displacement and tip opening

The reed displacement  $y$  and tip opening  $h = y + H$  are two related quantities that are commonly used in different studies. The conversion between these two quantities requires to know the equilibrium tip opening,  $H$ , of the reed. The reed displacement is typically used for characterizing the behavior of a reed, whereas the tip opening is more important in the flow characterization.

There exist several measures to measure the tip opening, which include optical methods, laser Doppler velocimetry, strain gauges, and high-speed cameras.

The application of optical methods was first introduced by McGinnis and Gallagher (1941)<sup>2</sup>, who measured the reed vibration frequency by adjusting the stroboscope flash speed. Backus (1961) was the first to apply the photoelectric method, which employed a photomultiplier tube to capture the reed motion by detecting light passing through the reed aperture from a light source placed at the bell of the clarinet. This method has been widely applied in various studies, especially for clarinets (Dalmont et al., 2003, Idogawa et al., 1993, Muñoz Arancón, 2017). It is occasionally applied in a saxophone mouthpiece without a resonator, because the bends in a saxophone may impede the optical signal from reaching the tip opening effectively.

A high-speed camera was used by Li et al. (2016b) to capture both the reed and tongue motions, and the reed positions are extracted using an image analysis routine.

Laser Doppler velocimetry (LDV) has been applied to measure the reed velocity (Gazengel, 1994). The velocity signal can then be integrated to obtain the reed displacement.

Chatziioannou et al. (2017, 2019) used strain gauges to measure the reed displacement, with the strain gauge calibration conducted using a high-speed camera (Pàmies-Vilà et al.,

---

<sup>2</sup>It may have been introduced even earlier by Aschoff (1936), but it is difficult to find the article online.

2017). Although the strain gauge may have some influence on the reed properties (Chatziioannou et al., 2016), it still provides an effective way of measuring the reed displacement considering that the playing frequency is normally lower than the reed resonant frequency.

It should be noted that while it is trivial to convert from  $h$  to  $y$  (as  $H$  simply corresponds to  $h$  at a rest condition when  $y = 0$ ), the conversion from  $y$  to  $h$  is not always straightforward because neither LDV nor the strain gauge provides information about  $H$ .

### A.2.3 Air flow rate

The air flow rate is an important variable in characterizing the nonlinear flow-pressure relationship. In a quasi-static experiment, the flow rate can be directly measured with a flow meter, or estimated using an orifice (Dalmont et al., 2003). For dynamic flow measurement, the hot-wire anemometry can be employed (Gilbert, 1991, Idogawa et al., 1993, Maurin, 1992). It is typically placed in the mouth box, right before the mouthpiece tip window to measure the flow velocity at the entrance of the instrument, and an addition calibration is required to convert the flow velocity to the flow rate.

### A.2.4 Lip force

The lip force can be measured with a force sensor (Chatziioannou et al., 2017), contact pressure gauge (Mayer, 2003) or a load cell (Yokoyama et al., 2020).

# Appendix B

## LBM benchmark problems

### B.1 Acoustic Point Source

In this section, an acoustic point source is simulated using the lattice Boltzmann method with three different collision models, including Bhatnagar-Gross-Krook (BGK), multirelaxation time (MRT) and recursive regularized BGK (rrBGK). A point source is set at the center of a  $100 \times 100$  domain in the lattice grid unit:

$$\rho(\mathbf{x}, t) = \rho_0 + \rho_s \sin\left(\frac{2\pi}{T}t\right), \quad (\text{B.1})$$

where  $\rho_s = 0.01$  is the strength of the source, and  $T = 20\Delta t$  is its period. The relaxation frequency is set as  $\omega = 1/\tau = 1.993$ . The simulation lasts 80 time steps, which terminates before the wavefront arrives at the boundary. The isocontours of the acoustic density  $\rho' = \rho - \rho_0$  at time  $t = 75\Delta t$  are compared in Fig. B.1, and the acoustic density along  $y = 50\Delta x$  is presented in Fig. B.2. According to the results, BGK is shown to introduce strong spurious fluctuations, which is a well-known problem that prevents BGK from being applied in acoustic problems (Suss et al., 2023, Xu and Sagaut, 2011). On the other hand, both MRT and rrBGK work better in mitigating such spurious fluctuations due to the higher dissipation of the model, which provides the base of a more stable simulation at high Mach number and Reynolds number flow. However, as shown in Fig. B.2, the density amplitude of MRT is over-dissipated because the numerical dissipation of MRT is too large. Xu and Sagaut (2011) observed a similar behavior of MRT and proposed an optimized MRT scheme, which tunes different MRT relaxation parameters independently to minimize the numerical

dispersion and dissipation. A comparison of the scheme proposed by Xu and Sagaut (2011) and rrBGK is left to further work.

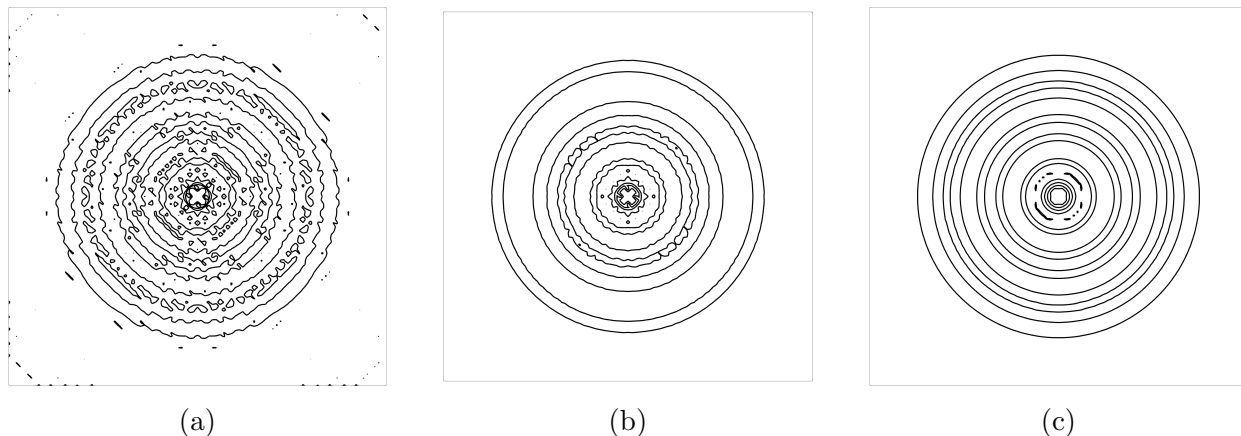


**Fig. B.1:** Isocontours of  $\rho'$  at time  $t = 75\Delta t$ : (a) BGK; (b) MRT; (c) rrBGK.

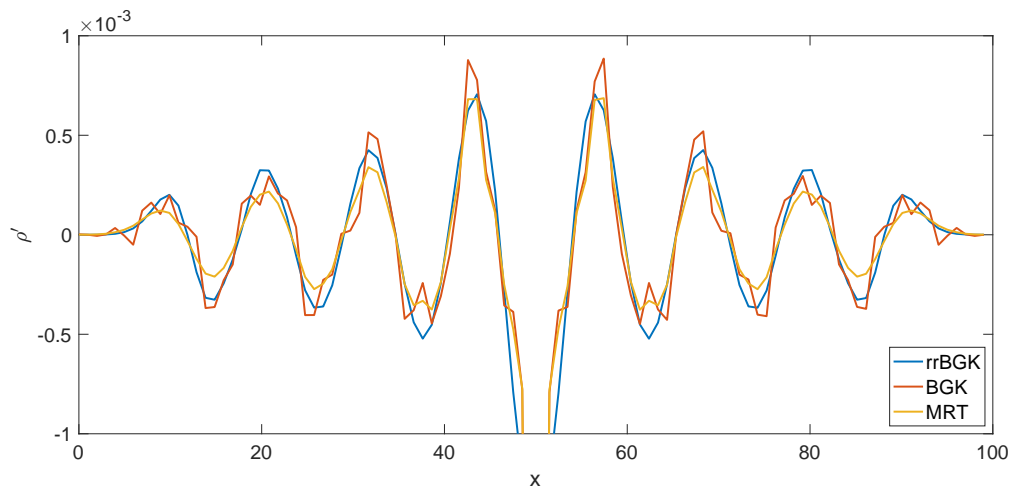


**Fig. B.2:** Comparisons of  $\rho'$  at  $y = 50\Delta x$  and  $t = 75\Delta t$  between three different collision models. (The  $y$ -axis of the plot is zoomed-in to  $[-0.001, 0.001]$  for a better comparison.)

## B.2 Flow passing 2D cylinder

The Aeolian tone generated by a two-dimensional circular cylinder immersed inside a low Mach number uniform flow is simulated with rrBGK-LBM in this section. The simulation

follows the same setup as described in the paper by Brogi et al. (2017), including a multi-domain grid refinement (Lagrava et al., 2012) and the non-reflective boundary condition (Xu and Sagaut, 2013). The only difference in this simulation is that Taylor-Green vortices are deployed around the cylinder as an initial condition to facilitate a faster transition to a stable vortex shedding from the cylinder. In Fig. B.3, the snapshots of the vorticity and acoustic fields at two different times corresponding to the minimum and maximum points of the lift coefficient, clearly present the dipole sound generation by the vortices. The calculated lift coefficient  $C_L \approx 0.55$  and Strouhal number  $St \approx 0.182$  agree well with the experimental values for a flow of Mach number  $Ma = 0.2$ . In addition, the acoustic pressure  $\Delta\tilde{p}(r, \theta)$  at different times measured along  $r$  at  $\theta = 90^\circ$  is plotted in Fig. B.4, demonstrating the sound pressure decay proportional to  $r^{-1/2}$ , which corresponds to the theoretical value.

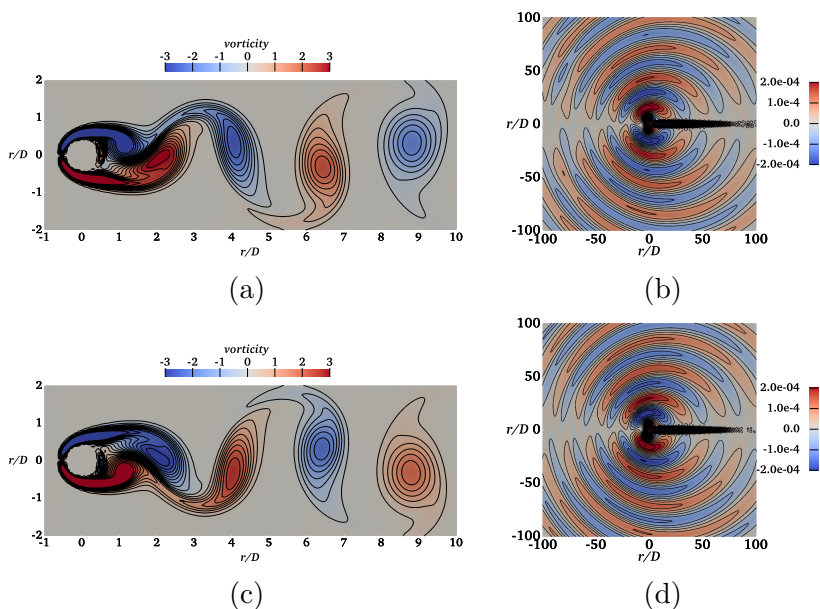


**Fig. B.3:** The snapshots of the vorticity (left) and acoustic (right) fields at  $t$  (up) and  $t + 2.74$  (bottom), where  $t$  corresponds to the negative peak of lift coefficient.

### B.3 Sound radiation of cylindrical ducts

In this section, the acoustic radiation of cylindrical ducts in the presence of the mean flow is tested using rrBGK. The far-field acoustic directivity at two different flow speeds, Mach

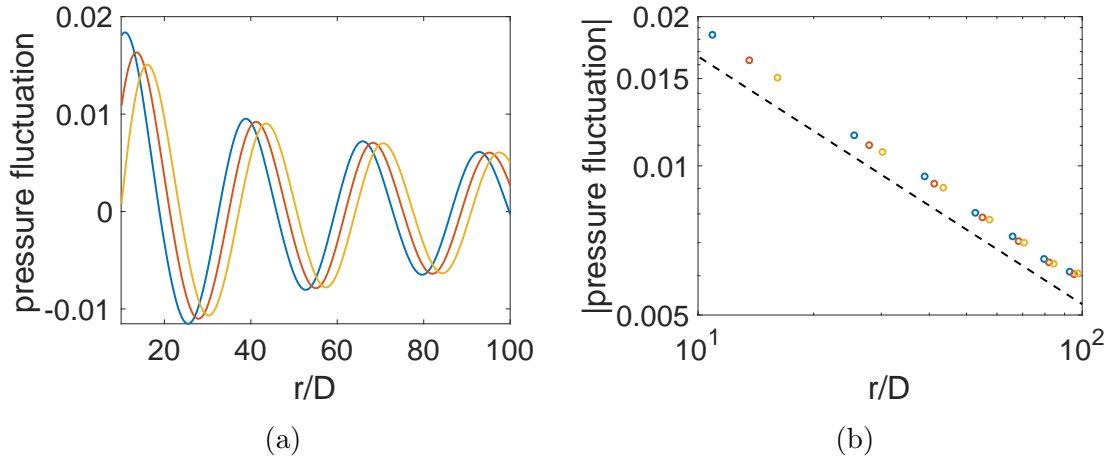


**Fig. B.4:** (a) Comparison of acoustic pressure ( $r, 90^\circ$ ) at time  $t + 1.83$  (—),  $t + 2.28$  (—),  $t + 2.74$  (—), with  $t$  corresponding to the negative peak of the lift coefficient. (b) Decay of pressure peaks ( $\circ, \circ, \circ$ ) and the reference line of  $r^{-1/2}$  (---).

number 0.036 and 0.15, is investigated and compared with the analytical solution derived by Gabard and Astley (2006) (Gabard and Astley, 2006).

In order to save the computation cost, an axisymmetric rrBGK scheme is employed, which will be shown in Sec. B.5. The computational domain is displayed in Fig. B.5 with a domain size of  $2000 \times 1000$ . The lower boundary of the domain is the axis of symmetry. As shown in the figure, a cylindrical pipe with a length of  $L = 1001$  and a radius of  $a = 30$  is placed inside the rectangular fluid domain. The inner wall of the pipe is set as a free-slip boundary and the outer wall as a no-slip boundary. The absorbing boundary condition (ABC) (introduced in Sec. 4.3.2) is applied to absorb the outgoing acoustic waves by deploying buffer zones outside the fluid domain with the target density  $\rho_t = 1.0$  and the target flow velocity  $\mathbf{u}_t = (0, 0)$ . An extra buffer is placed next to the inlet of the pipe, working as a sound source. The sound source is defined by the impulse response  $I(n)$  of an FIR filter, with a length of 501 and normalized cutoff frequency  $f_c = 0.015$  corresponding to the Helmholtz number  $ka = 4$ . The target velocity and density are given as

$$\begin{cases} \mathbf{v}^t = (v_0 + H(n - N_t)v'I(n), 0), \\ \rho^t = \rho_0 + H(n - N_t)\frac{v'\rho_0}{c_s}I(n), \end{cases} \quad (\text{B.2})$$

where  $v_0 = Mc_s$ ,  $v' = 0.05u_0$ ,  $\rho_0 = 1.0$  and  $H(n - N_t)$  is the Heaviside step function. By

applying the Heaviside function, the acoustic sound source is activated after  $N_t = 3L_x/v_0$  time steps, when the flow has reached the downstream boundary and the system has achieved a steady state.  $L_x$  is the width of the computational domain.

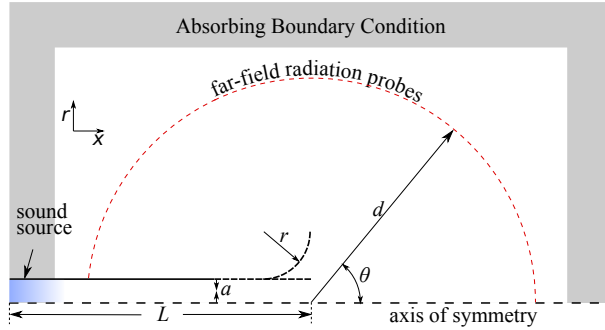


**Fig. B.5:** Schematic view of the computational domain.

A series of probes are set as a semicircle with a radius of  $d$ , centered at the pipe outlet. The probe pressure is recorded for the sound directivity calculation and the acoustic pressure is given by:

$$p(t) = (\rho(t) - \rho_0)c_s^2, \quad (\text{B.3})$$

where  $\rho(t)$  is the instantaneous density and  $\rho_0$  is calculated by averaging the steady-state part of the signal to remove the steady-state components. The far-field sound directivity is then calculated using

$$G(\theta, f) = \frac{P(\theta, f)}{P_{\text{rms}}(f)}, \quad (\text{B.4})$$

where  $P(\theta, f)$  is the discrete Fourier transform of  $p(t)$  at the radiation probes and  $P_{\text{rms}}(f)$  is the root-mean-square of the  $P(\theta, f)$ . The normalized  $G(\theta, f)$  is compared with theoretical results in Figs. B.6 and B.7 for different Mach numbers and shows good agreements.

## B.4 Sound radiation of horns

The acoustic directivity of a circular horn is studied in this section. As shown in Fig. B.5, a quarter circle of radius  $r = 2a$  is placed at the end of the cylindrical duct as a horn to replace the corresponding cylindrical part while maintaining the same total pipe length.

In order to better describe the effect of the horn on the acoustic directivity under different

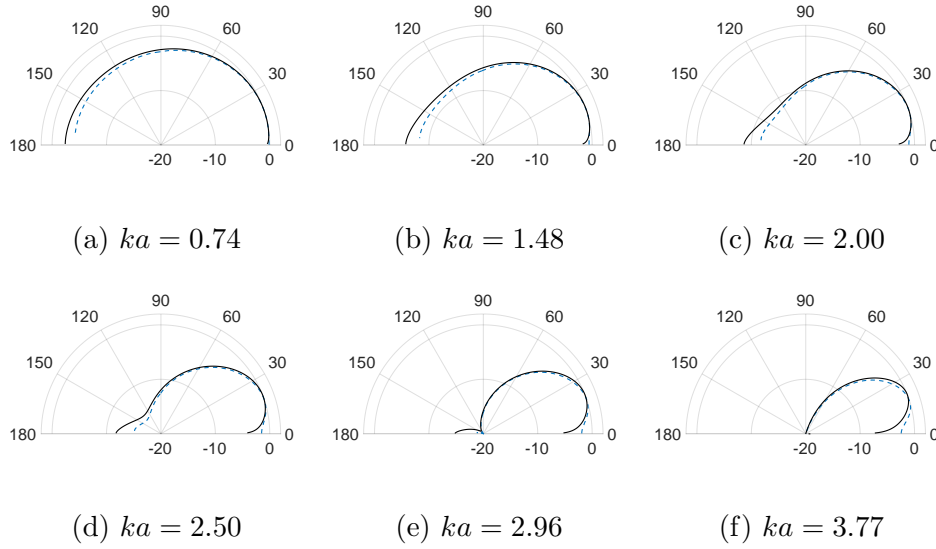


**Fig. B.6:** Comparison between LBM simulation results (---) and the analytical solution Gabard and Astley (2006) (—) at  $Ma=0.036$ .

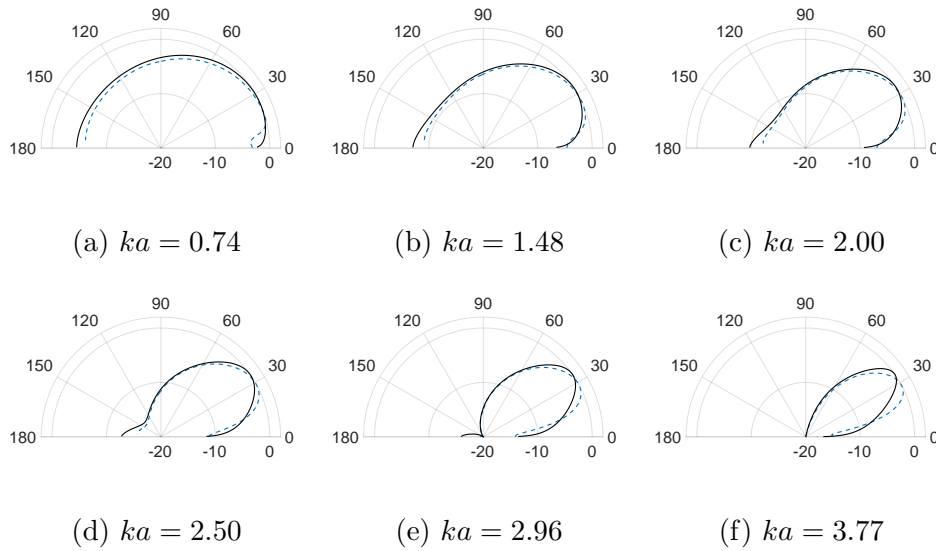


**Fig. B.7:** Comparison between LBM simulation results (---) and the analytical solution Gabard and Astley (2006) (—) at  $Ma=0.15$ .

flow velocities, a new coefficient is defined as

$$D(\theta, f) = \frac{P_{\text{horn}}^2(\theta, f) - P_{\text{cyl}}^2(\theta, f)}{P_{\text{cyl,rms}}^2(f)}, \quad (\text{B.5})$$

where subscripts ‘horn’ and ‘cyl’ represent the cases with and without a horn for the same flow velocity, respectively. The difference of their radiated acoustic energy is then normalized by the root-mean-square of the radiation energy of a cylinder.  $D(\theta, f)$  shows directly how much the horn helps radiate the sound. In Fig. B.8,  $D(\theta, ka)$  is plotted for different Mach numbers in the  $\theta - ka$  space.

As expected, the simulation results show that the horn generally helps the duct sound radiation both with and without a uniform flow. Such an improvement is because the horn works as an impedance matcher which decreases the sound reflection and increases the sound radiation. As shown in Fig. B.8, the effect of the horn on radiation is not uniform in the  $\theta - ka$  space. There exists a triangle zone about the range  $[\theta \in (0^\circ, 50^\circ), ka \in (0.5, 2)]$  where the radiation is boosted the most. However, in the area of  $[\theta \in (50^\circ, 170^\circ), ka \in (0.5, 3)]$ , the horn has a negative contribution to sound radiation. Such an effect is due to the geometry of the horn that blocks the sound wave from traveling in large angle directions. In this case, the low-frequency components are more easily diffracted than the high-frequency components to provide a better radiation efficiency.

In Table B.1, the maximum value of  $D(\theta, ka)$  in the  $\theta - ka$  map of different flow velocity is found and the corresponding radiation angle  $\theta$ , the Helmholtz number  $ka$ , and the value  $D_{\max}$  are listed. Though the  $ka$  doesn’t change that much, the  $\theta$  increases with the Mach number. This effect is similar to the directivity characteristic called the zone of relative silence where the radiated acoustic power is relatively smaller near the center axis of the pipe. The angle that has the largest sound radiation is called the characteristic angle  $\theta_s = \cos^{-1}(\frac{1}{1+M})$  and will increase with the Mach number. This similarity might be because both effects are related to the flow instability at the end of the pipe due to the non-zero ambient-pipe flow Munt (1977). However, more simulations of different flow velocity and horn geometries need to be tested before any conclusion can be drawn.

**Table B.1:** The maximum  $D(\theta, ka)$  in the  $ka - \theta$  map.

Mach number	$\theta$ (degree)	$ka$	$D_{\max}(\theta, ka)$
$M = 0.0$	0.1434	0.8120	10.5580
$M = 0.05$	9.9969	0.8071	8.1911
$M = 0.1$	13.3172	0.6775	7.9801
$M = 0.15$	15.5907	0.6825	7.7125

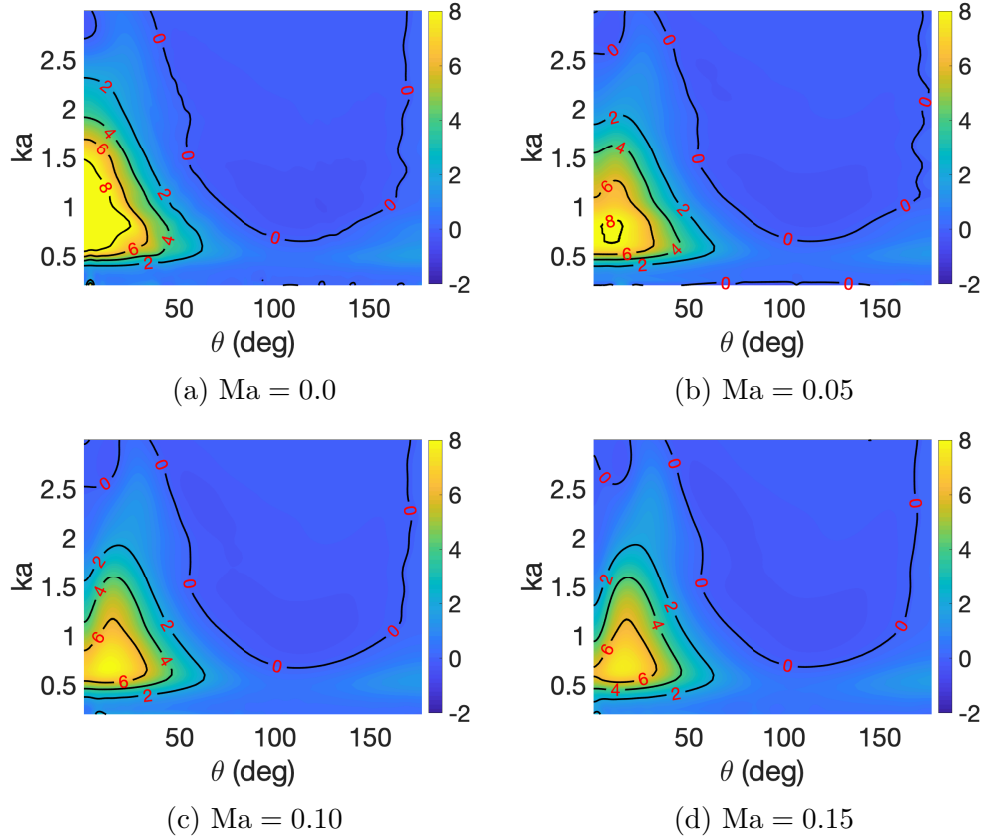


**Fig. B.8:** The comparison of  $D(\theta, f)$  LBM simulation results of the horn ( $r = 2a$ ) for different flow speeds.

## B.5 Axisymmetric LBM

The two-dimensional axisymmetric scheme is frequently used in simulating the 3D axisymmetric flow. The axisymmetric LBM proposed by Zhou (2011) is used in solving sound radiation from a pipe. In order to be able to recover the axisymmetric Navier-Stokes equation using Chapman-Enskog analysis, the original LBE is reformulated and added with the sink or source and the force terms, written as

$$f_i(\mathbf{x} + \mathbf{e}_i \Delta t, t + \Delta t) = f_i(\mathbf{x}, t) - \omega_i [f_i(\mathbf{x}, t) - f_i^{\text{eq}}(\mathbf{x}, t)] + w_i S \Delta t + \frac{\Delta t}{6e^2} e_{i\alpha} F_\alpha, \quad (\text{B.6})$$

where  $S$  is a source or sink term,

$$S = -\frac{\rho u_r}{r}, \quad (\text{B.7})$$

and  $F_\alpha$  the force term

$$F_\alpha = -\frac{\rho u_\alpha u_r}{r} - \frac{2\rho\nu u_\alpha}{r^2}\delta_{\alpha r} \quad (\text{B.8})$$

with  $\alpha = \{x, r\}$  in the axisymmetric coordinate, where  $x$  and  $r$  represent the axial and radial directions, correspondingly.  $\omega_i$  is the effective relaxation frequency<sup>1</sup> defined as

$$\omega_i = \begin{cases} \frac{1}{\tau}, & r = 0, \\ \frac{1}{\tau} \left[ 1 + \frac{(2\tau - 1)e_{ir}}{2r} \right], & r \neq 0. \end{cases} \quad (\text{B.9})$$

Finally, it is trivial to get the axisymmetric LBM with the rrBGK collision operator. The right-hand side (RHS) of Eq. (B.6) can be rewritten in terms of  $f_i^{\text{eq}}$  and  $f_i^{\text{neq}}$ :

$$f_i(\mathbf{x} + \mathbf{e}_i\Delta t, t + \Delta t) = f_i^{\text{eq}}(\mathbf{x}, t) + (1 - \omega_i) f_i^{\text{neq}}(\mathbf{x}, t) + w_i S \Delta t + \frac{\Delta t}{6} e_{i\alpha} F_\alpha, \quad (\text{B.10})$$

where  $f_i^{\text{eq}}$  and  $f_i^{\text{neq}}$  can be calculated with Eqs. 4.43 and 4.44, respectively.

---

<sup>1</sup>Despite that the term  $\omega_i$  defined here was denoted as  $\tau_i$  and called an effective relaxation time in the original paper by Zhou (2011), it is essentially an equivalent relaxation frequency, which is the reciprocal of the relaxation time  $\tau$ .

## Appendix C

# TLM-based mouthpiece design interface

In this section, a transmission line model (TLM)-based mouthpiece design interface is developed using the MATLAB App Designer. The interface consists of three main modules, as illustrated in Fig. C.1: *Area Function (AF) Creator*, *Impedance Calculator*, and *Sound Synthesizer*.

The *AF Creator* module allows the users to define the geometry of the mouthpiece by specifying a series of “Mouthpiece Basic Parameters” and adjusting the area of each individual cylindrical segment interactively using a graphical interface with computer-mouse control. The “Mouthpiece Basic Parameters” include the number of cylindrical segments of AF, mouthpiece volume, equivalent radius of the tip window, and radius of the mouthpiece bore, where the latter two radii define the areas of the first and last cylindrical segments, respectively. By switching on the “DRAW” button and holding the key “d”, users can customize the AF by moving the mouse on the “Area Function Drawing Canvas”. The user can click on “Update AF” button to confirm the modification, which temporarily stores a selected AF. The *AF Creator* allows storing up to three mouthpiece AFs for comparison and provides options to load or save AFs from/to a file.

The *Impedance Calculator* module allows users to calculate the closed mouthpiece input impedance, which will be updated automatically when a change is made to a selected AF. It also allows users to import measured or simulated input impedances of a saxophone bore, which can be taken as a load impedance applied to the mouthpiece. By selecting the

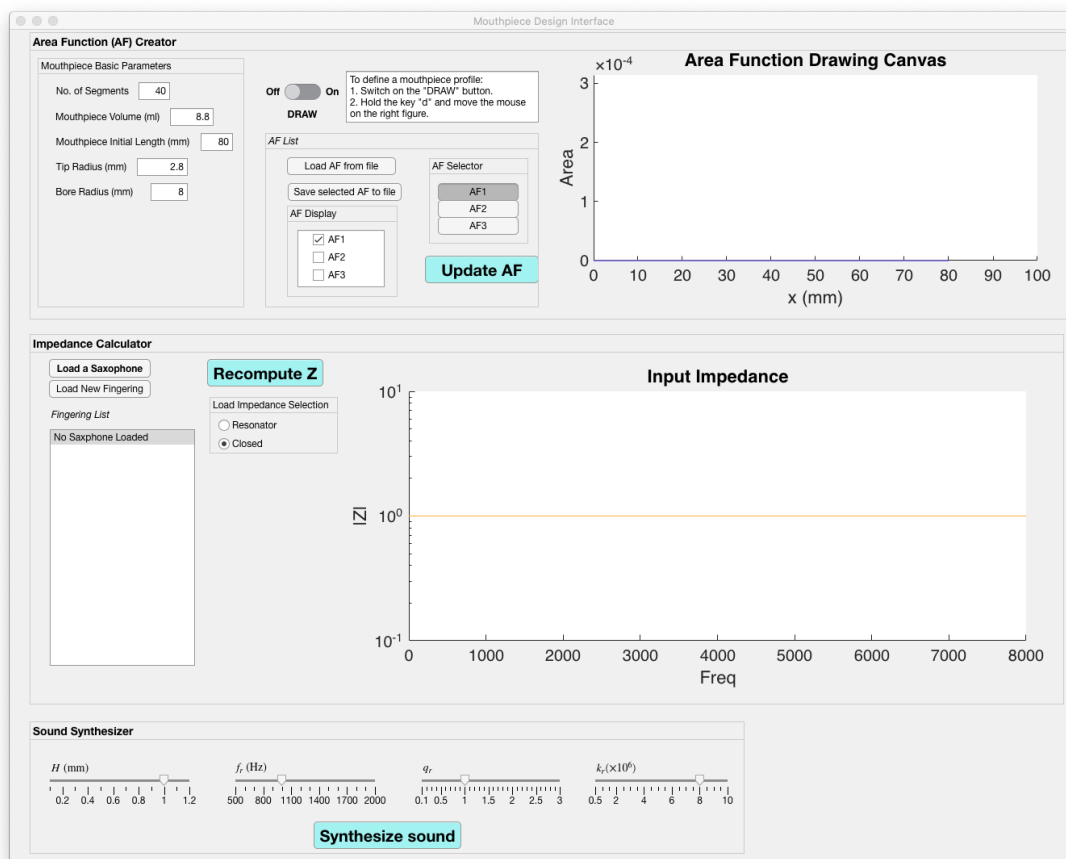


Fig. C.1: User interface of TLM-based mouthpiece design interface.

“Resonator” option in the “Load Impedance Selection” tab and a fingering in the imported “Fingering List”, the input impedance of the entire instrument (mouthpiece+saxophone) can be calculated by clicking on “Recompute Z” button. The module provides a comparison of input impedance modulus of mouthpieces with different AFs along with the load impedance. Figures. C.2 and C.3 demonstrate the definitions of three customized AFs, as well as the corresponding input impedance comparisons.

Finally, the *Sound Synthesizer* module allows users to synthesize sound using the calculated input impedance. The synthesis is implemented using the reflection coefficients as described in the paper by Gazengel et al. (1995). Users can adjust parameters including equilibrium tip opening  $H$ , reed resonant frequency  $f_r$ , reed damping coefficient  $q_r$  and the reed stiffness  $k_r$  to tune the synthesized sound.



Fig. C.2: Comparison of AFs and closed mouthpiece input impedances.

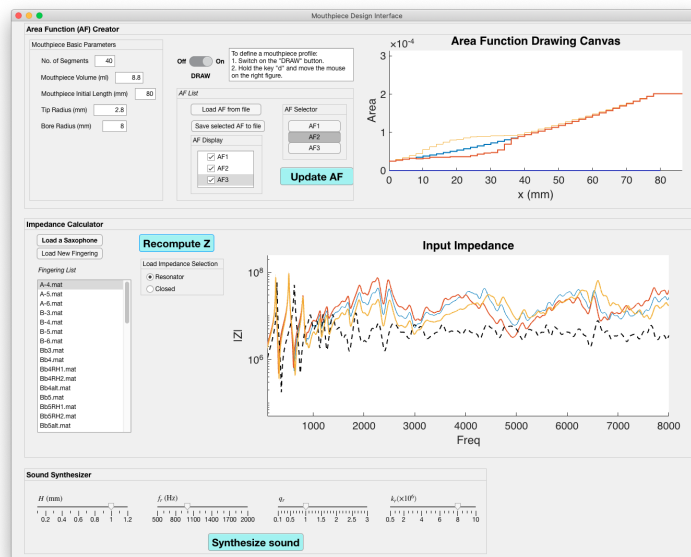


Fig. C.3: Comparison of AFs and saxophone input impedances.

## References

- A. Almeida, J. Lemare, M. Sheahan, J. Judge, R. Auvray, K. S. Dang, S. John, J. Geoffroy, J. Katupitiya, P. Santus, A. Skougarevsky, J. Smith, and J. Wolfe. Clarinet parameter cartography: Automatic mapping of the sound produced as a function of blowing pressure and reed force. In *Proceedings of International Symposium on Music Acoustics*, 2010.
- A. Almeida, D. George, J. Smith, and J. Wolfe. The clarinet: How blowing pressure, lip force, lip position and reed “hardness” affect pitch, sound level, and spectrum. *The Journal of the Acoustical Society of America*, 134(3):2247–2255, 2013.
- A. Almeida, W. Li, J. R. Smith, and J. Wolfe. The mechanism producing initial transients on the clarinet. *The Journal of the Acoustical Society of America*, 142(6):3376–3386, 2017.
- B. Andrieux, V. Gibiat, and J. Selmer. Modeling of a woodwind mouthpiece using a finite-element method and characterization of its acoustic input impedance. In *Proceedings of ISMA 2014*, Le Mans, France, 2014.
- B. Andrieux, J. Cottier, J. Selmer, and V. Gibiat. Caractérisation de l’impédance acoustique du couple bec-instrument par l’utilisation d’une méthode mixte mettant en jeu le calcul par éléments finis et la mesure par la méthode TMTC. In *Proceedings of Congrès Français D’Acoustique*, Le Mans, France, 2016.
- V. Aschoff. Experimentelle Untersuchungen an einer Klarinette. *Akustische Zeitschrift*, 1: 77–93, 1936.
- M. Atig, J.-P. Dalmont, and J. Gilbert. Saturation mechanism in clarinet-like instruments, the effect of the localised non-linear losses. *Applied Acoustics*, 65(12):1133–1154, 2004.
- F. Avanzini and M. van Walstijn. Modelling the mechanical response of the reed-mouthpiece-lip system of a clarinet. Part I. A one-dimensional distributed model. *Acta Acustica united with Acustica*, 90(3):537–547, 2004.
- R. D. Ayers, L. J. Eliason, and D. Mahgerefteh. The conical bore in musical acoustics. *American Journal of Physics*, 53(6):528–537, 1985.

- J. Backus. Vibrations of the reed and the air column in the clarinet. *The Journal of the Acoustical Society of America*, 33(6):806–809, 1961.
- J. Backus. Small-vibration theory of the clarinet. *The Journal of the Acoustical Society of America*, 35(3):305–313, 1963.
- J. Backus. The effect of the player’s vocal tract on woodwind instrument tone. *The Journal of the Acoustical Society of America*, 78(1):17–20, 1985.
- N. Bak and P. Dømler. The relation between blowing pressure and blowing frequency in clarinet playing. *Acustica*, 63(3):238–241, 1987.
- A. H. Benade. On the mathematical theory of woodwind finger holes. *The Journal of the Acoustical Society of America*, 32(12):1591–1608, 1960.
- A. H. Benade. Interactions between the player’s windway and the air column of a musical instrument. *Cleve Clin Q*, 53:27–32, 1986.
- A. H. Benade. *Fundamentals of Musical Acoustics*. Dover Publications, Inc, second edition edition, 1990.
- A. H. Benade and D. J. Gans. Sound production in wind instruments. *Annals of the New York Academy of Sciences*, 155(1):247–263, 1968.
- B. Bergeot, A. Almeida, B. Gazengel, C. Vergez, and D. Ferrand. Response of an artificially blown clarinet to different blowing pressure profiles. *The Journal of the Acoustical Society of America*, 135(1):479–490, 2014.
- P. L. Bhatnagar, E. P. Gross, and M. Krook. A Model for Collision Processes in Gases. I. Small Amplitude Processes in Charged and Neutral One-Component Systems. *Physical Review*, 94(3):511–525, 1954.
- S. Bilbao. Direct simulation of reed wind instruments. *Computer Music Journal*, 33(4):43–55, 2009a.
- S. Bilbao. *Numerical Sound Synthesis: Finite Difference Schemes and Simulation in Musical Acoustics*. John Wiley & Sons, 2009b.
- A. Bozorgi, L. Siozos-Rousoulis, S. A. Nourbakhsh, and G. Ghorbaniasl. A two-dimensional solution of the FW-H equation for rectilinear motion of sources. *Journal of Sound and Vibration*, 388:216–229, 2017.
- F. Brogi, O. Malaspinas, B. Chopard, and C. Bonadonna. Hermite regularization of the lattice Boltzmann method for open source computational aeroacoustics. *The Journal of the Acoustical Society of America*, 142(4):2332–2345, 2017.

- S. Carral, V. Lorenzoni, and J. C. Verlinden. Influence of mouthpiece geometry on saxophone playing. In *Proceedings of the 3rd Vienna Talk on Music Acoustics*, Vienna, Austria, 2015.
- D. J. Casadonte. *The Clarinet Reed: An Introduction to Its Biology, Chemistry, and Physics*. Doctoral dissertation, The Ohio State University, Ohio, United States, 1995.
- R. Caussé, J. Kergomard, and X. Lurton. Input impedance of brass musical instruments—comparison between experiment and numerical models. *The journal of the Acoustical Society of America*, 75(1):241–254, 1984.
- A. Chaigne and A. Askenfelt. Numerical simulations of piano strings. I. A physical model for a struck string using finite difference methods. *The Journal of the Acoustical Society of America*, 95(2):1112–1118, 1994.
- A. Chaigne and J. Kergomard. *Acoustics of Musical Instruments*. Springer-Verlag, New York, 2016.
- S. Chapman and T. G. Cowling. *The Mathematical Theory of Non-uniform Gases: An Account of the Kinetic Theory of Viscosity, Thermal Conduction and Diffusion in Gases*. Cambridge University Press, 3rd edition, 1970.
- V. Chatziioannou and A. Hofmann. Modeling articulation techniques in single-reed woodwind instruments. *Proceedings of Meetings on Acoustics*, 19(1):035059, 2013.
- V. Chatziioannou and A. Hofmann. Physics-based analysis of articulatory player actions in single-reed woodwind instruments. *Acta Acustica united with Acustica*, 101(2):292–299, 2015.
- V. Chatziioannou and M. van Walstijn. Reed vibration modelling for woodwind instruments using a two-dimensional finite difference method approach. In *International Symposium on Musical Acoustics*, 2007.
- V. Chatziioannou and M. van Walstijn. A refined physical model of the clarinet using a variable air jet height. In *2008 3rd International Symposium on Communications, Control and Signal Processing*, pages 1297–1301, 2008.
- V. Chatziioannou and M. van Walstijn. Estimation of clarinet reed parameters by inverse modelling. *Acta Acustica united with Acustica*, 98(4):629–639, 2012.
- V. Chatziioannou, A. Hofmann, A. Mayer, and T. Statsenko. Influence of strain-gauge sensors on the vibrational behavior of single reeds. In *Proceedings of Meetings on Acoustics 22ICA*, volume 28, page 035001. Acoustical Society of America, 2016.

- V. Chatziioannou, A. Hofmann, and M. Pàmies-Vilà. An artificial blowing machine to investigate single-reed woodwind instruments under controlled articulation conditions. *Proceedings of Meetings on Acoustics*, 31(1):035003, 2017.
- V. Chatziioannou, S. Schmutzhard, M. Pàmies-Vilà, and A. Hofmann. Investigating clarinet articulation using a physical model and an artificial blowing machine. *Acta Acustica united with Acustica*, 105(4):682–694, 2019.
- J. M. Chen, J. Smith, and J. Wolfe. Experienced Saxophonists Learn to Tune Their Vocal Tracts. *Science*, 319(5864):776–776, 2008.
- J.-M. Chen, J. Smith, and J. Wolfe. Saxophone acoustics: Introducing a compendium of impedance and sound spectra. *Acoustics Australia*, 37(1):18–23, 2009.
- J.-M. Chen, J. Smith, and J. Wolfe. Saxophonists tune vocal tract resonances in advanced performance techniques. *The Journal of the Acoustical Society of America*, 129(1):415–426, 2011.
- L.-J. Chen. *Investigations of Mechanical Stresses within Human Vocal Folds during Phonation*. Doctoral dissertation, Purdue University, 2009.
- B. Cochelin and C. Vergez. A high order purely frequency-based harmonic balance formulation for continuation of periodic solutions. *Journal of sound and vibration*, 324(1-2):243–262, 2009.
- T. Colinot, L. Guillot, and J. Kergomard. Direct and inverse Hopf bifurcation in a neutral delay differential equation model of reed conical instrument. In *Proceedings of the 23rd International Congress on Acoustics*, 2019.
- T. Colinot, P. Guillemain, C. Vergez, J.-B. Doc, and P. Sanchez. Multiple two-step oscillation regimes produced by the alto saxophone. *The Journal of the Acoustical Society of America*, 147(4):2406–2413, 2020.
- T. Colinot, C. Vergez, P. Guillemain, and J.-B. Doc. Multistability of saxophone oscillation regimes and its influence on sound production. *Acta Acustica*, 5:33, 2021.
- C. Coreixas, G. Wissocq, G. Puigt, J.-F. Boussuge, and P. Sagaut. Recursive regularization step for high-order lattice Boltzmann methods. *Physical Review E*, 96(3):033306, 2017.
- C. G. Coreixas. *High-Order Extension of the Recursive Regularized Lattice Boltzmann Method*. Doctoral dissertation, Institut National Polytechnique de Toulouse, 2018.
- W. L. Coyle, P. Guillemain, J. Kergomard, and J.-P. Dalmont. Predicting playing frequencies for clarinets: A comparison between numerical simulations and simplified analytical formulas. *The Journal of the Acoustical Society of America*, 138(5):2770–2781, 2015.

- N. Curle. The influence of solid boundaries upon aerodynamic sound. In *Proceedings of the Royal Society of London A: Mathematical, Physical and Engineering Sciences*, volume 231, pages 505–514. The Royal Society, 1955.
- A. R. da Silva. *Numerical Studies of Aeroacoustic Aspects of Wind Instruments*. Doctoral dissertation, McGill University, Canada, 2008.
- A. R. da Silva and G. P. Scavone. Lattice Boltzmann simulations of the acoustic radiation from waveguides. *Journal of Physics A: Mathematical and Theoretical*, 40(3):397, 2007.
- A. R. da Silva, G. P. Scavone, and M. van Walstijn. Numerical simulations of fluid-structure interactions in single-reed mouthpieces. *The Journal of the Acoustical Society of America*, 122(3):1798–1809, 2007.
- A. R. da Silva, Y. Shi, and G. Scavone. Computational analysis of the dynamic flow in single-reed woodwind instruments. In *Proceedings of Meetings on Acoustics ICA2013*, volume 19, page 035043. ASA, 2013.
- J.-P. Dalmont. Acoustic impedance measurement, part II: A new calibration method. *Journal of sound and vibration*, 243(3):441–459, 2001a.
- J.-P. Dalmont. Acoustic impedance measurement, Part I: A review. *Journal of Sound and Vibration*, 243(3):427–439, 2001b.
- J. P. Dalmont. Analytical and experimental investigation of the dynamic range of conical reed instruments. In *Proceedings of International Symposium on Musical Acoustics*, Barcelona, Spain, 2007.
- J.-P. Dalmont and C. Frappe. Oscillation and extinction thresholds of the clarinet: Comparison of analytical results and experiments. *The Journal of the Acoustical Society of America*, 122(2):1173–1179, 2007.
- J.-P. Dalmont and J. C. Le Roux. A new impedance sensor for wind instruments. *The Journal of the Acoustical Society of America*, 123(5):3014–3014, 2008.
- J. P. Dalmont, B. Gazengel, J. Gilbert, and J. Kergomard. Some aspects of tuning and clean intonation in reed instruments. *Applied Acoustics*, 46(1):19–60, 1995.
- J.-P. Dalmont, J. Gilbert, and J. Kergomard. Reed instruments, from small to large amplitude periodic oscillations and the Helmholtz motion analogy. *Acta Acustica united with Acustica*, 86(4):671–684, 2000.
- J.-P. Dalmont, C. J. Nederveen, and N. Joly. Radiation impedance of tubes with different flanges: Numerical and experimental investigations. *Journal of Sound and Vibration*, 244(3):505–534, 2001.

- J.-P. Dalmont, C. J. Nederveen, V. Dubos, S. Ollivier, V. Meserette, and E. te Sligte. Experimental determination of the equivalent circuit of an open side hole: Linear and non linear behaviour. *Acta Acustica united with acustica*, 88(4):567–575, 2002.
- J.-P. Dalmont, J. Gilbert, and S. Ollivier. Nonlinear characteristics of single-reed instruments: Quasistatic volume flow and reed opening measurements. *The Journal of the Acoustical Society of America*, 114(4):2253–2262, 2003.
- J.-P. Dalmont, J. Gilbert, J. Kergomard, and S. Ollivier. An analytical prediction of the oscillation and extinction thresholds of a clarinet. *The Journal of the Acoustical Society of America*, 118(5):3294–3305, 2005.
- D. d’Humières. Multiple-relaxation-time lattice Boltzmann models in three dimensions. *Philosophical Transactions of the Royal Society of London A: Mathematical, Physical and Engineering Sciences*, 360(1792):437–451, 2002.
- P. Dickens, J. Smith, and J. Wolfe. Improved precision in measurements of acoustic impedance spectra using resonance-free calibration loads and controlled error distribution. *The Journal of the Acoustical Society of America*, 121(3):1471–1481, 2007.
- J.-B. Doc and C. Vergez. Oscillation regimes produced by an alto saxophone: Influence of the control parameters and the bore inharmonicity. *The Journal of the Acoustical Society of America*, 137(4):1756–1765, 2015.
- J.-B. Doc, C. Vergez, and S. Missoum. A minimal model of a single-reed instrument producing quasi-periodic sounds. *Acta Acustica united with Acustica*, 100(3):543–554, 2014.
- D. Dragna, P. Pineau, and P. Blanc-Benon. A generalized recursive convolution method for time-domain propagation in porous media. *The Journal of the Acoustical Society of America*, 138(2):1030–1042, 2015.
- V. Dubos, J. Kergomard, A. Khettabi, J.-P. Dalmont, D. H. Keefe, and C. J. Nederveen. Theory of Sound Propagation in a Duct with a Branched Tube Using Modal Decomposition. *Acta Acustica united with Acustica*, 85(2):153–169, 1999.
- É. Ducasse. *Modélisation et Simulation Dans Le Domaine Temporel d’instruments à Vent à Anche Simple En Situation de Jeu : Méthodes et Modèles*. Doctoral dissertation, Le Mans, 2001.
- E. Ducasse. A physical model of a single-reed wind instrument, including actions of the player. *Computer Music Journal*, 27(1):59–70, 2003.
- M. L. Facchinetti, X. Boutillon, and A. Constantinescu. Numerical and experimental modal analysis of the reed and pipe of a clarinet. *The Journal of the Acoustical Society of America*, 113(5):2874–2883, 2003.

- Z.-G. Feng and E. E. Michaelides. The immersed boundary-lattice Boltzmann method for solving fluid–particles interaction problems. *Journal of Computational Physics*, 195(2): 602–628, 2004.
- D. Ferrand and C. Vergez. Blowing machine for wind musical instrument: Toward a real-time control of the blowing pressure. In *Control and Automation, 2008 16th Mediterranean Conference On*, pages 1562–1567. IEEE, 2008.
- J. E. Ffowcs Williams. Hydrodynamic noise. *Annual Review of Fluid Mechanics*, 1(1): 197–222, 1969.
- J. E. Ffowcs Williams and D. L. Hawkings. Sound generation by turbulence and surfaces in arbitrary motion. *Philosophical Transactions of the Royal Society of London A*, 264 (1151):321–342, 1969.
- J. E. Ffowcs Williams and M. S. Howe. The generation of sound by density inhomogeneities in low Mach number nozzle flows. *Journal of Fluid Mechanics*, 70(3):605–622, 1975.
- N. H. Fletcher and T. Rossing. *The Physics of Musical Instruments*. Springer-Verlag, New York, 2nd edition, 1998.
- V. Fréour, L. Guillot, H. Masuda, S. Usa, E. Tominaga, Y. Tohgi, C. Vergez, and B. Cochelin. Numerical continuation of a physical model of brass instruments: Application to trumpet comparisons. *The Journal of the Acoustical Society of America*, 148(2):748–758, 2020.
- U. Frisch, B. Hasslacher, and Y. Pomeau. Lattice-gas automata for the Navier-Stokes equation. *Physical review letters*, 56(14):1505, 1986.
- C. Fritz and J. Wolfe. How do clarinet players adjust the resonances of their vocal tracts for different playing effects? *The Journal of the Acoustical Society of America*, 118(5): 3306–3315, 2005.
- K.-Y. Fung and H. Ju. Broadband time-domain impedance models. *AIAA journal*, 39(8): 1449–1454, 2001.
- G. Gabard and R. J. Astley. Theoretical model for sound radiation from annular jet pipes: Far- and near-field solutions. *Journal of Fluid Mechanics*, 549:315–341, 2006.
- B. Gazengel. *Caractérisation Objective de La Qualité de Justesse, de Timbre et d’émission Des Instruments à Vent à Anche Simple*. Doctoral dissertation, Université du Maine, 1994.
- B. Gazengel, J. Gilbert, and N. Amir. Time Domain Simulation of Single Reed Wind Instrument. From the Measured Input Impedance to the Synthesis Signal. Where are the Traps? *Acta acustica (Les Ulis)*, 3(5):445–472, 1995.

- B. Gazengel, T. Guimezanes, J.-P. Dalmont, J. B. Doc, S. Fagart, and Y. Léveillé. Experimental investigation of the influence of the mechanical characteristics of the lip on the vibrations of the single reed. In *Proceedings of the International Symposium on Musical Acoustics*, Barcelona, Spain, 2007.
- M. Geier, M. Schönherr, A. Pasquali, and M. Krafczyk. The cumulant lattice Boltzmann equation in three dimensions: Theory and validation. *Computers & Mathematics with Applications*, 70(4):507–547, 2015.
- R. N. Ghosh. Theory of the Clarinet. *The Journal of the Acoustical Society of America*, 9(3):255–264, 1938.
- V. Gibiat and F. Laloë. Acoustical impedance measurements by the two-microphone-three-calibration (TMTTC) method. *The Journal of the Acoustical Society of America*, 88(6):2533–2545, 1990.
- J. Gilbert. *Étude Des Instruments de Musique à Anche Simple: Extension de La Méthode d'équilibrage Harmonique, Rôle de l'inharmonicité Des Resonances, Mesure Des Grandeurs d'entrée*. Doctoral dissertation, Université du Maine, 1991.
- J. Gilbert, S. Maugeais, and C. Vergez. From the bifurcation diagrams to the ease of playing of reed musical instruments. A theoretical illustration of the Bouasse-Benade prescription? In *International Symposium on Music Acoustics (ISMA 2019)*, Proceedings of the International Symposium on Music Acoustics 2019, Detmold, Germany, 2019.
- J. Gilbert, S. Maugeais, and C. Vergez. Minimal blowing pressure allowing periodic oscillations in a simplified reed musical instrument model: Bouasse-Benade prescription assessed through numerical continuation. *Acta Acustica*, 4(6):27, 2020.
- J. Gill, R. Fattah, and X. Zhang. Towards an effective non-reflective boundary condition for computational aeroacoustics. *Journal of Sound and Vibration*, 392(Supplement C):217–231, 2017.
- I. Ginzburg, F. Verhaeghe, and D. d'Humieres. Study of simple hydrodynamic solutions with the two-relaxation-times lattice Boltzmann scheme. *Communications in computational physics*, 3(3):519–581, 2008a.
- I. Ginzburg, F. Verhaeghe, and D. d'Humieres. Two-relaxation-time lattice Boltzmann scheme: About parametrization, velocity, pressure and mixed boundary conditions. *Communications in computational physics*, 3(2):427–478, 2008b.
- N. Giordano and J. W. Thacker. Navier-Stokes-based model of the clarinet. *The Journal of the Acoustical Society of America*, 148(6):3827–3835, 2020.

- S. Glegg and W. Devenport. *Aeroacoustics of Low Mach Number Flows: Fundamentals, Analysis, and Measurement*. Academic Press, 2017.
- H. Grad. Note on N-dimensional hermite polynomials. *Communications on Pure and Applied Mathematics*, 2(4):325–330, 1949a.
- H. Grad. On the kinetic theory of rarefied gases. *Communications on pure and applied mathematics*, 2(4):331–407, 1949b.
- N. Grand, J. Gilbert, and F. Laloë. Oscillation threshold of woodwind instruments. *Acta Acustica united with Acustica*, 83(1):137–151, 1997.
- T. Grothe. *Experimental Investigations of Bassoon Acoustics*. Doctoral dissertation, Technische Universität Dresden, 2013.
- P. Guillemain and F. Silva. De l'utilisation de la décomposition modale pour la synthèse sonore temps réel: écueils et solutions. In *10ème Congrès Français d'Acoustique*, Lyon, 2010.
- P. Guillemain, J. Kergomard, and T. Voinier. Real-time synthesis of clarinet-like instruments using digital impedance models. *The Journal of the Acoustical Society of America*, 118(1):483–494, 2005.
- Y. P. Guo. Application of the Ffowcs Williams/Hawkings equation to two-dimensional problems. *Journal of Fluid Mechanics*, 403:201–221, 2000.
- D. E. Hall. Piano string excitation. VI: Nonlinear modeling. *The Journal of the Acoustical Society of America*, 92(1):95–105, 1992.
- J. Hardy, Y. Pomeau, and O. De Pazzis. Time evolution of a two-dimensional model system. I. Invariant states and time correlation functions. *Journal of Mathematical Physics*, 14(12):1746–1759, 1973.
- X. He and L.-S. Luo. Theory of the lattice Boltzmann method: From the Boltzmann equation to the lattice Boltzmann equation. *Physical Review E*, 56(6):6811, 1997.
- G. W. Hedstrom. Nonreflecting boundary conditions for nonlinear hyperbolic systems. *Journal of computational Physics*, 30(2):222–237, 1979.
- T. Hélie and X. Rodet. Radiation of a pulsating portion of a sphere: Application to horn radiation. *Acta Acustica united with Acustica*, 89(4):565–577, 2003.
- H. Helmholtz. *On the Sensations of Tone as a Physiological Basis for the Theory of Music*. Peter Smith, New York, 2nd english edition edition, 1885.

- F. L. Hemke. *The Early History of the Saxophone*. Doctoral dissertation, The University of Wisconsin, United States, Wisconsin, 1975.
- D. Heubes, A. Bartel, and M. Ehrhardt. Characteristic boundary conditions in the lattice Boltzmann method for fluid and gas dynamics. *Journal of Computational and Applied Mathematics*, 262:51–61, 2014.
- A. Hirschberg, R. W. A. Van de Laar, J. P. Marrou-Maurieres, A. P. J. Wijnands, H. J. Dane, S. G. Kruijswijk, and A. J. M. Houtsma. A quasi-stationary model of air flow in the reed channel of single-reed woodwind instruments. *Acta Acustica united with Acustica*, 70(2):146–154, 1990.
- G. C. J. Hofmans. *Vortex Sound in Confined Flows*. Doctoral dissertation, Technische Universiteit Eindhoven, 1998.
- J. Horstmann. *Hybrid Numerical Method Based on the Lattice Boltzmann Approach with Application to Non-Uniform Grids*. Doctoral dissertation, Université de Lyon, 2018.
- M. S. Howe. *Acoustics of Fluid-Structure Interactions*. Cambridge university press, 1998.
- M. S. Howe. *Theory of Vortex Sound*. Cambridge Texts in Applied Mathematics. Cambridge University Press, 2003.
- A. Huber, P. Romann, and W. Polifke. Filter-Based Time-Domain Impedance Boundary Conditions for CFD Applications. In *ASME Turbo Expo 2008: Power for Land, Sea, and Air*, pages 901–911. American Society of Mechanical Engineers Digital Collection, 2008.
- T. Idogawa, T. Kobata, K. Komuro, and M. Iwaki. Nonlinear vibrations in the air column of a clarinet artificially blown. *The Journal of the Acoustical Society of America*, 93(1):540–551, 1993.
- T. Inamuro. Lattice Boltzmann methods for moving boundary flows. *Fluid Dynamics Research*, 44(2):024001, 2012.
- U. Ingard. Influence of fluid motion past a plane boundary on sound reflection, absorption, and transmission. *The Journal of the Acoustical Society of America*, 31(7):1035–1036, 1959.
- S. Izquierdo and N. Fueyo. Characteristic nonreflecting boundary conditions for open boundaries in lattice Boltzmann methods. *Physical Review E*, 78(4):046707, 2008.
- S. Jaensch, C. Sovardi, and W. Polifke. On the robust, flexible and consistent implementation of time domain impedance boundary conditions for compressible flow simulations. *Journal of Computational Physics*, 314:145–159, 2016.

- H. Jasak. OpenFOAM: Open source CFD in research and industry. *International Journal of Naval Architecture and Ocean Engineering*, 1(2):89–94, 2009.
- N. Jung, H. W. Seo, and C. S. Yoo. Two-dimensional characteristic boundary conditions for open boundaries in the lattice Boltzmann methods. *Journal of Computational Physics*, 302:191–199, 2015.
- R. Kaess, A. Huber, and W. Polifke. A Time-Domain Impedance Boundary Condition for Compressible Turbulent Flow. In *14th AIAA/CEAS Aeroacoustics Conference*, Vancouver, Canada, 2008.
- E. W. Kam, R. M. So, and R. C. Leung. Non-reflecting boundary conditions for one-step LBM simulation of aeroacoustics. In *12th AIAA/CEAS Aeroacoustics Conference (27th AIAA Aeroacoustics Conference)*, page 2416, 2006.
- E. W. S. Kam, R. M. C. So, and R. C. K. Leung. Lattice Boltzmann method simulation of aeroacoustics and nonreflecting boundary conditions. *AIAA journal*, 45(7):1703, 2007.
- S. Karkar, C. Vergez, and B. Cochelin. Toward the systematic investigation of periodic solutions in single reed woodwind instruments. In *International Symposium on Music Acoustics 2010*, 2010.
- S. Karkar, C. Vergez, and B. Cochelin. Oscillation threshold of a clarinet model: A numerical continuation approach. *The Journal of the Acoustical Society of America*, 131(1):698–707, 2012.
- D. H. Keefe. Experiments on the single woodwind tone hole. *The Journal of the Acoustical Society of America*, 72(3):688–699, 1982a.
- D. H. Keefe. Theory of the single woodwind tone hole. *The Journal of the Acoustical Society of America*, 72(3):676–687, 1982b.
- D. H. Keefe. Woodwind air column models. *The Journal of the Acoustical Society of America*, 88(1):35–51, 1990.
- C. Kemp, S. Wang, and G. P. Scavone. Design of a mechanical player system for fatigue-life evaluation of woodwind reeds. In *International Symposium on Music Acoustics 2019*, Detmold, Germany, 2019.
- J. Kergomard. Elementary considerations on reed-instrument oscillations. In *Mechanics of Musical Instruments*. Springer, 1995.
- J. Kergomard, S. Ollivier, and J. Gilbert. Calculation of the Spectrum of Self-Sustained Oscillators Using a Variable Truncation Method: Application to Cylindrical Reed Instruments. *Acta Acustica united with Acustica*, 86(4):685–703, 2000.

- J. Kergomard, P. Guillemain, F. Silva, and S. Karkar. Idealized digital models for conical reed instruments, with focus on the internal pressure waveform. *The Journal of the Acoustical Society of America*, 139(2):927–937, 2016.
- J. Kergomard, P. Guillemain, and C. Vergez. Playing frequency of conical reed instruments. *The Journal of the Acoustical Society of America*, 141(5):3801–3801, 2017.
- W. Kim and H. Choi. Immersed boundary methods for fluid-structure interaction: A review. *International Journal of Heat and Fluid Flow*, 75:301–309, 2019.
- L. E. Kinsler, A. R. Frey, A. B. Coppens, and J. V. Sanders. *Fundamentals of Acoustics*. Wiley, 1999.
- M. J. Krause, A. Kummerländer, S. J. Avis, H. Kusumaatmaja, D. Dapelo, F. Klemens, M. Gaedtke, N. Hafen, A. Mink, R. Trunk, J. E. Marquardt, M.-L. Maier, M. Haussmann, and S. Simonis. OpenLB—Open source lattice Boltzmann code. *Computers & Mathematics with Applications*, 2020.
- T. Krüger, H. Kusumaatmaja, A. Kuzmin, O. Shardt, G. Silva, and E. M. Viggén. *The Lattice Boltzmann Method*. Springer, 2017.
- H. Kühnelt. *Studying the Vortex Sound of Recorder- and Flute-like Instruments by Means of the Lattice Boltzmann Method and Helmholtz Decomposition*. Doctoral dissertation, University of Music and Performing Arts Vienna, Vienna, 2016.
- D. Lagrava, O. Malaspinas, J. Latt, and B. Chopard. Advances in multi-domain lattice Boltzmann grid refinement. *Journal of Computational Physics*, 231(14):4808–4822, 2012.
- J. Latt and B. Chopard. Lattice Boltzmann Method with regularized non-equilibrium distribution functions. *arXiv:physics/0506157*, 2005.
- J. Latt and B. Chopard. Lattice Boltzmann method with regularized pre-collision distribution functions. *Mathematics and Computers in Simulation*, 72(2-6):165–168, 2006.
- J. Latt, O. Malaspinas, D. Kontaxakis, A. Parmigiani, D. Lagrava, F. Brogi, M. B. Belgacem, Y. Thorimbert, S. Leclaire, and S. Li. Palabos: Parallel lattice Boltzmann solver. *Computers & Mathematics with Applications*, 81:334–350, 2021.
- A. Lefebvre. *Computational Acoustic Methods for the Design of Woodwind Instruments*. Doctoral dissertation, McGill University, Canada, 2010.
- A. Lefebvre and G. P. Scavone. A comparison of saxophone impedances and their playing behaviour. In *Proceedings of 2011 Forum Acusticum*, pages 539–544, Aalborg, Denmark, 2011.

- A. Lefebvre and G. P. Scavone. Characterization of woodwind instrument toneholes with the finite element method. *The Journal of the Acoustical Society of America*, 131(4):3153–3163, 2012.
- R. J. LeVeque. *Finite Difference Methods for Ordinary and Partial Differential Equations: Steady-State and Time-Dependent Problems*. Society for Industrial and Applied Mathematics, 2007.
- H. Levine and J. Schwinger. On the radiation of sound from an unflanged circular pipe. *Physical Review*, 73(4):383–406, 1948.
- W. Li, J.-M. Chen, J. Smith, and J. Wolfe. Effect of vocal tract resonances on the sound spectrum of the saxophone. *Acta Acustica United with Acustica*, 101(2):270–278, 2015.
- W. Li, A. Almeida, J. Smith, and J. Wolfe. How clarinetists articulate: The effect of blowing pressure and tonguing on initial and final transients. *The Journal of the Acoustical Society of America*, 139(2):825–838, 2016a.
- W. Li, A. Almeida, J. Smith, and J. Wolfe. The effect of blowing pressure, lip force and tonguing on transients: A study using a clarinet-playing machine. *The Journal of the Acoustical Society of America*, 140(2):1089–1100, 2016b.
- X. Y. Li, X. D. Li, and C. K. W. Tam. Improved multipole broadband time-domain impedance boundary condition. *AIAA journal*, 50(4):980–984, 2012.
- M. J. Lighthill. On sound generated aerodynamically I. General theory. *Proceedings of the Royal Society of London A: Mathematical, Physical and Engineering Sciences*, 211(1107):564–587, 1952.
- M. J. Lighthill. On sound generated aerodynamically II. Turbulence as a source of sound. *Proceedings of the Royal Society of London A: Mathematical, Physical and Engineering Sciences*, 222(1148):1–32, 1954.
- D. P. Lockard. An efficient, two-dimensional implementation of the Ffowcs Williams and Hawkings equation. *Journal of Sound and Vibration*, 229(4):897–911, 2000.
- G. Lodato, P. Domingo, and L. Vervisch. Three-dimensional boundary conditions for direct and large-eddy simulation of compressible viscous flows. *Journal of Computational Physics*, 227(10):5105–5143, 2008.
- V. Lorenzoni and D. Ragni. Experimental investigation of the flow inside a saxophone mouthpiece by particle image velocimetry. *The Journal of the Acoustical Society of America*, 131(1):715–721, 2012.

- V. Lorenzoni, E. L. Doubrovski, and J. C. Verlinden. Embracing the digital in instrument making: Towards a musician-tailored mouthpiece by 3D printing. In *Proceedings of the Stockholm Music Acoustics Conference 2013, SMAC 2013, Stockholm (Sweden), 30 July-3 August, 2013*, 2013.
- C. A. Macaluso and J.-P. Dalmont. Trumpet with near-perfect harmonicity: Design and acoustic results. *The Journal of the Acoustical Society of America*, 129(1):404–414, 2011.
- E. Maestre and G. P. Scavone. Experimental modal analysis/synthesis of saxophone input impedances. *The Journal of the Acoustical Society of America*, 140(4):3092–3092, 2016.
- E. Maestre, G. P. Scavone, and J. O. Smith. Design of recursive digital filters in parallel form by linearly constrained pole optimization. *IEEE Signal Processing Letters*, 23(11):1547–1550, 2016.
- E. Maestre, J. O. Smith, and G. P. Scavone. Analysis-synthesis of saxophone input impedances via recursive parallel filters. In *Proceedings of the 2017 International Symposium on Musical Acoustics*, pages 105–108, Montreal, Canada, 2017.
- E. Maestre, G. P. Scavone, and J. O. Smith. Joint modeling of impedance and radiation as a recursive parallel filter structure for efficient synthesis of wind instrument sound. In *Proceedings of the 21th International Conference on Digital Audio Effects*, pages 157–164, Aveiro, Portugal, 2018.
- C. Maganza, R. Caussé, and F. Laloë. Bifurcations, period doublings and chaos in clarinetlike systems. *EPL (Europhysics Letters)*, 1(6):295, 1986.
- O. Malaspinas. *Lattice Boltzmann Method for the Simulation of Viscoelastic Fluid Flows*. Doctoral dissertation, École Polytechnique Fédérale de Lausanne, 2009.
- O. Malaspinas. Increasing stability and accuracy of the lattice Boltzmann scheme: Recursivity and regularization. *arXiv preprint arXiv:1505.06900*, 2015.
- S. Marié, D. Ricot, and P. Sagaut. Comparison between lattice Boltzmann method and Navier–Stokes high order schemes for computational aeroacoustics. *Journal of Computational Physics*, 228(4):1056–1070, 2009.
- L. Maurin. Confrontation théorie expérience des grandeurs d’entrée d’un exciteur à anche simple. Technical report, Université du Maine, 1992.
- A. Mayer. Riam (reed instrument artificial mouth) a computer controlled excitation device for reed instruments. In *Proceedings of Stockholm Music Acoustics Conference*, volume 1, pages 279–282, 2003.

- C. S. McGinnis and C. Gallagher. The mode of vibration of a clarinet reed. *The Journal of the Acoustical Society of America*, 12(4):529–531, 1941.
- M. E. McIntyre, R. T. Schumacher, and J. Woodhouse. On the oscillations of musical instruments. *The Journal of the Acoustical Society of America*, 74(5):1325–1345, 1983.
- G. R. McNamara and G. Zanetti. Use of the Boltzmann Equation to Simulate Lattice-Gas Automata. *Physical Review Letters*, 61(20):2332–2335, 1988.
- S. Mendez, M. Shoeybi, S. K. Lele, and P. Moin. On the Use of the Ffowcs Williams-Hawkings Equation to Predict Far-Field Jet Noise from Large-Eddy Simulations. *International Journal of Aeroacoustics*, 12(1-2):1–20, 2013.
- R. Mittal and G. Iaccarino. Immersed boundary methods. *Annu. Rev. Fluid Mech.*, 37:239–261, 2005.
- E. Moers and J. Kergomard. On the cutoff frequency of clarinet-like instruments. geometrical versus acoustical regularity. *Acta Acustica united with Acustica*, 97(6):984–996, 2011.
- P. M. Morse, A. S. of America, and A. I. of Physics. *Vibration and Sound*, volume 2. McGraw-Hill New York, 1948.
- A. Muñoz Arancón. *New Techniques for the Characterisation of Single Reeds in Playing Conditions*. Doctoral dissertation, Université du Maine, 2017.
- A. Muñoz Arancón, B. Gazengel, J.-P. Dalmont, and E. Conan. Estimation of saxophone reed parameters during playing. *The Journal of the Acoustical Society of America*, 139(5):2754–2765, 2016.
- A. Muñoz Arancón, B. Gazengel, and J.-P. Dalmont. Comparison of Human and Artificial Playing of a Single Reed Instrument. *Acta Acustica united with Acustica*, 104(6):1104–1117, 2018.
- R. M. Munt. The interaction of sound with a subsonic jet issuing from a semi-infinite cylindrical pipe. *Journal of Fluid Mechanics*, 83(4):609–640, 1977.
- M. K. Myers. On the acoustic boundary condition in the presence of flow. *Journal of Sound and Vibration*, 71(3):429–434, 1980.
- A. Najafi-Yazdi and L. Mongeau. An absorbing boundary condition for the lattice Boltzmann method based on the perfectly matched layer. *Computers & Fluids*, 68:203–218, 2012.
- C. J. Nederveen. *Acoustical Aspects of Woodwind Instruments*. Northern Illinois University Press, 1969.

- Y. Nomura, I. Yamamura, and S. Inawashiro. On the Acoustic Radiation from a Flanged Circular Pipe. *Journal of the Physical Society of Japan*, 15(3):510–517, 1960.
- A. N. Norris and I. C. Sheng. Acoustic radiation from a circular pipe with an infinite flange. *Journal of Sound and Vibration*, 135(1):85–93, 1989.
- M. Ozdemir, V. Chatziioannou, J. Verlinden, G. Cascini, and M. Pàmies-Vilà. Towards 3D printed saxophone mouthpiece personalization: Acoustical analysis of design variations. *Acta Acustica*, 5:46, 2021.
- Y. Özyörük, L. N. Long, and M. G. Jones. Time-domain numerical simulation of a flow-impedance tube. *Journal of Computational Physics*, 146(1):29–57, 1998.
- M. Pàmies-Vilà, A. Hofmann, and V. Chatziioannou. Strain to displacement calibration of single-reeds using a high-speed camera. In *Proceedings of the International Symposium on Music Acoustics*, pages 5–8, 2017.
- M. Pàmies-Vilà, A. Hofmann, and V. Chatziioannou. Analysis of Tonguing and Blowing Actions During Clarinet Performance. *Frontiers in Psychology*, 9, 2018.
- C. S. Peskin. Flow patterns around heart valves: A numerical method. *Journal of computational physics*, 10(2):252–271, 1972.
- C. S. Peskin. The immersed boundary method. *Acta numerica*, 11:479–517, 2002.
- E. Petersen, P. Guillemain, J. Kergomard, and T. Colinot. The effect of the cutoff frequency on the sound production of a clarinet-like instrument. *The Journal of the Acoustical Society of America*, 145(6):3784–3794, 2019.
- E. Petersen, T. Colinot, J. Kergomard, and P. Guillemain. On the tonehole lattice cutoff frequency of conical resonators: Applications to the saxophone. *Acta Acustica*, 4(4):13, 2020a.
- E. A. Petersen, T. Colinot, P. Guillemain, and J. Kergomard. The link between the tonehole lattice cutoff frequency and clarinet sound radiation: A quantitative study. *Acta Acustica*, 4(5):18, 2020b.
- A. D. Pierce. *Acoustics: An Introduction to Its Physical Principles and Applications*. Springer International Publishing, 3 edition, 2019.
- M. R. Pipes. *A Comparison of Saxophone Mouthpieces Using Fourier Analysis to Quantify Perceived Timbre*. Doctoral dissertation, University of Northern Colorado, United States, 2018.

- T. J. Poinsot and S. K. Lele. Boundary conditions for direct simulations of compressible viscous flows. *Journal of computational physics*, 101(1):104–129, 1992.
- W. Polifke and C. Wall. Non-reflecting boundary conditions for acoustic transfer matrix estimation with LES. In *Proceedings of the Summer Program 2002*, pages 345–356, 2002.
- W. Polifke, C. Wall, and P. Moin. Partially reflecting and non-reflecting boundary conditions for simulation of compressible viscous flow. *Journal of Computational Physics*, 213(1):437–449, 2006.
- Y.-H. Qian, D. d’Humières, and P. Lallemand. Lattice BGK models for Navier-Stokes equation. *EPL (Europhysics Letters)*, 17(6):479, 1992.
- Y. Reymen, M. Baelmans, and W. Desmet. Time-domain impedance formulation suited for broadband simulations. In *13th AIAA/CEAS Aeroacoustics Conference (28th AIAA Aeroacoustics Conference)*, page 3519, 2007.
- S. S. Rienstra and A. A. Hirschberg. *An Introduction to Acoustics*. 2004.
- S. Rodriguez, V. Gibiat, A. Lefebvre, and S. Guilain. Input impedance in flow ducts: Theory and measurement. *The Journal of the Acoustical Society of America*, 132(3):1494–1501, 2012.
- T. R. Rose. The Early Evolution of the Saxophone Mouthpiece. *Journal of the American Musical Instrument Society*, 46:99–125, 2020.
- D. H. Rudy and J. C. Strikwerda. A nonreflecting outflow boundary condition for subsonic Navier-Stokes calculations. *Journal of Computational Physics*, 36(1):55–70, 1980.
- R. D. Sandberg and N. D. Sandham. Nonreflecting zonal characteristic boundary condition for direct numerical simulation of aerodynamic sound. *AIAA journal*, 44(2):402–405, 2006.
- G. P. Scavone. *An Acoustic Analysis of Single-Reed Woodwind Instruments with an Emphasis on Design and Performance Issues and Digital Waveguide Modeling Techniques*. Doctoral dissertation, Stanford University, United States, 1997.
- G. P. Scavone. Time-domain synthesis of conical bore instrument sounds. In *Proceedings of the 2002 International Computer Music Conference*, pages 9–15, Göteborg, Sweden, 2002.
- G. P. Scavone. Modeling vocal-tract influence in reed wind instruments. In *Proc. Stockholm Music Acoustics Conference 2003*, pages 291–294. Citeseer, 2003.
- G. P. Scavone and J. O. Smith. A stable acoustic impedance model of the clarinet using digital waveguides. In *Proceedings of the 9th International Conference on Digital Audio Effects*, pages 89–94, Montreal, Canada, 2006.

- G. P. Scavone, A. Lefebvre, and A. R. da Silva. Measurement of vocal-tract influence during saxophone performance. *The Journal of the Acoustical Society of America*, 123(4):2391–2400, 2008.
- J. Schindelin, I. Arganda-Carreras, E. Frise, V. Kaynig, M. Longair, T. Pietzsch, S. Preibisch, C. Rueden, S. Saalfeld, B. Schmid, J.-Y. Tinevez, D. J. White, V. Hartenstein, K. Eliceiri, P. Tomancak, and A. Cardona. Fiji: An open-source platform for biological-image analysis. *Nature Methods*, 9(7):676–682, 2012.
- B. Schuermans, H. Luebcke, D. Bajusz, and P. Flohr. Thermoacoustic Analysis of Gas Turbine Combustion Systems Using Unsteady CFD. In *ASME Turbo Expo 2005: Power for Land, Sea, and Air*, pages 287–297. American Society of Mechanical Engineers, 2005.
- R. T. Schumacher. Ab Initio Calculations of the Oscillations of a Clarinet. *Acta Acustica united with Acustica*, 48(2):71–85, 1981.
- X. Shan and H. Chen. Lattice Boltzmann model for simulating flows with multiple phases and components. *Physical Review E*, 47(3):1815–1819, 1993.
- X. Shan and X. He. Discretization of the Velocity Space in the Solution of the Boltzmann Equation. *Physical Review Letters*, 80(1):65–68, 1998.
- X. Shan, X.-F. Yuan, and H. Chen. Kinetic theory representation of hydrodynamics: A way beyond the Navier–Stokes equation. *Journal of Fluid Mechanics*, 550:413–441, 2006.
- Y. Shi. *A Numerical Framework for Fluid-Acoustic-Structure Interaction in Clarinet-like Instruments*. Doctoral dissertation, McGill University, 2016.
- F. Silva, J. Kergomard, C. Vergez, and J. Gilbert. Interaction of reed and acoustic resonator in clarinetlike systems. *The Journal of the Acoustical Society of America*, 124(5):3284–3295, 2008.
- F. Silva, P. Guillemain, J. Kergomard, B. Mallaroni, and A. N. Norris. Approximation formulae for the acoustic radiation impedance of a cylindrical pipe. *Journal of Sound and Vibration*, 322(1):255–263, 2009.
- F. Silva, C. Vergez, P. Guillemain, J. Kergomard, and V. Debut. MoReeSC: A framework for the simulation and analysis of sound production in reed and brass instruments. *Acta Acustica united with Acustica*, 100(1):126–138, 2014.
- J. O. Smith. Efficient simulation of the reed-bore and bow-string mechanisms. In *Proceedings of the International Computer Music Conference*, pages 275–280, 1986.
- S. D. Sommerfeldt and W. J. Strong. Simulation of a player–clarinet system. *The Journal of the Acoustical Society of America*, 83(5):1908–1918, 1988.

- S. E. Stewart and W. J. Strong. Functional model of a simplified clarinet. *The Journal of the Acoustical Society of America*, 68(1):109–120, 1980.
- G. G. Stokes. On the theories of the internal friction of fluids in motion, and of the equilibrium and motion of elastic solids. *Transactions of the Cambridge Philosophical Society*, 8:287–319, 1845.
- S. H. Strogatz. *Nonlinear Dynamics and Chaos with Student Solutions Manual: With Applications to Physics, Biology, Chemistry, and Engineering*. CRC press, 2nd edition, 2015.
- A. Suss, I. Mary, T. Le Garrec, and S. Marié. Comprehensive comparison between the lattice Boltzmann and Navier–Stokes methods for aerodynamic and aeroacoustic applications. *Computers & Fluids*, 257:105881, 2023.
- P.-A. Taillard. *Theoretical and Experimental Study of the Role of the Reed in Clarinet Playing*. Doctoral dissertation, Université du Maine, 2018.
- P.-A. Taillard and J. Kergomard. An analytical prediction of the bifurcation scheme of a clarinet-like instrument: Effects of resonator losses. *Acta Acustica united with Acustica*, 101(2):279–291, 2015.
- P.-A. Taillard, J. Kergomard, and F. Laloë. Iterated maps for clarinet-like systems. *Nonlinear dynamics*, 62(1):253–271, 2010.
- P.-A. Taillard, F. Silva, P. Guillemain, and J. Kergomard. Modal analysis of the input impedance of wind instruments. Application to the sound synthesis of a clarinet. *Applied Acoustics*, 141:271–280, 2018.
- C. K. Tam and L. Auriault. Time-domain impedance boundary conditions for computational aeroacoustics. *AIAA journal*, 34(5):917–923, 1996.
- M. M. Tekitek, M. Bouzidi, F. Dubois, and P. Lallemand. Towards perfectly matching layers for lattice Boltzmann equation. *Computers & Mathematics with Applications*, 58(5):903–913, 2009.
- K. W. Thompson. Time dependent boundary conditions for hyperbolic systems. *Journal of computational physics*, 68(1):1–24, 1987.
- K. W. Thompson. Time-dependent boundary conditions for hyperbolic systems, II. *Journal of computational physics*, 89(2):439–461, 1990.
- M. van Walstijn. *Discrete-Time Modelling of Brass and Reed Woodwind Instruments with Application to Musical Sound Synthesis*. Doctoral dissertation, University of Edinburgh, Edinburgh, United Kingdom, 2002.

- M. van Walstijn and F. Avanzini. Modelling the mechanical response of the reed-mouthpiece-lip system of a clarinet. Part II: A lumped model approximation. *Acta Acustica united with Acustica*, 93(3):435–446, 2007.
- M. van Walstijn and M. Campbell. Discrete-time modeling of woodwind instrument bores using wave variables. *The Journal of the Acoustical Society of America*, 113(1):575–585, 2003.
- M. van Walstijn, M. Campbell, J. Kemp, and D. Sharp. Wideband measurement of the acoustic impedance of tubular objects. *Acta acustica united with acustica*, 91(3):590–604, 2005.
- J. C. P. van Zon, A. Hirschberg, J. Gilbert, and A. P. J. Wijnands. Flow through the reed channel of a single reed music instrument. *Journal de Physique Colloques*, 51(C2):821–824, 1990.
- J. P. C. van Zon. Stromingsgeinduceerde klepinstabiliteiten. Master’s thesis, Eindhoven University of Technology, 1989.
- E. M. Viggen. *The Lattice Boltzmann Method: Fundamentals and Acoustics*. Doctoral dissertation, Norwegian University of Science and Technology, 2014.
- C. Wagner, T. Hüttl, and P. Sagaut. *Large-Eddy Simulation for Acoustics*, volume 20. Cambridge University Press, 2007.
- S. Wang and G. P. Scavone. Computational Aeroacoustic Modeling of Single-Reed Mouthpiece Using Palabos. In *International Symposium on Music Acoustics 2019*, Detmold, Germany, 2019.
- Z. Wang, J. Fan, and K. Luo. Combined multi-direct forcing and immersed boundary method for simulating flows with moving particles. *International Journal of Multiphase Flow*, 34(3):283–302, 2008.
- T. A. Wilson and G. S. Beavers. Operating modes of the clarinet. *The Journal of the Acoustical Society of America*, 56(2):653–658, 1974.
- G. Wissocq, N. Gourdain, O. Malaspinas, and A. Eyssartier. Regularized characteristic boundary conditions for the Lattice-Boltzmann methods at high Reynolds number flows. *Journal of Computational Physics*, 331:1–18, 2017.
- W. E. Worman. *Self-Sustained Nonlinear Oscillations of Medium Amplitude in Clarinet-Like Systems*. Doctoral dissertation, Case Western Reserve University, 1971.
- F. S. Wyman. *An Acoustical Study of Alto Saxophone Mouthpiece Chamber Design*. Doctoral dissertation, University of Rochester, United States, 1972.

- H. Xu and P. Sagaut. Optimal low-dispersion low-dissipation LBM schemes for computational aeroacoustics. *Journal of Computational Physics*, 230(13):5353–5382, 2011.
- H. Xu and P. Sagaut. Analysis of the absorbing layers for the weakly-compressible lattice Boltzmann methods. *Journal of Computational Physics*, 245:14–42, 2013.
- H. Yokoyama, M. Kobayashi, and A. Iida. Analysis of flow and acoustic radiation in reed instruments by compressible flow simulation. *Acoustical Science and Technology*, 41(5):739–750, 2020.
- C. S. Yoo and H. G. Im. Characteristic boundary conditions for simulations of compressible reacting flows with multi-dimensional, viscous and reaction effects. *Combustion Theory and Modelling*, 11(2):259–286, 2007.
- C. S. Yoo, Y. Wang, A. Trouvé, and H. G. Im. Characteristic boundary conditions for direct simulations of turbulent counterflow flames. *Combustion Theory and Modelling*, 9(4):617–646, 2005.
- T. Yoshinaga, H. Yokoyama, T. Shoji, A. Miki, and A. Iida. Global numerical simulation of fluid-structure-acoustic interaction in a single-reed instrument. *The Journal of the Acoustical Society of America*, 149(3):1623–1632, 2021.
- Z. Zhang. *Experimental Study of Sound Generation by Confined Jets with Application to Human Phonation*. Doctoral dissertation, Purdue University, United States – Indiana, 2002.
- Z. Zhang, L. Mongeau, and S. H. Frankel. Experimental verification of the quasi-steady approximation for aerodynamic sound generation by pulsating jets in tubes. *The Journal of the Acoustical Society of America*, 112(4):1652–1663, 2002.
- W. Zhao, S. H. Frankel, and L. Mongeau. Numerical Simulations of Sound from Confined Pulsating Axisymmetric Jets. *AIAA journal*, 39(10), 2001.
- W. Zhao, C. Zhang, S. H. Frankel, and L. Mongeau. Computational aeroacoustics of phonation, Part I: Computational methods and sound generation mechanisms. *The Journal of the Acoustical Society of America*, 112(5):2134–2146, 2002.
- S. Zhong, X. Zhang, and X. Huang. A controllable canonical form implementation of time domain impedance boundary conditions for broadband aeroacoustic computation. *Journal of Computational Physics*, 313:713–725, 2016.
- J. G. Zhou. Axisymmetric lattice Boltzmann method revised. *Physical review E*, 84(3):036704, 2011.

- 
- Z. Zhou, H. Wang, Z. Zang, and S. Wang. A frequency-domain formulation for predicting multi-frequency noise generated by flows with periodically moving boundaries. *Journal of Theoretical and Computational Acoustics*, 2023.
- Q. Zou and X. He. On pressure and velocity boundary conditions for the lattice Boltzmann BGK model. *Physics of fluids*, 9(6):1591–1598, 1997.